Microcavity Enhancement of Silicon Vacancy Centres in Diamond and Europium Ions in Yttria

Julia Maria Helene Benedikter

München 2019

Microcavity Enhancement of Silicon Vacancy Centres in Diamond and Europium Ions in Yttria

Julia Maria Helene Benedikter

Dissertation
an der Fakultät für Physik
der Ludwig-Maximilians-Universität
München

vorgelegt von
Julia Maria Helene Benedikter
aus München

München, den 14.6.2019

Erstgutachter: Prof. Dr. Theodor W. Hänsch
Zweitgutachter: Prof. Dr. David Hunger
Tag der mündlichen Prüfung: 26.7.2019

meiner Großmutter Maria Kroiß gewidmet

Zusammenfassung

Diverse zur Zeit im Aufstreben begriffene Quanteninformationstechnologien beruhen auf einer effizienten Schnittstelle zwischen ortsgebundenen Quantensystemen und 'fliegenden Qubits', das heißt Photonen, wobei die Licht-Materie-Wechselwirkung durch optische Resonatoren verstärkt werden kann. Diese Arbeit untersucht Festkörperemitter gekoppelt an faserbasierte optische Mikroresonatoren, welche eine hohe Finesse und Modenvolumina in der Größenordnung von wenigen λ^3 mit offenem Zugang sowie vollständiger Durchstimmbarkeit vereinen.

Die Behandlung allgemeiner technischer Aspekte faserbasierter Mikroresonatoren ist ein wichtiger Teil dieser Arbeit. Gewöhnlich werden sie in der Rasterresonatorkonfiguration verwendet, wobei eine nanoskalige Probe, aufgebracht auf einen Planspiegel, bildgebend mit der Lichtmode des Resonators abgerastert wird. Insbesondere wird hier näher auf die resonante Transversalmodenkopplung eingegangen, welche durch die endliche Ausdehnung des Mikrospiegels sowie dessen Abweichungen von der Kugelform hervorgerufen wird und zu zusätzlichen Verlusten, Linienverschiebungen und Modenverzerrungen bei bestimmten longitudinalen Modenordnungen führt. Der Effekt kann präzise modelliert werden um das Verhalten gewisser Resonatorgeometrien vorherzusagen und mögliche Verbesserungen aufzuzeigen. Es wird gezeigt, dass bei der Rasterresonatormikroskopie (engl. *scanning cavity microscopy*) Bildartefakte auftreten, welche durch nahresonante Modenkopplung verursacht werden und empfindlich von der Spiegeltopographie abhängen. Eine detaillierte experimentelle Untersuchung dieser Strukturen macht den Mechanismus, der ihrem Auftreten zu Grunde liegt, deutlich und zeigt, dass sie sich als hochempfindliches Werkzeug zur Charakterisierung qualitativ hochwertiger Spiegel für Präzessionsanwendungen eignen könnten.

In einem Experiment mit dem Ziel, eine effiziente Einzelphotonenquelle bei Umgebungsbedingungen zu verwirklichen, wird die schmale und dominante Null-Phononen-Linie einzelner Silizium-Fehlstellen-Zentren in Nanodiamanten an einen Mikroresonator mit einem Modenvolumen von $3,4\,\lambda^3$ und einer Güte von $1,9 \cdot 10^4$ gekoppelt, wobei effektive Purcell-Faktoren bis zu 9 erreicht werden, sowie Photonenemissionsraten in die Resonatormode von um die 20 MHz. Die interne Ratendynamik des Systems wird durch die Untersuchung leistungsabhängiger Photonenkorrelationen ermittelt und ein verbessertes Ratenmodell zur Beschreibung dieser Dynamik wird eingeführt. Die Ergebnisse sind durch die geringe Quanteneffizienz der Emitter limitiert, welche durch Vergleich zwischen der Verstärkung der Photonenemissionsrate und der Lebenszeitverringerung ermittelt werden kann, sowie durch die erhebliche Größe der Nanodiamanten. Jedoch verspricht der dargelegte Ansatz Einzelphotonenraten in der Größenordnung von GHz für eine verbesserte Probe. Des Weiteren wurden Faserresonatoren mit hohen Güten bis zu $Q = 3,2 \cdot 10^7$ hergestellt, welche das Emissionsspektrum der Silizium-Fehlstellen-

Zentren ausreichend trichtern könnten um ununterscheidbare Einzelphotonen bei Raumtemperatur zu erzeugen.

In einem weiteren, kryogenen Experiment wird die Resonatorkopplung von Europium-dotierten Yttriumoxid-Nanoteilchen gezeigt. Die außergewöhnlich lange Kernspinkohärenzzeit seltener Erden und insbesondere von Europium-Ionen machen sie zu einem vielversprechenden Kandidaten für Knoten in einem Quantennetzwerk, mit optischem Zugang über den $^5\mathrm{D}_0 - ^7\mathrm{F}_0$ Übergang in den 4f-Orbitalen. Diesen nur schwach erlaubten Übergang mit einem optischen Mikroresonator zu verstärken, stellt für einzelne Ionen Photonenemissionsraten in der Größenordnung von 10^5 Hz in Aussicht, was den Weg für eine effiziente Auslese und Manipulation einzelner Ionen ebnen würde. Während erste Messungen bereits die Kopplung eines Ensembles weniger Ionen in einem einzelnen Yttriumoxid-Nanoteilchen an einen Mikroresonator zeigen, ist das Experiment noch durch das hochfrequente mechanische Rauschen beschränkt, welches durch den Kryostaten hervorgerufen wird, was die aktive Stabilisierung des Resonators auf Resonanz verhindert. Um ein stabilisiertes Resonatorsystem bei kryogener Temperatur zu gewährleisten und gleichzeitig die vollständige Durchstimmbarkeit sowie eine hohe Abtastrate des Resonators ermöglichen zu können, wurde ein selbstgebautes kryogeeignetes Nanopositioniersystem realisiert. Es übertrifft bereits kommerziell erhältliche Geräte bezüglich passiver Stabilität und Abtastgeschwindigkeit und hat das Potential das erforderliche Stabilitätsniveau in naher Zukunft zu erreichen. Des Weiteren wird eine neuartige Methode zur Probenpräparation vorgestellt, bei der Europium-dotierte Yttriumoxid-Nanoteilchen in einen Dünnfilm auf dem Spiegel eingebettet werden, was zu einer signifikanten Lebenszeitverkürzung führt und verspricht die Streuverluste im Resonator zu verringern.

Abstract

Various emerging quantum information applications require an efficient interface between stationary quantum systems and 'flying qubits', i.e. photons, where light-matter interaction can be enhanced with optical resonators. This work studies solid state emitters coupled to a fibre-based optical microcavity, which allows for a high finesse and mode volumes on the order of few λ^3 in an open access design, while offering full tunability.

The study of general technical aspects of fibre-based microcavities is an important part of this thesis. They are typically used in the scanning cavity configuration, where a nanoscaled sample on a planar mirror can be imaged by raster-scanning it with the cavity mode. In particular, transverse-mode coupling is explored in detail, where the finite extent as well as shape imperfections of the micromirror are found to be the cause of resonant coupling of transverse modes leading to excessive loss, line shifts, and mode deformations for specific longitudinal mode orders. The effect can be accurately modelled to predict the performance of a particular cavity geometry and improve upon cavity design. In scanning cavity microscopy, near-resonant mode coupling is shown to cause artefacts, which sensitively depend on the mirror topography. A detailed experimental study of these structures reveals the underlying mechanisms of their occurrence, potentially constituting a sensitive tool for characterising high quality mirrors for precision applications.

In an experiment with the aim of creating an efficient single photon source at ambient conditions, the narrow and dominant zero phonon line of single silicon vacancy centres in nanodiamonds is coupled to a microcavity with a mode volume of $3.4\,\lambda^3$ and a quality factor of 1.9×10^4, where effective Purcell factors up to 9 are achieved as well as photon emission rates into the cavity mode on the order of 20 MHz. The internal rate dynamics of the system are determined by studying power-dependent photon correlations and a revised rate model is introduced to describe these dynamics. The results are limited by the small quantum efficiency of the emitters, which could be determined by comparing the enhancement of the photon emission rate with the lifetime reduction, and the large size of the nanodiamonds. However, the presented approach promises single-photon rates on the order of GHz for an improved sample. Furthermore, fibre cavities featuring a high quality factor up to $Q = 3.2 \times 10^7$ are fabricated, which could funnel the silicon vacancy emission spectrum sufficiently to produce indistinguishable single photons at room temperature.

In a further, cryogenic experiment, cavity-coupling of a europium doped yttrium oxide nanoparticles is demonstrated. The exceptionally long nuclear spin coherence time of rare earths and especially europium ions make them a promising candidate for a quantum node, optically accessible via the $^5\mathrm{D}_0 - ^7\mathrm{F}_0$ transition in the 4f orbitals. Enhancing this only weakly allowed transition in an optical microcavity has the prospect of single ion

photon emission rates on the order of 10^5 Hz, which would pave the way for efficient single ion detection and manipulation. While first measurements show cavity coupling of a few-ion ensemble in a single yttrium oxide nanoparticle, the experiment is limited by the high frequency mechanical noise introduced by the cryostat, which prevents locking the cavity on resonance. To allow for an actively stabilised cavity system at cryogenic temperature while maintaining full tunability and fast cavity scanning, a home-built cryocompatible nanopositioning stage is implemented. It already outperforms commercially available options in terms of passive stability and scanning speed and has the potential to reach the required stability level in the near future. Furthermore, a novel sample preparation method, where europium-doped yttrium oxide nanoparticles are embedded into a thin film on a mirror, shows a significant lifetime reduction and promises to reduce scattering loss in the cavity.

Contents

1. Introduction

Since the advent of quantum theory in the early twentieth century, a fascinating and at times mind-boggling cosmos of quantum phenomena has been unravelled. Apart from basic research and having gained a fundamental understanding of basic physical, chemical, and biological phenomena, technological advances based on quantum effects have become indispensable in our modern world. Without claiming completeness, one can mention the transistor, having opened the path to the age of information; nuclear magnetic resonance spectroscopy having brought advances in chemistry and molecular biology as well as its medical application, magnetic resonance tomography; the atomic clock, which enables high precision metrology, is used for tests of general and special relativity, and is the base of the Global Positioning System; and not least the laser, having opened a whole new field of research and a plethora of applications [1].

The invention of the laser has enabled selective manipulation of atomic states, and laser cooling and trapping gives control over individual atoms or ions, allowing to faithfully manipulate and read out their quantum states. Since the first demonstration of a quantum logic gate in 1995 [2], quantum information processing [3, 4] has become a hot field of research, where quantum entanglement and coherence are exploited for the implementation of quantum bits (qubits) and gates. On the theory side, quantum algorithms have been developed [5, 6], while quantum simulation [7, 8] and computation [9] schemes were implemented using various quantum systems. Meanwhile, first quantum computers with tens of qubits are commercially available[1] and the current scaling record of a 72 qubit chip based on superconducting circuits was recently announced by Google[2]. In this pioneering spirit, some sense a new era, which is reflected in the proclamation of the 'second quantum revolution' [10] and the promotion and funding of emerging quantum technologies, such as in the 'European Quantum Flagship' project launched by the European Commission[3]. Despite the advances, there is still a long way to go until quantum computers will outperform classical computers at generally useful tasks. A main challenge is maintaining coherence for a growing number of entangled systems. Quantum error correction protocols are applied to reduce decoherence and sustain the quantum state [11, 12], but require a large overhead of qubits [13], which is why the current system sizes need to be scaled up by several orders of magnitude. A long term goal would be a large, perspectively world-wide, quantum network [14, 15], where individual quantum information processing nodes are connected via photonic links, potentially allowing for large-scale distributed quantum computing [16–18]. This goal motivates the need for efficient light-matter interfaces linking 'stationary' to 'flying'

[1] IBM Q System One, 20 superconducting qubits, www.research.ibm.com/ibm-q/system-one/
[2] March 2018, ai.googleblog.com/2018/03/a-preview-of-bristlecone-googles-new.html
[3] qt.eu

qubits, i.e. photons. Here, solid state quantum emitters coupled to optical microcavities constitute a promising platform.

An important application of a quantum network, based on the impossibility of a simultaneous measurement in two conjugate bases, is secure quantum communication, where a secret key for cyphering information is shared between sender and receiver, the so-called quantum key distribution [19, 20]. More precisely, qubits encoded by the sender in one of two randomly chosen conjugate bases are sent to the receiver, who conducts a measurement in one of the bases, again randomly chosen. Via a classical channel, the basis choices are communicated and the measurement results of the cases were the same bases have been chosen by coincidence are kept as secure key. As any measurement on the quantum channel with the wrong basis can alter the state, a public comparison of a control sample from the secure key can reveal potential eavesdropping. A typical qubit choice is the polarisation of photons, where the two measurement bases are rotated by 45° with respect to each other. This protocol has been successfully implemented, where the record distance of 1200 km was achieved in a satellite-to-ground scheme [21].

Single photon sources Quantum key distribution requires a single photon per bit of information, as a state containing two or more photons is prone to the so-called 'photon-number splitting attack' [22]. As high brightness, on-demand single photon sources, reliably producing photon number states at a high rate are currently still at the level of basic research, one nowadays typically applies faint laser pulses. Restricting the mean photon number to values much smaller than one makes multiple photon states unlikely, but greatly limits the repetition rate. With the decoy-state scheme based on different photon intensities [22–24], the mean photon number can be increased to 0.5, greatly enhancing the secure key rate [25, 26]. Nevertheless, deterministic single photon sources, which are typically based on excited state decay of two-level quantum systems, emit photons in the single photon number state and would outperform weak coherent pulses for device efficiencies larger than 0.5, where the photon rate is limited by the excited state lifetime. This means that quantum communication would strongly benefit from high brightness, high efficiency single photon sources.

Many further applications of single photon sources are based on entanglement and therefore rely on photon indistinguishability, which means that the photons occupy the exact same mode, spatially, temporally, polarisation-wise, and spectrally. As will be introduced in the next section, end to end long-distance quantum communication requires quantum repeaters [27–29], typically based on quantum memories and entanglement swapping. While applying correlated pair sources for this is possible [27, 28], deterministic single photon sources would allow for significantly higher entanglement distribution rates [30, 31]. A more exotic implementation of a quantum repeater, which does not require a quantum memory, is the all-optical quantum repeater [32, 33], which is based on photonic cluster states [34]. These demand high purity deterministic single photon sources at a high level of indistinguishability, efficiency, and brightness [26].

Furthermore, deterministic single photon sources play an important role in photonic quantum information processing. Quantum states can be encoded in photons using

several degrees of freedom like polarisation, orbital angular momentum, photon number, time bin, and optical path states. Photons have the advantage that they are fast, hardly interact with the environment, and their quantum state can be well manipulated [35, 36]. All-optical quantum computing uses linear optical elements such as beam splitters to implement quantum gates. Typically, such schemes require single photons [37] and have the substantial drawback that deterministic entanglement is not possible, which is compensated by a large circuit overhead [38]. Scalable fault-tolerant all-optical quantum computing protocols are again based on photonic cluster states and set high requirements on the purity, efficiency, and indistinguishability of the single photon source [26, 38]. A more short term goal compared to programmable linear quantum computing are photonic quantum simulators, which typically consist of single photon sources, a waveguide circuit, and a single photon detector array and apply boson sampling and photonic quantum walks [39, 40]. They are supposed to simulate less easily accessible quantum systems as for instance in chemistry or solid state physics. The number of correlated photons and the required level of indistinguishability are significantly reduced in this case as compared to linear quantum computing [26, 41], such that providing suitable single photon sources for optical quantum simulation seems feasible.

Single photon emission has been observed from various quantum systems, where solid state systems are particularly promising in terms of scalability, efficiency, and a possible integrated design. While high purity, high indistinguishability single photon sources using quantum dots in micro-resonating structures have been demonstrated [42–44], they require a cryogenic environment, which makes them intricate and expensive. This motivates the efforts taken towards a solid-state-based, high performance single photon source, which can be operated in an ambient environment. Suitable candidates are colour centres in diamond, where in particular the nitrogen vacancy (NV) and recently also the silicon vacancy (SiV) centres have been investigated in greater detail. For an enhanced and well collectible emission, it is useful to couple the colour centres to optical resonators or plasmonic structures. The NV centre features a dominant broad phonon side band, which can be enhanced by a broad line resonator to obtain a bright broadband source [45, 46]. Alternatively, narrow-line resonators can selectively enhance part of the band, leading to a narrowband tunable source [47, 48]. The SiV centre features an inversion symmetry, which makes it less susceptible to fluctuations of the local field and reduces the coupling to phonons [26]. This leads to a narrow bright zero phonon line, which comprises 70% of the total fluorescence light and whose linewidth can be below 1 nm [49].

In the case of relatively broad-band solid state emitters, the Purcell factor, being the enhancement factor of the spontaneous emission rate in an optical resonator, scales with the linewidth of the emitter and the inverse mode volume of the resonator. This motivates coupling narrow-line SiV centres to optical microcavities with a minimised mode volume to achieve a bright, efficient single photon source at room temperature [50, 51]. In this work, single narrow-line SiV centres were coupled to fibre-based optical microcavites [52], demonstrating a single-photon source with high efficiency, increased emission rate, and improved spectral purity compared to the intrinsic emitter proper-

ties [53]. As shall be motivated, this scheme has the potential for creating an efficient indistinguishable single photon source at room temperature [54].

Quantum repeaters, memories, and registers The no-cloning theorem, being at the heart of quantum key distribution, is also the major obstacle for scalability to larger distances: As a measurement destroys the quantum state, the signal cannot easily be amplified, such that transmission losses and decoherence limit the possible secure communication distances. If one does not want to rely on trusted repeater nodes [55, 56], quantum repeaters [27, 57] need to be applied, where large distance entanglement is established by dividing the distance by quantum nodes and combining entanglement swapping and purification with quantum memories [58]. While this scheme was successfully demonstrated in proof of concept experiments [59], a central remaining obstacle is the lack of a quantum memory with a sufficiently long storage time and a high retrieval efficiency. It should be noted that quantum communication is not restricted to cryptography, i.e. quantum key distribution, were encoded classical information is supposed to be transmitted, but comprises a wider field including long distance teleportation [60] of quantum states in a future quantum network [14, 15] and large-scale distributed quantum computing [16–18], which require long-range entanglement. To teleport a quantum state, the two qubits of a Bell state are shared between sender and receiver. Performing a Bell measurement on the qubit of the sender and the state to be teleported projects this state into one of four Bell states. Communicating the outcome of this measurement to the receiver allows retrieving the original state by applying a unitary operation to the receiver qubit. The crucial point is that the qubit needs to be stored until the classical information is received explaining the need for a quantum memory (except for the rather exotic case of an all-optical quantum repeater [32, 33]) [58]. For entanglement distribution around the globe, storage times on the order of at least 100 µs would be necessary.

For a quantum memory, the quantum state of a photon must be coherently mapped to a stationary qubit. This can, for example, be achieved by electromagnetically induced transparency or off-resonant Raman interaction in warm or ultracold atomic gases [61, 62], which however still suffer from low retrieval efficiencies. Rare earth ion doped crystals constitute a particularly promising candidate for a quantum node as they feature an outstanding nuclear spin coherence with time constants up to hours [63], unique in the solid state. The nuclear spin can be assessed optically via $4f - 4f$ transitions, which also show an exceptional coherence [64–66]. Various implementations of quantum memories have been demonstrated in ensembles of rare earth ions using techniques like optical gradient echo [67] and an atomic frequency comb [65, 68–74]. The latter harnesses the broad inhomogeneous line of the ensemble, where equally spaced spectral holes allow for a delocalised storage of a photon, being released again as photon echo after a rephasing time determined by the comb spacing. The main figures of merit are the storage time and the retrieval efficiency, where the current best values are tens of seconds [75] and 70% efficiency [67], which can however not yet be achieved together. These ensemble-based approaches bear the disadvantage of not being easily scalable to a universal quantum

node allowing for performing quantum computational operations, which motivates the interest in addressing single ions and harnessing their interactions with each other for the implementation of quantum gates.

Due to the dipole-forbidden character of the 4f − 4f transitions, the emission rates are very low, making the read-out of single ions challenging. This motivates coupling the optical transition to a microcavity, an approach, which recently led to the detection of single erbium and neodymium ions [76, 77]. For rare earth ions featuring zero total electron spin, which for example is the case for europium ions, the large electric dipole interactions between dopant ions in their host matrix leads to an excitation blockade effect, similar to Rydberg blockade, which can be used to perform quantum gates [78, 79]. This implies that some rare earth doped crystals have the potential to be used as a quantum register, consisting of several qubits which can be addressed individually and coherently manipulated [80].

Europium-doped yttrium oxide nanocrystals feature a nuclear spin coherence time of 8 ms [81] and a homogeneous linewidth of 45 kHz (at 1.5 K) [82–84], extraordinary values in a nanoscale host. In this work, europium ions are coupled to a fibre-based microcavity, demonstrating first signatures of Purcell enhancement and spectroscopy of a few ion ensemble [85]. Applying a high finesse resonator, this approach has the potential for efficient read-out of single europium ions opening the path for the implementation of quantum logic with very beneficial coherence properties. As the narrow resonance linewidth of a high finesse cavity requires a high relative length stability of the cavity mirrors on the order of 1 pm in a cryogenic environment, a cryocompatible nanopositioning stage was designed in the course of this work, which combines a high passive stability with full tunability.

Fibre-based microcavities For an enhanced light-matter interaction, the solid state quantum emitters are coupled to an optical microcavity, which constitutes an efficient interface between 'stationary' and 'flying' qubits. Due to a modified density of states in an optical resonator, the excited state decay rate of a quantum system is suppressed or enhanced according to Fermi's golden rule, depending on whether or not the resonance condition is met, with the Purcell factor describing the modified rate with respect to the free space emission rate. In addition to an enhanced spontaneous decay (which implies a lifetime reduction), the emission into the single cavity mode is almost unity for a high Purcell factor, allowing for an efficient collection of the light. For a system with multiple decay channels, the branching ratio of the transition in resonance with the cavity is enhanced. Furthermore, enhancement and filtering with a narrow cavity resonance leads to a spectral compression of the broadband emission spectrum typical in the solid state. The Purcell factor scales inversely with the resonator's mode volume, which explains the emergence of various micro-resonating structures in recent years.

While some monolithic resonator platforms like photonic crystal cavities [50, 86–88] and micropillar cavities [43, 44, 89, 90] aim for minimal mode volume, they have the drawback of being rather inflexible: Their tunability is limited and an individual cavity needs to be machined for every single emitter, impeding comparability. The fibre-based

microcavity is a miniaturised Fabry-Pérot style resonator, which comprises at least one micro-machined mirror on the end-facet of an optical fibre [52, 91]. It thereby allows for an ultra-small mode volume [46] in combination with an open access design, full tunability, and easy coupling to the cavity mode via the fibre. For the experiments presented in this work, the scanning cavity design was used, where a fibre mirror is combined with a macroscopic planar mirror. The nano-scaled sample placed onto the latter can then be spatially imaged by raster-scanning with the fibre, where the cavity mode acts as a scanning probe [92, 93]. This approach is particularly useful for heterogeneous systems, as it allows individual addressing of different nanoparticles containing quantum emitters (whose properties typically vary), as well as considering the empty cavity as comparison.

Apart from the study of quantum emitters coupled to a microcavity, the behaviour of fibre-based microcavities themselves is a major point of interest in this work. In contrast to macroscopic resonators, the cavity mode size can be comparable to the extent of the micromirror, such that diffraction loss becomes important. Moreover, the profile shape of the machined mirror deviates from a perfect sphere leading to mode deformation and coupling between simultaneously resonant transverse modes. A reduced finesse and transmission for certain longitudinal mode orders is the consequence, which is modelled as well as studied experimentally [94]. In scanning cavity microscopy, slight imperfections in the surface topography of the planar mirror can shift transverse modes in and out of resonance with each other leading to distinct measurement artefacts, which reveal characteristics of the mirror [95].

Scope of this work In chapter 2, I shall concentrate on the fundamentals of cavity-enhanced light matter interaction, where the use of microcavities will be motivated, alluding to the different varieties, their typical specifications, and fields of use. Next, the fibre-based microcavity is explained in more detail, stating all important figures of merit like the finesse, the quality factor, and the resonance condition. A section on light matter interaction in resonators follows, distinguishing between the strong and weak coupling regime depending on the relations of the central cavity parameters. The Purcell effect shall be treated for both broad and narrow line emitters, also explaining effects on collection efficiency and branching ratio.

Chapter 3 deals with technical considerations on fibre-based microcavities, starting with a description of the machining process and the typically accessible mirror geometries. A section on transverse-mode coupling follows, which first explains the general mechanism how a non-perfect mirror profile can lead to coupling of simultaneously resonant transverse modes, coming with a broadening of the cavity line. A model based on resonant state expansion accurately reproduces the experimental findings. Artefacts in scanning cavity microscopy are traced back to a topography of the macroscopic mirror deviating from planar as well as surface roughness. I shall explain how transverse-mode coupling sets limits on possible cavity geometries and present extreme cases of cavity design. The following section deals with dielectric mirrors and how transmission and field distribution can be modelled, also alluding to the directed radiation of a dipole on such a mirror. The chapter is concluded by a section on absorption and scattering,

where measurements are presented, which show a recollection effect of scattered light by the cavity mode.

In chapter 4, the experiments on cavity coupling of single SiV centres with the aim of creating an efficient single photon source are presented. The chapter starts off by recapitulating single photon sources, also going into a theoretical description of photon correlations, before introducing colour centres in diamond in general and the SiV centre in particular, stating its major properties as well as treating nanodiamonds as host material. After explaining the experimental setup, the sample shall be characterised in detail in terms of suitability of certain emitters, excited state lifetime, brightness, and photostability. Comparing the emission of the SiV centres in free space to the cavity-coupled case, a lifetime reduction and enhanced emission is observed, including an estimate for the Purcell factor. From second order correlation measurements, the rate dynamics of the system is deduced, proposing a modified model for its description. The chapter concludes with an outlook on an indistinguishable single photon source at room temperature, which would be possible with readily available cavities and an improved sample.

Chapter 5 presents the rare earth ion project, where europium-doped yttrium oxide nanoparticles are coupled to a cavity. After having introduced rare earths and their role in current research, the europium ion is treated, explaining its level scheme and coherence properties. A sample preparation method is described, where embedding the nanoparticles into a thin film is shown to significantly reduce the lifetime. After treating the cryogenic cavity setup, first spectroscopic measurements of a europium few ion ensemble are presented.

The home-built cryocompatible nanopositioning stage is introduced in chapter 6, alluding to the required stability and the importance of passive stiffness. The mechanical design as well as cavity stabilisation schemes are treated, discussing noise spectra and possible ideas for a further optimisation of the setup.

The last chapter summarises the work and gives an outlook.

2. Fundamentals of cavity-enhanced light matter interaction

After C. Fabry and A. Pérot had first described a simple optical resonator consisting of two planar semi-transparent mirrors in 1899 [96], such structures were primarily used for spectroscopic and metrologic purposes as well as spectral light filtering. But already the inventors anticipated a rich future of their interferometer: 'We believe that the applications of these fringes are far from being exhausted.' [97] Nevertheless, it took about half a century until E. M. Purcell predicted that the spontaneous emission of an atom can be enhanced in a (radio-frequency) resonator in 1946 [98]. For decades, this effect awaited experimental proof. In the meantime, the optical resonator led to the invention of the maser in 1955 by Gordon, Zeiger, and Townes [99] and not least to the laser in 1960 by Maiman [100]. Not until 1983 was Purcell enhancement shown experimentally for Rydberg atoms flying through a high-Q millimeter-wave superconducting cavity [101]. The proof for an off-resonant cavity and therefore a reduced density of states leading to Purcell suppression was brought soon after [102]. In the optical domain, the first demonstration of Purcell enhancement and suppression was performed by Heinzen et al. [103] making use of a confocal resonator and therefore taking advantage of mode degeneracy. Other groundbreaking advances, especially in the field of cavity quantum electrodynamics (CQED) shall not be discussed here, but can for example be found in [1]. In the context of emerging quantum technologies, optical resonators play a crucial role in establishing an efficient interface between matter-based quantum systems and photons. They are applied to efficiently extract single photons from quantum emitters and to create efficient spin-photon interfaces, building blocks for a future quantum network [14, 15].

In this chapter, I shall focus on the enhanced light matter interaction in optical microcavities. First, the need for a reduced mode volume is motivated and different types of microcavities are introduced and compared. Then, I will focus on fiber-based microcavities and introduce the central figures of merit before treating the different coupling regimes of light and matter in a cavity and the Purcell effect.

2.1. Microcavities

2.1.1. Motivation and classification

One of the main reasons for coupling quantum emitters or nanomaterials to optical resonators is a more efficient interaction of light and matter. As shall be discussed in more detail in section 2.2.2.2, a quantum emitter experiences an enhanced spontaneous

emission rate γ when coupled to an optical resonator due to an increased density of modes and a larger vacuum field as compared to free space (γ_0). The figure of merit is the Purcell factor

$$C = \frac{\gamma}{\gamma_0} = \frac{3}{4\pi^2}\left(\frac{\lambda}{n}\right)^3 \frac{Q}{V_m}, \tag{2.1.1}$$

where λ is the emission wavelength, Q the quality factor of the cavity, and V_m its mode volume. Not only can the emission be increased, but a welcome side-effect is that the higher the Purcell factor, the higher the fraction

$$\beta = \frac{C}{C+1} \tag{2.1.2}$$

of light which is emitted into the single well-collectible cavity mode. So in contrast to a hard to collect dipole mode, collection efficiencies close to 1 can be achieved. Furthermore, Purcell enhancement on resonance and suppression off resonance lead to a spectral compression of broad emission lines, meaning a combination of spectral filtering and enhancement.

If the emitter linewidth is not negligible compared to the width of the cavity resonance, the quality factor of the cavity needs to be replaced by an effective quality factor

$$Q_{\text{eff}} = \left(Q_c^{-1} + Q_e^{-1}\right)^{-1} \tag{2.1.3}$$

containing both the quality factor of the cavity Q_c and the quality factor of the emitter $Q_e = \nu/\delta\nu$ with the emission frequency ν and the linewidth $\delta\nu$. It is limited to $Q_{\text{eff}} = Q_e$ for $Q_c \gg Q_e$. So especially for broad line emitters in the solid state, it is crucial to reduce the mode volume as much as possible. This fundamental thought of an increased Purcell factor achieved by a reduction of the mode volume led to the invention of a plethora of micro- and nanoscaled resonator structures, each optimised to fit a certain purpose. A good overview of the field is provided by Vahala [104]. Typically, one has to find a trade-off between quantities like Q and V_m, but also take into account the outcoupling efficiency, tunability, machining limitations, and scalability.

Cavity experiments with trapped atoms or ions require a rather large mirror distance on the order of a few tens of µm to mm to accompany trapping beams or keep charged particles at a distance, such that air-slit Fabry-Pérot bulk optical cavities with high reflectivity distributed Bragg reflectors (DBR) are commonly used. Due to long cavity length, high quality factors on the order of 10^8 are achieved at the cost of a relatively large mode volume $V_m \sim 10^4 - 10^6\lambda^3$, leading to Purcell factors $\sim 10^2$ [105, 106]. In the solid state, a monolithic two mirror design can greatly reduce the mode volume while keeping up a high quality factor, however losing full tunability. A typical design are micropillar cavities, which consist of two DBR layer stacks with a dielectric spacer layer containing the emitter in between. Lateral mode confinement is achieved by etching the diameter of the structures down to the order of µm. As the mirror distance can be chosen almost arbitrarily small (few $\lambda/2$), small mode volumes of around $5\,(\lambda/n)^3$ are

possible. Together with quality factors of 10^5 [89], the ideal Purcell factor can be on the order of 10^4. With these micropillars, the to date highest indistinguishability, high efficiency single photon sources have been demonstrated with self-assembled quantum dots [43, 44, 90].

Beyond Fabry-Pérot style optical resonators where the light circulates between two mirrors, other ways of mode confinement can be exploited: In whispering gallery mode (WGM) resonators, total internal reflection at the surface of a dielectric microdisc, microsphere or microtoroid leads to the occurrence of a ring-shaped light mode along the circumference. Light is typically brought into the resonator via evanescent coupling to a tapered optical fibre or prism, which allows tuning the coupling by changing the distance between incoupling device and resonator. This approach allows for quality factors $> 10^9$ for resonators with a few hundred µm diameter at the cost of a large mode volume [107]. Optimising the ratio Q/V_m leads to significantly smaller radii of a few tens of microns (with $Q \sim 10^8$,$V_m < 200\,(\lambda/n)^3$), where the Purcell factor may reach $\sim 10^5$ [108]. WGM resonators are used for CQED applications [109, 110], but also for biosensing [111–113].

The smallest mode volumes can be achieved with photonic crystal cavities, making them most suitable for broad line solid state emitters. The cavity consists of a photonic crystal having its bandgap at the wavelength to be enhanced and a 'defect', i.e. missing hole(s), leading to field enhancement, where the emitter is placed. The strength of these resonators are the ultrasmall mode volumes, which can be $< \lambda^3$. Q-factors range from 10^2 to 10^5, yielding Purcell factors up to 10^5, possibly 10^6 in the infrared. The structures can be 3-, 2-, or 1-dimensional, where light confinement in the other dimensions is granted by wave guidance. They can, in many cases, be directly machined into the host material of the quantum emitter like for colour centres in diamond and quantum dots in semiconductors [50, 86–88]. Drawbacks are the limited tunability of photonic crystal cavities and the missing flexibility and comparability, as an individual cavity is needed for each emitter. Moreover, the exact positioning of the emitter in the field maximum is not trivial.

2.1.2. Fibre-based microcavities

Fibre-based microcavities consist of a micromirror machined on the end-facet of an optical fibre [52, 91]. They combine an ultrasmall mode volume with full tunability and an open access design making them useful for numerous applications ranging from imaging and sensing [92, 93], over cavity optomechanics [114–116], cavity enhanced Raman spectroscopy [117], and experiments with atoms [118–120] and ions [121–123] to various cavity-coupled solid state quantum emitters like colour centres in diamond [46, 47, 53, 124–126] (see chapter 4), transition metal dichalcogenides [127, 128], quantum dots [129, 130], and rare earth ions [85] (see chapter 5). The light can be conveniently coupled into the cavity through the single mode optical fibre. The outcoupling mirror can also be a micromachined fibre-mirror on a multimode fibre, as can be seen in Fig. 2.1.1(b), or a macroscopic planar mirror (Fig. 2.1.1(a)). The latter geometry, the scanning cavity configuration, allows for lateral scanning such that a sample placed on the planar mirror can be moved into the cavity mode on demand. This opens up the

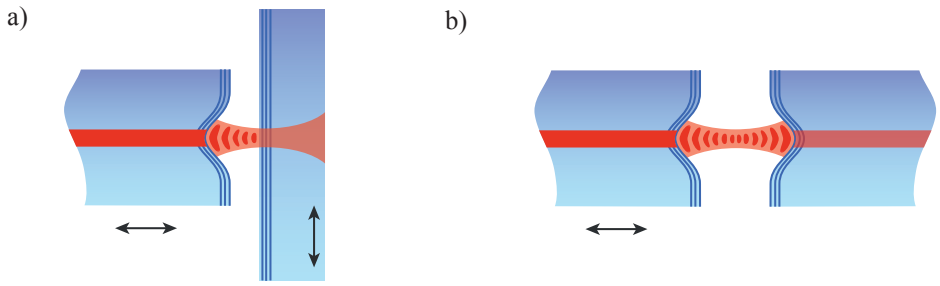

Figure 2.1.1.: (a) Schematic of scanning cavity configuration with a fibre mirror on the left and a laterally movable planar mirror on the right. (b) Fibre-fibre configuration consisting of two fibre mirrors.

possibility of imaging the sample and comparing a cavity-emitter coupled system to the bare cavity or to other emitters. The experiments presented in this work make use of this flexible design.

Before discussing light-matter interaction in cavities, I will give a brief overview of some basic figures of merit of optical resonators in general and fiber-based microcavities in particular. A more detailed treatment can for example be found in Saleh and Teich [131], Hodgson and Weber [132], Zinth [133] and in the theses of Matthias Mader [93] and Hanno Kaupp [126].

Free spectral range Considering a simple Fabry-Pérot interferometer with two planar mirrors facing each other, light can circulate and build up a standing wave when the resonator length d is equal to a multiple of half the wavelength λ of the incoming light. The cavity becomes resonant and the transmission through the outcoupling mirror maximal, in the ideal loss-less case unity. Off resonance, the light is reflected and the transmission in the ideal case goes to zero. The spectral distance between neighbouring resonances is referred to as the free spectral range (FSR) and is given by

$$\Delta\nu = \frac{c}{2d}. \tag{2.1.4}$$

Hanno Kaupp achieved the shortest possible Fabry-Pérot cavity with $d = \lambda/2$ using silver coated mirrors and a very shallow fibre profile [46], but even for typical microcavity mirror separations of a few µm, the FSR is easily on the order of tens of THz.

Losses and lineshape In real resonators with a mirror reflectivity $0 < R < 1$ (referring to intensity) the resonance is not infinitely sharp but is rather described by an Airy function. The light does not infinitely oscillate but eventually gets lost by being transmitted through the mirrors at transmittivities T_1 and T_2, respectively. Other loss channels are absorption and scattering by the two mirrors, A_1 and A_2, as well as diffraction loss D, which shall be summarised by the loss $L = A_1 + A_2 + D$. In case of the high reflectivity dielectric mirror coatings used for the microcavities, the transmittivities can be as low as

10 ppm and are not higher than $1.5 \cdot 10^{-3}$ for the experiments discussed here. Absorption and scattering loss per mirror depend on the wavelength (larger for smaller wavelength) and the coating. They range from 2 ppm (for the planar mirror in [134], calculation by Thomas Hümmer) to around 30 ppm for Layertec mirrors [135]. Diffraction losses depend on the exact geometry of the microcavity and are discussed in section 3.2. As the total losses $T_1 + T_2 + L \ll 1$, the lineshape can be approximated by a Lorentzian. The ratio of the transmitted intensity I_T with respect to the initial intensity I_0 before the cavity as a function of the frequency is then given by

$$\frac{I_T}{I_0} \approx T_{\max} \cdot \frac{\left(\frac{\delta\nu}{2}\right)^2}{\left(\frac{\delta\nu}{2}\right)^2 + (q\Delta\nu - \nu)^2}, \quad q \in \mathbb{N}. \tag{2.1.5}$$

$$\delta\nu = \Delta\nu \cdot \frac{T_1 + T_2 + L}{2\pi} \tag{2.1.6}$$

is the full width at half maximum (FWHM) of the resonance and the pre-factor

$$T_{\max} = \frac{4T_1T_2}{(T_1 + T_2 + L)^2} \tag{2.1.7}$$

gives the maximal transmission on resonance.

Finesse As $\Delta\nu$ decreases linearly with the mirror separation, so does $\delta\nu$, but their ratio

$$\mathcal{F} = \frac{\Delta\nu}{\delta\nu} \tag{2.1.8}$$

$$= \frac{2\pi}{T_1 + T_2 + L}, \tag{2.1.9}$$

the so-called finesse, is constant (for a non-perfect geometry it can vary, see section 3.2). The second equality is again an approximation for small total losses. An intuitive picture for this quantity is the number of roundtrips the light takes until it leaves the cavity: The ringdown time τ of the resonator is given by

$$\tau = \frac{d}{\pi c} \cdot \mathcal{F}, \tag{2.1.10}$$

which means that after τ only 1/e of the initial energy remains in the cavity.

$$\kappa = 1/\tau = 2\pi\delta\nu \tag{2.1.11}$$

is called the cavity decay rate, corresponding to the linewidth in angular frequency. The highest finesse, achieved with a fibre-based microcavity, was 190 000 [136].

Quality factor The quality factor is a figure of merit of resonators in general and is defined by

$$Q = \frac{2\pi \cdot \text{stored energy}}{\text{energy loss per cycle}} = \frac{\nu}{\delta\nu} \tag{2.1.12}$$

$$= q\mathcal{F}, \tag{2.1.13}$$

where $q \in \mathbb{N}$ is the longitudinal mode order with $d = q\frac{\lambda}{2}$ [1] and ν is the resonance frequency. Equation 2.1.13 shows that a high quality factor implies a large mirror separation and it is readily apparent that one cannot maximise Q and reduce V_m at the same time, but rather has to find a suitable trade-off, i.e. maximise the ratio Q/V_m. For Fabry-Pérot cavities, this is achieved at the shortest mirror separation. While the quality factor is on the order of the finesse for the shortest cavities, it can reach up to 10^8 in fibre cavities [137], where up to 10^7 was measured in the scanning cavity configuration (see section 3.3.3).

Intra-cavity power Due to the circulating character of the standing wave light field, the intra-cavity power builds up to

$$P_{\text{peak}} \approx 4T_1 \left(\frac{\mathcal{F}}{\pi}\right)^2 P_{\text{in}} \tag{2.1.14}$$

at an antinode, where P_{in} is the incoming power and T_1 the transmittivity of the in-coupling mirror. The temporally averaged power on an antinode is given by $P_{\text{peak}}/2$. A detailed treatment can be found in [138].

Stability For beam confinement, resonators typically have at least one concave mirror with a radius of curvature r_C to refocus the beam on every round trip. A resonator is called stable, if the beam keeps a constant size and does not diverge in consecutive cycles. Using ray transfer matrices, one can show that this is the case when the stability condition

$$0 < \left(1 - \frac{d}{r_{C,1}}\right)\left(1 - \frac{d}{r_{C,2}}\right) < 1 \tag{2.1.15}$$

is met. For the scanning cavity design used in this work, where one mirror is planar ($r_C = \infty$), this condition reduces to

$$r_C > d. \tag{2.1.16}$$

However, this only strictly holds for spherical mirrors, while the non-perfect geometry of fibre mirrors introduces diffraction losses, which decreases the stability limit (see section 3.2). A conclusion is that one cannot indefinitely increase the Q-factor by increasing the mirror separation, but is limited by the radius of curvature.

[1] This expression is only approximately correct as it lacks the Gouy-phase, see equation 2.1.32.

Gaussian beams In the paraxial approximation, which assumes that the component of the electric field perpendicular to the optical axis changes slowly, the Helmholtz equation is solved by Gaussian beams

$$\Phi(r,\, z) = \frac{\sqrt{2}}{\sqrt{\pi} w} \exp\left(-\frac{r^2}{w^2} - i\left(kz + k\frac{r^2}{2R} - \theta\right)\right), \tag{2.1.17}$$

where z is the coordinate along the optical axis and r the distance from it. A derivation can be found in [131]. The following definitions and expressions are used:

- The minimal $1/e^2$ beam radius w_0 at the focus $z = 0$, called beam waist.
- The Rayleigh range z_0 giving the distance from the focus where the beam radius has increased to $\sqrt{2}w_0$:
$$z_0 = \frac{\pi w_0^2}{\lambda} \tag{2.1.18}$$
- The $1/e^2$ beam radius as a function of z:
$$w = w\,(z) = w_0\sqrt{1 + \left(\frac{z}{z_0}\right)^2} \tag{2.1.19}$$
- The Gouy-phase θ, a phase shift adding up to π for a wave travelling from $-\infty$ to ∞:
$$\theta = \arctan\frac{z}{z_0} \tag{2.1.20}$$
- The radius of curvature of the phase fronts:
$$R\,(z) = z\left(1 + \left(\frac{z_0}{z}\right)^2\right) \tag{2.1.21}$$

The radial intensity profile of the beam is described by a Gaussian. The Gaussian beam has one free parameter, which is set by the boundary conditions. In the case of a Gaussian beam in an optical resonator, the radii of curvature of the phase fronts at positions z_1 and z_2 of the two mirrors have to match the radii of of curvature of the mirrors, $R(z_i) = r_{C,i}$ for $i = 1, 2$. This then sets all other parameters. As in our case, where one mirror is planar, $z = 0$ is the position of the planar mirror, i.e. the beam has its smallest radius w_0 there. The resonance condition, an expression for the frequencies at which the light becomes resonant with the cavity, is found to be

$$v_q = \Delta\nu\left(q + \frac{\theta(z = d)}{\pi}\right), \tag{2.1.22}$$

where the Gouy phase is evaluated for the cavity length d.

Hermite-Gaussian modes The Gaussian beam is not the only solution of the paraxial Helmholtz equation, but there are also higher order transverse electromagnetic (TEM) modes satisfying it. In cylindrically symmetric systems, so-called Laguerre-Gaussian modes, whose intensity profiles are described by Laguerre polynomials, are solutions. When Cartesian coordinates are the natural coordinates of the system, we observe Hermite-Gaussian (HG) modes with an intensity profile given by Hermite Polynomials. Any paraxial beam can be expanded in terms of these modes as they form a complete and orthonormal set of solutions. For details, see [139].

The profile of the fibre mirrors discussed here does not exhibit a cylindrical symmetry, but has approximately elliptical contour lines and can be described by a Gaussian along both principal axes with different widths. One observes modes which closely resemble HG modes $\Phi^{\pm}_{mn}$,being separable into an x and y component:

$$\Phi^{\pm}_{mn}(x,\, y) = \Phi^{\pm}_{m}(x) \cdot \Phi^{\pm}_{n}(y) \tag{2.1.23}$$

Due to the elliptical shape of the profile, $\Phi^{\pm}_{m}(x)$ and $\Phi^{\pm}_{n}(y)$ do not have the same waist, as the radii of curvature are different for x and y. Plus and minus denote the ingoing and outgoing directions and m and n is the degree of the Hermite polynomial and is called the transverse mode order. These one-dimensional components are given by

$$\Phi^{\pm}_{k}(j) = \frac{N_k}{\sqrt{w_j}} \cdot H_k\left(\frac{\sqrt{2}j}{w_j}\right) \cdot \exp\left(-\frac{j^2}{w_j^2} \mp i\left(\frac{\pi j^2}{\lambda R_j} - \theta_{k,j}\right)\right) \tag{2.1.24}$$

with $j = x,\, y$ and $k = m,\, n$. $H_k(x)$ are the Hermite polynomials

$$H_k(x) = (-1)^k \cdot e^{x^2} \cdot \frac{\mathrm{d}^k}{\mathrm{d}x^k} e^{-x^2} \tag{2.1.25}$$

with $H_0 = 1$, which implies that the Gaussian mode introduced in the previous paragraph is the fundamental Hermite-Gaussian mode Φ_{00}. w and R are still the same as above, and the waist w_0 is replaced by the respective $w_{0,j}$,

$$N_k = \sqrt{\frac{\sqrt{2}}{\sqrt{\pi} \cdot 2^k \cdot k!}} \tag{2.1.26}$$

is a normalisation factor, and the Gouy-phase in one dimension now reads

$$\theta_{k,j} = \left(\frac{1}{2} + k\right) \arctan \zeta_j \tag{2.1.27}$$

$$= \left(\frac{1}{2} + k\right) \arccos \sqrt{1 - \frac{d}{r_C^{(j)}}}. \tag{2.1.28}$$

The two-dimensional counterpart is given by

$$\theta_{mn} = \theta_{m,x} + \theta_{n,y}, \tag{2.1.29}$$

which reduces to

$$\theta_{mn} = (1 + m + n) \arctan \zeta \tag{2.1.30}$$

for a rotationally symmetric system. The intensity distribution of the first few HG modes can be seen in the inset of Fig. 2.1.2(a).

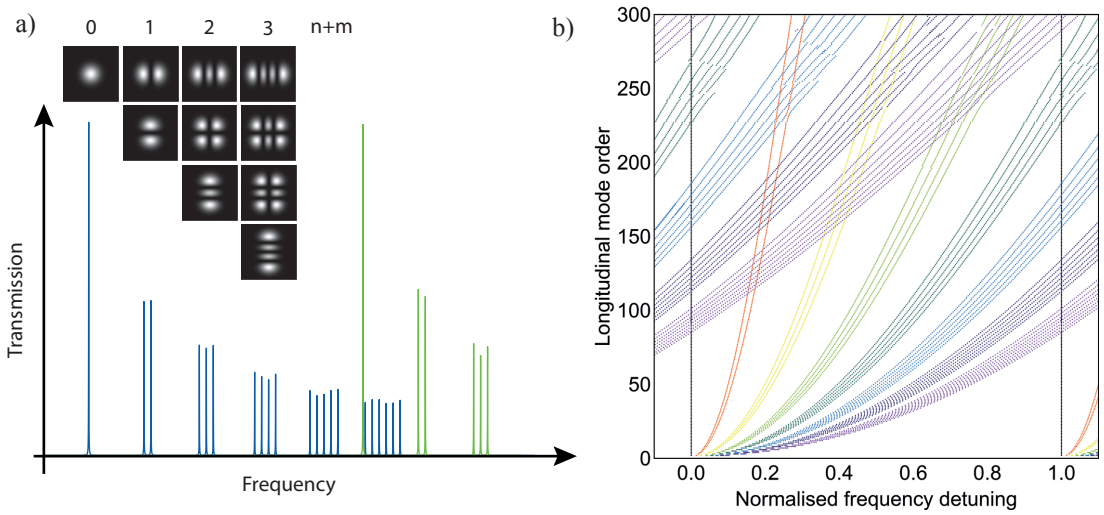

Figure 2.1.2.: (a) Schematic illustration of the cavity transmission as a function of frequency. Blue and green denote different longitudinal orders q. Inset: intensity distribution of the transverse modes up to order 3. (Adapted from Matthias Mader.) (b) Resonant state expansion model simulation (details, see section 3.2) of relative detuning of transverse modes from the ground mode (black), increasing with increasing longitudinal mode order. Modes are shown for $m+n=1$ (red), $m+n=2$ (yellow), ... , $m+n=7$ (purple).

Resonance condition Inserting equation 2.1.29 into the resonance condition 2.1.22, one arrives at the resonance frequency ν_{qmn} of a Hermite-Gaussian mode with longitudinal mode order q and transverse mode order (m,n):

$$\nu_{qmn} = \Delta\nu \left(q + \frac{\theta_{m,x}}{\pi} + \frac{\theta_{n,y}}{\pi} \right) \tag{2.1.31}$$

Notably, this implies that the modes of order $m+n$ are not degenerate like in the rotationally symmetric case, but rather split up into a family of $m+n+1$ modes, where the splitting becomes larger for an increased ellipticity of the mirror profile. A schematic illustration of a cavity spectrum is shown in Fig. 2.1.2(a). Rewriting the resonance condition for the resonant mirror separations d_{qmn} gives

$$d_{qmn} = \frac{\lambda}{2} \left(q + \frac{\theta_{m,x}}{\pi} + \frac{\theta_{n,y}}{\pi} \right). \tag{2.1.32}$$

So higher order transverse modes appear at a larger cavity length than the fundamental mode of a longitudinal mode order q and the splitting of the modes becomes larger the larger the mirror separation. Figure 2.1.2(b) illustrates this by depicting the detuning of higher order transverse modes from the ground mode for different longitudinal mode orders.

For elliptical mirror profiles, the resonances feature yet another splitting into doublets corresponding to orthogonal polarisations, which cannot be explained in the scalar

paraxial picture, but rather requires a full vectorial treatment. Uphoff et al. [136] showed that this splitting can in first order be expressed as

$$\nu_x - \nu_y = \frac{\Delta\nu\lambda}{(2\pi)^2} \frac{r_C^{(x)} - r_C^{(y)}}{r_C^{(x)} r_C^{(y)}}, \tag{2.1.33}$$

that is it increases with larger eccentricity of the profile, where ν_x and ν_y are the resonance frequencies for light polarised along the principal axes x and y of the profile. For small fibre profiles, whose ellipticity is typically rather small, the splitting can be smaller than the linewidth, even for high finesse. For the experiments treated in this work, the polarisation of the incoupled light was always chosen such, that only one of the two lines was addressed.

Limitations of the paraxial approximation The Gaussian beam as given by equation 2.1.17 has parabolic wavefronts in the centre, which are flattening out as the distance from the optical axis increases. HG modes are thus the eigenmodes of a system of parabolic mirrors. The rigorous solution to the (non-paraxial) Helmholtz equation would however yield spherical wavefronts, such that spherical mirrors would ideally reflect a beam back into itself [140]. So when machining mirror profiles, a spherical profile should be aimed for as any other shape does not perfectly self-reproduce the modes. So the paraxial approximation is legitimate as long as the real mirror profile can be sufficiently well approximated by a parabola on an area larger than the mode radius on the mirror. More rigorously, the beam waist has to be much larger than the wavelength. For very small radii of curvature and short mirror separations in fibre-based microcavities, it can happen that the two quantities become similar in size, such that significant deviations from the paraxial solution are expected. In this case one can include additional non-paraxial terms [140, 141] or apply resonant state expansion [142].

Mode radii Solving equation 2.1.21 for w_0 when setting $z = d$ and $R(d) = r_C$ yields the mode radius on the planar mirror:

$$w_0 = \sqrt{\frac{\lambda d}{\pi} \sqrt{\frac{r_C}{d} - 1}} \tag{2.1.34}$$

For fibre cavities, mode waists of $w_0 < 2\,\lambda$ up to $w_0 \approx 36\,\lambda$ [137] were demonstrated. The mode radius w_c on the fibre mirror can then be obtained by inserting this expression for w_0 into equation 2.1.19 with $z = d$:

$$w_c = \sqrt{\frac{\lambda d}{\pi} \sqrt{\frac{r_C^2}{d\,(r_C - d)}}} \tag{2.1.35}$$

Higher order HG modes feature an increased mode radius according to the inverse quadratic expression

$$w_k^{(j)} = w_0^{(j)} \cdot \sqrt{k+1} \tag{2.1.36}$$

with $j = x, y$ and $k = m, n$. [132].

Peak intensity From equation 2.1.14, one can now derive the peak intensity in the field maximum on the planar mirror:

$$I_{\text{peak}} = \frac{P_{\text{peak}}}{\pi w_0^2} \tag{2.1.37}$$

For typical values of w_0, $\mathcal{F}$, and P_{in}, intensities on the order of up to $10^9\,\text{W/cm}^2$ can be reached.

Mode volume Minimisation of the mode volume in combination with high Q is the main purpose of microcavities. The mode volume is given by the spatially integrated field intensity normalised by the maximum field intensity:

$$V_m = \frac{\int \mathrm{d}^3 r\, |\mathbf{E}(\mathbf{r})|^2}{\max |\mathbf{E}(\mathbf{r})|^2} \tag{2.1.38}$$

For Fabry-Pérot cavities, this expression yields

$$V_m = \frac{\pi w_0^2 d}{4}. \tag{2.1.39}$$

It should be noted that the cavity length d is a non-trivial quantity when using DBR mirrors as the field penetrates into the layer stack (for details see section 3.4.3). Hence, one has to distinguish between the geometric mirror separation $d_{\text{geo}} = q\frac{\lambda}{2}$, defined as the distance between the plane mirror and the centre of the concave mirror, and the optical cavity length $d_{\text{opt}} = d_{\text{geo}} + 2d_{\text{pen}}$, where d_{pen} is the penetration depth into each mirror. To calculate the mode volume, $d = d_{\text{opt}}$ needs to be chosen. However, as the wavefront curvature of the cavity mode is in good approximation defined by the top-most layers of the mirror, the geometric length is more appropriate for determining w_0 using expression 2.1.34.

The smallest mode volume was obtained by Hanno Kaupp with a metallic mirror coating and a shallow fibre profile, reaching $V_m = \lambda^3$ with $d = \lambda/2$ [46]. High finesse cavities require DBR mirrors, whose penetration depth prevents reaching the fundamental longitudinal mode, such that the smallest mode volumes are typically a few λ^3.

Mode matching Light can be conveniently coupled into fibre cavities through the fibre mirror. The mode matching describes the fraction of the fibre mode which is coupled to the cavity mode and is given by their overlap integral:

$$\epsilon = \langle \psi_F | \psi_C \rangle = \int_{-\infty}^{\infty} \psi_F^* \psi_C \,\mathrm{d}x\mathrm{d}y \tag{2.1.40}$$

In case the mirror profile is well centred, i.e. fibre mode and cavity mode share an optical axis, the mode matching is given by

$$\epsilon = \frac{4}{\left(\frac{w_f}{w_0} + \frac{w_0}{w_f}\right)^2 + \left(\frac{s\lambda}{\pi w_0 w_f}\right)^2}, \tag{2.1.41}$$

where w_f is the mode field diameter of the optical fibre and $s = d_{\text{geo}} + d_{\text{mirror}}$ is the optical distance between the two mode waists, which consists of the geometric mirror separation d_{geo} and the optical thickness of the fibre's dielectric mirror stack d_{mirror} [52, 143]. The value obtained with this expression can be seen as an upper boundary, as a slight misalignment of the imprinted mirror profile with respect to the core of the optical fibre as well as poor angular alignment can significantly reduce the mode matching.

Outcoupling efficiency An important quantity, especially for experiments aiming for high efficiency, is the outcoupling efficiency, i.e. the fraction of the light, which leaves the cavity through the outcoupling mirror:

$$\eta_c = \frac{T_2}{T_1 + T_2 + L} \tag{2.1.42}$$

T_2 is the transmittivity of the outcoupling mirror, so an asymmetric cavity design with $T_2 > T_1$ is beneficial for a high η_c.

2.2. Light matter interaction in resonators

So far, the bare optical resonator was treated. In this section, I shall discuss the interaction of quantum emitters with the cavity light field, following M. Fox [144]. The system can be viewed as two coupled quantum mechanical damped oscillators – a two-level system for the quantum emitter and a harmonic oscillator for the light field. The damping constants are the cavity decay rate $\kappa = 2\pi\delta\nu$ (see eq. 2.1.11) for the cavity light field and the spontaneous emission rate γ of the quantum emitter. Note that in the following κ and γ are defined as the FWHM of the cavity and emitter line, respectively, in contrast to some treatments in literature.The cavity-emitter coupling strength is denoted by

$$g_0 = \sqrt{\frac{\pi\mu_{12}^2\nu}{\epsilon_0\hbar V_m}}, \tag{2.2.1}$$

with ν being the mode frequency and $\mu_{12} = -e\langle g|x|e\rangle$ the electric dipole transition matrix element, where e is the elementary charge and $|g\rangle$ and $|e\rangle$ are the ground and excited state of the two-level system, respectively. It scales with $1/\sqrt{V_m}$, such that for high coupling, small mode volumes are beneficial. For an ensemble of N resonantly coupled emitters, the coupling strength is increased to $g = \sqrt{N}g_0$.

So far, an idealised non-dephasing two-level system was considered. In reality, a quantum emitter could decay by various non-resonant transitions, as shall be seen in section 4.1.1. Furthermore, especially in solid state systems, the emitter linewidth is not lifetime-limited but broadened by decoherence and dephasing due to coupling to the surrounding matrix. This is indicated by an additional damping constant, the pure dephasing rate $\gamma^\star$, which can become significantly larger than the spontaneous emission rate γ. The inverse of these rates is the population decay time $T_1 = 1/\gamma$, the pure

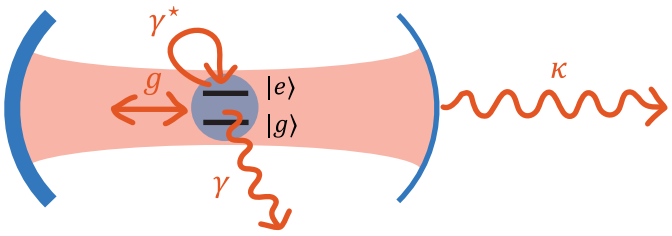

Figure 2.2.1.: Schematic overview of the CQED parameters. Adapted of [54].

dephasing time $T_2^\star = 2/\gamma^\star$, and the total dephasing time[2] $T_2 = (1/(2T_1) + 1/T_2^\star)^{-1}$ [54, 146, 147]. A schematic overview of these CQED parameters is given in Fig. 2.2.1. Depending on the relations of the parameters γ, $\gamma^\star$, κ, and g, the behaviour of the coupled system can substantially vary and it is useful to individually consider the following limiting cases: In the limit of $2g \gg \gamma + \gamma^\star + \kappa$, the so called strong coupling regime, we observe a coherent evolution of the system undergoing Rabi oscillations. In the weak coupling regime, when $2g \ll \gamma + \gamma^\star + \kappa$, the decay channels dominate and the system is governed by incoherent rate dynamics [54]. In the following these cases shall be treated more in depth.

2.2.1. Strong coupling regime

An intuitive picture of the strong coupling regime is that the photons stay sufficiently long in the cavity to be reabsorbed by the quantum emitter, i.e. that an excitation oscillates back and forth between the light field and the emitter many times until it is eventually lost. This behaviour is described by the Jaynes-Cummings Hamiltonian [148]

$$H_{JC} = H_{em} + H_c + H_{\text{int}}, \tag{2.2.2}$$

which consists of the Hamiltonian of a two-level system for the quantum emitter,

$$H_{em} = \hbar\omega_0\, \sigma^+\sigma^-, \tag{2.2.3}$$

where $\hbar\omega_0$ is the energy difference between ground state $|g\rangle$ and excited state $|e\rangle$ and $\sigma^+ = |e\rangle\langle g|$ and $\sigma^- = |g\rangle\langle e|$ are the creation and annihilation operator, respectively, and the harmonic oscillator Hamiltonian of the cavity

$$H_c = \hbar\omega_c\, a^\dagger a \tag{2.2.4}$$

with $\omega_c = 2\pi\nu$ the angular resonance frequency of the cavity and $a^\dagger$ (a) the creation (annihilation) operator. The eigenenergies are $E_c = (n + 1/2)\,\hbar\omega_c$ with $n = \left\langle a^\dagger a \right\rangle$ being the photon number. The interaction Hamiltonian is given in the rotating wave approximation:

$$H_{\text{int}} = \hbar g_0 \left(a^\dagger\sigma^- + \sigma^+ a\right) \tag{2.2.5}$$

[2] There is an error in the expression for T_2 in Grange et al. [54]. For the correct expression (as given here), see [145].

This implies that when the emitter relaxes, a photon is created in the cavity, and when the number of photons is lowered by one, the emitter gets excited. The temporal evolution of a system comprising a single excitation exhibits vacuum Rabi oscillations, meaning that the systems oscillates between the states $|e,0\rangle$ and $|g,1\rangle$ at an angular frequency $\Omega = 2g_0$. The pure photonic eigenstates each split up into a pair of so-called dressed states $|\pm\rangle = 1/\sqrt{2}\,(|e,0\rangle \pm i\,|g,1\rangle)$, eigenstates of the coupled system, with an energy gap of $2\sqrt{n}\hbar g_0$ (assuming the resonant case of $\omega \equiv \omega_0 = \omega_c$). The eigenenergies are given by

$$E_n^{\pm} = (n + 1/2)\,\hbar\omega \pm \sqrt{n}\hbar g_0 \tag{2.2.6}$$

The appearance of this normal mode splitting is an indicator for a strongly coupled system. For a more detailed treatment of the Jaynes-Cummings model, see [1].

Reaching the strong coupling regime is experimentally challenging as a narrow line, weakly dissipative quantum emitter (like an atom) needs to be coupled to a high Q, small V_m cavity. Ensembles facilitate the task as the coupling scales with $\sqrt{N}$, making collective strong coupling easier to observe. Normal mode splitting was first observed with atoms in the microwave domain [149, 150] and later in the optical domain [106, 151]. In the solid state at room temperature, collective strong coupling was shown for excitons in transition metal dichalcogenides coupled to optical microcavities [127, 128, 152].

Note that in the presence of pure dephasing, strictly speaking, the strong coupling regime is reached when $2g > |\gamma + \gamma^\star - \kappa|$, which implies that the spontaneous emission spectrum consists of two distinct peaks. Coherent dynamics, i.e. vacuum Rabi oscillations, however, requires the stricter criterion $2g > \gamma + \gamma^\star + \kappa$. In addition, one can define the so-called good cavity regime for $2g > \sqrt{\kappa\,(\kappa + \gamma + \gamma^\star)}$. In this regime, the excitation released from the emitter stays in the cavity without being reabsorbed, which is only possible in the presence of pure dephasing [147].

2.2.2. Weak coupling regime

Most solid state emitters coupled to an optical cavity exhibit weak coupling due to the large dephasing rate $\gamma^\star$. As g_0 is now much smaller than all damping parameters, an emitted photon leaves the coupled emitter-cavity system before it can be coherently reabsorbed. One could also speak of the overdamped regime. The emission of a photon can be treated like in free space, but as the emitter experiences a modified density of states in the cavity, the emission rate can significantly differ.[3]

[3] To avoid confusion, note that what I am calling the 'weak coupling regime' is referred to as the 'bad cavity regime' in the papers by the Auffèves group [54, 146, 147] with the condition $2g < \sqrt{\kappa\,(\kappa + \gamma + \gamma^\star)}$. The regimes referred to as 'bad cavity' and 'bad emitter' regime in the Hunger group and some textbooks (these terms shall also be used here) are subcases of this weak coupling regime.

2.2.2.1. Spontaneous emission

It is useful to first treat spontaneous emission in free space. Perturbation theory is used to describe the effect of external (vacuum) fields on the two level system. Fermi's golden rule states that the transition rate is proportional to the square of the transition matrix element M_{12} and the density of states $\rho(\omega)$:

$$\gamma_0 = \frac{2\pi}{\hbar} M_{12}^2 \rho(\omega) \tag{2.2.7}$$

Assume a dipole transition, where $M_{12} = \langle \mathbf{d} \cdot \mathbf{E_{vac}} \rangle$ with $\mathbf{d} = -e\mathbf{r}$ the electric dipole and $\mathbf{E_{vac}}$ the vacuum electric field with

$$E_{\text{vac}} = \sqrt{\frac{\hbar\omega}{2\epsilon_0 V_0}}. \tag{2.2.8}$$

V_0 is the mode volume of the vacuum field. Forming the average over all dipole orientations, one gets

$$M_{12}^2 = \frac{1}{3}\mu_{12}^2 E_{\text{vac}}^2 = \frac{\mu_{12}^2 \hbar\omega}{6\epsilon_0 V_0}. \tag{2.2.9}$$

The density of states in free space is given by

$$\rho(\omega) = \frac{\omega^2 V_0}{\pi^2 c^3} \tag{2.2.10}$$

Inserting into eq. 2.2.7 yields

$$\gamma_0 = \frac{\mu_{12}^2 \omega^3}{3\pi\epsilon_0 \hbar c^3}. \tag{2.2.11}$$

Note that $\tau_r = 1/\gamma_0$ is the radiative lifetime. A more rigorous derivation of the spontaneous decay rate can be found in the book by Novotny and Hecht [153], section 8.4.

2.2.2.2. The Purcell effect

The Purcell effect describes the modification of the spontaneous emission rate of an emitter in an optical cavity. In most textbooks, like the one by Fox [144] used here, the quantum emitter is taken to be an atom whose line is negligibly narrow as compared to the cavity resonance. As this is not true for many solid state emitters, I shall present a more general formalism following Meldrum et al. [154].

Fermi's golden rule is now extended by the density of states of the emitter $\Lambda(\omega)$:

$$\gamma_0 = \frac{2\pi}{\hbar^2} \int_0^\infty M_{12}(\omega)^2 \rho(\omega) \Lambda(\omega) \mathrm{d}\omega \tag{2.2.12}$$

I am now introducing the two limiting cases of the emitter linewidth $\delta\nu_{em}$ being much more narrow than the cavity linewidth $\delta\nu_c$, the so-called bad cavity regime, the opposite case of $\delta\nu_{em} \gg \delta\nu_c$, called the bad emitter regime, and the general case, where the linewidths are comparable.

Bad cavity regime $\delta\nu_{em} \ll \delta\nu_c$ implies that the cavity decays much faster than the emitter, that is $\kappa \gg \gamma + \gamma^\star \gg 2g_0$. This description is accurate for most atomic cavity experiments, but also for rare earth ions in solid state host matrices in optical cavities like the system presented in chapter 5. The density of states of the emitter will be approximated by a delta function $\Lambda(\omega) = \delta(\omega - \omega_0)$, while the density of states of the cavity is given by a Lorentzian:

$$\rho(\omega) = \frac{1}{\pi} \frac{\frac{\delta\omega_c}{2}}{(\omega - \omega_c)^2 + \left(\frac{\delta\omega_c}{2}\right)^2} \tag{2.2.13}$$

Note that due to the delta function, this expression needs to be evaluated at the frequency of the emitter, so

$$\rho(\omega_0) = \frac{2}{\pi\kappa} \frac{(\kappa/2)^2}{\Delta^2 + (\kappa/2)^2} \tag{2.2.14}$$

with $\Delta \equiv \omega_0 - \omega_c$ being the detuning of the cavity resonance from the emitter line. Note that $\delta\omega_c = 2\pi\delta\nu = \kappa$ also denotes the FWHM of the resonance. The constraint that only one mode is supposed to be resonant with the emitter, i.e. $\int \rho(\omega)\mathrm{d}\omega = 1$, gives the normalisation factor. In the resonant case $\omega_0 = \omega_c$, this amounts to

$$\rho(\omega_0) = \frac{2}{\pi\kappa} = \frac{2Q}{\pi\omega_0} \tag{2.2.15}$$

The transition matrix element is given by

$$M_{12}^2 = \xi^2 \mu_{12}^2 E_{\mathrm{vac}}^2 = \xi^2 \frac{\mu_{12}\hbar\omega}{2\epsilon_{0V_m}} \tag{2.2.16}$$

with

$$\xi = \frac{|\mathbf{d} \cdot \mathbf{E}|}{|\mathbf{d}|\,|\mathbf{E}|} \tag{2.2.17}$$

the dipole orientation with respect to the field. Inserting eq. 2.2.14 and 2.2.16 into Fermi's golden rule, eq. 2.2.12, yields the spontaneous emission rate:

$$\gamma_c = \frac{2Q\mu_{12}^2}{\hbar\epsilon_0 V_m} \xi^2 \frac{(\kappa/2)^2}{\Delta^2 + (\kappa/2)^2} \tag{2.2.18}$$

The Purcell factor C is defined as the ratio of the spontaneous emission rate in the cavity to the one in free space (eq. 2.2.11):

$$C = \frac{\gamma_c}{\gamma_0} = \frac{3}{4\pi^2} \left(\frac{\lambda}{n}\right)^3 \frac{Q}{V_m} \xi^2 \frac{(\kappa/2)^2}{\Delta^2 + (\kappa/2)^2}, \tag{2.2.19}$$

where c/ω was replaced by $(\lambda/n)/2\pi$ with n being the refractive index of the intra-cavity medium. For an emitter on the cavity resonance, that is $\Delta \to 0$, whose dipole is aligned with the electric field, one obtains

$$C_0 = \frac{3}{4\pi^2} \left(\frac{\lambda}{n}\right)^3 \frac{Q}{V_m}. \tag{2.2.20}$$

With the mode volume $V_m = (\pi w_0^2 d)/4$ and $Q = \frac{d}{\lambda/2}\mathcal{F}$, the Purcell factor can also be written as a function of finesse and mode waist:

$$C_0 = \frac{6}{\pi^3}\left(\frac{\lambda}{n}\right)^2 \frac{\mathcal{F}}{w_0^2} \tag{2.2.21}$$

Furthermore, the Purcell factor can be expressed using the rates κ, γ_0, and g_0 as follows:

$$C_0 = \frac{4g_0^2}{\kappa\gamma_0} \tag{2.2.22}$$

Purcell factors $C_0 > 1$ indicate an enhancement of the spontaneous emission rate into the cavity mode with respect to free space, which is referred to as the Purcell effect. For a cavity with a mode volume on the order of λ^3, the decay rate experiences an enhancement on the order of Q.

Bad emitter regime In this regime, the resonance of the cavity is much more narrow than the broad emitter line, $\delta\nu_{em} \gg \delta\nu_c$, which means that $\gamma + \gamma^\star \gg \kappa \gg 2g_0$. This is true for the SiV experiments in chapter 4. Here, the cavity density of states can be approximated by a delta function $\rho(\omega) = \delta(\omega - \omega_c)$ and the emitter density of states is given by a Lorentzian:

$$\Lambda(\omega) = \frac{1}{\pi}\frac{\frac{\delta\omega_0}{2}}{(\omega-\omega_0)^2 + \left(\frac{\delta\omega_0}{2}\right)^2} \tag{2.2.23}$$

with $\delta\omega_0$ the FWHM of the emitter line in angular frequency. With introducing the quality factor of the emitter

$$Q_e = \frac{\omega_0}{\delta\omega_0} = \frac{\nu_0}{\delta\nu_0} = \frac{\omega_0}{\gamma + \gamma^\star} \tag{2.2.24}$$

one finds in analogy to the above derivation that

$$\gamma_c = \frac{2Q_e\mu_{12}^2}{\hbar\epsilon_0 V_m}\xi^2 \frac{(\delta\omega_0/2)^2}{\Delta^2 + (\delta\omega_0/2)^2} \tag{2.2.25}$$

leading to the Purcell factor of a perpendicular dipole on an antinode

$$C = \frac{3}{4\pi^2}\left(\frac{\lambda}{n}\right)^3 \frac{Q_e}{V_m}. \tag{2.2.26}$$

Notably, the Purcell factor no longer depends on the quality factor of the cavity, which means that the minimisation of the mode volume becomes even more crucial.

General description When the cavity and emitter linewidth are of similar width, both densities of states need to be described as Lorentzians, such that the derivation (see [154]) gets quite lengthy as the integral in eq. 2.2.12 needs to be explicitly solved. Here,

I content myself with stating the resulting expression for the spontaneous emission rate into the cavity mode, which is valid in good approximation:

$$\gamma_c \approx \frac{2\mu_{12}^2}{\hbar\epsilon_0 V_m}\xi^2 \frac{\omega_0\kappa/2 + \omega_c\delta\omega_0/2}{\Delta^2 + (\kappa/2 + \delta\omega_0/2)^2} \tag{2.2.27}$$

It is apparent that expressions 2.2.18 and 2.2.25 follow from this general formula by setting $\kappa = 0$ and $\delta\omega_0 = 0$, respectively. With cavity and emitter being on resonance ($\omega_c = \omega_0$) and a dipole orientation perpendicular to the optical axis, one finds

$$C_{\text{eff}} = \frac{3}{4\pi^2}\left(\frac{\lambda}{n}\right)^3 \frac{Q_{\text{eff}}}{V_m} \tag{2.2.28}$$

with

$$Q_{\text{eff}} = \left(Q_{em}^{-1} + Q_c^{-1}\right)^{-1}, \tag{2.2.29}$$

called the effective quality factor. The generalised Purcell factor can also be expressed in terms of the CQED parameters (for a derivation, see [146, 147]) as

$$C = \frac{R}{\gamma}, \tag{2.2.30}$$

where

$$R = \frac{4g_0^2}{\kappa + \gamma + \gamma^\star} \tag{2.2.31}$$

can be pictured as an effective coupling rate between a separate emitter and cavity system, decaying at a rate of γ and κ, respectively. This corresponds to an additional loss channel for the emitter (in addition to γ) through the cavity at a rate

$$R_{\text{eff}} = \frac{R\kappa}{R + \kappa}. \tag{2.2.32}$$

Notably, eq. 2.2.22 for the Purcell factor in the bad cavity regime is restored for $\gamma + \gamma^\star \ll \kappa$. In the bad emitter regime, when $\gamma + \gamma^\star \gg \kappa$, C becomes independent of κ as shown in the previous paragraph.

In the treatment presented here, the cavity couples to one transition only, which should be approximately valid for the experiments in this work. Note, however, that when enhancing a continuum of transitions (like a phonon side band), modifications become necessary. For details, see [124]. Furthermore, only the resonant case $\omega_0 = \omega_c$ was presented. Adding a detuning Δ can lead to the intriguing effect that a larger $\gamma^\star$ can actually increase the spontaneous emission rate leading to a larger effective Purcell factor by a factor Δ/κ [147].

It should be noted that in spite of the quantum mechanical derivation presented here, the Purcell effect does not require quantum mechanical systems but can as well be derived for classical light matter interaction like enhanced Rayleigh or Raman scattering in an optical cavity [155, 156].

Emission rates, lifetime, and collection efficiency Note that γ_c is the spontaneous emission rate into the cavity mode and that, in addition, there is emission into free space. Furthermore, radiation can get lost through the open sides of the cavity, which subtends a limited solid angle $\Delta\Omega < 4\pi$, such that light is emitted into free space at a rate

$$\gamma_{\text{fs}} = \gamma_0 \left(1 - \frac{3\Delta\Omega}{8\pi}\right), \tag{2.2.33}$$

where the dipole orientation is perpendicular to the optical axis leading to the factor 3/2. The total emission rate including the emission into the cavity mode and into free space is therefore given by [157]

$$\gamma_{\text{tot}} = \gamma_{\text{fs}} + \gamma_c = \gamma_0 \left(1 - \frac{3\Delta\Omega}{8\pi} + C\right) \tag{2.2.34}$$

In the case of the microcavities treated here,

$$\frac{\Delta\Omega}{4\pi} = \sin^2\left(\frac{1}{2}\arctan\frac{w_c}{d}\right) \tag{2.2.35}$$

spans a rather small fraction of the solid angle, where d is the cavity length and w_c the mode radius on the fibre mirror. In the case of the cavity used for the SiV experiments in chapter 4, this would amount to $\frac{\Delta\Omega}{4\pi} = 9\%$. For the large radius of curvature cavities discussed in section 3.3.3, over 15% can be reached. In many cases,

$$\gamma_{\text{tot}} \approx \gamma_0 \left(C + 1\right) \tag{2.2.36}$$

is a legitimate approximation. However, note that in experiment, typically only the emission into the cavity mode is collected.

An increased spontaneous emission goes along with a reduced lifetime τ_c as compared to the lifetime in free space τ_0:

$$\frac{\tau_0}{\tau_c} = \frac{\gamma_{\text{tot}}}{\gamma_0} \approx C + 1 \tag{2.2.37}$$

The fraction of the total light, which is emitted into the cavity mode can be expressed as

$$\beta = \frac{\gamma_c}{\gamma_c + \gamma_0} = \frac{C}{C+1} \tag{2.2.38}$$

Or in terms of the effective coupling rate (eq. 2.2.32):

$$\beta = \frac{R_{\text{eff}}}{\gamma_0 + R_{\text{eff}}} \tag{2.2.39}$$

This implies that even for a moderate Purcell factor, a large fraction of the light gets directed into the easily collectible cavity mode. This is very advantageous compared to trying to collect a free space dipole mode, even with a high NA objective (see section 4.4.4).

Quantum efficiency and branching ratio So far, two level systems have been discussed. In real systems, the excited state can often decay into several states or, in solid state emitters, relax non-radiatively, for example via phonon-assisted decay. In the latter case the total decay rate is composed of a radiative part γ_r and a non-radiative part γ_{nr}:

$$\gamma = \gamma_r + \gamma_{nr} \tag{2.2.40}$$

The radiative fraction of the total rate is referred to as the quantum efficiency or quantum yield [153]

$$\mathrm{QE} = \frac{\gamma_r}{\gamma_r + \gamma_{nr}}. \tag{2.2.41}$$

In the cavity, the radiative rate gets enhanced to $\gamma_{r,\,\mathrm{tot}} = (C+1)\,\gamma_r$, whereof $C\gamma_r$ is emitted into the cavity mode:

$$\gamma_{r,c} = \beta\gamma_{r,\,\mathrm{tot}} = \beta\,(C+1)\,\gamma_r = C\gamma_r \tag{2.2.42}$$

So the ratio of the collected light in the cavity mode compared to free space light emission is again given by the Purcell factor, independent of the quantum efficiency. However, when considering lifetime reduction, the quantum efficiency plays a crucial role as the lifetime is given by the inverse of the total emission rate:

$$\frac{\tau_0}{\tau_c} = \frac{(C+1)\,\gamma_r + \gamma_{nr}}{\gamma} = \frac{(C+1)\,\mathrm{QE}\,\gamma + \gamma - \mathrm{QE}\,\gamma}{\gamma} = C\,\mathrm{QE} + 1 \tag{2.2.43}$$

Note that QE here is the quantum efficiency in free space. The modified quantum efficiency in the cavity is given by

$$\mathrm{QE}_c = \frac{(C+1)\,\gamma_r}{(C+1)\,\gamma_r + \gamma_{nr}} = \frac{C+1}{C+1/\mathrm{QE}}, \tag{2.2.44}$$

which is $>$ QE for $C > 0$.

But even when non-radiative decay is negligible like in the Eu experiment, there can be several final states the excited state can decay into. The ratio of the emission into the desired state as compared to all possible final states is called the branching ratio ζ. Just like in the case of QE, the ratio of the light emitted into the cavity mode (at a rate γ_c) compared to the light emitted into the desired state in free space (at a rate γ_0) is given by the Purcell factor:

$$\gamma_c = C\gamma_0 \tag{2.2.45}$$

However, one typically compares the light emitted into the cavity mode with the whole spectrum in free space (total free space emission rate γ_{all}), such that with

$$\zeta = \frac{\gamma_0}{\gamma_{\mathrm{all}}} \tag{2.2.46}$$

one gets

$$\gamma_c = \zeta C\gamma_{\mathrm{all}} \equiv C_{\mathrm{eff}}\gamma_{\mathrm{all}} \tag{2.2.47}$$

where an effective Purcell factor including the branching ratio was defined. Analogous to eq. 2.2.43, the lifetime reduction reads

$$\frac{\tau_0}{\tau_c} = \zeta C + 1 = C_{\text{eff}} + 1 \tag{2.2.48}$$

and the branching ratio in the cavity is enhanced to

$$\zeta_c = \frac{C+1}{C+1/\zeta}. \tag{2.2.49}$$

Furthermore, the emitter-cavity coupling constant of the desired transition undergoes a reduction by a factor $\sqrt{\zeta}$ compared to the total coupling constant of all transitions:

$$g_0 = g_{\text{all}}\sqrt{\zeta} \tag{2.2.50}$$

3. Microcavities – technical considerations

While the previous chapter introduced fibre-based microcavities and gave some theoretical insights, this chapter is supposed to shed light on some more practical aspects of this technology, starting with a brief introduction to the fabrication of concave mirror profiles on optical fibres and followed by a section about transverse mode coupling. Then, possible cavity geometries will be discussed including current limitations and subsequently, I shall treat the dielectric mirror coatings thereby also alluding to penetration depth. The chapter will be concluded by a section on cavity scattering experiments investigating how Rayleigh scattering is affected by the cavity geometry.

3.1. Fabrication of mirror profiles

The heart of our microcavities is the laser-machined micromirror on the end-facet of an optical fibre. The structure is created by shooting one or several pulses of a CO_2 laser at a wavelength of 10.6 µm onto the cleaved fibre tip, thereby thermally evaporating silica from the fibre and leaving a near Gaussian depression due to strong absorption of silica in the mid infrared. In addition to evaporation, the glass surface is molten such that surface tension leads to a near atomic smoothness of the profile (surface roughness below 1.5 Å[126]) allowing for the application of high reflectivity coatings. The technique was first applied by David Hunger and Jakob Reichel [52, 91] and has since been adopted by various other groups [122, 129, 136, 158]. A detailed treatment can also be found in the theses by Kaupp [126] and Mader [93].

In a first step, the fibre tip is well cleaved and placed into a holder (design by Benedikt Schlederer and Matthias Mader [93, 159]) which grants alignment with the laser beam. A micropositioning stage allows for moving the fibre holder back and forth between the laser focus and a white light interferometer (WLI) for characterisation. Back-lighting the fibre core with a bright red LED makes it possible to aim at the centre of the fibre, which is crucial to maximise mode matching between the fibre mode and the fundamental Gaussian cavity mode, forming together with a second mirror. The depth of the machined profile can be varied by changing the impinging pulse power or the number of pulses. Note that the absorption of different substrates (even if they are all made of silica) can be rather different; in particular, there can be a significant difference between the core and the cladding of a fibre. In addition the relation between the laser power and the profile depth is highly nonlinear such that a suitable parameter range has to be found prior to shooting onto the 'good' fibres. To achieve a variety of radii of curvature, the beam waist needs to be changed. For a coarse adjustment, focusing lenses with different focal lengths are available. For smallest structures, one can also expand the

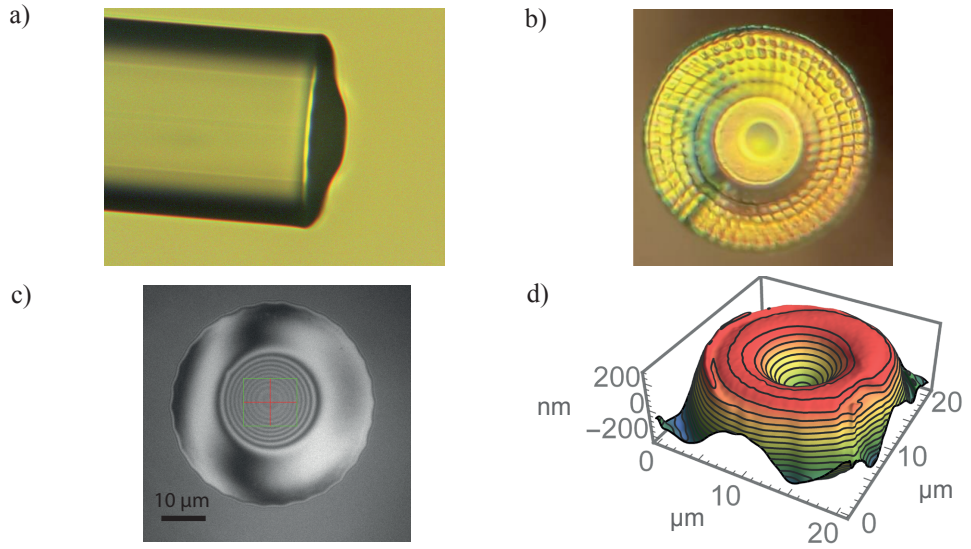

Figure 3.1.1.: (a, b) Light microscope images of the machined fibre tip. (a) Side view of cropped tip. Picture taken by Hanno Kaupp. (b) Top view with visible depression on the central plateau and ring-wise cropped rim. Appears yellow due to central coating wavelength of 585 nm. The fibre diameter is 125 µm. (c) WLI image of cropped fibre (fibre 39B, 740 nm coating run, $a = 8.0\,\mu\text{m}$, $t = 2.3\,\mu\text{m}$, $r_C = 19.7\,\mu\text{m}$ (parabolic fit with 3 µm radius)). (d) Example of reconstructed fibre surface showing plateau and depression (fibre used for SiV experiments in chapter 4).

beam before the focusing lens leading to a reduced waist. For fine adjustment, there is a diaphragm to reduce the beam diameter before the focusing lens, thereby increasing the waist. With these setting options, radii of curvature between 5 and 500 µm are possible. The typical fibre diameter is 125 µm, so much larger than the smallest structures. As the desired small mode volume requires shortest possible mirror separations and as small angles between the fibre surface and the planar mirror are hard to avoid, the rim of the fibre is cropped by shooting pulses in rings around a central plateau of a few tens of µm, increasing the power towards the edge. The resulting beveling can be seen in Fig. 3.1.1. It allows for more angular freedom and shorter cavity lengths. Fig. 3.1.1(c) shows a WLI image of a cropped fibre, where the height distance corresponding to one period of the interference fringes is $\lambda_{\text{WLI}}/2 = 463.25\,\text{nm}/2 = 231.63\,\text{nm}$. Phase unwrapping yields a height map (see Fig. 3.1.1(d)).

The central part of the intensity profile of the CO_2 laser, which is proportional to the temperature profile, is well approximated by a parabola. As the ablation of glass scales exponentially with temperature, the resulting depression left on the fibre surface is nearly Gaussian [93]. The depth t denotes the vertical distance from the plateau to the deepest point of the profile; a is the $1/e$-radius of the Gaussian structure. An overview of the cavity geometry parameters is given in Fig. 3.1.2. For a Gaussian, the minimal

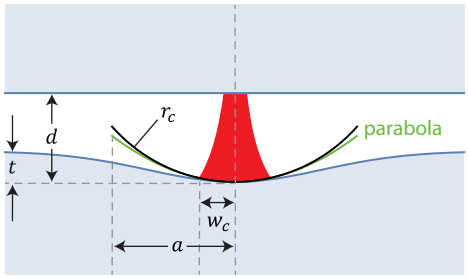

Figure 3.1.2.: Schematic overview of cavity geometry.

radius of curvature in the centre is

$$r_C = \frac{a^2}{2t}. \tag{3.1.1}$$

As we are not dealing with a spherical structure, the radius of curvature is smallest in the centre and increases to all sides until it diverges at a distance $a/\sqrt{2}$ from the centre, which can be seen as an effective radius of the mirror. As the cavity mode has a finite size on the fibre mirror with radius w_C, the effective radius of curvature the mode sees is somewhat larger. For real structures, one finds that the central part of the profile is not very well approximated by a Gaussian and can be more closely fit with a parabola at a slightly larger radius of curvature. A cut through a typical fibre profile with Gaussian fit and residual is shown in Fig. 3.1.3(a).

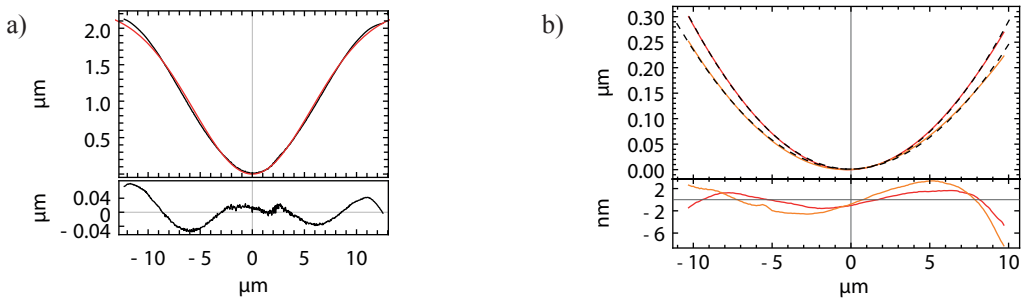

Figure 3.1.3.: (a) Cut through fibre profile shown in Fig. 3.1.1(c) with Gaussian fit (red). Lower panel: residual. (b) Example of a larger fibre profile with high eccentricity (fibre used for the experiments in section 3.2). Cuts along principal axes (black) with parabolic fit (red, orange). Lower panel: residual.

The resulting structures tend to be not perfectly rotationally symmetric but rather have elliptical contour lines. With the current laser machining setup it is reliably possible to achieve deviations of the radii along the principle axes from each other of less than 5%. For small r_C it is easier to get small ellipticity. Cuts through the central part of a fibre profile with larger ellipticity are shown in Fig. 3.1.3(b) along with a parabolic fit.

When machining large structures with $r_C > 200\,\mu\text{m}$, the profile size is on the same order as the lateral extent of the fibre, which has a diameter of 125 µm, leading to a

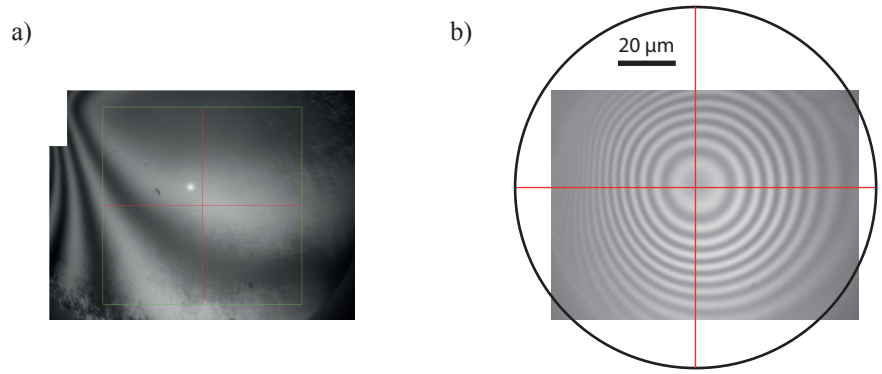

Figure 3.1.4.: (a) WLI image of cleave of fibre 29A before shot. The white spot in the middle is the back-lit fibre core. Cross hair is not meaningful. (b) WLI image after shot. Black circle indicates position of fibre. Red cross: centre of fibre. Deterioration of fibre rim is visible (e.g. top left). Central r_C from polynomial fit: 350 µm.

deterioration of the fibre rim, as depicted in Fig. 3.1.4. The quality of the cleave towards the rim can now play a role and the rim typically gets molten such that the profile bends down towards it. Apart from a good cleave quality, a well centred shot is crucial.

Figure 3.1.5 shows radius of curvature vs. profile depth for all fibres machined for one coating run (740 nm central wavelength, 10 ppm minimal transmission) on a logarithmic scale. Clearly, two regimes are visible: Profiles with $r_C > 100\,\mu\text{m}$ were produced with a focusing lens with a focal length of 2", the others with a focal length of 1/2". Different colours denote different settings of the diaphragm before the focusing lens and thus different profile radii. Due to eq. 3.1.1, the values for each setting tend to lie on a line in this log-log plot. The smallest structures feature a radius of curvature around 10 µm and a depth between 0.5 and 0.9 µm. The largest radii of curvature are between 400 and 500 µm at a depth of 1.2 to 1.6 µm. Note that for the large structures, due to a lack of baseline, the depth obtained from a Gaussian fit is less precise.

3.2. Transverse mode coupling

In fibre-based microcavities, the extent of the cavity mode can be comparable to the effective mirror diameter, such that the finite mirror size becomes relevant. Furthermore, due to the fabrication with Gaussian laser pulses, the mirror profile typically deviates from a spherical shape and further imperfections may occur, such as coating defects and excessive roughness. These deviations affect the cavity mode and lead to additional loss, mode deformation, and shifted resonance frequencies at particular mirror separations. This section will explain how these effects can be ascribed to coupling between simultaneously resonant transverse modes and that the experimental findings can well be accounted for by a model based on resonant state expansion. The section closely follows [94, 95, 135], containing identical passages. [94] is in parts reproduced under the Creative Commons Attribution 3.0 licence (CC BY 3.0); [95] is submitted for

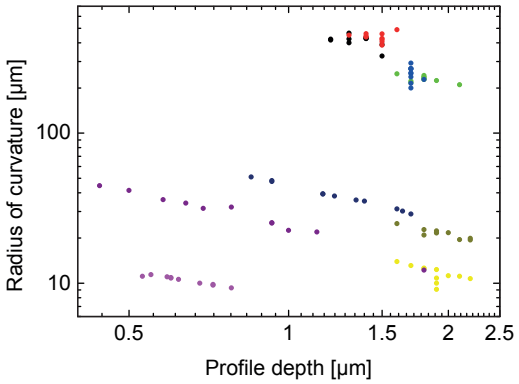

Figure 3.1.5.: Radius of curvature vs. profile depth of the fibres machined for a planned experiment on a room temperature indistinguishable single photon source (section 4.6). Different colours denote different settings of the diaphragm before the focusing lens. Profiles with $r_C > 100\,\mu m$ were produced with a focal length of 2", the others with a focal length of 1/2".

publication.

3.2.1. Experimental observations

In virtually all experiments with fibre-based microcavities, one observes additional losses, which reproducibly occur for particular mirror separations and cannot be accounted for by transmittivity, absorption, and scattering losses of the mirror coatings. Fig. 3.2.1(a) shows a measurement of the finesse as a function of the cavity length and it becomes apparent that in spite of good performance for most mirror separations, there are distinct dips in finesse for certain longitudinal orders, mainly for $d \gtrsim r_C/4$. In addition, one observes an overall degradation of the finesse although it should be independent of the cavity length according to eq. 2.1.9. Most strikingly, an abrupt drop of the finesse is observed for mirror separations $d \gtrsim r_C/2$, i.e. much before the theoretical stability limit, with few moderately working mode orders appearing for larger d. The findings are attributed to resonant coupling of different transverse modes with the fundamental mode of the cavity and mode-dependent diffraction loss, caused by the non-spherical mirror profile.

The effect is also observed in various scanning cavity microscopy experiments, where a planar mirror is sampled by raster-scanning it through the cavity mode [92, 93, 117]. No matter which coatings, cavity geometries, and wavelengths are used, two classes of artefacts can be observed as can be seen in the scan in Fig. 3.2.1(b): spatially localised contour lines with deteriorated cavity performance for certain longitudinal mode orders (ii), as well as a weak periodic background pattern (iii). Notably, these structures feature smaller details than the point spread function given by the cavity mode waist, which becomes visible by a reduced transmission when scanning over a nanoparticle (i). The worm-like structures can be explained by spatially varying resonance conditions

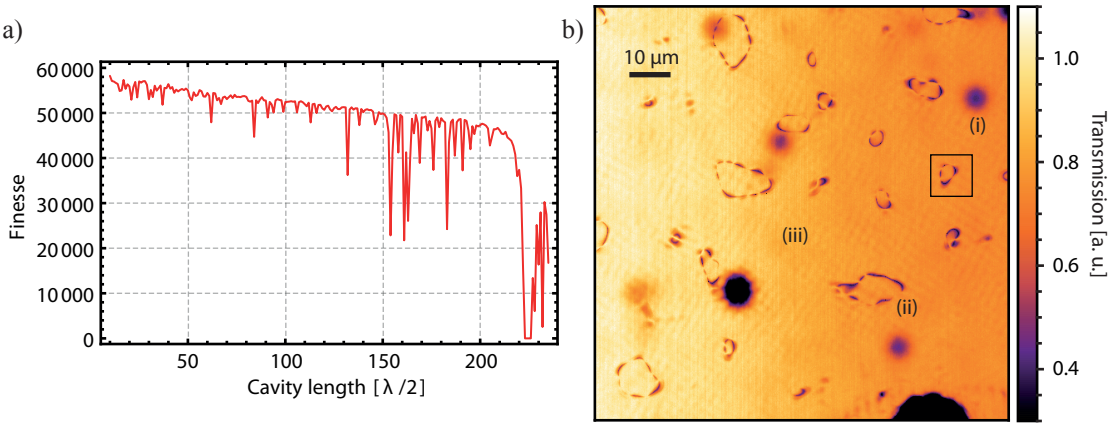

Figure 3.2.1.: (a) Finesse as a function of cavity length for a fibre with $r_C^{(x)} = 161\,\mu\text{m}$, $r_C^{(y)} = 201\,\mu\text{m}$. At particular longitudinal mode orders distinct dips in finesse are visible, together with an overall degradation with increasing length and a final breakdown for $d < r_C$. (b) Resonant cavity transmission scan of a $100 \times 100\,\mu\text{m}$ area at $q = 15$. (i) Additional losses due to a nanoparticle. It reveals the ground mode point spread function. (ii) Typical isocontour mode coupling artefact. (iii) Periodic background pattern. Black square: scan area of Fig. 3.2.9. [94, 95]

shifting transverse modes in and out of resonance with the fundamental mode, while the background pattern derives from higher transverse mode components of the modified fundamental mode in combination with mirror roughness.

For all experiments presented in this section, a rather elliptic, large r_C fibre profile was used (see profile cuts in Fig. 3.1.3(b)), where the radii of curvature along the principal axes x and y of the elliptical structure are $r_C^{(x)} = 161\,\mu\text{m}$ and $r_C^{(y)} = 201\,\mu\text{m}$. A color plot of the structure is shown in Fig. 3.2.4(a), where the principal axes are aligned with the plot axes. The fibre mirror features a DBR coating at a central wavelength of 780 nm (ATF Boulder) with a transmittivity of 10 ppm and 12 ppm absorption losses. The dielectric coating of the macroscopic planar mirror (Layertec) also has its central wavelength at 780 nm with a transmittivity of 60 ppm and 34 ppm absorption losses. These values yield a finesse of about 60 000 for negligible diffraction loss. An overview of the cavity parameters is given in appendix A (fibre A). The mirror separation could be tuned over the whole stability range and the planar mirror could be laterally raster scanned, while the transmission was recorded. In addition, sidebands could be imprinted onto the laser with an electro-optical modulator (EOM) as a frequency ruler (modulation frequency 2 GHz) allowing to determine the cavity linewidth and thereby the quality factor in absolute units. The finesse is obtained from the quality factor and the cavity length according to eq. 2.1.13. Details of the experimental setup can be found in [135].

As it can be observed that a decreased finesse mainly appears when higher order transverse modes become degenerate with the ground mode, it is useful to study transmission spectra and map out the relevant intersection regions. Figure 3.2.2 shows transmission spectra of one FSR as a function of the cavity length, where the fundamental modes

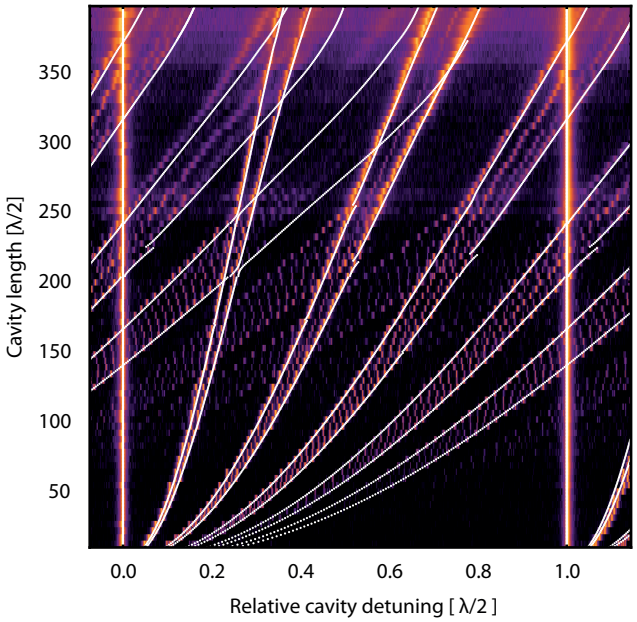

Figure 3.2.2.: Cavity transmission spectra as a function of axial mode order q for $\mathcal{F} \approx 1200$, shown in logarithmic colour scale for a wavelength of 856 nm. White: model for modes $(0,\, m+n)$ and $(m+n,\, 0)$. [94]

have been aligned and appear as vertical lines. For easier sampling, the spectra were taken at a wavelength of 856 nm, corresponding to $\mathcal{F} \approx 1200$ due to the higher transmission of the DBR at this wavelength. According to the resonance condition (eq. 2.1.31), the transverse modes move further apart with increasing mirror separation, eventually running into the fundamental mode of the next FSR (on the right). When evaluating the spectral positions of the transverse modes, a deviation from the spectrum given by the simple resonance condition is found. The white lines are computed using the more accurate model described in the next section for modes $(0,\, m+n)$ and $(m+n,\, 0)$, so the outer modes of each order $m+n$. Note that this is no fit, but a simulation using but the measured mirror profile.

A close-up at the crossover of modes $(0, 4)$ and $(1, 3)$ with the fundamental mode reveals an avoided crossing behaviour, which is typically found when mode coupling occurs. Figure 3.2.3(a) shows spectra around the fundamental mode for every longitudinal mode order from $q = 198$ to $q = 220$. As can be seen in Fig. 3.2.3(b), which shows the maximal transmission of each spectrum, the transmission of the ground mode decreases close to resonance with the higher order transverse modes, which in turn increase their transmission until they both are approximately equal in height at the point of resonant coupling, where their separation is minimal. In case of the $(0, 4)$ mode, this splitting is measured to be 8.6 GHz, which matches the value obtained from the simulation within errors.

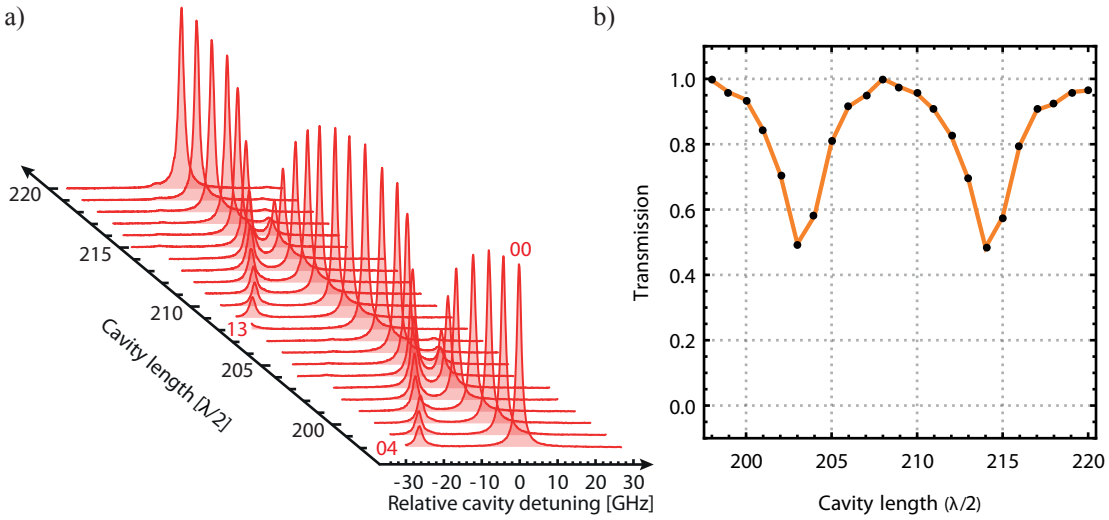

Figure 3.2.3.: (a) Measured cavity transmission spectra as a function of relative cavity detuning at a wavelength of 856 nm. Shows avoided crossings between the fundamental mode and fourth order modes $(0, 4)$ and $(1, 3)$. (b) Maximal transmission of each spectrum in (a), normalised. [94]

3.2.2. Modeling

As the fibre profile is not a perfect sphere, Hermite-Gaussian modes are no longer the exact eigenmodes of the system[1]. But as long as the deviations are not too large, one can effectively describe the real eigenmodes Ψ_i as a series expansion of HG modes Φ_k:

$$\Psi_i = \sum_k c_{ik}\Phi_k, \; k = (m, n) \tag{3.2.1}$$

The real eigenmodes and corresponding resonance frequency and loss can then be determined following the approach of Kleckner et al. [160]: Introducing the mode-mixing matrix M, which accounts for the change a mode undergoes during one round trip through the cavity, the task reduces to the eigenvalue problem

$$\gamma_i \Psi_i = M\Psi_i. \tag{3.2.2}$$

The mode mixing operator can be written as

$$M = A \cdot B \, \exp\left(-i\frac{4\pi}{\lambda}d\right) \tag{3.2.3}$$

with A and B being the contributions of the flat and curved mirror, respectively, multiplied with the phase acquired in one round trip in the cavity. The matrix elements of

[1] Note that in the paraxial approximation, which is used here, the 'perfect' profile shape leading to an orthonormal set of HG eigenmodes would be parabolic with slight deviations due to the Gouy phase. However, including non-paraxial terms shows that spherical mirrors are indeed the desired ones [140, 141].

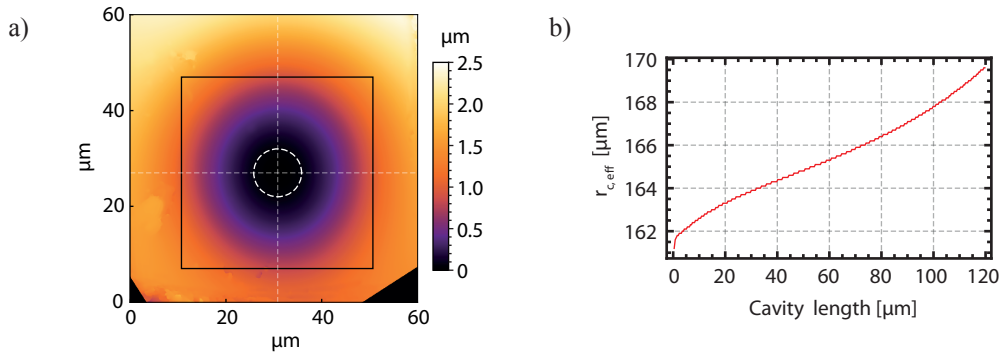

Figure 3.2.4.: (a) WLI image of mirror profile. Dashed circle: typical mode diameter. Dashed lines: Principal axes. Black square: simulation area. (b) Effective radius of curvature as a function of cavity length, determined by optimisation of the mode waist. [94]

A and B can be calculated by mode overlap integrals between an ingoing mode and an outgoing mode in the other direction over a sufficiently large area of the mirrors:

$$A_{st} = \int_{-x_0}^{x_0} \int_{-y_0}^{y_0} \Phi_s^+ \Phi_t^{-*} \exp\left(\frac{4i\pi}{\lambda} \Delta_a(x, y)\right) \mathrm{d}x\mathrm{d}y \tag{3.2.4}$$

$$B_{st} = \int_{-x_0}^{x_0} \int_{-y_0}^{y_0} \Phi_s^- \Phi_t^{+*} \exp\left(-\frac{4i\pi}{\lambda} \Delta_b(x, y)\right) \mathrm{d}x\mathrm{d}y \tag{3.2.5}$$

$\Delta_{a/b}(x, y)$ is the deviation of the mirror profiles from planar and $s = (m, n)$ and $t = (m', n')$ each denote a certain transverse mode, (x_0, y_0) gives the extent of the mirror, and $\pm$ indicates the sign of the phase factor of Φ_k. As $\Delta_a = 0$ due to the planarity of the macroscopic mirror, $A_{st} = \delta_{st}$ as the HG modes form an orthonormal set, which leads to A being the identity matrix. If the curved mirror were a perfect sphere covering the entire half-space, M would also become an identity matrix and the eigenvalues γ_i would be unity, but as soon as $\Delta \equiv \Delta_{a/b}(x, y)$ deviates from spherical or the mirror is finite, M has off-diagonal elements and transverse-mode coupling occurs.

For an accurate treatment, it is best to use the measured surface profile for Δ, which is shown in Fig. 3.2.4(a) for the experiments in this section. The black square indicates the simulation area, which must be well larger than the mode radius, shown as dashed circle. The profile data needs to be centred at the fibre core, which needs to be set to zero, $\Delta(0, 0) = 0$, the angle should be corrected, and the principal axes should be aligned with the axes of the data set, which requires shifting, tilting and rotating the raw data.

To find a suitable basis set Φ_k for each mirror separation, the overlap of the fundamental mode Φ_{00} with its reflected counterpart $|M_{00}|$ is maximised by varying its mode waist w_0. From the obtained values for w_0, an effective radius of curvature $r_{C,\mathrm{eff}}$ can be calculated. The result for the x-direction is shown in Fig. 3.2.4(b), showing that the effective radius of curvature is larger than the central one, $r_C = 161\,\mu\mathrm{m}$, and increases

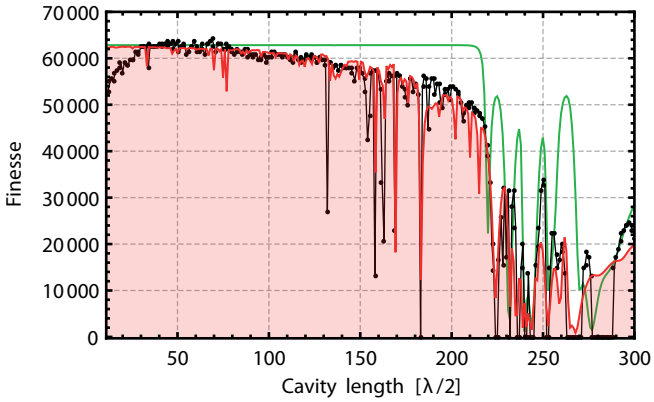

Figure 3.2.5.: Data points: cavity finesse extracted from 22 500 measurements for each datapoint. Wavelength: 780 nm. Red: simulation of the cavity finesse as a function of the mirror separation for measured surface profile assuming mirror transmission and absorption to be 100 ppm. Green: simulation for a 2D Gaussian profile fitted to the measured surface. [94]

with d. Consequently, the stability range is expected to extend beyond the limit of $d = r_C$.

The simulation presented in this section takes into account mode orders up to $m+n = 20$. Using more modes does not significantly alter the results but strongly increases the computation time, which grows approximately as $(m+n)^4$. The required minimal size of the area used for the simulation depends on the profile details. Several sizes have been tested to confirm that a larger area does not significantly change the simulation results. The pixel size is chosen such that the features of the highest mode order are still well resolved. For a fibre profile of 400×400 pixels covering an area of $40 \times 40\,\mu\text{m}^2$, the simulation of 300 mirror separations could be conducted with a personal computer within a few hours.

Simulation of finesse The diffraction loss D_i, of a mode Ψ_i can be obtained from the absolute value of the corresponding eigenvalue γ_i:

$$D_i = 1 - |\gamma_i|^2 \tag{3.2.6}$$

Loss here does not necessarily mean dissipation, but rather power can be transferred between transverse modes. But due to the finite extent of the mirror, absolute diffraction loss can actually occur, when power is transferred to too large higher order modes. The corresponding finesse is given by

$$\mathcal{F}_i = \frac{2\pi}{T_1 + T_2 + A_1 + A_2 + D_i}. \tag{3.2.7}$$

Figure 3.2.5 shows the finesse of the ground mode obtained from simulation with the measured profile in red using the measured values for transmission and absorption. The

simulation is compared to a finesse measurement (black data points), which was obtained from a resonant cavity transmission measurement using the relation $T_c \propto \mathcal{F}^2$ and the measured finesse at short cavity length. The transmission rather than the finesse is measured here because one cannot determine the finesse reliably under mode mixing conditions as well as for low transmission. The rise of the finesse for short cavities can be attributed to a systematic error of the measurement: An iris aperture was used to suppress the transmission of higher order modes, which leads to clipping loss for short cavity lengths, at which the mode waist is smaller and the mode divergence larger. The overall shape, the position of localised finesse dips, and the decrease around $q = 220$ can be reproduced by the simulation with a high level of detail. However, to match the data, the lateral size of the mirror profile had to be rescaled by about 2.5% for the simulation. The same correction has been made for the simulation of the spectrum shown in Fig. 3.2.2, where the normalised phase of the eigenvalues γ_i is plotted. The mismatch might result from a calibration uncertainty of the interferometric surface reconstruction. The localised finesse dips correspond to narrow mode resonances involving high mode orders (see next paragraph), which are not resolved by the $\lambda/2$ -discrete sampling. As can be seen in the scan in Fig. 3.2.1(b), the resonance condition depends on the exact position on the planar mirror, making the finesse values at the dips somewhat arbitrary, such that both measurement and simulation may miss particular resonances. To capture the typical behaviour in the measurement, scans of a $30 \times 30\,\mu\text{m}$ area with 22 500 pixels were taken and the most prevalent value was taken for each data point shown.

It is instructive to compare the results with a simulation for a profile obtained from a Gaussian fit to the measured fibre surface as Δ. The result is shown as green solid line in Fig. 3.2.5. The smooth surface does not lead to the overall weak decline for increasing mirror separation, and the sharp features at intermediate d are missing. Yet, the finesse drop around $d = r_C/2$, which effectively limits the stability range, is reproduced. The difference can be explained by the presence of additional (and in particular asymmetric) surface deviations with mostly larger spatial frequencies and particle-like features in the measured profile. Due to the symmetry of the Gaussian it only couples the fundamental mode to transverse modes of even order. High spatial frequencies couple the fundamental mode to many transverse modes with large mode index, causing a smooth finesse decrease and significant resonant mixing for particular modes.

Composition of the ground mode The computed eigenvectors contain information about the composition of the system's eigenmodes from HG modes according to eq. 3.2.1. In Fig. 3.2.6(a), the coefficients $|c_{0k}|^2$ giving the contributions of HG modes to the fundamental mode are plotted as a function of mirror separation. The Gaussian mode Φ_{00} is clearly the dominant one, and for most cavity lengths, the ground mode shows negligible deviation from it (see inset). However, for certain distinct mirror separations where resonant mode coupling occurs, higher order modes can have significant contributions and lead to a severe distortion of the fundamental mode as can be seen in the sample mode plots in Fig. 3.2.6(b). The larger spatial extent of higher-order modes (see eq. 2.1.36) causes larger diffraction loss, from which also the fundamental mode

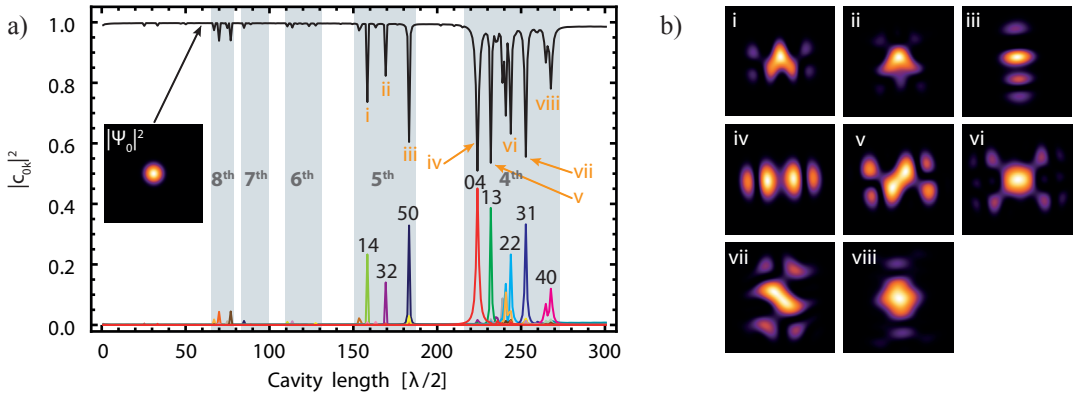

Figure 3.2.6.: (a) Composition of ground mode Ψ_0 of HG modes Φ_k; contributions $|c_{0k}|^2$ are shown. Black: $|c_{00}|^2$. Black numbers: transverse mode order of other important contributions. Shaded areas show impact zones of specified mode orders. Inset: $|\Psi_0|^2$ for a region of low coupling ($q = 60$). (b) Examples of mode shapes of fundamental mode $|\Psi_0|^2$ for selected mirror separations indicated by roman numbers in (a) exhibiting large coupling. The edge length is 40 µm. [94]

suffers under coupling conditions. Notably, the locations of high loss and strong mode mixing do mostly but not necessarily coincide [160].

Regions of impact of certain mode families (shaded areas) cover a significant fraction of the stability range. Still, for applications where the exact mirror separation is not essential, extended regions of negligible mode mixing remain. The different influence of e.g. mode orders 4 and 5 can be attributed to the larger values of $B_{0,k}$, for even modes due to the almost symmetric mirror profile. Also, for larger mode index differences, the differential Gouy phase evolves faster and the resonance condition is sharper. The coupling strength can be directly inferred from the mode splitting at an avoided crossing.

The presented model allows to investigate certain cavity geometries without the need for experimental testing. This makes it a useful tool to predict the cavity performance of fabricated profiles or find suitable parameter regimes for machining runs (see section 3.3.1).

3.2.3. Artefacts in scanning cavity microscopy

In many experiments [46, 53, 92, 117, 124] it is useful to laterally raster-scan the planar mirror with the cavity mode to obtain spatially resolved measurements of a sample placed upon the mirror. For this scanning cavity microscopy (SCM) [92, 93], small changes in the resonant cavity transmission are recorded to acquire information about e.g. sample induced scattering and absorption. In consequence, any background changes in transmission originating from the bare cavity alone need to be as small as possible to enable the resolution of small signals. The observed artefacts introduced in section 3.2.1 (see Fig. 3.2.1(b)) were studied in detail using the same fibre as for the other experiments in this section and a pristine mirror without sample. For all accessible longitudinal mode

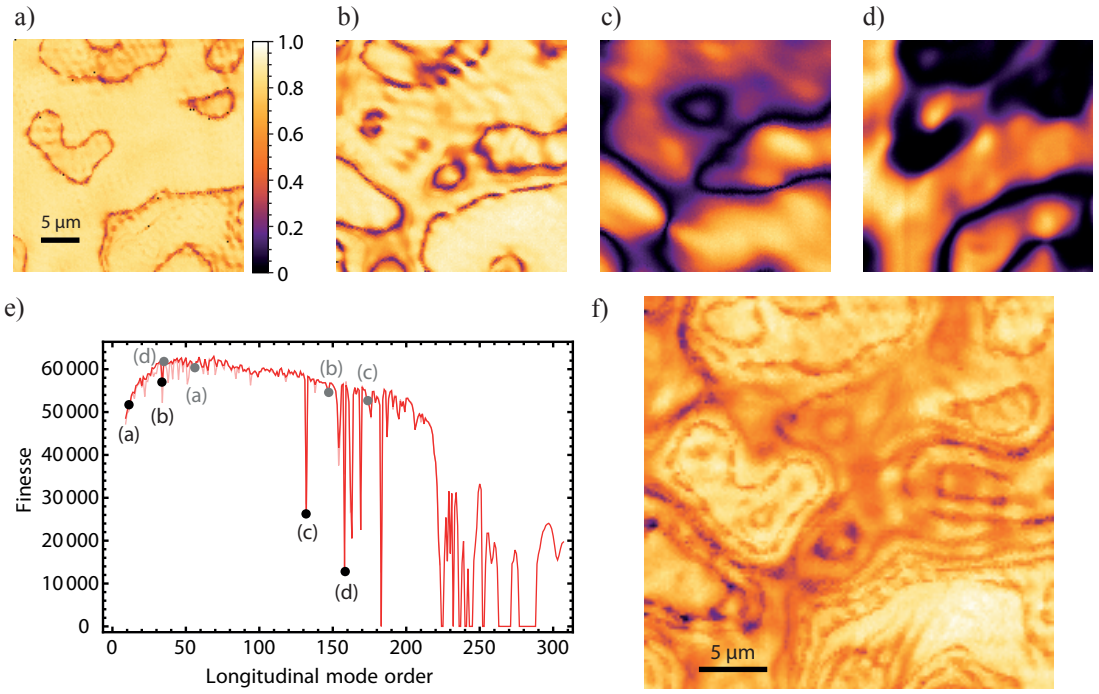

Figure 3.2.7.: (a – d) Resonant cavity transmission scans of a $30 \times 30\,\mu m$ area on a clean mirror for mode orders $q = 11, 34, 132, 158$. Transmission normalised to the peak value. (e) Cavity finesse as a function of longitudinal mode order, deduced from taking the most prevalent (solid red) and the average (opaque red) value of each transmission scan and converted to finesse knowing the mirror losses. Black dots: mode orders of scans (a) to (d). Grey dots: mode orders of scans (a) to (d) in Fig. 3.2.14. (f) Overlay of transmission scans of longitudinal mode orders $q = 11, 12, 14, 16, 22, 24, 28, 38$ showing isocontours of the varying resonance condition due to the mirror topography (Arbitrary units, same colour scale as in (a)). [95]

orders, SCM scans of the same $30 \times 30\,\mu m$, defect-free area were taken at a resolution of 200 nm. They are shown in appendix B.2.

Transverse-mode resonance isocontours Figures 3.2.7(a – d) show example measurements with distinct ring-like mode coupling artefacts at $q = 11, 34, 132, 158$, with the corresponding mode orders being indicated in the finesse plot in Fig. 3.2.7(e). Note that the artefacts cannot be observed for all mirror separations, but the transmission remains unaltered for axial orders with negligible mode coupling. It can be observed that the overall shape of certain contours is very similar across different measurements, and that the width of the contour lines increases continuously with increasing q. As can for example be seen in scan (a), the contours can be much more narrow than the wavelength of the light. Figure 3.2.7(f) shows the superposition of measurements taken at mode orders $q = 11, 12, 14, 16, 22, 24, 28, 38$. Remarkably, the individual measurements combine to a consistent isocontour map.

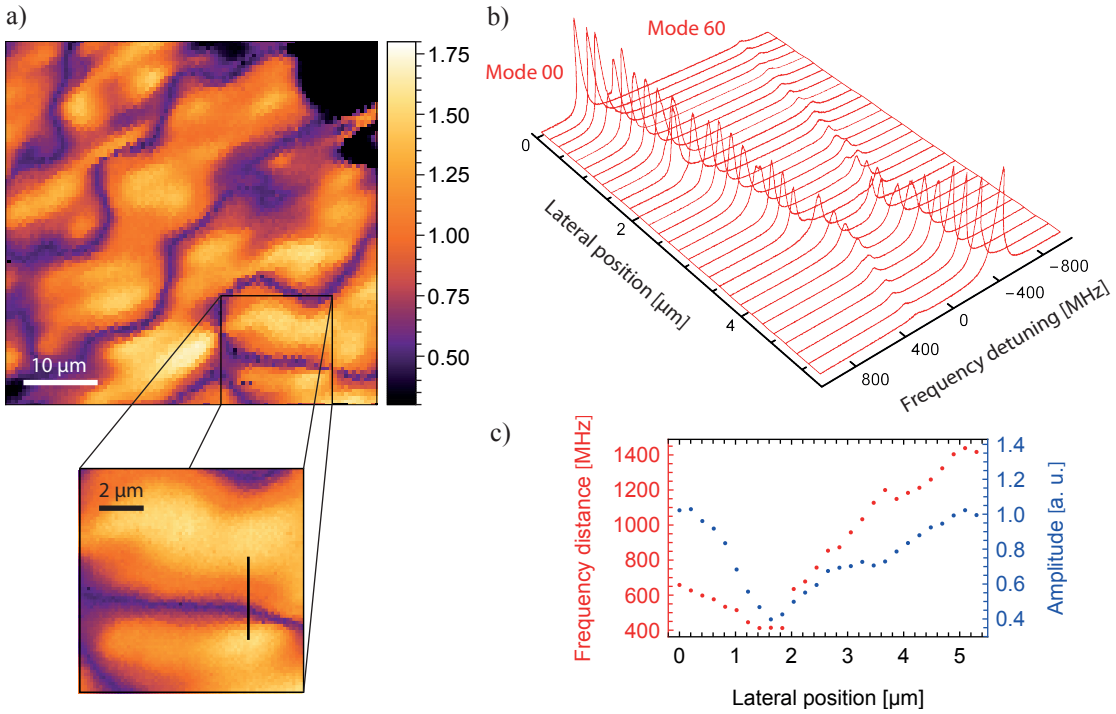

Figure 3.2.8.: (a) Transmission scan at $q = 132$ with a close up higher resolution scan. Pixel size: 0.5 and 0.2 µm. Black line indicates 5.4 µm long path along which spectra in (b) are taken. (b) Cavity transmission spectrum around the ground mode for different lateral positions showing an avoided crossing with mode $(6, 0)$, where the point of minimal distance corresponds to the darkest spot in (a) along the path. (c) Maximal amplitude of the spectra in (b) (blue) and frequency distance of the two modes $(0, 0)$ and $(6, 0)$ along the path. [95]

When having a closer look at the spectra of the cavity resonances in the surrounding of contour lines, one finds degeneracy with higher order transverse modes occurring at these exact spatial locations. Figure 3.2.8(a) shows an example transmission map taken at $q = 132$, where one can also observe a distinct dip in finesse (see Fig. 3.2.7(e)). Following a linear path of 5.4 µm length perpendicular to a contour line as indicated in the close up scan, cavity transmission spectra are taken at lateral distances of 0.2 µm (see Fig. 3.2.8(b)). One can observe, in addition to the fundamental mode, the presence of a higher order mode, which is found to be mode (6, 0), whose frequency detuning and strength changes with the mirror position in the manner of an avoided level crossing. The frequency axis of the data is centered on the average frequency of the two modes to make this apparent. The higher order mode can be assigned unambiguously from the knowledge of q and the mode frequency simulation shown in Fig. 2.1.2(b), as well as from counting the higher-order modes in the cavity transmission spectrum. At the location of the contour line, the mode separation is minimal, and the two modes have the same amplitude. Figure 3.2.8(c) shows the quantitative evaluation of the data in

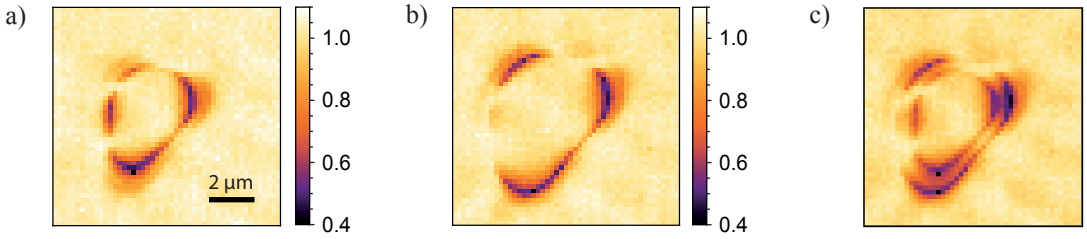

Figure 3.2.9.: (a), (b) Transmission scans at $q = 15$. Changing the wavelength from $\lambda = 780.1400\,\mathrm{nm}$ (a) to $\lambda = 780.2328\,\mathrm{nm}$ (b) increases the size of the artefact. (c) Scans (a) and (b) added up for clarity. Arbitrary units. [95]

(b) yielding a variation of the frequency separation $\mathrm{d}\nu \approx \pm 1$ GHz or equivalently ± 18 cavity linewidths, which is 7×10^{-4} of the free spectral range ($\Delta\nu = 2.91\,\mathrm{THz}$). This gives evidence that the contour lines result from a spatially varying transverse-mode resonance, and the minimal line separation of 412 MHz on the contour line directly yields the inter-mode coupling strength. This observation implies that the transverse modes experience different frequency shifts depending on the location on the mirror.

When considering the resonance condition (eq. 2.1.31), we find that the mode frequency difference

$$\mathrm{d}\nu = \nu_{qmn} - \nu_{(q+1)00} = \Delta\nu \frac{m+n}{\pi} \left(\zeta\left(d, r_C\right) - \zeta\left(d', r'_C\right)\right) \tag{3.2.8}$$

of a mode pair with a given set of (q, m, n) can be varied by a change of q, the laser wavelength λ, a change of the effective radius of curvature r_C the modes experience, and the field penetration depth $d_{\mathrm{pen}} = d_{\mathrm{pen}}^{\mathrm{fibre}} + d_{\mathrm{pen}}^{\mathrm{plan}}$ into the dielectric mirror stack and thereby the effective mirror separation $d = q\frac{\lambda}{2} + d_{\mathrm{pen}}$. The optical penetration depth for a DBR, whose last layer has a low refractive index (spacer layer), which is the case for the planar mirror, is given by [161]

$$d_{\mathrm{pen}}^{\mathrm{plan}} = \frac{\lambda_0}{4\Delta n}\bar{n}^2 \tag{3.2.9}$$

with $\Delta n = n_H - n_L$ being the refractive index contrast, λ_0 the central wavelength of the DBR, and

$$\bar{n} = 2\left(n_L^{-1} + n_H^{-1}\right)^{-1} \tag{3.2.10}$$

the average refractive index. Here, it amounts to $d_{\mathrm{pen}}^{\mathrm{plan}} = 893\,\mathrm{nm}$. For a mirror with a last high refractive index layer, which is the case for the fibre mirror, the penetration depth is smaller,

$$d_{\mathrm{pen}}^{\mathrm{fibre}} = \frac{\lambda_0}{4\Delta n}, \tag{3.2.11}$$

303 nm in this case. This leads to a total penetration depth $d_{\mathrm{pen}} = 1.2$ µm.

The overall behaviour of an increasing width of spatial mode resonances for increasing q as seen in Fig. 3.2.7(a – d) can be explained by the dispersion of the modes involved.

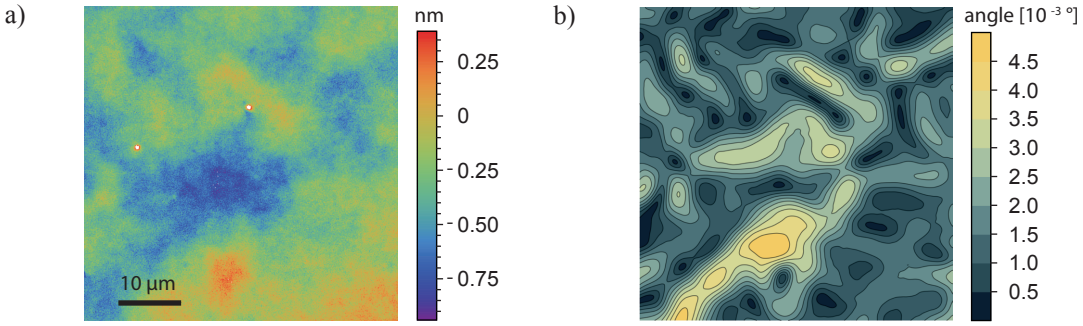

Figure 3.2.10.: (a) WLI measurement of the mirror surface. (b) Calculated modulus of the local surface angle of the area shown in (a). [95]

From eq. 3.2.8, the resonance condition (eq. 2.1.31), and the condition of degeneracy, one can estimate the mode order leading to degeneracy at a given mirror separation by

$$m + n = \frac{\pi}{\arccos\sqrt{1 - d/r_C}}. \tag{3.2.12}$$

More accurately, the relative frequency of the modes (see Fig. 2.1.2(b)) and the admixture of higher order modes (see Fig. 3.2.6(a) and 3.2.13) can be deduced from the mode coupling simulation. For short cavities, transverse modes with large $m+n$ become degenerate with the fundamental mode and lead to a mode crossing under a large angle $\propto m + n$, which can be seen in Fig. 2.1.2(b). This means that small variations lead to a large frequency detuning between the modes, restricting resonant mode coupling to small spatial regions and thus the observed sharp features. For long cavities, by contrast, the transverse-mode spacing is much larger and the modes with small $m + n$ become resonant with the fundamental mode. The angle between the dispersion of the modes $\propto m + n$ is consequently smaller such that the resonant coupling region is large, consistent with the much broader features observed for longer cavities.

The dependence of the mode degeneracy location upon the wavelength can be directly visualised by taking SCM images at different laser wavelengths. Figure 3.2.9(a) and (b) show an example feature, measured at q = 15 at a wavelength of $\lambda = 780.1400\,\text{nm}$ (a) and $\lambda = 780.2328\,\text{nm}$ (b). This variation of 10^{-4} changes the size of the isocontour by about its spatial width. A wavelength change can thus globally change the observed isocontour pattern, but is not the origin of the structure.

Next, let us consider a spatial change in the effective radius of curvature of the fibre mirror as possible origin of the spatial variation of the mode degeneracy condition. Unevenness of the planar mirror leads to a spatially varying orientation of the cavity's optical axis, such that the cavity mode samples different areas on the fibre mirror. Since the mirror shape is non-spherical, this translates into a change in r_C. Figure 3.2.11(a) shows schematically how an uneven mirror surface makes the mode impinge outside the centre of the mirror profile such that it experiences a larger radius of curvature. To analyse the effect, WLI images of the planar mirror topography were taken for several locations to infer the typical variation of surface inclination. Figure 3.2.10(a) shows an

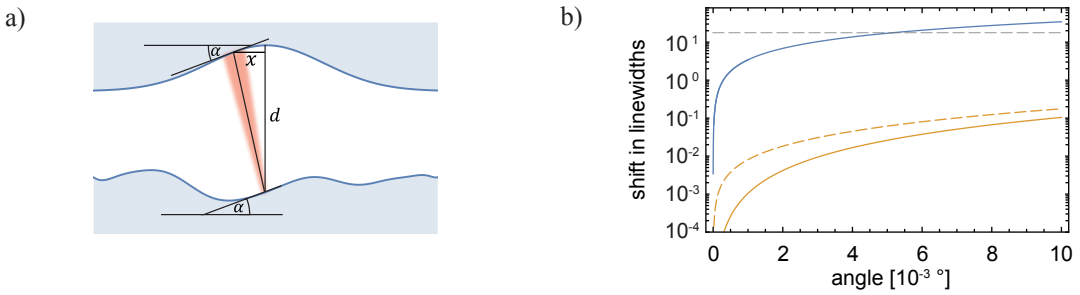

Figure 3.2.11.: (a) Schematic drawing of the mechanism leading to a variation of mode degeneracy. (b) Calculated change of transverse-mode frequency separation $\Delta\nu_{00,60}$ as a function of surface angle at $q = 132$ in units of linewidths. Yellow solid line: Frequency shift due to changing r_C for an aligned cavity. Yellow dashed line: Shift due to changing r_C and changing penetration depth. Blue line: Frequency shift due to r_C for an initial misalignment of $\alpha_0 = 1.5°$. Gray dashed line: Observed maximal shift. [95]

example of a measured surface profile $h(x, y)$, and (b) shows the calculated modulus of the local surface angle $\alpha = \arctan\sqrt{(\Delta h/\Delta x)^2 + (\Delta h/\Delta y)^2}$ on the same area after smoothing the data with a Gaussian filter of $1/e^2$ radius 4.2 µm, which matches the mode radius w_0 on the mirror. One observes typical height variations of up to $\Delta h \sim 1$ nm on length scales of $\Delta x \sim 10$ µm, yielding angles up to $\alpha = 0.005°$. Assuming that the cavity mode will form on the curved mirror where the two local surface angles match, one can calculate the change in the effective radius of curvature for a Gaussian profile $h(x) = -t\exp(-x^2/a^2)$ by solving for x_α for which $\theta = \arctan(\mathrm{d}h(x)/\mathrm{d}x) = \alpha$ and evaluating

$$r_C(x_\alpha) = \frac{\left[1 + (\mathrm{d}h/\mathrm{d}x)^2\right]^{3/2}}{\mathrm{d}^2h/\mathrm{d}x^2}. \tag{3.2.13}$$

For the angles found above and the fibre mirror geometry used here, this translates into lateral shifts of the cavity mode of $x_\alpha < 20$ nm. For a perfectly aligned cavity where the average surface normals of both mirrors are parallel, this leads to relative changes in r_C of $\Delta r_C/r_C \approx 10^{-6}$. Figure 3.2.11(b) shows a calculation of the resulting frequency shift $\mathrm{d}\nu$ in linewidths as a function of α (yellow solid line), too small to explain the observed frequency shifts shown in Fig. 3.2.8(b) (indicated by the dashed gray line in Fig. 3.2.11(b)). However, when the cavity is slightly misaligned, the change in r_C with x is much larger, and for an initial misalignment of 1.5°, the calculation shows that the observed range of frequency shifts is expected for the measured range of surface angles α; see blue line in Fig. 3.2.11(b). Misalignments of this order of magnitude are reasonable for scanning cavity experiments. This effect can thus be relevant to explain the observed behaviour.

The remaining parameter that can additionally contribute to the observed effect is a spatial variation of the field penetration depth on the planar mirror. From the observed variation of $\mathrm{d}\nu$ one can quantify the necessary spatial variation of either the refractive index contrast or the layer thickness (or a combination of both). The observed shift

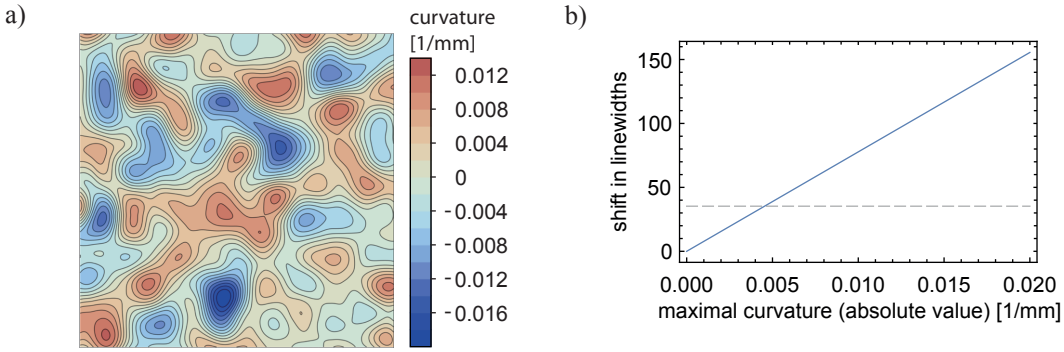

Figure 3.2.12.: (a) Average curvature of the area shown in Fig. 3.2.10(a). (b) Calculated change of transverse-mode frequency separation $\Delta\nu_{00,60}$ as a function of the maximal local curvature in units of linewidth over the range of values observed in (a). Dashed line: Maximal shift observed in Fig. 3.2.8. [95]

corresponds to a change in the penetration depth of 73 nm, which is about 8.1% of $d_{\mathrm{pen}}^{\mathrm{plan}}$. So for a variation of the penetration depth, either the central wavelength or the refractive index contrast has to vary. Fluctuations of the refractive index of this magnitude are not likely and a varying central wavelength would imply a systematic change of the layer thicknesses by a several percent over a lateral length of a few µm, which is about an order of magnitude too large to be realistic.

Finally, one can also consider a combination of the two effects above: a change in coating thickness on both mirrors sampled due to the changing location of the cavity mode, which in turn is caused by the unevenness of the planar mirror. Due to the partial directionality of the coating process [162], the layer thickness depends on the local surface orientation: The coating is thinner $\propto \cos(\theta + \theta_0) / \cos(\theta_0)$ at the incline locations, with θ_0 being the incident deposition direction. For the fibre geometry discussed here, a maximal thickness variation up to $\pm 3\%$ is expected for a fully directional deposition under $\theta_0 = 30°$. The yellow dashed line in Fig. 3.2.11(b) shows that this effect is comparable in magnitude to the one caused by a changing r_C for a perfectly aligned cavity. However, as the thickness variation is almost independent of α_0, it does not contribute significantly for a tilted cavity.

A further important contribution comes from the local surface curvature of the 'planar' mirror, which can be pictured as a second (very slightly) concave mirror, leading to a change in Gouy phase. To determine the magnitude of this effect, the mean curvature (inverse of the radius of curvature) was computed for every position of the area shown in Fig. 3.2.10(a). The curvature map in Fig. 3.2.12(a) was achieved by fitting a two-dimensional second order polynomial to each datapoint over a 4.3 µm area. Diagonalisation of the Hessian matrix, which contains all second derivatives, allows for the calculation of the curvatures along the orthogonal principal axes at each point. These are averaged to obtain the mean curvature. One finds corresponding radii of curvature down to about 70 mm. Figure 3.2.12(b) shows a calculation of the resulting relative frequency shift $\Delta\nu_{00,60}$ in linewidths as a function of curvature upon curvature inver-

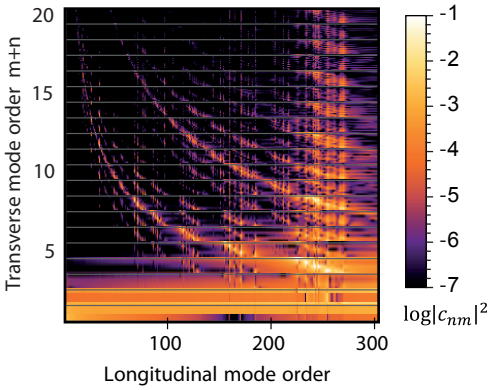

Figure 3.2.13.: Contributions $c_{0k} \equiv c_{mn}$ of HG modes (m, n) to the ground mode shown as $\log |c_{mn}|^2$ for different longitudinal mode orders. Each horizontal box separated by grey lines corresponds to $m+n+1$ modes of order $m+n$ ranging from (0, $m+n$) to ($m+n$, 0). [95]

sion (i.e. a change in sign). Comparing the shifts obtained for the observed curvature values with the maximal shift observed in experiment (Fig. 3.2.8, dashed line in Fig. 3.2.12(b)), one finds a similar magnitude. This suggests that this is a dominant effect in the experiments. The influence of curvature was quantitatively analysed by Thea Moosmayer [95, 163], who observed a relative shift in Gouy phase of different transverse modes for laser-written structures on the planar mirror[2].

In summary, the varying slight local curvature of the macroscopic mirror is found to be the main contribution leading to the observed contour lines, while the changed inclination can also play a significant role for a tilted mirror.

Periodic background patterns The periodic checker-board like background patterns are present for most axial mode orders, even when there are no mode coupling contour lines or a noteworthy finesse reduction. It should be noted that these patterns are by far fainter than the isocontours described in the previous paragraph. To get a better understanding of how they arise, let us first consider the composition of the fundamental mode of HG modes. Figure 3.2.13 shows the contributions of higher order transverse HG modes for different longitudinal mode orders on a logarithmic scale. Each horizontal box separated by grey lines corresponds to a mode order $m + n$ and therefore contains a different number of modes (pixel rows) $m + n + 1$. For instance, at the bottom of the plot are the modes (1, 0) and (0, 1) with significant contributions, likely due to a slight tilt of the profile. Further large contributions of small mode orders (2 and 3) across all axial mode orders may be explained by a slight unevenness at the centre of the fibre profile favouring these modes. Apart from that, one can see how certain mode families systematically contribute at a few dominant cavity lengths in agreement

[2]This can for example also be seen for mirror markings like the one in Fig. 6.2.3(b), which constitute blow-up bumps of the coating and appear in SCM scans with densely spaced mode-coupling isocontour lines.

with their impact zones (compare to Fig. 3.2.2 and Fig. 3.2.6). This implies that for virtually all axial mode orders there are slight contributions of certain higher order transverse mode families.

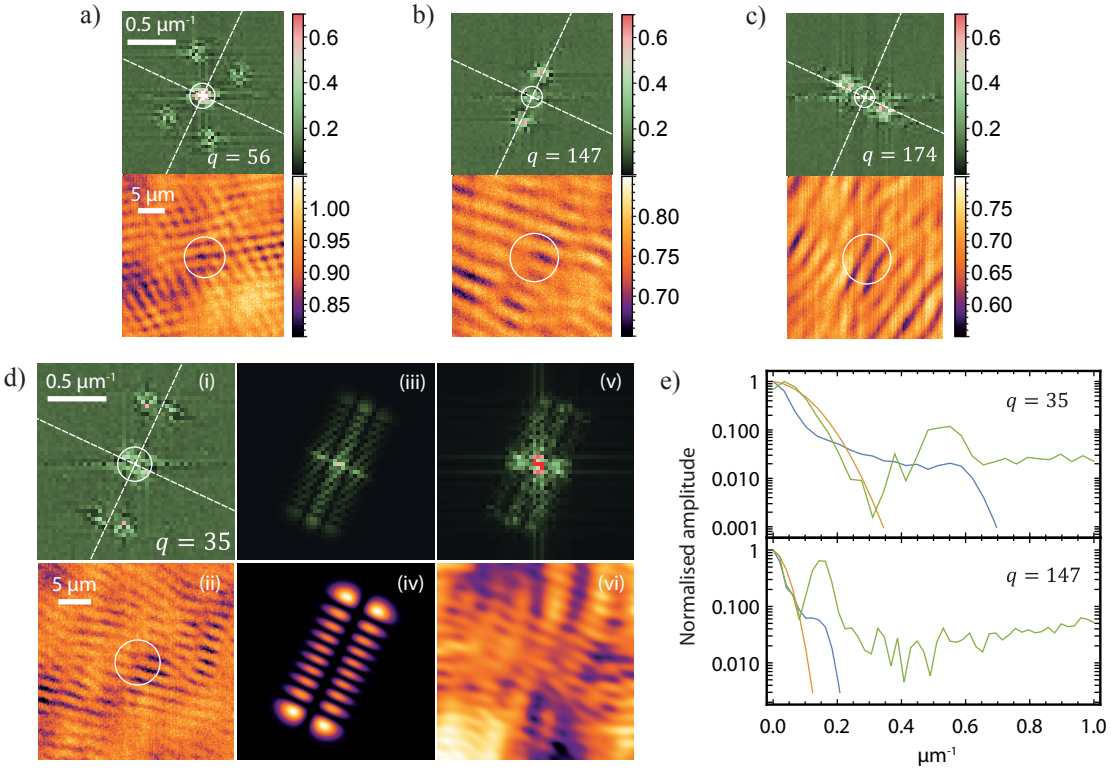

Figure 3.2.14.: (a – c) Lower panels: Transmission scans showing periodic background artefacts at different longitudinal mode orders. White circle indicates $1/e^2$-radius of Gaussian mode at the respective cavity length. Upper panels: Fourier transform of scans. White circle: $1/e^2$-radius of Fourier-transformed Gaussian mode. Dashed lines: Assumed principal axes of HG modes. (d) (i), (ii) Same as in (a – c) for $q = 35$. (iv) HG mode (9, 1) with its Fourier transform (iii). (vi) Convolution of normally distributed random numbers with mode (9, 1) and Fourier transform of the image (v). (e) Radial integration of Fourier transformed scans in (d) and (b) (green) together with the Gaussian mode (yellow) and a sum of modes of the order, which is contributing most to the ground mode: $\sum_{i=0}^{n+m}(i, m+n-i)$ (blue), where $m+n = 10$ for $q = 35$ and $m+n = 5$ for $q = 147$. [95]

It is useful to spectrally analyse the patterns, which is exemplarily demonstrated in Fig. 3.2.14(a - c) for resonant cavity transmission scans at different mirror separations. The lower panels show the original SCM measurement where the white circle indicates the $1/e^2$-radius of the Gaussian mode for the respective cavity lengths. It is clearly visible that the patterns exhibit features smaller than the fundamental mode. Scan (a) shows a checker-board pattern whereas in scans (b) and (c) linear shapes occur, seemingly perpendicular to one another. The upper panels show a two-dimensional discrete Fourier transform of the scans, where the white circle denotes the $1/e^2$-radius of the Fourier-

transformed Gaussian mode. While the observed low frequency part matches well to the expected Gaussian mode spectrum for the particular longitudinal mode order, it is apparent that there are large frequency components, which are incompatible with the Gaussian mode only. They are typically aligned along two perpendicular axes indicated by dashed lines in the plots, which seem to be the principal axes of the HG modes. A Hermite-Gaussian mode contains spatial frequencies up to $f_m^{(x)} = f_0^{(x)}\sqrt{m+1}$ ($f_n^{(y)} = f_0^{(y)}\sqrt{n+1}$), where $f_0^{(x,y)}$ is the $1/e^2$ frequency of the fundamental mode. This results from the increase of the number of transverse field nodes $\propto m$ (n) and the increase in mode size according to eq. 2.1.36. A further observation is that the additional spectral components are at larger frequencies for smaller cavity lengths. All scans featuring a pronounced background pattern together with their Fourier transform can be found in appendix B.1.

In Fig. 3.2.14(d), the scan at $q = 35$ is presented together with its Fourier transform. Panel (iv) shows HG mode (9, 1), which according to the evaluation presented in Fig. 3.2.13 constitutes the dominant admixture at this length. It is orientated along the principle axes obtained from the Fourier transforms and the lateral scale is the same as in (ii). Clearly, the fringes of the mode match the pattern in the scan much better than merely the Gaussian mode and in particular, the spatial frequency seems similar. This becomes apparent when taking the Fourier transform of the mode as displayed in panel (iii). It very well matches the extent of the features in (i), giving evidence for contributions of this mode order.

So far, the argument hints at higher order modes to play a role in the formation of the background patterns, but the underlying mechanism has not yet been discussed. To study the effect of surface roughness, a matrix of normally distributed random numbers with the same extent as the scans was convoluted with the mode in (iv). The result is displayed in panel (vi). The arising pattern shows a remarkable similarity in frequency and texture with the measured pattern, leading to the conclusion that nanoscaled surface roughness is likely to cause the observed background patterns. Panel (v) shows the Fourier transform of panel (vi), which is basically the same as in (iii) multiplied with noise.

Figure 3.2.14 (e) shows a radial integration of the 2D Fourier spectrum and compares it to the spectrum of the Gaussian fundamental mode and the spectrum of the mode family that dominantly contributes to mode mixing as identified from the simulation shown in Figure 3.2.13. While the observed low frequency part matches well to the expected Gaussian mode spectrum for the particular longitudinal mode order, additional high frequency components agree with the frequencies of dominantly admixing modes. In particular, the localized peaks observed in the 2D Fourier spectra occur at the peak frequency of the most strongly admixing higher order mode. Components at higher frequency do not show any structure and can be attributed to uncorrelated measurement noise. The overall scaling of observed and expected frequencies with q can be clearly seen from the comparison of spectra for $q = 35$ and $q = 147$ (top and bottom panel of Fig. 3.2.14 (e)). The question remains why the Fourier transforms of the scans consistently feature large frequency components and components in a frequency range

which can be attributed to the ground mode, but not so much in between, in contrast to the Fourier transforms of the higher order modes. The difference could be a sign for destructive interference with additionally contributing modes, which are indeed expected to be relevant from the simulation of admixing modes.

So examining the background patterns not only gives insight into the composition of the fundamental mode but also hints at a small-scaled roughness of the planar mirror. Notably, ripple formation on the mirror as described in [164] does not seem to be a significant contribution as the image in (vi) was obtained with fully unordered random numbers.

Outlook Two types of mode coupling artefacts in SCM measurements have been analysed: The characteristic ring-shaped isocontours could be traced back to the few-µm-scale topology of the planar mirror, whereas the regular background patterns likely arise from nanoscaled surface roughness. The first effect could be further investigated by tuning the laser frequency in steps and performing SCM measurements. The resulting contour map should give insight to mirror properties otherwise not easily accessible. Furthermore, knowing that transverse-mode coupling does not necessarily affect the whole sample mirror and that spatial positions which exhibit mode coupling can be shifted by a slight change of wavelength, allows avoiding reduced cavity performance. Applying a broadband light source, mode coupling effects can be averaged out such that they are typically no longer visible.

3.3. Extreme geometries and limitations

For many applications it is desirable to push the boundaries of possible cavity geometries to obtain for instance a minimal mode volume or maximal quality factor. This section sheds light on extreme cavity geometries and the limitations which can be faced there.

3.3.1. Limitations due to mode coupling effects

As the effective area of the mirror becomes smaller, mode coupling and diffraction loss set in. The important figure of merit here is the ratio of the mode radius on the curved mirror and the effective area of the mirror, which in case of near Gaussian geometries can be approximated by the $1/e$-radius of the profile. To study the limiting effect of diffraction loss on the cavity geometry, mode coupling simulations (as introduced in section 3.2.2) were conducted exemplarily for several Gaussian profiles with $1/e$-radius a, depth t, and $r_C = a^2/(2t)$. When assuming a cavity with $d = r_C/2$, the mode radius on the curved mirror is $w_c = \sqrt{\lambda r_C/\pi}$, such that the relevant ratio

$$\frac{w_c}{a} = \sqrt{\frac{\lambda}{2\pi t}} \tag{3.3.1}$$

only depends on the profile depth. Therefore, the simulations are performed for fixed r_C and ellipticity $\epsilon = \sqrt{1 - r_C^{(x)}/r_C^{(y)}} = 0.23$ (value taken from [136]) and w_c/a is varied.

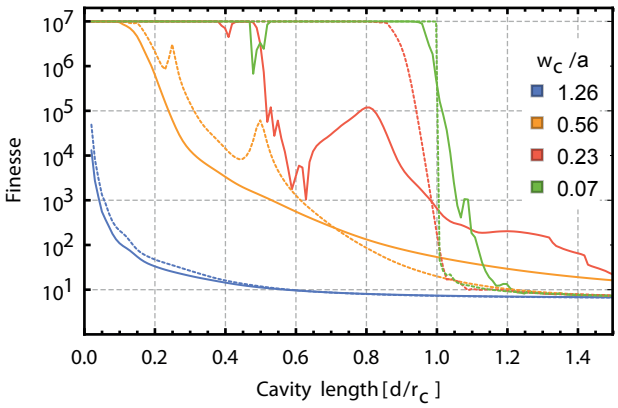

Figure 3.3.1.: Simulated finesse for different mirror profile size at fixed radius of curvature r_C using various ratios of w_c/a defined at $d = r_C/2$. Solid lines: Gaussian profile. Dashed lines: parabolic profile. Assumed additional loss: $\pi \times 10^{-7}$ for each mirror. [94]

The resulting finesse is plotted in Fig. 3.3.1 (solid lines), where additional losses of $\pi \times 10^{-7}$ were assumed for each mirror. While profiles as small as $a = 2\,w_c$ already achieve a performance, which is not limited by diffraction for small mirror separation, it requires a profile radius $a > 4\,w_c$ to extend this range to $d = r_C/2$ and $a > 10\,w_c$ to avoid mode coupling over the entire stability range. For comparison, simulations are performed for a rotationally symmetric parabolic profile with $r_C = r_C^{(x)}$ and an edge length of $2a$ (dashed lines). While the overall behaviour is similar, the calculation for $w_c = 0.56\,a$ shows that resonant transverse-mode coupling can also lead to a reduction of diffraction loss [160]. This can be understood by the destructive interference between the fundamental and the higher-order mode at the outer part of the mode, reducing the effective mode size [92]. Furthermore, the stability range can extend beyond $d = r_C$ for Gaussian profiles due to the effective radius of curvature growing with the cavity length, while $d = r_C$ marks a final point of stability for parabolic profiles. As a consequence, a useful rule of thumb for fibre machining is $a > 4w_c$, yielding a stability range to $d = r_C/2$, which is equivalent to $t > 8\lambda/\pi$. The findings in this paragraph are presented in [94] and are partly excerpted.

Taken the above results demonstrating that small structures lead to diffraction loss, the question arises, which cavity geometries are beneficial for a maximal Purcell effect. To analyse this, a mode coupling simulation was conducted for fixed d, using a Gaussian profile with varying t and a. As the computation is quite extensive, the maximum mode order included in the simulation was reduced to $m + n = 15$. The simulation area is $8 \times 8\,\mu\text{m}$ large and comprises 300×300 pixels and the wavelength was chosen as $\lambda = 740\,\text{nm}$, which is at the zero phonon line of the silicon vacancy centre. Figure 3.3.2(a) shows the resulting diffraction loss as a function of the profile parameters. For each combination of a and t, the cavity length was chosen as short as possible:

$$d = \left\lceil \frac{t + d_{\text{pen}} + 100\,\text{nm}}{\lambda/2} \right\rceil \frac{\lambda}{2} \tag{3.3.2}$$

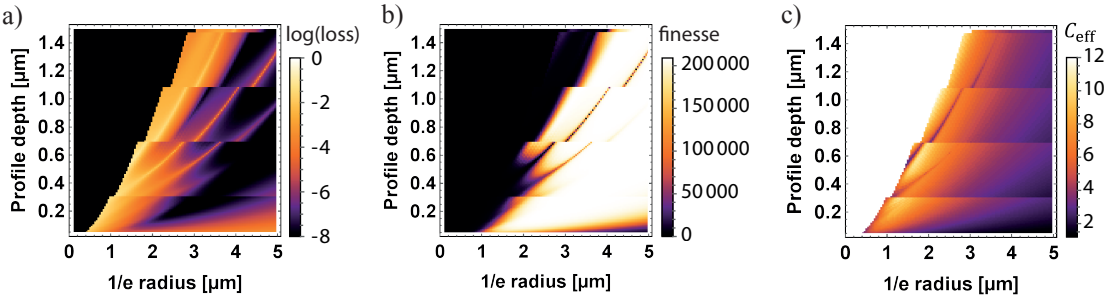

Figure 3.3.2.: (a) Simulation of diffraction losses as a function of profile depth t and $1/e$-radius a. Logarithmic plot. (b) Finesse deduced from diffraction losses in (a) and additional losses of 30 ppm. (c) Effective Purcell factor, assuming a silicon vacancy centre with $Q_e = 400$ as emitter. For all plots, the shortest possible cavity length (see text) was chosen, causing the visible steps. The step line fulfills $d = r_C$ and in the blank area on the left of it the cavity is unstable.

with $d_{\text{pen}} = 1.15\,\mu\text{m}$ and 100 nm alignment play, where $\lceil x \rceil$ denotes the ceiling function returning the next integer $> x$. This leads to the visible steps in the plot as soon as the depth becomes too large and the length needs to be increased by $\lambda/2$. In the blank area on the left, the cavity is unstable and the step-like border line fulfills $d = r_C$. One can see that significant additional losses are present for some geometries, especially close to the stability limit. Assuming transmittivity and absorption losses of 30 ppm altogether, the finesse is deduced from these diffraction losses and shown in Fig. 3.3.2(b). Again, we see that geometries close to the stability limit are not useful when high finesse is required. The situation looks somewhat different when dealing with a broad-band emitter. Figure 3.3.2(c) shows the effective Purcell factor for an emitter with $Q_e = 400$, which is a typical value for SiV centres. As the Purcell factor scales as Q_{eff}/V_m, the diffraction losses are not as crucial and due to their small volumes, the cavity geometries along the stability limit are in fact beneficial. It is nevertheless wise to choose slightly larger structures in a trade-off between highest possible Purcell factor and good experimental handling.

3.3.2. Smallest radii of curvature

To obtain small mode volumes, it is crucial to minimise the radius of curvature of the fibre profile. An alternative machining technique to reliably produce very small structures down to a few µm radius of curvature is focused ion beam milling. The advantage is that the resulting structures are very close to the ideal geometry, coming at the cost of significant surface roughness, which restricts the usability to applications at moderate finesse up to a few thousand [125, 165].

Laser machining in principle allows for very small radii of curvature as well and structures down to around $r_C = 5\,\mu\text{m}$ have been produced [126]. However, various problems arise in praxis: When the angles of the profile become too steep, 'shadowing' effects can occur in the ion beam sputtering (IBS) coating procedure, meaning that the coating, which is applied under an angle, is not homogeneously spread. As a rule of thumb the

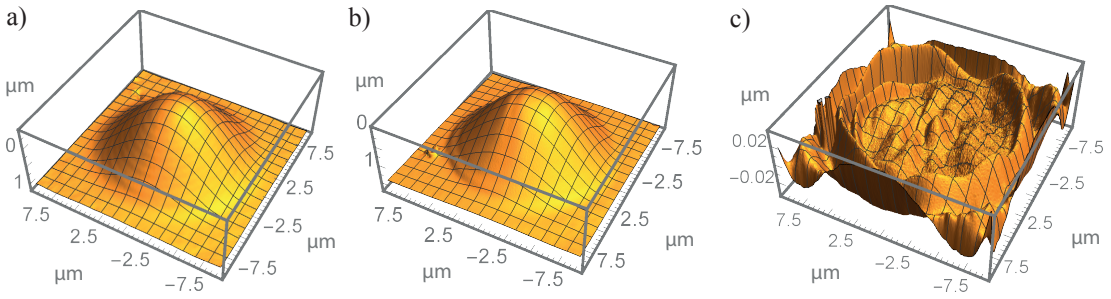

Figure 3.3.3.: WLI measurements of fibre profile for Eu experiment (fibre 26A) before (a) and after (b) the coating is applied. $r_C = 12.1\,\mu\text{m}$ (from polynomial fit). (b) shows ripples in the coating. (c) Residual of 6th order polynomial fit to coated profile.

maximal angle should be $\theta \lesssim 15°$, where

$$\theta = \arctan\left(\sqrt{\frac{2}{e}}\frac{t}{a}\right) \tag{3.3.3}$$

for a Gaussian profile, i.e. $t/a \lesssim 0.3$ [166]. Fulfilling this criterion for a given small r_C implies going to rather shallow structures as the smallest possible a value is about 2 µm. However, this leads to a very unfavourable w_C/a ratio (see eq. 3.3.1) and therefore notable diffraction losses already for small mirror separations. Furthermore, the growth of the coating by IBS is not purely mono-directional, but partly isotropic meaning that the layers grow 'inward' leading to a slightly reduced radius of curvature and possible deformations of the coating deteriorating cavity performance [162]. Figure 3.3.3 shows an example fibre profile ($r_C = 12.1\,\mu\text{m}$) before (a) and after (b) the coating was applied. There are step-like lines going through the structure. In addition, one can see ripples in the profile centre, which become visible when looking at the residual of a 6th order polynomial fit to the coated structure as shown in (c). While the exact cause of the deformations remains unclear, it can be observed that they only appear for the smallest structures with $r_C \lesssim 15\,\mu\text{m}$. The possibility remains that the observed ripples are an artefact of the surface reconstruction, which however is unlikely as they systematically appear for minimal r_C and are not observed for the uncoated profiles.

How well small fibre profiles perform, also seems to depend on the coating. For the SiV experiment, a DBR consisting of alternating layers of SiO_2 and TiO_2 was chosen to increase the refractive index contrast compared to the more typical SiO_2/Ta_2O_5 coating and thereby reduce the penetration depth (see eq. 3.2.9). While the resulting cavity performance is as expected for large r_C, a drastic reduction in finesse could be observed in measurements conducted by Franziska Oehl for $r_C \lesssim 20\,\mu\text{m}$ together with increased unevenness of the coating as seen from WLI measurements. However, this relation could not be confirmed in general, as for SiO_2/Ta_2O_5 coating, some fibres with $r_C \approx 10\,\mu\text{m}$ show the expected finesse.

The small stability range of small r_C cavities makes their alignment experimentally challenging. As there can be only few working axial mode orders before the two mirrors

touch, 'blind' alignment down to a distance of few µm is required.

3.3.3. High Q fibre cavities

For a planned experiment, the idea is creating an indistinguishable single photon source at room temperature using SiV centres (see sec. 4.6 for details). For this, fibres with large radius of curvature, $r_C = 200 - 400\,\mu\text{m}$, were produced. They feature a high reflectivity coating with $T = 10\,\text{ppm}$ at 740 nm and are therefore optimised for high quality factors. As no laser was available at 740 nm, the performance of an example fibre with $r_C = 350\,\mu\text{m}$ (fibre 29A, fibre D in appendix A) was tested at 786 nm. The profile is shown in Fig. 3.1.4. From a mirror coating calculation (see section 3.4.2), the transmittivity at this wavelength was found to be 45 ppm. As a planar mirror with the same coating was used, the expected finesse, omitting absorption and diffraction loss, is 69 800. From a measured finesse of 57 500 at short mirror separation, were diffraction loss should be negligible, a total absorption loss of 19 ppm can be deduced.

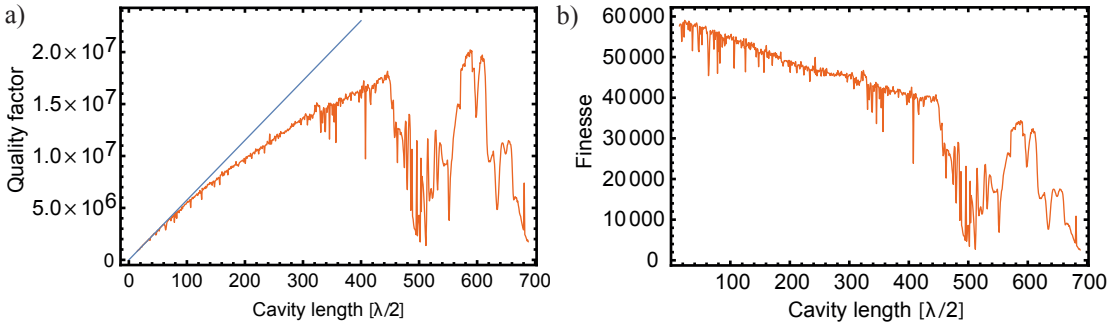

Figure 3.3.4.: (a) Quality factor as function of cavity length for $r_C = 350\,\mu\text{m}$ (fibre 29A). Blue line: linear fit to first 30 orders to deduce cavity length. (b) Finesse obtained from (a) together with cavity length.

The quality factor was measured by imprinting sidebands at 2 GHz to the laser with an EOM as a frequency ruler for the linewidth. The measurement as function of the mirror separation is shown in Fig. 3.3.4(a). The mirror separation was calibrated by linear fitting to Q for the first 30 orders and shifting the length scale such that the line intersects at the origin. It can be seen that the quality factor follows the linear relation $Q = q\mathcal{F}$ only for small axial orders. For larger lengths, diffraction loss sets in and deteriorates the quality factor. From $q = 450$ to $q = 570$, there are clear signs of mode coupling coming with bad cavity performance. Nevertheless, Q is restored after this region, reaching its highest value of 2.0×10^7 for $q = 589$, before diffraction loss takes over leading to a final drop. Deducing the finesse from these values leads to the data shown in Fig. 3.3.4(b). It should be noted that the transmission at the point of maximal Q is only about 10% of the transmission at short length, which can be partly attributed to a mode matching of maximally 54% at this length.

Taking the values for diffraction and absorption loss from this measurement, the expected maximal quality factor at the design wavelength of 740 nm can be predicted to

be $Q = 3.2 \times 10^7$, which is the largest value so far for fibres produced with our setup. The ideal Purcell factor for this length would be $C = 144$, the cavity ring-down time $\tau = 13\,\mathrm{ns}$, and the cavity decay parameter $\kappa = 80\,\mathrm{MHz}$.

3.3.4. Operation close to the stability limit

For typical fibre-based cavities, the stability range is limited by diffraction loss to lengths much shorter than the radius of curvature. However, if the fibre profile were almost a complete hemisphere, light should not be diffracted out and the stability range should extend much further. The mode waist should become very small when approaching $r_C = d$, which is interesting for SCM. This idea was tested in collaboration with Harald Gießen, whose group specialises on micromachined optics systems by femtosecond two-photon direct laser writing [167]. They wrote an almost hemispherical structure with a radius of curvature of 78 µm, as obtained from a spherical fit to the centre of the WLI measured profile. It is coated with a thin layer of gold. A cavity was formed using a dielectric planar mirror with a central wavelength of 740 nm. It has a transmittivity of 0.3% at the probe wavelength 780 nm. Figure 3.3.5(a) shows transmission spectra at different cavity lengths, where a white-light super-continuum laser was coupled into the cavity and the transmission recorded with a spectrometer. From the spectral distance of the resonances, the exact longitudinal orders can be obtained. At about 27 µm effective cavity length, the mirrors start touching. Several more orders appear when pressing the mirrors further together leading to high passive stiffness of the device. At a length of about 77 µm, no more resonances are visible within the mirror stop band. This agrees very well with the measured radius of curvature, meaning that the the stability range indeed almost extends to $d = r_C$.

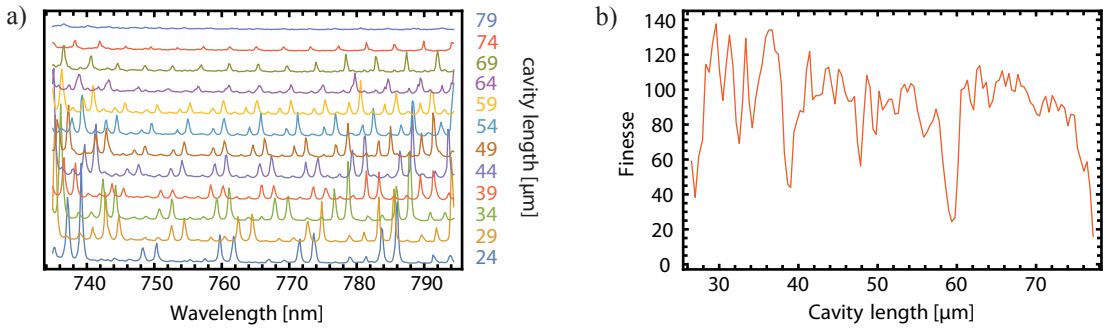

Figure 3.3.5.: (a) Cavity transmission spectra at different cavity lengths. Excitation with white-light super-continuum laser. (b) Finesse as a function of cavity length.

The finesse was measured with the 780 nm laser for all accessible axial mode orders by scanning the cavity length over an FSR, fitting two Lorentzians, and taking the ratio of FSR to linewidth. The result is shown in Fig. 3.3.5(b). The measurement contains a certain error due to the piezo nonlinearity, which is estimated to be about 11%. The dips can be attributed to transverse-mode coupling. Again, one observes the final breakdown

at a length of 77 µm. The finesse reaches a value of about 135. As the transmission of the planar mirror is known, and the absorption losses of the silver layer can be estimated to be $A = 4\%$, the maximal transmission of the fibre mirror can be computed to be $T_2 = {}^{2\pi}/_{\mathcal{F}} - A - T_1 = 0.4\%$, a reasonable value for a metallic mirror.

At a length of 74 µm, were still a decent finesse can be measured, the mode waist is calculated to be 2.1 µm. Achieving small waists below 1 µm would require $d > 99.7\%\, r_C$, which seems rather unrealistic. Taken this waist, the ideal Purcell factor can be computed to be 2.5, which is a reasonable value for a metallic mirror.

So the usage of hemispherical mirrors for high resolution imaging appears to be in reach, especially if smaller r_C structures are used. A better surface smoothness of the fibre profile would further reduce losses due to diffraction and mode coupling and would allow the application of a high reflectivity dielectric coating.

3.4. Dielectric layer systems

High reflectivity coatings are dielectric layer stacks with alternating refractive index. A quantitative understanding of their transmission and reflection properties as well as the electric field distribution in the layer system allows to optimise the design for a specific application. This section introduces the transfer matrix method as a simulation tool and gives useful examples for its application.

3.4.1. Transfer matrix method

In the transfer matrix method, the effect of a dielectric layer upon the electromagnetic field is described as a complex matrix containing the thickness and refractive index of the material. A derivation of the formalism from the Fresnel formulas can be found in the book by Furman and Tikhonravov [168].

The change the electric field E and the magnetic field H undergo by passing through a dielectric layer with a complex refractive index n_j is given by

$$\begin{pmatrix} E_{\text{out}} \\ H_{\text{out}} \end{pmatrix} = M_j \begin{pmatrix} E_{\text{in}} \\ H_{\text{in}} \end{pmatrix} \tag{3.4.1}$$

$$= \begin{pmatrix} \cos\phi_j & i/q_j \sin\phi_j \\ iq_j \sin\phi_j & \cos\phi_j \end{pmatrix} \begin{pmatrix} E_{\text{in}} \\ H_{\text{in}} \end{pmatrix} \tag{3.4.2}$$

with

$$\phi_j = \frac{2\pi}{\lambda} q_j d_j, \tag{3.4.3}$$

d_j being the geometric layer thickness, $q_j = n_j \cos\gamma_j$, and γ_j the wave propagation angle. To obtain the effect of the whole dielectric layer stack one simply multiplies the matrices M_j:

$$\begin{pmatrix} E_{\text{out}} \\ H_{\text{out}} \end{pmatrix} = M \begin{pmatrix} E_{\text{in}} \\ H_{\text{in}} \end{pmatrix} \tag{3.4.4}$$

with

$$M = M_N \cdot M_{N-1} \cdots M_j \cdots M_1 = \begin{pmatrix} m_{11} & m_{12} \\ m_{21} & m_{22} \end{pmatrix}, \tag{3.4.5}$$

where M_j is the j-th layer in the stack and N the number of layers. Note that M_1 must be the matrix of the layer the light hits first. The field transmission can then be calculated from the matrix elements as

$$t(\lambda) = \frac{2q_0}{q_0\, m_{11} + q_S\, m_{22} + q_0 q_S\, m_{12} + m_{21}} \tag{3.4.6}$$

and the intensity transmission is given by

$$T(\lambda) = \frac{q_S}{q_0} |t(\lambda)|^2, \tag{3.4.7}$$

where $q_{S/0} = n_{S/0} \cos\gamma_{S/0}$ with $n_{S/0}$ being the refractive index of the material after the stack (the 'substrate') and before the stack, respectively. Analogously, the complex field reflectivity reads

$$r(\lambda) = \frac{q_0\, m_{11} - q_S\, m_{22} + q_0 q_S\, m_{12} - m_{21}}{q_0\, m_{11} + q_S\, m_{22} + q_0 q_S\, m_{12} + m_{21}} \tag{3.4.8}$$

and the intensity reflectivity is

$$R = |r|^2. \tag{3.4.9}$$

Without absorption, i.e. all parameters being real, $R = 1 - T$ follows from these relations.

As soon as the light incidence is not perpendicular to the layer stack, polarisation matters. The relations presented so far are valid for s polarisation, that is the polarisation is perpendicular to the plane of incidence and parallel to the surface. In the p case, where the polarisation is parallel to the plane of incidence, the expressions for transmission and reflection stay essentially the same with the difference that $q_j = n_j/\cos\gamma_j$ and $q_{S/0} = n_{S/0}/\cos\gamma_{S/0}$.

Moreover, the formalism can be used to compute the field amplitude in the layered material. The field $E(z)$ at a given position z normalised to the incidence field amplitude E_0 is given by

$$\frac{E(z)}{E_0} = (m_{11}(z) + q_S\, m_{12}(z))\, t \tag{3.4.10}$$

with $m_{11}(z)$ and $m_{12}(z)$ being matrix elements of

$$M(z) = M_j(\delta z) \cdot M_{j-1} \cdots M_1 \tag{3.4.11}$$

and t the total field transmission of the stack. Here, the position z lies in the j-th layer and $\delta z = z - d_{j-1} - ... - d_1$ is the fraction of this layer after which the field is to be computed meaning that for the calculation of $M_j(\delta z)$, $d_j = \delta z$. Repeating this computation for different positions z across the stack using a sufficiently high sampling (several points per layer), results in the field distribution in the medium.

If absorption in the media is supposed to be considered, it suffices to include the imaginary part of the refractive index in the calculation. The resulting absorption can then be obtained as $A = 1 - T - R$.

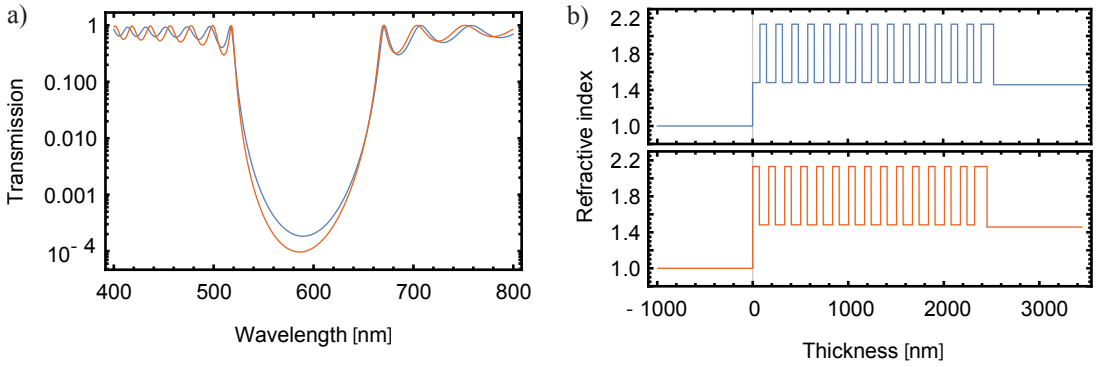

Figure 3.4.1.: (a) Transmission of $\lambda/4$-stack as function of the wavelength with central wavelength 585 nm (for Eu experiment) consisting of 15 layer pairs of Ta_2O_5 and SiO_2 with (blue) and without (orange) 77 nm spacer layer to shift the field maximum 40 nm above the surface. (b) Refractive index sequence for both cases as function of geometric thickness.

3.4.2. Distributed Bragg reflector

Distributed Bragg reflectors consist of alternating layers of high (n_H) and low (n_L) refractive index materials with an optical thickness of $\lambda_0/4$, which leads to constructive interference in reflection. The reflectivity can be obtained from the matrix formalism (eq. 3.4.8). For the centre wavelength, it can also be approximated by [169]

$$R = \left(\frac{n_0 n_L^N - n_S n_H^N}{n_0 n_L^N + n_S n_H^N} \right)^2 \tag{3.4.12}$$

where N is the number of layers. The resulting mirror is reflective for a range of wavelengths around the centre wavelength, which is referred to as the stop band. Its width is given by

$$\frac{\Delta\lambda}{\lambda_0} = \frac{4}{\pi} \arcsin \left| \frac{n_H - n_L}{n_H + n_L} \right|, \tag{3.4.13}$$

where the stop band is defined as the wavelength region around the central wavelength, where $|(m_{11} + m_{22})/2| \geq 1$ holds, meaning that the reflectivity increases when adding further layer pairs [170, 171]. As an example for the transmission curve of a dielectric mirror, the coating of the Eu experiment was chosen. Figure 3.4.1(a) shows the transmission as a function of wavelength as obtained from the transfer matrix formalism of 14 layer pairs of Ta_2O_5 ($n_H = 2.13$ at 585 nm) and SiO_2 ($n_L = 1.48$) and a final layer of Ta_2O_5 (29 layers altogether) leading to a central transmission of 100 ppm (orange line). The lower panel in (b) shows the corresponding refractive index sequence, which follows a geometric thickness table provided by the coating manufacturer Laseroptik. The refractive indices for different wavelengths are obtained with the empiric Sellmeier equation, where the coefficients again come from the manufacturer. Adding further layer pairs to the stack does not change the width of the stop band but reduces the transmission within and the frequency of the wiggles outside. A detailed treatment of dielectric mirrors can be found in the book by Macleod [171], chapter 6.

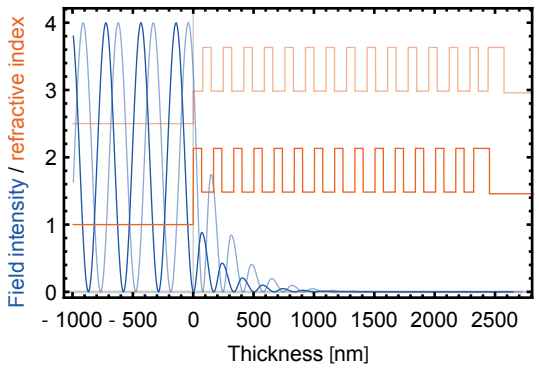

Figure 3.4.2.: Field intensity distribution in the mirror stack (blue) without (solid) and with (opaque) 77 nm spacer layer. Orange: refractive index sequence. Sequence for the case with spacer is shifted upwards by 1.5 for clarity. The light impinges from the left (air) and the stack starts at zero thickness. It ends on a glass substrate.

A typical dielectric mirror uses the high refractive index material as final layer, which leads to a field node at the surface of the stack and a reflection phase of π. This design has the advantage of a minimised penetration depth (see next section) and a minimised sensitivity to surface roughness. It is typically chosen for the fibre mirrors. However, when a sample is placed onto the planar mirror, one aims for highest light matter interaction. It is therefore desirable to have a field maximum at the position of the sample. To shift the field distribution accordingly, a low refractive index spacer layer can be applied to the coating. This is exemplarily shown in Fig. 3.4.2: The solid blue line gives the field intensity distribution without a spacer layer normalised to the input intensity, corresponding to the orange transmission curve in Fig. 3.4.1(a). Note that the light is impinging from the left and that the maximal intensity before the stack is 4 as a standing wave with field amplitude 2 is present there. Penetrating the stack, the field intensity decays exponentially. Here, the spacer layer was chosen such, that the field intensity is greatest 40 nm above the surface to reside in the centre of 80 nm large nanoparticles. The field intensity distribution is shown in opaque blue in Fig. 3.4.2 and the transmission in blue in Fig. 3.4.1(a). One can observe that the field now penetrates deeper into the mirror stack and that the transmission is increased to 180 ppm. Note that the application of a spacer layer thereby automatically leads to a higher outcoupling in the direction of the planar mirror if the coatings are otherwise the same. Furthermore, the spacer layer implies a change in reflection phase shift, which gets zero for a $\lambda/4$ 'spacer layer'. In this case, the field maximum would be at the surface.

3.4.3. Penetration depth

Already from Fig. 3.4.2 one can get an impression of the penetration crucially depending on the exact arrangement of the dielectric stack. As the penetration depth enters the mode volume of a short cavity as an important parameter, it needs to be determined quite precisely, starting with the consideration what penetration depth actually means.

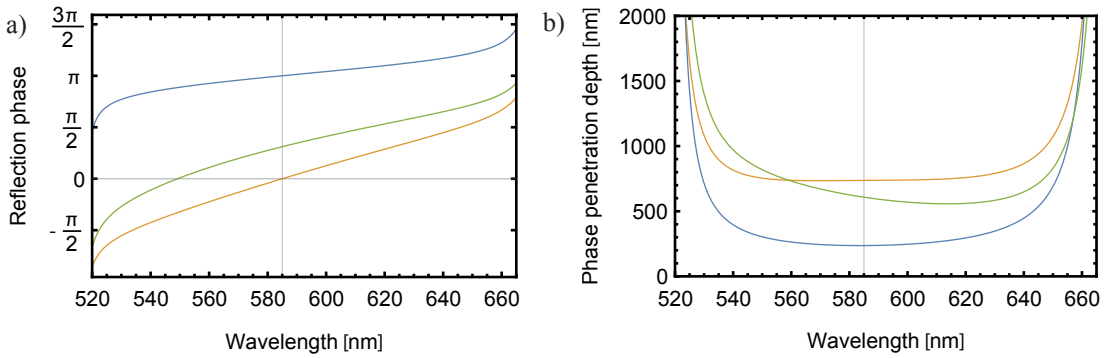

Figure 3.4.3.: Reflection phase (a) and phase penetration depth (b) for the stop band as function of the wavelength for $\lambda/4$ stacks with a final high refractive layer (blue), low refractive layer (orange), and a 77nm spacer layer (green).

There exist two definitions: the phase penetration depth and the energy penetration depth. The discussion in this section follows [138, 161, 170].

The phase penetration depth d_{ph} is defined as the distance behind the mirror surface a perfect reflector would have to be placed to obtain the same phase response for the central part of the stop band. In this central area, the reflection phase depends approximately linear on the wavelength, such that the optical phase penetration depth is proportional to the slope of this phase with respect to the wavelength, which can be seen as the reflection delay:

$$d_{ph} = \frac{\lambda^2}{4\pi} \frac{\mathrm{d}}{\mathrm{d}\lambda} \arg r \tag{3.4.14}$$

This leads to the penetration depth being approximately constant in the centre of the stop band, but it quite drastically changes to the sides. For the centre of the stop band of a $\lambda/4$ stack, simple expressions for the optical penetration depth can be derived [161]. In the case of a final high refractive layer, one obtains

$$d_{ph} = \frac{\lambda_0}{4\Delta n} \tag{3.4.15}$$

with $\Delta n = n_H - n_L$. For the above example, this would amount to 225 nm optical depth, while the rigorous calculation using the matrix formalism to obtain r results in 236 nm. When the stack ends with a low refractive layer, the depth increases to

$$d_{ph} = \frac{\lambda_0}{4\Delta n} \bar{n}^2 + \frac{\lambda_0 \Delta n}{2\pi^2} \tag{3.4.16}$$

where the latter term does not contribute much and

$$\bar{n} = 2 \left(n_H^{-1} + n_L^{-1} \right)^{-1} \tag{3.4.17}$$

is an averaged refractive index. For the example mirror with a final low refractive $\lambda/4$ mirror, this results in 708 nm or 737 nm using the matrix formalism. Figure 3.4.3 shows

the reflection phase (a) and the resulting penetration depth (b) for the stop band as a function of the wavelength as obtained from the matrix formalism for $\lambda/4$ stacks with a final high or low refractive layer or the 77 nm spacer layer discussed above.

The energy penetration depth d_e is defined as the fraction of the energy in the stack, W_{pen}, normalised to the energy length density outside the mirror, that is the fraction of the energy in one period of the standing wave, W_0, divided by $\lambda/2$:

$$d_e = \frac{W_{\text{pen}}}{\frac{W_0}{\lambda/2}} = \frac{\int_0^\infty |E_{\text{pen}}|^2 \, n^2 \mathrm{d}z}{\int_{-\lambda/2}^0 |E_0|^2 \, \mathrm{d}z} \frac{\lambda}{2} \tag{3.4.18}$$

For the latter equality the relation $w = \frac{1}{2}\epsilon_0 \epsilon_r \, |E|^2 \propto n^2 \, |E|^2$ for the energy density was used. So practically, one has to integrate up the field distribution inside the mirror and of one node outside and take the ratio. Intuitively, one can understand the energy penetration depth such, that when rearranging the total energy in the stack such that the energy length density stays the same as outside the mirror and constant, then the energy would be 'used up' after d_e. For high reflectivity mirrors with many layers, the difference between d_{ph} and d_e is negligible [138, 170].

3.4.4. Simulation of a cavity

When simulating the complete cavity one has to take care to get the order of transfer matrices correctly. When coupling the light in through the fibre, the total matrix reads

$$M = (M_H \cdot M_L \cdots M_L \cdot M_H \cdot M_{\text{spacer}}) \cdot M_d \cdot (M_H \cdot M_L \cdots M_L \cdot M_H) \tag{3.4.19}$$

with M_H and M_L being the transfer matrices of $\lambda/4$ layers of high and low refractive index, respectively, M_{spacer} the matrix of the spacer layer, and M_d the matrix for the air gap between the mirrors with $n_d = 1$ and the thickness being variable. The rightmost matrix is the one of the layer seeing the light first. This implies that the order of matrices of the incoupling mirror needs to be reversed compared to the treatment of a single mirror, which becomes important for more complex stack designs. It should also be noted, that both n_0 and n_S are the refractive index of the substrate, now. Details about simulating a cavity with transfer matrices can be found in [172]. Figure 3.4.4(a) shows the resulting cavity transmission as a function of wavelength and air gap using the mirrors introduced above of the Eu experiment. One can observe how the resonances shift to longer wavelengths when increasing the cavity length and the non-linear behaviour towards the edge of the stop band. Note that the resonances are too sharp to be resolved in this plot and can only be seen due to the logarithmic scale. The corresponding field distribution is shown in Fig. 3.4.4(b): The light impinges from the left and is greatly enhanced between the mirrors and the field intensity decays into the mirror stacks exponentially. Such simulations are very useful when designing custom layer stacks or modeling media inside the cavity [173].

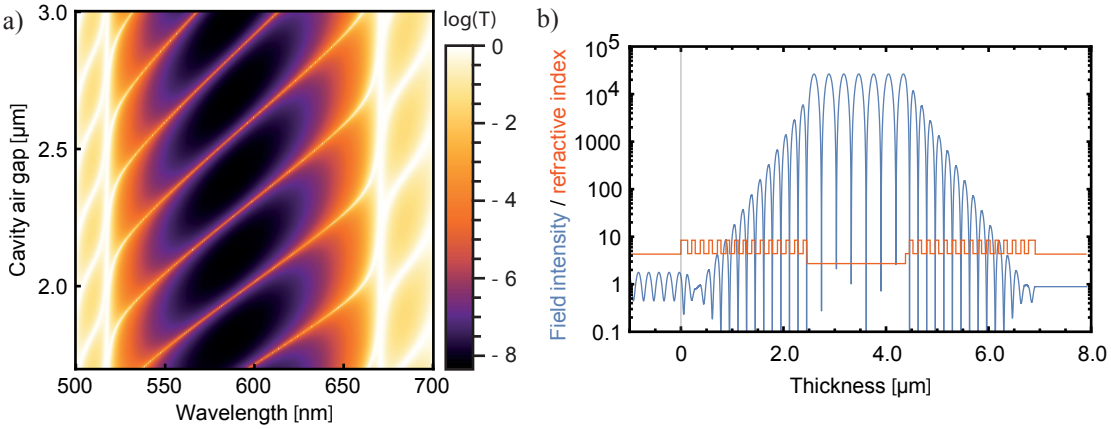

Figure 3.4.4.: (a) Cavity transmission as a function of wavelength and mirror separation. Logarithmic scale. Resonances are not resolved. (b) Field distribution in a cavity of length 1926.673 nm together with refractive index sequence. Field nodes are not resolved. Logarithmic scale.

3.4.5. Radiating dipole on a mirror

So far plane waves were impinging on the mirrors. For simulating cavity experiments with quantum emitters, it is, however, also necessary to regard the redirection of dipole radiation by a mirror. Notably, the following discussion not only holds for radiative dipole transitions, but also for induced dipoles as discussed in section 3.5. In the latter case the dipole is perpendicular to the propagation direction of the exciting light, whereas in the case of dipole radiation from a quantum emitter the dipole orientation is arbitrary. The treatment follows [53, 174] and contains excerpts from [53].

The normalised power radiated by a dipole is given by

$$P_s(\alpha, \theta, \phi) = \frac{3}{8\pi} \sin^2\theta \sin^2\phi \tag{3.4.20}$$

for s polarisation and

$$P_p(\alpha, \theta, \phi) = \frac{3}{8\pi} (\cos\theta \sin\alpha + \sin\theta \cos\alpha \cos\phi)^2 \tag{3.4.21}$$

for p polarisation, where α is the azimuthal angle between the optical axis and the emission direction, ϕ the polar angle, and θ the angle between the dipole and the optical axis. The total power emitted by the dipole on the mirror into a certain direction normalised to free-space power is the interference of the directly emitted and reflected light in both polarisations:

$$P_{\text{em}}(\alpha, \theta, \phi) = \sum_{i \in \{s,p\}} |1 + |r_i(\alpha)| \exp(2ik \cos\alpha z_0 + i \arg r_i(\alpha))|^2 P_i(\alpha, \theta, \phi) \tag{3.4.22}$$

The term $2k \cos\alpha z_0$, with k being the wave number, is an additional phase acquired if the dipole is at a distance z_0 from the surface of the mirror. r is deduced from the

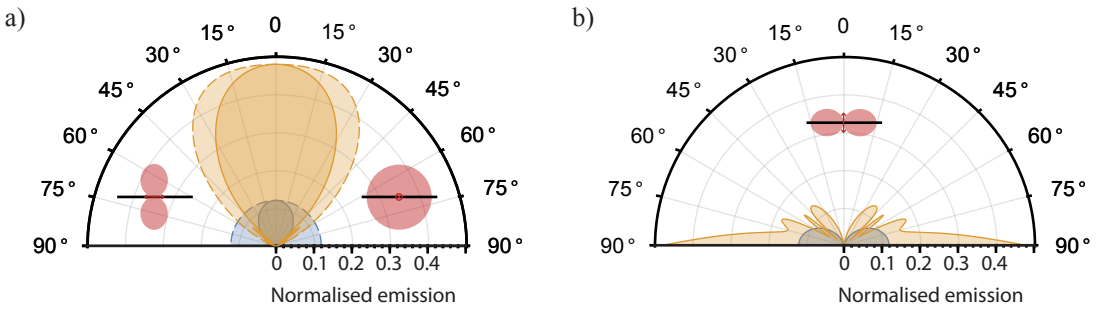

Figure 3.4.5.: Radiation pattern of a dipole in free space (blue) and a dipole on a dielectric mirror (orange) for the upper hemisphere. (a) Dipole parallel to the surface. Cuts along the dipole (solid line) and perpendicular to the dipole (dashed line) are shown. The insets schematically depict the radiation pattern for both cuts for a free space dipole. The black line indicates the mirror surface. (b) Dipole perpendicular to surface. The pattern is rotationally symmetric to the axis of the dipole. An arbitrary cut is shown in the inset.

transfer matrix formalism. The radiation pattern critically depends on the final layer of the mirror, the distance z_0, and the dipole orientation.

Figure 3.4.5 shows the computed radiation pattern $P_{\mathrm{em}}(\alpha, \theta, \phi)$ (orange lines) for the upper hemisphere for a mirror with 15 layer pairs and a centre wavelength of 780 nm. The mirror has a final low refractive layer and the dipole resides directly on the surface ($z_0 = 0$), i.e. in the field maximum. Note that the calculation of r is now more complex than before as we are now dealing with arbitrary incidence angles and need to distinguish between the polarisations. The resulting patterns are displayed for the case of the dipole being parallel (a) and perpendicular (b) to the mirror surface and compared to the radiation pattern of a free space dipole (blue). The radiation power is normalised to the total radiation power of a free space dipole. In case (a), two perpendicular cuts through the emission pattern are displayed: parallel (solid lines) and perpendicular (dashed lines) to the dipole. A schematic drawing of the radiation pattern of a free space dipole is shown for both cuts. Clearly, in this case the radiation gets redirected into a club-shaped geometry perpendicular to the mirror. As a dipole does not radiate along its axis, the emission perpendicular to the mirror is zero in case (b). The radiation for large angles with the mirror also increases here compared to the free space case. However, the radiation is largest to the sides. This illustrates that the dipole orientation is crucial for the question how much light can be collected.

3.5. Absorption and Scattering

In experiments with solid state quantum emitters coupled to fibre-based microcavities, nanoparticles are commonly used. But not only the fluorescence is enhanced by the Purcell effect, but likewise absorption and scattering at the nanoparticle leading to additional loss. This section introduces these loss channels and gives a brief discussion on scattering particles in small cavities.

3.5.1. In free space

First, I will very briefly allude to light extinction at nanoparticles in free space. A detailed treatment can be found in [175, 176]; the discussion here follows [93]. When shining a beam of light onto a classical particle, a fraction of the light can be absorbed, an inelastic process converting photons to e.g. thermal energy, or scattered, where the photons are elastically redirected and therefore lost from the original beam. The overall process is called extinction and characterised by the extinction cross section

$$\sigma_{\text{ext}} = \sigma_{\text{abs}} + \sigma_{\text{sc}} \tag{3.5.1}$$

consisting of the absorption cross section σ_{abs} and the scattering cross section σ_{sc}. The cross section is an area assigned to the loss, which is the effective area the scatterer eliminates from the beam. Note that the extinction cross section can substantially differ from the geometric cross section of the particle.

For particles which are significantly smaller than the wavelength of the light, the driving field inside the particles can be approximated as constant and the particle can be treated as an induced dipole. This is the assumption I shall make in the following. For larger particles, the field variation inside needs to be taken into account, which complicates the description tremendously. For spherical particles, Mie scattering is a useful description and details can be found in [175–177]. The limit of small particles is referred to as Rayleigh scattering. It implies that placing the particle into an electric field $\mathbf{E}$ induces a dipole moment

$$\mathbf{p} = \alpha \mathbf{E} \tag{3.5.2}$$

with α being the polarisability. For homogeneous particles it is a scalar property and is for spheres given by the Clausius-Mossotti relation:

$$\alpha = 3\epsilon_0 V \frac{\epsilon_p - \epsilon_m}{\epsilon_p + 2\epsilon_m} \tag{3.5.3}$$

V is the particle's volume and ϵ_p and ϵ_m the relative permittivity of the particle material and the surrounding medium, respectively. Note that when absorption is present, the permittivity and therefore α is a complex quantity. The induced dipole radiates off in a dipole mode, where the field amplitude in spherical coordinates is given by

$$E_{\text{dip}}(\theta, r) = \sqrt{\frac{3}{8\pi}} \frac{1}{r} \cos\theta \tag{3.5.4}$$

with $-\pi/2 \leq \theta \leq \pi/2$ [155]. The scattering cross section can be derived to be

$$\sigma_{\text{sc}} = \frac{k^4}{6\pi\epsilon_0^2} |\alpha|^2 \tag{3.5.5}$$

with $k = 2\pi/\lambda$ the wavenumber, while the absorption cross section becomes

$$\sigma_{\text{abs}} = \frac{k}{\epsilon_0} \Im(\alpha) \tag{3.5.6}$$

where the imaginary part of the polarisability can be seen as damping of the dipole oscillator.

In fibre-cavity experiments, the nanoparticles reside on the planar mirror, which influences their polarisability. In the simpler case of an induced dipole on a dielectric surface, it reads

$$\alpha = \epsilon_0 V \frac{\epsilon_p - \epsilon_m}{\epsilon_m + L\,(\epsilon_p - \epsilon_m)} \tag{3.5.7}$$

with the factor

$$L = \frac{1}{3}\left(1 - \frac{1}{8}\frac{\epsilon_s - \epsilon_m}{\epsilon_s + \epsilon_m}\right) \tag{3.5.8}$$

for a dipole parallel to the surface where ϵ_s is the relative permittivity of the surface material [178, 179]. Note that expression 3.5.3 is restored for $\epsilon_s = \epsilon_m$. It does not yet include the effect of interference with light reflected from the surface.

3.5.2. In the cavity: size statistics

When a scatterer is placed into a cavity, it scatters light out of the cavity mode, which is typically regarded as an additional loss channel. The loss per round trip can be quantified using the extinction cross section as

$$B = \frac{4\sigma_{\text{ext}}}{\pi w_0^2}, \tag{3.5.9}$$

when the particle is placed in an antinode of the standing wave field in the cavity. Notably, the scattering loss introduced by a spherical nanoparticle scales with its radius to the sixth power as $\sigma_{\text{sc}} \propto |\alpha|^2 \propto V^2 \propto r^6$. Experimentally, the extinction cross section is determined by measuring the cavity transmission with, T, and without, T_0, the presence of the scatterer. From eq. 2.1.7, one then obtains

$$B = (T_1 + T_2 + A_1 + A_2)\left(\sqrt{\frac{T_0}{T}} - 1\right). \tag{3.5.10}$$

In the following, the discussion shall concentrate on spherical particles with negligible absorption. In this case, the particles' size can be directly inferred from such a loss measurement. To test this, polystyrene nanospheres (Polysciences) are spin-coated onto a dielectric planar mirror with central wavelength 780 nm. According to the manufacturer, they have a mean diameter of 100 ± 1.3 nm with a standard deviation of 12.1 nm. From this, one can infer an expected mean scattering cross section of $65\,\text{nm}^2$ with a spread from 30 to $125\,\text{nm}^2$. To compare this to a measurement, a total area of $300 \times 400\,\mu\text{m}$ was scanned recording the resonant transition values. A sample sub-scan is shown in Fig. 3.5.1(a). The finesse of the bare cavity was 58 000 and $w_0 = 2.2\,\mu\text{m}$. Using equations 3.5.9 and 3.5.10, transmission is converted to scattering cross section. Out of 612 detected dark spots, irregular shapes, too dark areas, and spots much larger or smaller than the mode waist are excluded to avoid the inclusion of particle clumps or measurement artefacts. A smooth density histogram of the remaining 447 particles is shown

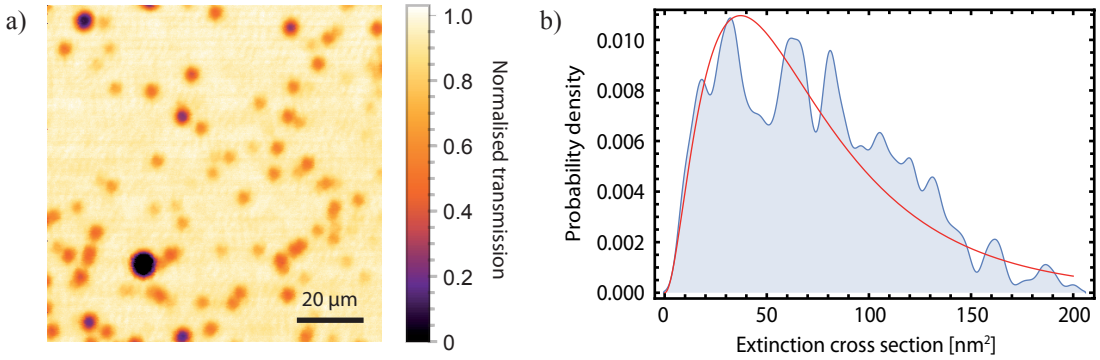

Figure 3.5.1.: (a) SCM scan of polystyrene spheres on an area of $100 \times 100\,\mu m$. Measurement performed by Eric Bersin. (b) Blue: Smooth density histogram of extinction cross sections of 447 scanned particles with a Gaussian kernel of $3\,nm^3$corresponding to the standard deviation of the measurement. Red: Fit yielding a particle diameter of $102 \pm 13\,nm$.

in Fig. 3.5.1(b), where a Gaussian kernel of $3\,nm^3$ was applied corresponding to the standard deviation of the measurement. A fitted distribution function (red line) on the basis of a Gaussian size distribution yields a particle diameter of 102 nm with a standard deviation of 13 nm, in good agreement with the manufacturer value. This is an indicator that the simple scattering formalism sufficiently well explains the observed losses and that absorption is indeed negligible. The presented measurements were conducted by the visiting student Eric Bersin under my supervision.

3.5.3. Scattering into the cavity mode

However, when the cavity length is short and the mode covers a substantial solid angle, scattered light is not necessarily completely lost, but can be scattered back into the cavity mode. This effect can be investigated by measuring the scattering loss for different cavity lengths. The measurements presented in this section were conducted in the course of Lukas Husel's bachelor's thesis [180].

The cavity for this experiment has a design wavelength of 780 nm and a maximal finesse of about 48 000. The radius of curvature is 38 µm and the profile depth 0.7 µm (fibre 14H). The profile features a good rotational symmetry, which is why the point spread function can be well fitted with a rotationally symmetric Gaussian. The smallest accessible axial order is $q = 9$. In analogy to the experiment in the previous section, the scattering cross section of polystyrene nanoparticles is deduced from resonant cavity transmission scans. Figure 3.5.2 shows the obtained cross sections for two selected particles at various axial mode orders. Note that data points are not displayed for all orders as transverse mode coupling artefacts at some orders deteriorated the fitting. The considerable spread of the data points is not a measurement uncertainty as the standard deviation of subsequent measurements at the same mirror separation is only $0.8\,nm^2$, i.e. smaller than the spread. The individual data points reproducibly lie above

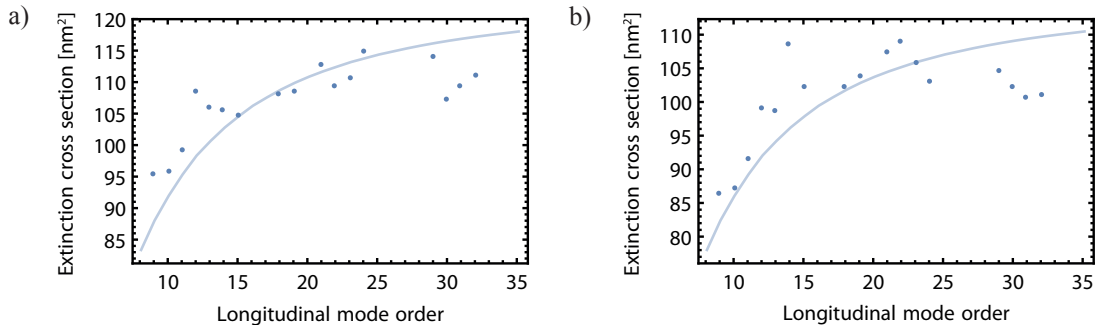

Figure 3.5.2.: Scattering cross section as a function of longitudinal mode order as obtained from resonant cavity transmission scans at various mirror separations for two different particles (a) and (b). At mode orders without data points, transverse mode coupling occurred. Measurement performed by Lukas Husel. Faint lines: Theoretical model based on integration of dipole mode (see text).

or below a guidance line. This systematic offset could be due to the variation in finesse for different lengths as the basic losses of the system were determined for each axial mode order individually from a finesse measurement. Nevertheless, a clear trend towards smaller scattering cross section for short cavities is present. This implies that part of the scattered light is recollected by the cavity mode, thereby reducing the loss. Interestingly, some few particles did not feature this behaviour but rather a constant extinction cross section, independent of the mirror separation. Presumably, these are not polystyrene spheres but nanosized dirt on the mirror surface, which is absorbing. The described effect discriminates between scatterers and absorbers, as the light is not redirected by the latter but finally lost.

The sample mirror had been marked by writing a cross with the CO_2-laser, which was visible in SCM scans. This allowed to identify particles in an atomic force microscope (AFM) and thereby determine their size. The two particles (a) and (b) were found to have radii of 58 and 67 nm, respectively, with an uncertainty of 0.5 nm. The expected scattering cross sections for these sizes would be 370 and 163 nm^2, i.e. much larger than the measured cross sections of 100 and 105 nm^2. This systematic deviation is present for all observed particles. Taken that the scattering cross section obtained from the size distribution using the simple Rayleigh scattering formalism fits the measured cross sections well for a larger cavity as shown in the previous section, this may pose another hint towards a recollection effect. As this systematic offset is rather large, there could however also be some additional so far overseen effect.

For a quantitative treatment of this effect, one can follow the approach introduced by Motsch et al. [155], who compute the overlap integral of a scattered dipole mode with a Gaussian cavity mode. Doing this for the parameters of the experiment, one finds that theory underestimates the experimental effect, i.e. the theoretical curve bends down more slowly for shorter cavity lengths. The reason could be the modified dipole radiation characteristics by the mirror as described in section 3.4.5, leading to a larger overlap between dipole mode and cavity mode. To investigate this, the radiation pattern

shown in Fig. 3.4.5(a) was integrated over the solid angle spanned by the mode radius on the curved mirror. This gives a measure of the loss reduction by recollection. The length dependent effective scattering cross section excluding the light scattered back into the mode is then given by

$$\sigma_{\mathrm{sc}}(d) = \sigma_{\mathrm{sc},0}\left(1 - \int_0^{2\pi}\int_{-\arctan(w_c/d)}^{\arctan(w_c/d)} P_{\mathrm{em}}\left(\alpha, \frac{\pi}{2}, \phi\right) \mathrm{d}\alpha\, \mathrm{d}\phi\right) \tag{3.5.11}$$

as the loss enters σ_{sc} linearly, with $\sigma_{\mathrm{sc},0}$ being the scattering cross section for large mirror separations. $\theta = \pi/2$ as the dipole induced by the cavity mode is perpendicular to the optical axis. The faint lines in Fig. 3.5.2 show the result of this calculation with $\sigma_{\mathrm{sc},0} = 125$ and $117\,\mathrm{nm}^2$, respectively, as a free fit parameter. It can be seen that this simple model already describes the effect quite well, however the discrepancy with the AFM measurement remains. For a more rigorous treatment, the overlap integral between the reflected dipole mode with the cavity mode including interference would have to be computed and the vectorial character of the field taken into account, which is challenging due to the lack of rotational symmetry.

In conclusion, for small cavities, scattering loss can be smaller than naively anticipated as part of the scattered light is recollected by the cavity mode. As cavities with a lot smaller r_C, operated at shorter lengths than the one used for the measurements in this section are quite commonly used for experiments including nanoparticles, the described effect is far from negligible. For example, for $r_C = 10\,\mu\mathrm{m}$ and $q = 5$ at $\lambda = 780\,\mathrm{nm}$, the scattering loss would be reduced by 35% according to the simplified model as given in eq. 3.5.11.

4. An effective single photon source at room temperature

Single photon sources (SPS) are an integral part in various quantum technologies, but a deterministic, efficient SPS operational at room temperature is still a matter of ongoing research. Solid state quantum emitters appear to be a promising implementation. Especially, the silicon vacancy centre in diamond is well-suited due to its dominant narrow zero phonon line at room temperature. In the course of this work, the fluorescence of individual SiV centres in nanodiamonds was coupled to a fibre-based microcavity to demonstrate an SPS with high efficiency, increased emission rate, and improved spectral purity compared to the intrinsic emitter properties. This chapter first gives an introduction to single photon sources and their figures of merit and compares different approaches. Next, the silicon vacancy centre in diamond is introduced, alluding to its properties in general and in nanodiamonds. Subsequently, the experimental realisation of the cavity setup is discussed as well as the theoretically expected specifications of the single photon emission. After a detailed sample characterisation, the resulting values for emission rates and lifetimes in the cavity are presented and compared to the free space behaviour. A discussion of modifications of the internal rate dynamics follows, including the proposition of an alternative rate model for the SiV centre. The chapter concludes with an outlook on an indistinguishable single photon source at room temperature using the SiV centre and high Q fibre-based microcavities. Parts of the content of this chapter are published in [53] and are used with permission of the publisher[1].

4.1. Single photon sources

Single-photon sources are a fundamental component of the toolbox for quantum information technologies that promise transformational advances in the communication and processing of information [36, 181]. There is thus large interest in developing scalable sources fulfilling certain requirements: The source should be of high purity meaning that it emits exactly one photon at a time. The photons should be emitted into a collectible mode and thereby extracted from the source with high efficiency. Furthermore, especially for quantum communication applications a high brightness is important, which is quantified by the excitation rate, requiring short lifetimes. For quantum information, typically high spectral purity is needed, that is a narrow, ideally Fourier-limited spectrum. On-demand operation, where a single photon is deterministically released

[1] American Physical Society reuse and permissions license; license number: RNP/19/JUN/015741

upon excitation with a single pulse, is beneficial for a range of applications compared to probabilistic single photon emission.

Historically, the first successful single photon generation was conducted by Clauser in 1974 using a cascade transition of calcium atoms [182]. Photon anti-bunching, i.e. sub-Poissonian photon statistics was observed for the first time for sodium atoms in an attenuated beam, where it was statistically unlikely for two atoms to be simultaneously located in the excitation beam [183, 184]. In spite of these sources being very faint and non-deterministic as the atom arrival time could not be controlled, they had an important application in tests of Bell's inequality [185, 186] and the observation of classical interference effects with single photons [187]. With the advent of single trapped ions, single photons from one and the same emitter could be continuously collected [188]. An important probabilistic single photon source, which is in abundant use even today, are correlated photon pairs created by parametric down-conversion [189, 190]. It offers higher rates than the previously available sources and the detection of one photon of the pair can herald the arrival of the other. Starting from the 90s, photon anti-bunching was observed for the fluorescence of various quantum emitters like single organic molecules [191], single semiconductor hetero-structures like quantum wires [192] and quantum dots [193–195], single atoms and ions in a cavity [196, 197], and colour centres in diamond [198–200]. To increase the efficiency of single photon emission, microcavities were first applied to enhance the single photon emission of quantum dots [201, 202]. A good overview of the development of SPS can be found in [203] and in Hanno Kaupp's thesis [126].

This section starts by a discussion of the photon statistics of various light sources giving a more concrete notion of single photon emission. Next, the figures of merit of single photon sources are presented, alluding to the importance for different applications. Last, an overview and comparison of the currently available SPS shall be given.

4.1.1. Photon correlations

A classical light source can be distinguished from a quantum emitter by its photon statistics. A laser, being a coherent light source, features a Poissonian photon distribution, while photons from a classical thermal light source follow super-Poissonian statistics. Sub-Poissonian statistics can only be realised when the quantum nature of light becomes apparent. The treatment in this section follows [126, 144, 203, 204].

Classical theory The temporal second-order correlation function $g^{(2)}(\tau)$ correlates light intensities at times t and $t+\tau$:

$$g^{(2)}(\tau) = \frac{\langle E^\star(t)\, E^\star(t+\tau)\, E(t)\, E(t+\tau)\rangle}{\langle E^\star(t)\, E(t)\rangle \langle E^\star(t+\tau)\, E(t+\tau)\rangle} = \frac{\langle I(t)\, I(t+\tau)\rangle}{\langle I(t)\rangle^2} \tag{4.1.1}$$

with $E(t)$ and $E^\star(t)$ being the electric field amplitude and its complex conjugate, $I(t) = E^\star(t)\, E(t)$ the field intensity, and $\langle\rangle$ represents a temporal average. The function is evaluated at time delays τ. For the second equality, $\langle I(t)\rangle = \langle I(t+\tau)\rangle$ was applied as

the average over long times should not differ with a temporal offset. It can be proven with the Cauchy-Schwartz inequality that $\langle I(t)\rangle^2 \leq \left\langle I(t)^2 \right\rangle$ as well as $\langle I(t)\, I(t+\tau)\rangle \leq \left\langle I(t)^2 \right\rangle$ holds, which, inserted into eq. 4.1.1 yields

$$g^{(2)}(0) \geq 1 \tag{4.1.2}$$

and

$$g^{(2)}(\tau) \leq g^{(2)}(0)\,. \tag{4.1.3}$$

For $\tau \to \pm\infty$, $g^{(2)}(\tau) \to 1$ as on large time scales, the light is completely uncorrelated.

The above relations imply that for a classical light source, the intensity correlation function cannot be smaller than 1 and has its maximal value for vanishing time delay. For coherent light as emitted from a laser, $g^{(2)}(\tau) = 1$ for all delays τ meaning that the intensity is completely uncorrelated. Speaking in terms of photons, the arrival time of a photon upon detection of a previous photon is completely random, governed by Poissonian statistics, that is the probability for detecting a certain number of photons n within a certain time interval is given by

$$P(n) = \frac{\bar{n}^n}{n!}\mathrm{e}^{-\bar{n}} \tag{4.1.4}$$

where $\bar{n}$ is the average photon number for this interval. The standard deviation is given by $\sqrt{\bar{n}}$. This fluctuation is referred to as shot noise and constitutes the theoretical minimum of noise of a classical light source.

For a thermal light source consisting of a large ensemble of radiating atoms, leading to a Doppler-broadened (i.e. Gaussian) emission line, the $g^{(2)}$-function reads

$$g^{(2)}(\tau) = 1 + \exp\left[-\pi\left(\frac{\tau}{\tau_c}\right)^2\right] \tag{4.1.5}$$

with τ_c the coherence time. For a lifetime-broadened ensemble , which has a Lorentzian line shape, one obtains

$$g^{(2)}(\tau) = 1 + \exp\left[-2\frac{|\tau|}{\tau_0}\right] \tag{4.1.6}$$

where τ_0 is the excited state lifetime and $g^{(2)}(0) = 2$. The photon statistics of such sources is super-Poissonian, meaning that the standard deviation is greater than $\sqrt{\bar{n}}$ and the probability to detect another photon upon detection of a photon is larger for short time intervals. This behaviour is referred to as photon bunching.

Quantum systems A quantum mechanical treatment implies expressing the electric field in terms of the photon creation and annihilation operators, $a^\dagger$ and a, which increase or lower the photon number state $|n\rangle$ according to

$$a^\dagger |n\rangle = \sqrt{n+1}\,|n+1\rangle \tag{4.1.7}$$

and

$$a\left|n\right\rangle = \sqrt{n}\left|n-1\right\rangle. \tag{4.1.8}$$

The electric field operator is then given by

$$E\left(t\right) = E^{+}\left(t\right) + E^{-}\left(t\right) \propto a\left(t\right)\mathrm{e}^{-i\omega t} + a^{\dagger}\left(t\right)\mathrm{e}^{i\omega t} \tag{4.1.9}$$

being the sum of two Hermitian-conjugate terms with the angular frequency ω. The second order correlation function then reads

$$g^{(2)}(\tau) = \frac{\left\langle E^{-}\left(t\right)E^{-}\left(t+\tau\right)E^{+}\left(t+\tau\right)E^{+}\left(t\right)\right\rangle}{\left\langle E^{-}\left(t\right)E^{+}\left(t\right)\right\rangle^{2}} \tag{4.1.10}$$

$$= \frac{\left\langle a^{\dagger}\left(t\right)a^{\dagger}\left(t+\tau\right)a\left(t+\tau\right)a\left(t\right)\right\rangle}{\left\langle a^{\dagger}\left(t\right)a\left(t\right)\right\rangle^{2}} \tag{4.1.11}$$

with $\langle A\rangle = \langle\psi\left|A\right|\psi\rangle$ the expectation value of an operator A. At $\tau = 0$ one gets

$$g^{(2)}\left(0\right) = \frac{\left\langle n^{2}\right\rangle - \left\langle n\right\rangle}{\left\langle n\right\rangle^{2}} \tag{4.1.12}$$

having applied $\left[a, a^{\dagger}\right] = 1$ and defined the photon number operator $n = a^{\dagger}a$. For photon number states $\left|\psi\right\rangle = \left|n\right\rangle$ with $n \neq 0$ this becomes

$$g^{(2)}\left(0\right) = 1 - \frac{1}{n}, \tag{4.1.13}$$

which is less than one, in contradiction to classical theory, indicating true quantum behaviour. For a single photon mode, $g^{(2)}\left(0\right)$ reaches zero, which is the indicator of a clean single photon source. As two photons lead to $g^{(2)}\left(0\right) = 1/2$, values of $g^{(2)}\left(0\right) < 1/2$ prove single photon emission. The photon statistics of a few photon source is sub-Poissonian with a standard deviation smaller than $\sqrt{\bar{n}}$. The probability for detecting a photon shortly after another photon is reduced, which is referred to as photon anti-bunching. It should be noted that anti-bunching does not in general imply sub-Poissonian statistics and vice versa as has been pointed out by Zou and Mandel [205], but that the two effects appear together in most cases. Expressions for $g^{(2)}\left(\tau\right)$ for incoherent two- and three-level quantum systems are to be derived in section 4.2.2.

Hanbury-Brown-Twiss interferometer A simple experimental setup to measure photon correlations is the Hanbury-Brown-Twiss (HBT) interferometer, which was introduced in 1956 to measure light coherence, originally to determine the angular diameter of stars [206, 207]. With a perfect detector the task of measuring the second order correlation function would reduce to measuring the exact arrival times of photons and correlate them. The trick played by the HBT interferometer to circumvent dead times and afterpulsing in real detectors is the application of two detectors, measuring coincidences. For characterising a photon source, one lets the photons impinge on a 50:50 beam splitter

with a single photon detector at each output port. It can be shown that multiplication of the two output signals integrated over a long time gives the desired second order correlation function. A derivation can for example be found in [208]. Hanbury Brown and Twiss used this design with the beam splitter to examine the correlations of photons in coherent beams [209]. Nowadays, time-to-digital converters are typically applied to time stamp the electric pulses from the photo detectors and generate histograms. It should be noted that the commonly used start-stop measurements, where the time interval between two subsequent photons on the two detectors is captured, do not result in the $g^{(2)}$-function but in the pair correlation function $\mathcal{C}$. For example for an uncorrelated source such as a laser, $g^{(2)}(\tau)$ is constant, while $\mathcal{C}$ is an exponentially decaying function. The two quantities are related via a Laplace transform. Only for count rates much smaller than the inverse of the time span of interest, the two functions converge [210].

4.1.2. Figures of merit

In the ideal case, one would wish for on-demand single photon emission upon sending an excitation pulse, where exactly one photon should be both emitted and collected with certainty. Photons emitted subsequently should be indistinguishable and single photon emission should occur at a high rate. Real single photon sources to date deviate from this behaviour [203, 211]. This section will discuss parameters to characterise and classify them.

Deterministic versus probabilistic In this context, I shall call an SPS deterministic when the photons are emitted in number states. There can be one photon, $|1\rangle$, or no photon, $|0\rangle$, in the collection mode upon excitation and I call it an on-demand SPS if exactly one photon is emitted in (almost) all cases. Deterministic photon emission is typically obtained by radiative excited state relaxation from single emitter quantum systems after excitation by an external control field. Probabilistic SPS like faint laser pulses emit photons in coherent states with a mean photon number much smaller than one such that the probability for two photons in the mode is small. They are not deterministic as one cannot predict whether a photon will be measured in a pulse or not, only at what probability a photon is detected. As coherent photon states are applied, $g^{(2)}(0) = 1$ in contrast to $g^{(2)}(0) = 0$ for a deterministic source. A special case of probabilistic SPS are correlated photon pair sources typically created by parametric down conversion. Although the photon emission is coherent with an average photon number much less than one, the correlated emission allows to detect one photon and thereby herald the arrival of the other. In this case, the $g^{(2)}$-function can go down to zero [211].

Efficiency The efficiency η is a measure for the probability to detect a photon upon excitation. A deterministic source with efficiency one is an on-demand SPS. The efficiency contains several factors: the quantum efficiency of the emitter, the extraction

efficiency being the probability that a photon is emitted into the collection mode, and the collection efficiency of the experimental system. For a quantum emitter in an optical cavity, the efficiency is given by

$$\eta = \mathrm{QE}_c \cdot \eta_c \cdot \beta \cdot \eta_{\mathrm{col}} \tag{4.1.14}$$

with QE_c the cavity quantum efficiency (eq. 2.2.44), η_c the outcoupling efficiency (eq. 2.1.42), β the fraction of the emission into the cavity mode (eq. 2.2.38), and η_{col} the collection efficiency of the system. When collecting through the fibre, η needs to be extended by the mode matching.

Brightness Brightness is here defined as the rate at which photons are emitted. Note that the terms 'brightness' and 'efficiency' are inconsistently used in literature. The brightness is ultimately limited by the inverse of the spontaneous emission lifetime. In an incoherent two-level system, the photon emission rate depends on the excitation power following a saturation curve. If such a system, which is object to pure dephasing, is coupled to a cavity in the weak coupling regime, the rate of photons emitted into the cavity mode, I_c, is given by

$$I_c = R_{\mathrm{eff}} \frac{P}{P + \gamma + R_{\mathrm{eff}}} \tag{4.1.15}$$

with P being the pumping rate and R_{eff} the effective emitter-cavity coupling rate as defined in eq. 2.2.32. For high excitation rates, the photon emission rate saturates to $I_c = R_{\mathrm{eff}}$ [147]. Note that this would only be valid for QE = 1. Hence, for a cavity-coupled emitter, high brightness can be reached by a large effective Purcell factor in addition to an emitter featuring a short lifetime.

Indistinguishability Two photons are called indistinguishable if they are in exactly the same mode, that is spatially, temporally, polarisation-wise, and spectrally. If the spectrum of an SPS is Fourier-transform-limited, which implies that the spectral width is the inverse of the lifetime, the emitted photons are indistinguishable. When two indistinguishable photons impinge on the two input ports of a 50:50 beam splitter, the two cases where there is one photon each at the output ports interfere destructively. This means that the photons can only both appear at one or the other output port together such that at zero time delay no coincidences between the two output ports are detected. This phenomenon is known as the Hong-Ou-Mandel effect and was first described in 1987 [212]. As soon as pure dephasing or spectral diffusion is present, the photons are no longer Fourier-limited and lose indistinguishability. The destructive interference is no longer perfect and the Hong-Ou-Mandel dip no longer reaches zero. Quantitatively, for a two-level system with pure dephasing, the indistinguishability I is defined as

$$I = \frac{\gamma}{\gamma + \gamma^\star} = \frac{T_2}{2T_1}. \tag{4.1.16}$$

Photons from solid state emitters, where $\gamma^\star \gg \gamma$, virtually have zero indistinguishability. They can however be made indistinguishable by spectral filtering at the cost of efficiency

[54]. This loss can be mitigated in a cavity-coupled system as shall be treated in more detail in section 4.6.

4.1.3. Overview

I shall now give a brief overview of the most important existing single photon sources, their specifications, and applications. A good summary of this topic can be found in [126, 203, 211].

Due to the lack of easy to operate deterministic SPS, probabilistic SPS are most widely used today, such as faint coherent pulses [213], four-wave mixing [214, 215], and, most prominently, spontaneous parametric down conversion [208, 216]. The latter features inherent indistinguishability and easy operation, and with heralding and strong filtering, $g^{(2)}(0)$-values below 0.0001 can be reached [217]. However, to minimise the probability for more than one photon in the mode, the source must be operated at very low mean photon numbers $\ll 1$ leading to very low rates.

Especially in some quantum information applications, deterministic SPS are beneficial, which is why they are intensely investigated, mostly single emitter quantum systems. Inherently indistinguishable single photon sources are single atoms [218–221] and ions [196, 222], whose emission rate can be enhanced by high Q optical resonators. Nevertheless, especially experiments with single atoms are technically involving, require ultra-high vacuum, and are therefore not really scalable and rather suited for proof of principle experiments. The highest achieved rates are with less than 10^5 cps (counts per second) rather low [197, 223]. Fluorescence from single dye molecules, typically embedded into crystalline host matrices, into the zero phonon line (ZPL) can yield indistinguishable single photons and different molecules can be shifted into resonance with each other via the Stark effect [224–227]. However, indistinguishability requires liquid helium temperatures and Hong-Ou-Mandel contrasts are still moderate. While room temperature operation is possible, photo-bleaching remains a problem [203] for many systems. Some molecules are nevertheless shown to be permanently photostable in suitable host matrices [227] and the system holds the record of the most regular single photon stream, where an intensity noise below the shot-noise limit is demonstrated [228]. The closest researchers have come towards an ideal deterministic SPS regarding simultaneous purity and indistinguishability is with self-assembled quantum dots in microresonating structures [42–44]. On the down-side, cryogenic temperatures are necessary, but $g^{(2)}(0) = 0.0028$ and $I = 0.9956$ are the best values demonstrated so far in the solid state [44], also featuring much higher efficiency than atomic systems. While individual quantum dots can be tuned into resonance with each other, the overall emission frequency is limited to the suitable semiconductor materials. In recent years, colour centres in diamond have emerged as promising candidates for single photon sources at room temperature. Single photon emission was observed from nitrogen vacancy (NV) [198], silicon vacancy (SiV) [229, 230], germanium vacancy (GeV) [231], and tin vacancy (SnV) centres [232], where especially NV centres but recently also SiV centres have been investigated in more detail. A fruitful approach is coupling colour centres to optical microcavities or plasmonic structures for an enhanced and narrow-band emission. The broad phonon side band of

the stable and bright NV centre allows for broadband bright [45, 46] or narrowband tunable sources [47, 48]. The SiV centre, whose narrow and dominant ZPL makes it better suited for Purcell enhancement, was successfully coupled to fibre-based microcavities [94] (this work) and photonic crystal cavities [50, 51] achieving the largest yet enhancement of colour centre single photon emission. Though a very promising candidate for a room temperature deterministic SPS, limitations like a low quantum efficiency [50, 233] have yet to be overcome from the sample point of view. Ideas towards a bright indistinguishable SPS using the SiV centre are presented in section 4.6. An extensive review of these and further solid state single photon emitters like colour centres in silicon carbide [234, 235] and vacancies in hexagonal boron nitride [236] can be found in [26].

In the light of this plethora of (potential and actual) SPS, the question about application-specific needs arises. One of the foremost applications of SPS is quantum key distribution (QKD) , which does not require photon indistinguishability [25, 237]. Nowadays, faint pulses are typically used, bearing a security problem due to potential multiple photon states (so called 'photon-number splitting side-channel attack'), which limits the transfer rate. Using the decoy-state method [22–24], which, greatly simplified, uses different intensity pulses to more precisely estimate how many measured events stem from single photons, mean photon numbers per pulse of around 0.5 can be used allowing for a drastic increase of the secure rate [25, 26]. This means that if one wants to surpass probabilistic sources, an efficiency of more than 0.5 is required for a deterministic source, while the brightness should be as high as possible. QKD was demonstrated over 120 km using a quantum dot source [238], but the secure rates are still 1-2 orders of magnitude below the decoy-state method [26]. So QKD could clearly benefit from new deterministic sources. However, these still have to improve substantially on efficiency and brightness.

Single photons could also contribute to high sensitivity spectroscopic measurements below the shot noise limit. As a coherent source with a mean photon number $\bar{n}$ features fluctuations of $\sqrt{\bar{n}}$, it becomes increasingly hard to for example measure weak absorptions which require a rather faint light source due to inherent photon shot noise. Amplitude squeezing, meaning that the fluctuations in amplitude are reduced at the cost of larger phase noise according to Heisenberg's uncertainty principle, represents an option to surpass this limit [239–242]. For example, squeezed light is used to enhance the sensitivity of gravitational wave detectors [243]. An ideal single photon source emits maximally amplitude squeezed light, which could open the path towards extremely low noise sensing [203]. With single organic molecules, whose emission was enhanced by a planar metallodielectric antenna, intensity squeezing of 2.2 dB was reached [228]. Indistinguishability is not needed for this application, but both efficiency and brightness should be high, being the reason why SPS are to date not typically used in the field of sensing.

Virtually all other applications of SPS require indistinguishability and potentially a high level of purity and efficiency. For instance, end to end long-distance quantum communication needs quantum repeaters [27–29]. While it is possible to build quantum-memory-based quantum repeaters applying correlated pair sources [27, 28], errors can be avoided applying deterministic single photon sources leading to signifi-

cantly higher entanglement distribution rates [30, 31]. The required specifications are $g^{(2)}(0) < 0.01$, $I > 0.9$, and $\eta > 0.9$ [26], which seems in reach for quantum dot sources and in the medium to long term room temperature SPS. Another implementation is the all-optical quantum repeater [32, 33] based on photonic cluster states [34] without the need for quantum memories, which, however, comes with very demanding requirements: $g^{(2)}(0) < 0.001$, $I > 0.99$, $\eta > 0.99$, and a brightness in the GHz regime [26], which seems to remain challenging in the near future.

Not least, many quantum computing protocols require single photons [37]. Fault-tolerant linear all-optical quantum computing, however, is also based on photonic cluster states and has similar requirements as mentioned above [26, 38]. The requirements are loosened for photonic quantum simulators applying boson sampling and photonic quantum walks [39, 40] as by far less correlated photons and lower indistinguishability [41] are required [26]. While compatible all-optical quantum computing is a long-term goal, operational primitives like the implementation of a CNOT gate have already been demonstrated with a quantum dot single photon source [244].

4.2. The silicon vacancy centre in diamond

After having given a brief overview of defects in diamond, this section will concentrate on the silicon vacancy centre and discuss its features, referring to why it is in principle very well suited for a bright single photon source at room temperature and what technical challenges have to be overcome towards this goal.

4.2.1. Defects in diamond

Diamond is a cubic crystalline form of carbon, which features exceptional properties like the well-known hardness and extraordinary thermal conductivity, chemical inertness, and a wide indirect bandgap of 5.5 eV. The latter makes it transparent for light with a wavelength longer than 230 nm [245, 246]. However, imperfections in the carbon lattice like vacancies and impurity atoms can be optically active by leading to discrete states within the band gap allowing for distinct light absorption in the visible and infrared. As these defects in sufficient concentration give the diamond a visible overall colour, they are named colour centres [126, 247].

Although over 500 colour centres are known [246], only few can be reliably produced, are well understood, and typically used in quantum optics research. Good reviews of the topic can be found in [126, 248–250].

Nitrogen vacancy centre The colour centre studied most intensely is the negatively charged nitrogen vacancy centre, where a nitrogen atom substitutes a carbon atom and a neighbouring lattice site remains vacant. It is perfectly photostable and features a zero phonon line at 637 nm [251]. However, due to a strong overall electric dipole moment [252], it couples well to external fields, which is why only a small fraction of the fluorescence (less than 4% at cryogenic temperatures) is emitted into the ZPL [253, 254],

while the prominent broad phonon side band with its peak around 690 nm spans around 100 nm. The quantum efficiency depends on crystal quality with typical values ranging from below 0.5 for nanocrystals [255] while reaching values of around 0.7 in bulk [256, 257]. The excited state lifetime is around 10 ns in bulk [198, 258], but can be significantly longer in nanodiamonds [259]. NV centres were the first single colour centres that were addressed [251, 260] and showed photon anti-bunching [198, 199]. A unique feature of the NV centre is that its electronic spin states can be addressed at room temperature making it interesting as spin photon interface and as building block of quantum optical networks [261] as well as precise magnetic sensing applications [262]. Notably, in 2015, the first loophole-free test of Bell's inequality was performed by entanglement of electronic spins in NV centres [263].

Silicon vacancy centre In the silicon vacancy centre, a silicon atom resides in the middle between two vacant carbon sites (see Fig. 4.2.1) giving this colour centre inversion symmetry such that it does not possess a permanent electric dipole moment and is less susceptible to local environmental fluctuations [26]. For the mainly studied negatively charged SiV^- centre, about 70% of fluorescence light is emitted into the ZPL at 737 nm, which was observed to be as narrow as 0.7 nm at room temperature [49]. This makes the SiV centre much better suited for cavity coupling. The lifetime is with around 1 ns [248] shorter than for the NV centre making it the brightest colour centre in diamond known to date. However, the quantum efficiency is still rather low, typically below 0.1 and highly depends on sample conditions [50, 233]. Optical manipulation of electronic and nuclear spin at cryogenic temperature was reported [264, 265], opening the path towards an efficient spin-photon interface. Photon anti-bunching was first observed in 2005 by Wang et al. [229] and the SiV centre was since studied as a potential bright single photon source. Single photon emission from multiple SiV centres with intrinsic indistinguishability was achieved at liquid helium temperature in low-strain bulk diamond, quite unique in the solid state [266], enabling Hong-Ou-Mandel interference without the need for detuning [267]. I shall allude to the negatively charged SiV centre more in depth in the following sections. Recently, an efficient conversion of implanted silicon in diamond to SiV^0 centres, the neutral charge state of the silicon vacancy centre, was demonstrated by carefully tailoring the Fermi level of the diamond host [268]. The SiV^0 centre has its ZPL at 946 nm, which comprises 90% of the total fluorescence light, and promises much longer spin coherence times than the SiV^- centre.

Other colour centres In recent years, novel colour centres have been reproducibly fabricated using other impurity atoms from the carbon group. The germanium vacancy (GeV) centre with a ZPL at 603 nm [231, 269] and the tin vacancy (SnV) centre with a ZPL at 620 nm [232, 270] were shown to emit single photons at room temperature. Like the silicon vacancy centre [271], they are used for precise thermometry at room temperature [270]. Research is still in its infancy, but GeV centres promise to be more reliably produced than SiV centres while having similar characteristics [231].

While single photon emission has been reported from other colour centres in diamond

like the nickel nitrogen complex (NE8) centre [272] and chromium related centres [273], these can so far not be reliably produced. An overview of colour centres in diamond emitting single photons can be found in [249].

4.2.2. Properties of SiV centres

Level scheme and spectral properties At room temperature, the ZPL appears as one line at around 737 nm as shown in the fluorescence spectrum of a single SiV centre (excitation at 690 nm) in Fig. 4.2.1(b). The linewidth of the example shown here is 1.25 nm (FWHM, obtained from Lorentzian fit) in accordance with reported values for single SiV centres in nanodiamonds [230]. However, in bulk diamond linewidths of 5 to 7 nm are typical [208, 229].

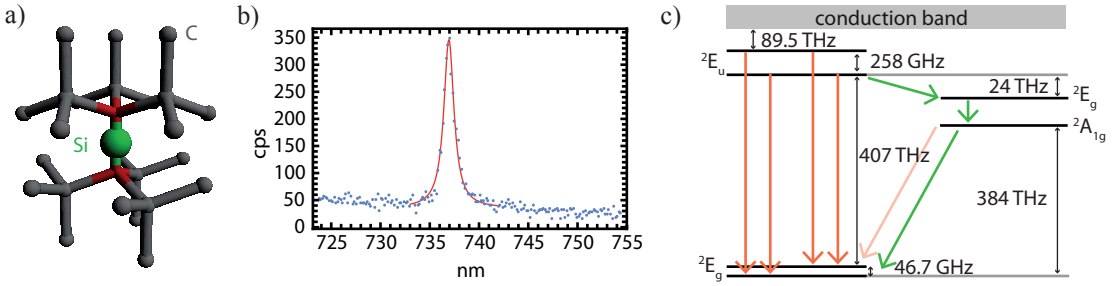

Figure 4.2.1.: (a) Geometric structure of SiV centre in diamond host lattice. Grey: sp^3-hybridised carbon atoms. Green: silicon atom. Red: vacancies. Vertical axis corresponds to $\langle 111 \rangle$ axis. (b) Room temperature spectrum of single SiV centre in nanodiamond. Red line: Lorentzian fit. FWHM: 1.25 nm. (c) Level scheme of negatively charged SiV centre. Left: doublet ground and excited states. Right: shelving states. Orange: radiative transitions. Green: non-radiative transitions. Faint orange: Weekly allowed radiative transition in the presence of strain. [230, 265, 274]

Going to liquid helium temperature, one can resolve that the ZPL is split up into two double lines [265, 275], indicating a two-fold level both for the excited and the ground state, which is sketched in Fig. 4.2.1(c) on the left. 10 electrons can be associated to the SiV centre, plus an additional one for the negatively charged SiV centre, which is typically studied. (For the neutral SiV centre, see [268, 276].) An unpaired electron leads to an effective spin 1/2 in both ground and excited state. Following a group theoretical approach, taking into account the D_{3d} symmetry of the SiV centre, one can show that the ground state configuration has the spectroscopic notation ^2E_g and the excited state ^2E_u [264]. For a detailed derivation, see [247]. A theoretical discussion based on density functional theory can predict the absolute positions of the energy levels [274]. Spin-orbit coupling and the Jahn-Teller effect, a spontaneous symmetry breaking effect which lifts the degeneracy of electronic states by geometric distortion, thereby lowering the energy [277], cause the observed splitting of the ground and excited state (energies are indicated in Fig. 4.2.1(c)) [247]. When applying a magnetic field, each of the four lines undergoes Zeeman splitting into a spin-up and spin-down state. Depending on the relative magnetic

field direction, spin flipping transitions can be allowed leading to a variation of the spin relaxation time from milliseconds to tens of nanoseconds. The most abundant isotope of silicon is ^{28}Si featuring no nuclear spin, while the smaller fraction of ^{29}Si has nuclear spin 1/2 leading to an optically addressable hyperfine splitting, which could be interesting as quantum memory [265].

From $g^{(2)}$-measurements it can be seen that photon bunching at short time delays occurs in SiV centres in addition to anti-bunching at zero time delay. This observation is explained by the existence of a third energy state residing between the excited state and the ground state, a so-called shelving state. The experimental findings are supported by theoretical calculations [274], which propose a ^2E_g and a $^2A_{1g}$ state slightly lower lying than the excited state with efficient non-radiative coupling to the excited state. Optical transitions are forbidden as the wavefunction of these states has the same parity as for ground and excited state due to the inversion symmetry. In strained diamond, the symmetry is partially lifted, such that the transition from the $^2A_{1g}$ state to the ground state becomes weekly allowed, which can explain an experimental observation [278] of a weak near-infrared transition at 823 nm [274]. The levels are illustrated in Fig. 4.2.1(c) on the right.

Gali and Maze [274] note that in the presence of external perturbing fields, the SiV centre can be ionised during optical excitation creating a stable doubly negative charge state, which appears as permanent photo-bleaching. The single negative charge state, and thus the fluorescence at 737 nm, can only be restored by ultraviolet excitation.

Rate dynamics I shall now discuss the saturation behaviour following [279]. When the SiV centre gets off-resonantly excited (for the experiments in this work, 690 nm light is used), it relaxes back to the excited state non-radiatively on a time scale much faster than the optical transitions, such that this process in the following will be assumed as instantaneous. The excitation rate k_{12} from the ground state 1 to the excited state 2 (see Fig. 4.2.2(a)) is then proportional to the excitation laser power P:

$$k_{12} = \sigma P \tag{4.2.1}$$

with σ being a proportionality constant. By further defining the relaxation rates k_{21} from the excited state 2 to the ground state 1, k_{23} from the excited state 2 to the shelving state 3, and k_{31} from the shelving state 3 to the ground state 1, one can set up a system of rate equations for the populations ρ_i in states $i \in \{1, 2, 3\}$:

$$\begin{pmatrix} \dot{\rho_1} \\ \dot{\rho_2} \\ \dot{\rho_3} \end{pmatrix} = \begin{pmatrix} -k_{12} & k_{21} & k_{31} \\ k_{12} & -k_{21} - k_{23} & 0 \\ 0 & k_{23} & -k_{31} \end{pmatrix} = \begin{pmatrix} \rho_1 \\ \rho_2 \\ \rho_3 \end{pmatrix} \tag{4.2.2}$$

We assume that the population is in the ground state for $t = 0$, i.e. $\boldsymbol{\rho} = (1, 0, 0)$ with the total population being constant over time, $\rho_1 + \rho_2 + \rho_3 = 1$. The fluorescence rate $I(P) = k_{21}\rho_2 (t \to \infty)$ is given by the steady state solution for the population in the excited state multiplied with the relaxation rate to the ground state, where the steady

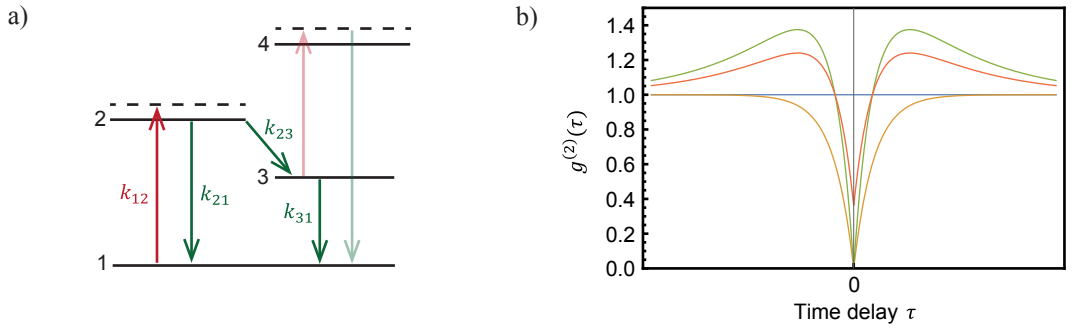

Figure 4.2.2.: (a) Level scheme of SiV centre according to [233] including transition rates. 1: ground state. 2: excited state. 3: shelving state. 4: de-shelving state. Green arrows: constant rates. Red arrows: intensity dependent rates. Faint arrows: proposed de-shelving process. (b) $g^{(2)}$-function for coherent source (blue), two-level system (yellow), three-level system (green), and three-level system with uncorrelated background (red). $a = 1$, $\tau_1 = 0.2$, $\tau_2 = 0.05$, $p = 0.8$.

state can be computed by setting the rates $\dot{\boldsymbol{\rho}} = 0$. Solving for ρ_2 yields

$$I(P) = k_{21}\rho_2(t \to \infty) = \frac{k_{21}k_{31}\sigma P}{(k_{23} + k_{31})\sigma P + k_{23}k_{31} + k_{21}k_{31}}. \tag{4.2.3}$$

This can be rearranged to obtain a function saturating with power:

$$I(P) = I^{\infty}\frac{P}{P + P_{\text{sat}}} \tag{4.2.4}$$

with

$$I^{\infty} \equiv I(P \to \infty) = k_{21}\rho_2^{\infty} \tag{4.2.5}$$

the saturation photon emission rate for large powers, where

$$\rho_2^{\infty} \equiv \rho_2(t \to \infty, P \to \infty) = \frac{1}{1 + k_{23}/k_{31}}, \tag{4.2.6}$$

and

$$P_{\text{sat}} = \frac{k_{23}k_{31} + k_{21}k_{31}}{(k_{23} + k_{31})\sigma} \tag{4.2.7}$$

the saturation power. So from a fit of the experimental saturation curve, one can deduce the proportionality constant σ as a function of transition rates and saturation power. Without shelving, ρ_2^{∞} would reach one and the emission rate becomes $I^{\infty} = k_{21}$. It is equivalent to the fraction of time the system spends in the fluorescence transition. The larger k_{31} compared to the shelving rate k_{23}, the longer the system is trapped in the shelving state, decreasing the brightness [126].

$g^{(2)}$-function of three-level system Normalising the excited state population $\rho_2(\tau)$ to ρ_2^∞ yields the $g^{(2)}$-function [198]:

$$g^{(2)}(\tau) = \frac{\rho_2(\tau)}{\rho_2^\infty} \tag{4.2.8}$$

By solving the differential equation system 4.2.2, one finds

$$g^{(2)}(\tau) = 1 - (1+a)\exp\left(-\frac{|\tau|}{\tau_1}\right) + a\exp\left(-\frac{|\tau|}{\tau_2}\right) \tag{4.2.9}$$

with the following parameters:

$$\tau_{1,2} = \frac{2}{A \pm \sqrt{A^2 - 4B}} \tag{4.2.10}$$

$$A = k_{12} + k_{21} + k_{23} + k_{31} \tag{4.2.11}$$

$$B = k_{12}k_{23} + k_{12}k_{31} + k_{21}k_{31} + k_{23}k_{31} \tag{4.2.12}$$

$$a = \frac{1 - \tau_2 k_{31}}{k_{31}(\tau_2 - \tau_1)} \tag{4.2.13}$$

For comparison, the $g^{(2)}$-function of a two-level system (that is $k_{31} = 0$ and $a = 0$) would be

$$g^{(2)}(\tau) = 1 - \exp\left(-\frac{|\tau|}{\tau_1}\right). \tag{4.2.14}$$

This is qualitatively illustrated in Fig. 4.2.2(b), where the blue line, constant at one, would be the $g^{(2)}$-function of a coherent light source, the yellow line corresponds to a two-level system featuring pure anti-bunching according to eq. 4.2.14, where τ_1 is the anti-bunching time constant. In the three-level case (green line), we get additional bunching at intermediate timescales governed by τ_2. Note that τ_1 was chosen the same for both cases. a is a measure for the amount of bunching. [279]

To get a more intuitive picture, why bunching occurs, picture the three-level system as an on-off two-level system [208]. It is off, while in the shelving state and on while cycling the fluorescence transition. The average length of an on-period is $T_{\text{on}} = 1/k_{23}$. During the off-time, which has an average duration of $T_{\text{off}} = 1/k_{31}$, no photons can be detected. For short time delays after the detection of a photon, the system is likely to still be in the on-state, while for longer time delays, the probability to find the system in the on state is $T_{\text{on}}/(T_{\text{on}} + T_{\text{off}}) = 1/(1 + k_{23}/k_{31})$. As the $g^{(2)}$-function is normalised to a long time average, the larger amount of subsequent photons detected during time delays smaller than T_{on} causes a higher value for short times. Another way of regarding it is to view the on-times as photon bunches separated by the off-times.

Uncorrelated background contribution In addition to fluorescence from the SiV ZPL, one typically observes background fluorescence from the diamond host material and, in our case, to a smaller fraction from the planar mirror. In diamond, it is assumed that sp^2-hybridised carbon for example on the surface or in lattice defects [280–282] or grain

boundaries [283] cause fluorescence. Introducing the purity parameter p, which gives the emitter fluorescence normalised to the total fluorescence, i.e. the probability that a detected photon was emitted by the SiV centre, the $g^{(2)}$-function in the presence of uncorrelated background fluorescence can be written as [279]

$$g_m^{(2)}(\tau) = 1 + p^2 \left(g^{(2)}(\tau) - 1 \right). \tag{4.2.15}$$

The red line in Fig. 4.2.2(b) shows a three-level $g^{(2)}$-function with $p = 0.8$ for the otherwise same parameters compared to the green line. One can see that both bunching and anti-bunching are no longer as pronounced. In particular, $g^{(2)}(0)$ now has a finite value of $1 - p^2$. This implies that if $p \lesssim 0.7$, $g^{(2)}(0) > 0.5$ even for a single emitter.

Power dependence of $g^{(2)}$-function As we have already seen, the excitation rate k_{12} is linearly dependent on excitation power (eq. 4.2.1), implying that the $g^{(2)}$-function is also power-dependent. Experiments [230, 233, 278] indeed showed a power dependence, which, however, could not be fitted assuming all rates except for k_{12} to be constant. In particular, τ_2 should be almost constant according to theory, but drastically increased for $P \to 0$ in the experiment. Neu et al. [233] therefore introduced a modified level scheme including de-shelving level 4 as depicted in Fig. 4.2.2(a). An intensity-dependent de-shelving process via level 4 allows depopulation of shelving level 3. In consequence, the system can now be regarded as a three-level system with the difference that the rate k_{31} no longer is constant but shows a saturation behaviour:

$$k_{31} = \frac{dP}{P + c} + k_{31}^0 \tag{4.2.16}$$

with c and d being fitting constants. It is useful to compute the values of $\tau_{1,2}$ and a for the limit of vanishing and infinite power to get a feeling whether the model could fit the data and to be able to set suitable starting values for the fit. For infinite power, $k_{12} \to \infty$, leading to $\tau_1^\infty = 0$, $\tau_2^\infty = 1/(k_{23} + k_{31}^\infty)$, and $a^\infty = k_{23}/k_{31}^\infty$. In the limit of vanishing power, $k_{12} = 0$ leading to $\tau_1^0 = 1/(k_{21} + k_{23})$, $\tau_2^0 = 1/k_{31}^0$, and $a^0 = 0$. These values are summarised in table 4.2.1. To apply the model, one measures the $g^{(2)}$-function for various excitation powers and fits the data with eq. 4.2.9. Note that a linear dependence of k_{31} would lead to $a^\infty = k_{23}/k_{31}^\infty \to 0$, in disagreement to measurement. With $k_{31}^\infty = d + k_{31}^0$ according to the model in eq. 4.2.16, one can solve the equations for the unknown rates as follows:

$$k_{31}^0 = \frac{1}{\tau_2^0} \tag{4.2.17}$$

$$d = \frac{1}{\tau_2^\infty (a^\infty + 1)} - \frac{1}{\tau_2^0} \tag{4.2.18}$$

$$k_{23} = \frac{1}{\tau_2^\infty} - k_{31}^0 - d \tag{4.2.19}$$

$$k_{21} = \frac{1}{\tau_1^0} - k_{23} \tag{4.2.20}$$

	$k_{12} \to 0$	$k_{12} \to \infty$
τ_1	$\frac{1}{k_{21}+k_{23}^0}$	0
τ_2	$\frac{1}{k_{31}^0}$	$\frac{1}{k_{23}^\infty+k_{31}^\infty}$
a	0	$\frac{k_{23}^\infty}{k_{31}^\infty}$

Table 4.2.1.: Fitting parameters $\tau_{1,2}$ and a for the limit of vanishing and infinite power. The displayed values are so far independent of the chosen power dependence model.

Substituting these values into eq. 4.2.10 to 4.2.13 allows fitting $\tau_{1,2}$ and a with the six fit parameters c, σ, τ_1^0, τ_2^0, τ_2^∞, and a^∞. Plugging these back into eq. 4.2.17 to 4.2.20 allows to determine the transition rates from $g^{(2)}$-measurements at varying power. In section 4.5.4, a modification to the introduced model will be presented.

4.2.3. SiV centres in nanodiamonds

To avoid losses due to total internal reflection as well as to be able to incorporate SiV centres into the microcavity, we apply nanodiamond samples. These can be directly grown by chemical vapour deposition (CVD) [230] or high-pressure high-temperature (HPHT) synthesis [284] or milled down from diamond films or bulk diamond [49]. Directly grown nanodiamonds can be single-crystalline and have good crystal properties. Near lifetime-limited SiV ensemble fluorescence was demonstrated in 200 nm HPHT nanodiamonds [284] and CVD-grown diamonds with 100-300 nm in diameter [285], coming close to the behaviour in bulk. Li et al. even report on single photon emission from their sample. Due to strongly size-dependent scattering losses (see sec. 3.5), fibre cavity experiments require rather small nanodiamonds, ideally well below 100 nm. A theoretical prediction states that SiV centres should be stable in diamonds down to a diameter of about 2 nm [286]. Indeed, SiV fluorescence from CVD crystals smaller than 10 nm has been observed [287]. Surprisingly, SiV emission could even be detected in < 2 nm diamonds from meteoric origin [288]. However, optical properties and photostability are still unsatisfactory in very small crystal samples. Polycrystalline nanoparticles with a size of 70-80 nm diameter have shown stable, bright fluorescence [49]. However, single photon emission is rarely observed. Encouragingly, new nanodiamond samples with diameters of a few tens of nm containing single SiV centres have recently been produced [289]. However, photostability and moderate brightness are still an issue. Producing high quality SiV centres in nanodiamonds could also be advantageous to achieve better spin coherence, as phonons at the critical frequency are not compatible with the boundary conditions imposed by the small size [284]. In summary, it remains a challenge to produce photostable single SiV centres in < 100 nm monocrystalline diamond having a good quantum efficiency and a narrow line.

In nanodiamonds, the reported quantum efficiencies still lie below 10% [233], but could presumably be increased by higher quality diamond hosts. The largest detected photon emission rates from single SiV centres in nanodiamonds without cavity enhancement

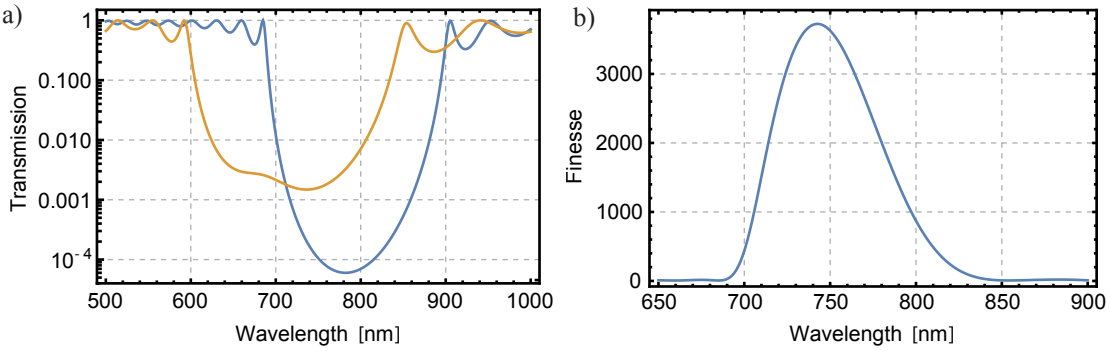

Figure 4.3.1.: (a) Computed mirror transmission of the fibre (yellow) and the planar mirror (blue). (b) Computed finesse assuming the mirror transmissions in (a) and 40 ppm absorption losses. [53]

were a few Mcps (megacounts per second) [233]. Note that the spontaneous decay rate is expected to be lower in nanodiamonds as compared to bulk due to the lower local density of states according to Fermi's golden rule.

Crystal strain plays an important role in nanodiamonds. It can shift the ZPL by up to a few nm and can lead to room temperature linewidths ranging from less than 1 to several nm. [230]. It is assumed that local strain acts on the non-radiative decay channel thereby having an influence on the quantum efficiency [290, 291]. Recently, the effect of strain on SiV [292] and GeV [293] centres was studied more in detail in bulk diamond at cryogenic temperatures, showing that the lines of colour centres can be reproducibly tuned by applying strain. Even the coherence properties could be changed by strain tuning [294]. So it appears likely, that an improvement of nanocrystal quality gives more control on SiV optical properties. For a detailed discussion of crystal strain, refer to [247, 295].

Apart from the quantum optical applications discussed so far, small nanodiamonds containing SiV centres are also investigated as bright, stable, and chemically inert labels for fluorescence microscopy of biological systems [296].

4.3. Experimental realisation

This section introduces the microcavity setup used for the SiV coupling experiment and alludes to the theoretically expected performance and the achievable Purcell factors, closely following and in parts identical to [53].

4.3.1. Setup

Cavity The integral part of the setup is the fibre-based microcavity. The fibre (fibre name 9A, fibre B in appendix A) is coated with a dielectric mirror (Laseroptik) with a transmission of 1500 ppm at a center wavelength of 740 nm and 2500 ppm at the excitation wavelength of 690 nm, such that no excitation light enters the fibre to avoid

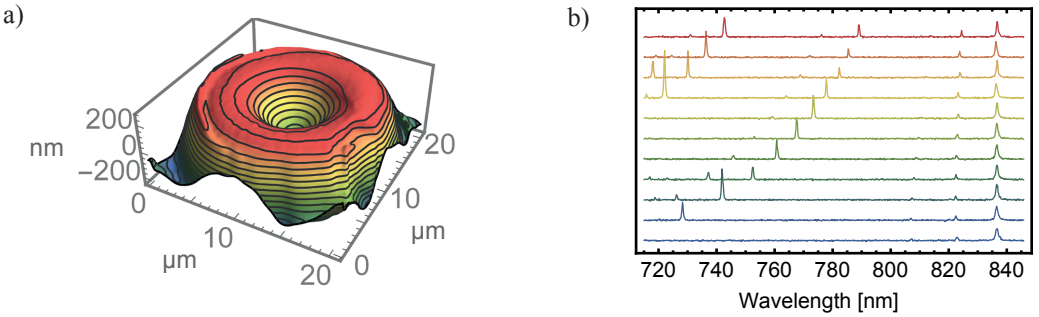

Figure 4.3.2.: (a) WLI measurement of the fibre profile. (b) Cavity transmission spectra for different cavity lengths, starting at $d = 5\,\lambda/2$ (the lowest curve), in steps of one free spectral range. Different resonance heights are due to the source spectrum and finite spectrometer resolution. [53]

fibre fluorescence. The planar mirror has a coating centered at 780 nm with a transmission of 60 ppm (200 ppm at 740 nm) and is designed to yield an electric-field maximum 30 nm above the mirror surface. The coating is almost transparent at 690 nm, and the excitation light is focused into the cavity with an aspheric lens through the planar mirror. The asymmetry in transmission leads to about 90% of the fluorescence light being emitted into the fibre, which is the collection channel. Note that this configuration was chosen as the SiV sample was pre-coated onto this mirror. Otherwise, primarily due to mode coupling and fibre fluorescence, it could be beneficial to excite through the fibre and collect through the mirror, where the coatings would have to be chosen such that the transmission is larger for the mirror. Figure 4.3.1(a) shows a simulation of the fibre and mirror coating using the transfer-matrix method (see section 3.4). Assuming a total absorption loss at the mirrors of 40 ppm, this yields the cavity finesse as shown in Fig. 4.3.1(b). The measured finesse of 2000 at 780 nm coincides well with the computation such that it is a fair assumption that the computed value of 3750 at 740 nm is also reached. [53]

The fibre profile is shown in Fig. 4.3.2(a). The fibre edge is cropped such that a plateau of about 18 µm in diameter remains. The profile features good spherical symmetry and has a central radius of curvature of 26 µm. To calibrate the optical cavity length, broadband cavity transmission spectra are recorded with a supercontinuum laser and the separation of subsequent cavity resonances is evaluated; see Fig. 4.3.2(b). The smallest accessible longitudinal mode order is found to be $q = 5$, limited by the profile depth (300 nm) and the penetration depth into the coating (in total 1160 nm at 740 nm). [53]

Two-in-one setup Fig. 4.3.3 shows a schematic drawing of the optical setup. For off-resonant excitation of the SiV centres, a home-built external cavity diode laser at 690 nm is applied. It is coupled to a single-mode optical transfer fibre (not shown) for mode

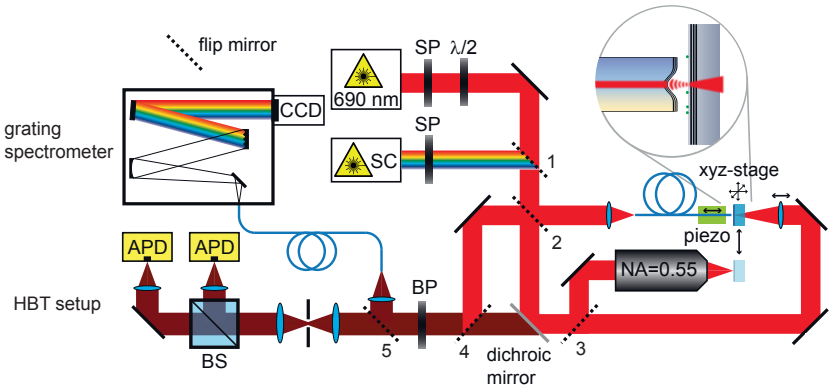

Figure 4.3.3.: Schematic drawing of the optical paths. Flip mirrors allow to couple in both light sources (1) through either cavity mirror (2) and to switch between collection from the cavity or the objective (2, 3, 4), detecting with the spectrometer or the HBT setup (5). SP: short-pass filter. BS: beam splitter.

cleaning, then passes a short pass filter[2] to get rid of fibre fluorescence and amplified spontaneous emission from the laser, a polariser[3] to get clean linear polarisation, and a half-wave plate in a motorised rotation mount[4] to align the polarisation. Alternatively, a pulsed supercontinuum laser source [5] is available, which is used for cavity transmission spectra as in Fig. 4.3.2(b) and for pulsed $g^{(2)}$ and lifetime measurements, for which a spectral line of 2-7 nm width is filtered out by an acousto-optic tunable filter (AOTF)[6]. The supercontinuum spans from about 460 to 2000 nm and is short-pass filtered to below 850 nm[7]. It emits pulses with a duration of 50 ps at a tunable repetition rate up to 20 MHz. When using the AOTF at 690 nm as pulsed excitation source, an additional band-pass filter[8] is added to block leaking light.

The central part of the experimental setup is displayed in a technical drawing in Fig. 4.3.4. An NA 0.55 microscope objective[9] with a working distance of 13 mm (2) is installed side by side with the cavity fibre, which is held by a PVC lid in an aluminium groove, which is in turn glued to a shear piezo stack[10] allowing to precisely scan the cavity length. The fibre holder and piezo are glued to a replaceable holding block (7), to which the fibre can be clamped. The planar mirror is held by a gimbal mount[11] (1) for angular alignment and can be reproducibly moved in all three directions with a

[2]Thorlabs FEL0700
[3]colorPol VIS 700 BC4 CW02, contrast $> 10^4$
[4]Radiant Dyes RD-RM-1"-M
[5]Fianium SC450-2-PP
[6]Fianium AOTF-VIS
[7]Thorlabs FES0850
[8]Semrock FF01-676/37-25
[9]50X Mitutoyo Plan Apo Infinity Corrected Long WD Objective
[10]PI ceramic P-121.03, maximal displacement 3 µm
[11]Newport U50-G21

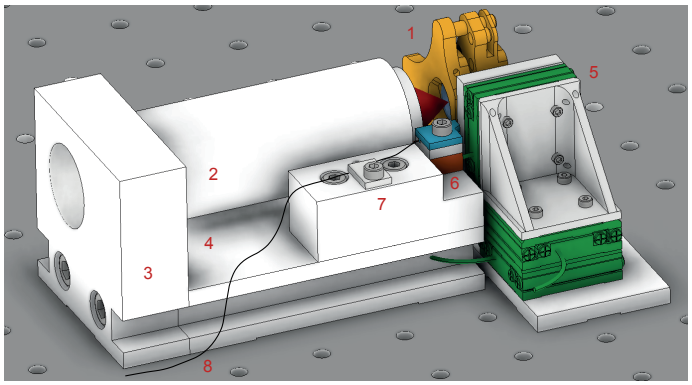

Figure 4.3.4.: Technical drawing of two-in-one setup. (1) Gimbal mirror mount with planar mirror. (2) Microscope objective. (3) Objective holder. Red cone indicates beam. (4) Ground plate. (5) XYZ slip-stick positioner. (6) Fibre holder. Red: Shear piezo stack. Grey: Fibre groove. Blue: Holding plate. (7) Fibre holding block with fixation plate. (8) Fibre. Design adopted by Hanno Kaupp.

nanopositioning stage[12] (5). It allows to quickly and reliably move the mirror back and forth between the objective for investigation in a confocal microscope configuration and the fibre to form a microcavity.

Several motorised flip mirror mounts[13] are in use to choose the light source and set the excitation and collection paths in an automatised and controlled manner. When working with the objective, the beam is coupled in from the left and the reflected and fluorescence light is collected through the same path. A dichroic mirror[14] separates the fluorescence. For further suppression of the excitation light, a long-pass filter[15] is applied. A selection of band-pass filters[16] mounted on a horizontal rotation mount to be able to shift the bands to lower wavelengths allows to select narrow bands of the fluorescence light in a range of 720 to 780 nm. The light can be either analysed spectrally with a grating spectrometer[17] or in an HBT setup. For the latter, the light is focused through a 50 µm pinhole and re-collimated by two aspheric lenses[18] to reduce stray light, then split by a 50:50 beam splitter and detected with two avalanche photo detectors (APDs). At 740 nm, the APDs have a detection efficiency of 70%.

The light can be coupled into the fibre cavity either through the fibre and collected through the planar mirror or coupled in through the planar mirror and collected in transmission through the fibre or in reflection back through the planar mirror. For the SiV experiments described here, the light was focused into the cavity mode through

[12] stack of three Attocube ECS3030 slip-stick positioning stages
[13] Radiant Dyes RD-KLS-1"-M
[14] Semrock FF700-Di01-25
[15] Semrock FF01-715/LP-25
[16] Semrock FF01-740/13-25, FF01-747/33-25, FF01-760/12-25, FF01-780/12-25
[17] Princeton Instruments Acton SP2500 with Andor iKon-M 934 (A-DU934N-BRDD), light coupled in via a multimode fibre
[18] Thorlabs AL50100-B

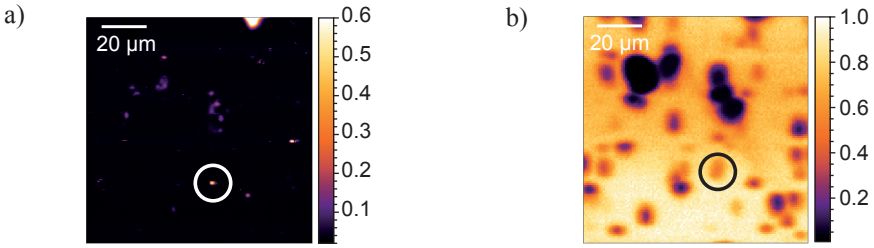

Figure 4.3.5.: (a) Confocal fluorescence map showing the count rate in MHz. Excitation at 690 nm, 500 µW. The marked spot is a narrow-line emitter. (b) Cavity transmission scan of the same area (with the transmission normalised to 1) for a cavity length of about 10 µm. The marked spot is the same location as in (a). [53]

the planar mirror by an aspheric lens[19] mounted on a three-axis micropositioning stage, collected by the cavity fibre, coupled out, and overlapped with the beam path to the detection optics.

Calibrating the distance between objective focus and cavity fibre (for details, see appendix C) allows to investigate the same emitters in the confocal microscope and in the cavity. Figure 4.3.5(a) shows a confocal fluorescence map of a $100\times100\,\mu\text{m}$ area of the mirror. Analysing the spectra reveals that the fluorescence stems from SiV centres. After characterising them, the mirror is moved to the cavity. Nanodiamonds precharacterised confocally can be easily found in the cavity via the Rayleigh scattering and absorption loss they introduce. An SCM image of the same area is shown in Fig. 4.3.5(b), where the cavity transmission of the supercontinuum source is measured, filtered to a 33-nm spectral band around 747 nm. The nanodiamonds appear as dark spots and can be directly related to the confocal fluorescence map in (a). The marked spot is a single bright SiV centre, whose moderate scattering loss indicates a rather small single nanodiamond.

4.3.2. Expected performance

At the shortest mirror separation $d = 5\,\lambda/2$, one obtains a cavity quality factor of $Q_c = 1.9\times10^4$. From an optimisation calculation as described in section 3.2.2, a mode waist $w_0 = 1.0\,\mu\text{m}$ is deduced, in agreement with SCM measurements. This results in a mode volume $V_m = 3.4\,\lambda^3$ yielding an ideal Purcell factor of $C_0 = 425$. Depending on the linewidth of the emitter, the emitter quality factor ranges from about 100 for very broad emitters to 1000 for the narrow-most observed emitters [49]. Figure 4.3.6 shows the computed effective Purcell factor (eq. 2.2.28) for different emitter linewidths as a function of cavity length, starting at the shortest accessible length. As can be seen, for a 1 nm broad emitter, $C_{\text{eff}} \gtrsim 15$ is reached, promising significant enhancement. Note that the dipole orientation (eq. 2.2.17) enters the Purcell factor quadratically, such that the above values are to be taken as an upper bound, i.e. for dipoles parallel to the mirror surface, located in the field maximum. For dipoles perpendicular to the mirror, the Purcell factor vanishes.

[19] Thorlabs AC254-035-B-ML

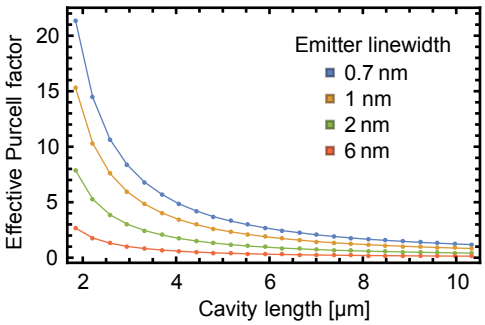

Figure 4.3.6.: Expected effective Purcell factors as a function of mirror separation (starting at the shortest accessible length $d = 5\,\lambda/2$) for varying emitter linewidth.

4.4. Sample characterisation

Now, I shall discuss the studied SiV sample, how single photon emission can be observed from ensembles, the lifetime, brightness, and difficulties with this sample, following [53] (some passages are identical).

4.4.1. Sample considerations

Due to the lack of a suitable bright SiV nanodiamond sample featuring single photon emission, the measurements presented in this work were conducted on nanodiamonds containing ensembles of SiV centres. The nanodiamonds of about 100 nm in size were obtained by milling down a polycrystalline CVD diamond film [49]. The milling was performed in the group of A. Krueger in Würzburg by bead-assisted sonic disintegration, where the diamond pieces are suspended in water together with ceramic beads, which crush the diamond when exposed to ultrasonic waves. The planar mirror was spin-coated with the nanodiamond sample in the group of C. Becher in Saarbrücken.

Investigating the mirror by confocal microscopy, one finds an even spread of emitters (several tens of emitters per $100 \times 100\,\mu m^2$), which typically feature a broad (7 nm) ZPL at the nominal wavelength of 738 nm, which can be assigned to SiV ensembles. In some crystals, one can also observe narrow (down to 1 nm) emission lines which are spectrally shifted and show pronounced photon anti-bunching. Figure 4.4.1(a) shows the free space spectra of 29 narrow line emitters found on a $400 \times 400\,\mu m^2$ area of the mirror. Almost all spectra show a more or less pronounced ensemble line centred at 738 nm in addition to shifted narrow lines in a wide spectral range from about 719 nm to 816 nm. Note that fluorescence could be measured down to 715 nm. The spectra are normalised, but show a large variation in brightness (note the different noise levels), where the narrow lines can be much brighter than the ensemble line. Some crystals even feature several narrow lines at different spectral positions. The linewidth of 56 narrow line emitters are plotted with respect to their centre wavelength in Fig. 4.4.1(b). It is visible that all lines are much more narrow than the typical 7 nm width of the ensemble line. These findings agree well with the study conducted on 50-100 nm milled CVD nanodiamonds by Lindner et

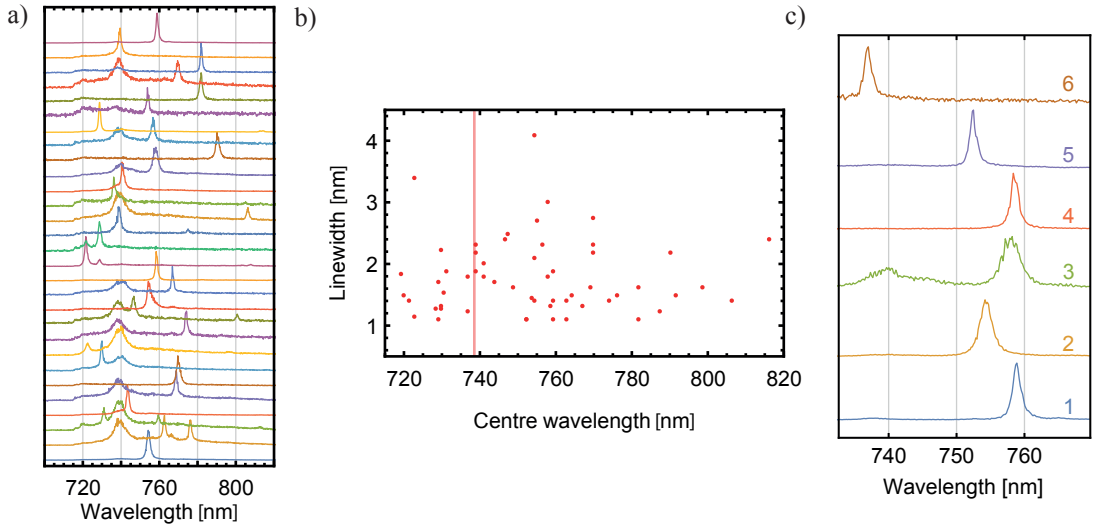

Figure 4.4.1.: (a) Free space spectra of 29 narrow line emitters found on a $400 \times 400\,\mu m^2$ area of the mirror, normalised to the maximum of each spectrum. Broad line around 738 nm belongs to SiV ensemble. (b) Linewidths (FWHM) deduced from Lorentzian fits with respect to central linewidth for the 56 studied narrow line emitters. Red line indicates ensemble wavelength. (c) Free space spectra of the emitters chosen for the cavity experiment. [53]

al. [295], who also report a wide spectral distribution of emitters with lines below 4 nm, while broad line emitters are found in the vicinity of the nominal wavelength, slightly red-shifted. While the slight shift to larger wavelengths of the broad-line emitters can be consistently explained by uniaxial strain, they attribute the wide-spread narrow-line emitters to a yet unknown Si-related defect like the association of SiV centres with nearby defects or modified SiV complexes [297]. Narrow line single photon emitters have been previously reported around 780 nm [298, 299]. Tran et al. [299] found that the investigated line does not split up into two doublet lines when cooled down like an SiV centre would. However, it remains unclear, whether they were possibly studying some other defect. It was also suggested, that grain boundaries and morphological defects can cause narrowband single photon emitters in nanodiamonds [300], however, rather at shorter wavelengths than the ones observed here.

From the 56 studied emitters, 25 were found to be suitable for further studies according to the following criteria: They are narrow ($\leq$ 3 nm), bright, show no fast blinking, and have a good polarisation contrast, that is, the line (almost) disappears when the polarisation is turned by 90° from the angle of maximal emission. Of these emitters, 17 featured significant anti-bunching, where some emitters could not be investigated, as suitable band-pass filters were not available or the emitters underwent permanent photobleaching before the $g^{(2)}$-measurement could be conducted. Seven of these nanodiamonds could be investigated in the cavity as the others either bleached or the diamond was too large and therefore introduced too much scattering loss. A more or less complete

emitter	λ [nm]	$\delta\lambda$ [nm]	Q_{em}	C_{eff}	$g^{(2)}(0)$
1	758.9	1.4	542	9.1	0.14
2	754.3	2.1	359	6.1	0.22
3	758.0	3.0	253	4.4	0.44
4	758.6	1.3	584	9.9	0.22
5	752.4	1.1	684	11.4	0.54
6	736.9	1.3	567	9.1	0.19

Table 4.4.1.: Overview of considered nanodiamonds. λ: centre wavelength of line. $\delta\lambda$: FWHM of emission spectrum. $Q_{\mathrm{em}} = \lambda/\delta\lambda$. The finesse at λ is used to compute Q_{eff} and C_{eff}. $g^{(2)}(0)$ is obtained from a pulsed measurement. An exception is that the value for emitter 5 is obtained from a cw measurement. [53]

characterisation both in free space and in the cavity could be conducted for six emitters, whose free space spectra are shown in Fig. 4.4.1(c) together with the numbering that will be used from now on. Table 4.4.1 summarises their properties.

4.4.2. Single photon emission

Pulsed $g^{(2)}$-measurements To verify single photon emission, pulsed $g^{(2)}$-measurements are performed. For this, an excitation band at 690 nm is selected with a band-pass filter. The pulse length is 50 ps and the emitters are strongly saturated. The minimum $g^{(2)}$-values are thus to be seen as an upper bound as the background increases linearly with power and therefore contributes more when $P > P_{\mathrm{sat}}$ increases. The electronic pulses from the APDs corresponding to detected photons were sent to a time-to-digital converter (TDC)[20]. It employs cross-correlation histograms to measure the $g^{(2)}$-function [301] and no further post-processing is necessary. Figure 4.4.2(a) shows an example measurement of emitter 1. Due to the repetition rate of 20 MHz, photons can arrive every 50 ns, which is the reason for the distinct spikes, each of which is an exponential function $\exp\left(-\left|\tau-\tau_n\right|/\tau_0\right)$ convoluted with the system response function, where τ_n is the temporal position of the peak and τ_0 the excited state lifetime. To evaluate how much the peak at zero delay is suppressed, each peak was integrated and the background subtracted. The mean height of the non-zero peaks was set to one. The last column of table 4.4.1 summarises $g^{(2)}(0)$ for all considered emitters. It can be seen that the values are below 0.5 and therefore evidence single photon emission. Emitter 5 is an exception, as it underwent photobleaching before pulsed measurements could be taken. Here, the given value is the minimum of the fit to a continuous wave 690 nm $g^{(2)}$-measurement. Although slightly larger than 0.5, the data are consistent with a single quantum emitter when taking into account the background fluorescence during this measurement (about 30%).

[20] qutools quTAU

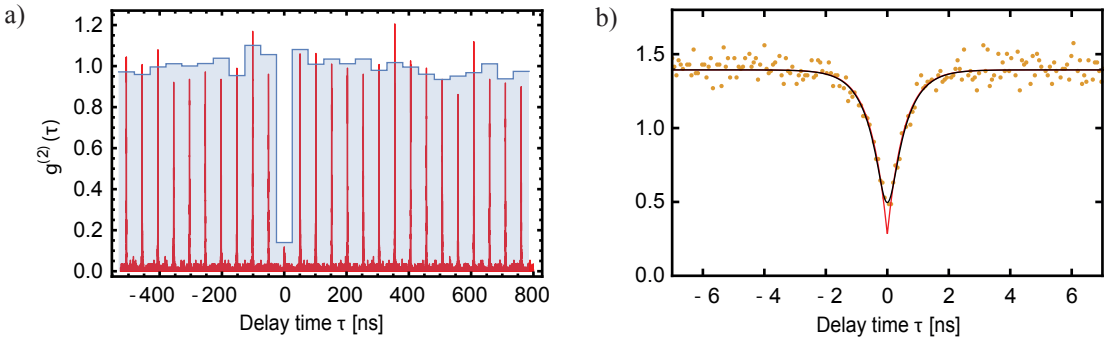

Figure 4.4.2.: (a) Free space $g^{(2)}$-measurement of emitter 1 using pulsed excitation (20 MHz repetition rate, 690 nm wavelength). Red curve: data. Blue histogram: integrated over each peak (background subtracted). (b) Free space $g^{(2)}$-measurement of emitter 1 using cw excitation. Excitation power is $0.17\,P_{\mathrm{sat}}$. Black line: fit with $g^{(2)}$-function convoluted with system response function. Red line: $g^{(2)}$-function without convolution. [53]

Continuous wave $g^{(2)}$-measurements In addition to pulsed measurements, continuous wave (cw) excitation measurements were conducted to obtain further insight into the system's dynamics. As the lifetime is not significantly larger than the response time of the system, the HBT dip gets washed out and a meaningful fit needs to take into account the system response function. It can be approximated by a Gaussian

$$j(\tau) = \frac{1}{\sqrt{2\pi}\sigma} \exp\left(-\frac{\tau^2}{2\sigma^2}\right) \tag{4.4.1}$$

containing contributions of the laser, the APDs and the TDC. The $1/e^2$ width of the timing jitter was deduced to be $\sigma = (170 \pm 20)$ ps, which is explained in more detail in appendix D. For a detailed treatment of timing jitter in $g^{(2)}$-measurements, see [208]. For fitting the $g^{(2)}$-data, the $g^{(2)}$-expression (eq. 4.2.15) is convoluted with the timing jitter (eq. 4.4.1). Fig. 4.4.2(b) shows an example cw measurement of emitter 1, where the black line was obtained by fitting the data with the convolution. The red line is the pure $g^{(2)}$-function with the resulting fit parameters. It was observed that the dip at zero delay was typically more pronounced for pulsed measurements. The likely reason is that the background can be well subtracted in that case, whereas it contributed up to 30% in the cw case as was found by fitting.

A detailed discussion of the rate dynamics deduced from $g^{(2)}$-measurements is postponed to section 4.5.4, where a comparison with a cavity measurement is presented.

Exotic results While most emitters showed moderate bunching with $a < 2$, extreme bunching with $a = 12 - 28$ was observed for emitter 2 as shown in Fig. 4.4.3 for different excitation powers. It seems the system is trapped in the shelving state for a considerable amount of time. Surprisingly, this emitter does not seem to be significantly darker than comparable narrow line emitters and shows clear anti-bunching below 0.5.

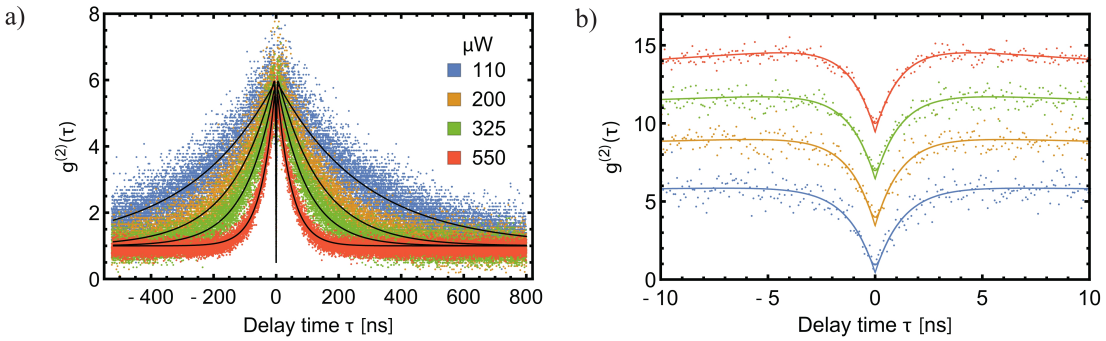

Figure 4.4.3.: (a) $g^{(2)}$-measurement for emitter 2 at different excitation powers showing pronounced bunching. Black lines: Fit. (b) Close-up. Solid lines show fit with convoluted $g^{(2)}$-function and raw function. Shifted upwards by 3, 6, and 9 for clarity.

Another exotic feature, which was observed for a few emitters, is bi-exponential bunching, meaning that an additional bunching time constant on the order of hundreds of ns was necessary to reliably fit the $g^{(2)}$-data. An additional long-lived trapping state could be present in these emitters.

4.4.3. Lifetime

The lifetime was measured under pulsed excitation at 690 nm employing start-stop measurements with the TDC, where trigger pulses from the supercontinuum source were taken as start and the APD pulses as stop signal. An exemplary trace is shown in Fig. 4.4.4(a). The blue data corresponds to emitter 6 and the yellow data to a broad ensemble line. The system response function was measured to have a $1/e^2$-width of $\sigma = 157\,\mathrm{ns}$. It is convoluted with an exponential decay multiplied to a step function as a fit function to reproduce the lifetime data. The lifetime of the uncorrelated background fluorescence could not be resolved and is therefore neglected. The example already shows that the lifetime of the narrow line emitter is significantly shorter than the one of the ensemble. This trend is confirmed when looking at Fig. 4.4.4(b), where all free space lifetime measurements are summarised. While the ensemble lifetime is typically around 1 ns, the narrow line emitters predominantly feature a significantly lower lifetime with a wide spread and no apparent correlation with the central wavelength. The values range from 180 ps (so hardly resolved) to 2.5 ns. For some emitters, two exponential functions had to be fitted to the data, which was especially necessary for emitters with significant background (fast decay) or contributions of the ensemble line (slow decay).

4.4.4. Brightness

To deduce the photon emission rate, saturation measurements were conducted, where the count rate was measured as a function of excitation power. The resulting traces were fitted with eq. 4.2.4 plus a linearly power-dependent background. Exemplary traces are given in section 4.5.2, where the photon emission rate in free space and in the cavity

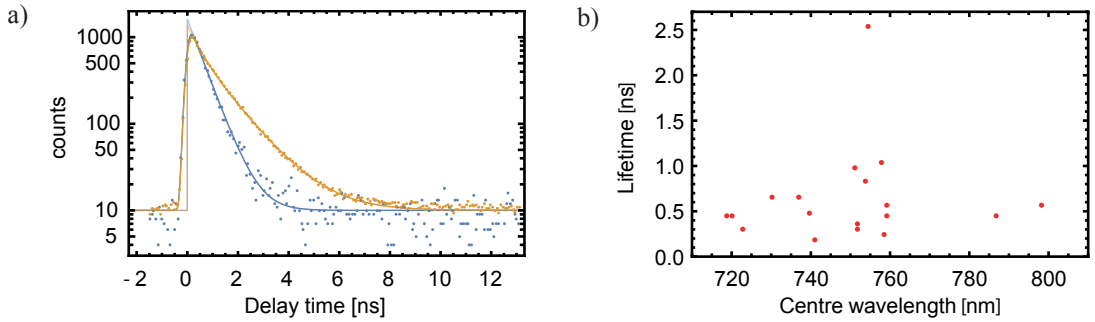

Figure 4.4.4.: (a) Free space lifetime measurement of emitter 6 (blue) compared to lifetime of broad ensemble (yellow). Solid lines: Fit with exponential function (faint lines) convoluted with system response function. Evaluated lifetime is 0.65 ns for narrow line and 0.93 ns for ensemble line. (b) Overview of all free-space lifetime measurements showing no apparent correlation of centre wavelength and lifetime.

is compared. Figure 4.4.5 shows an overview of all free space saturation measurements on single emitters. The detected saturation count rate is plotted with respect to (a) centre wavelength, (b) saturation power, and (c) lifetime. Several emitters (blue dots) did not show saturation. For them, the highest measured power is given. No clear correlations are visible and, most strikingly, there does not seem to be a convincing correlation between saturation count rate and lifetime, which indicates that the non-radiative decay channel is not equally pronounced for the different emitters. Especially emitter 2 is an outlier with its long lifetime of 2.54 ± 0.24 ns and large saturation count rate of 2.62 ± 0.34 Mcps. Note that a two-level emitter without non-radiative decay or shelving and an excited state lifetime of 1 ns, would have a photon emission rate of 1 GHz in saturation as $I^{\infty} = k_{21} = 1/\tau_0$ (see eq. 4.2.5). So clearly, the quantum efficiency is very low for the investigated emitters.

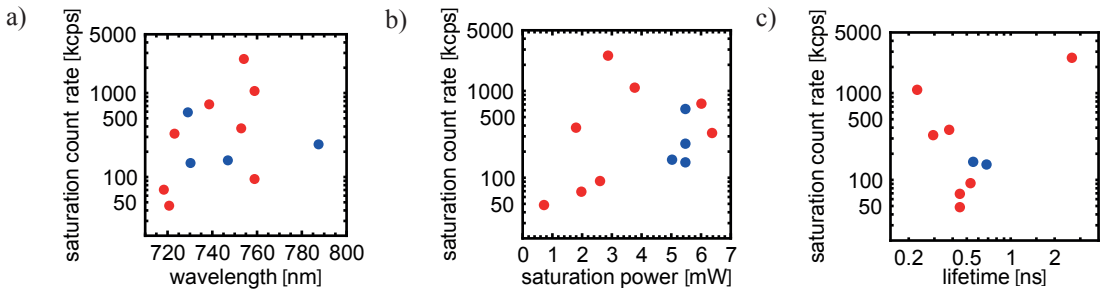

Figure 4.4.5.: Free space saturation count rate (red) for single emitter (logarithmic) with respect to (a) centre wavelength, (b) saturation power, and (c) lifetime (logarithmic). Blue: Emitters which did not show saturation. Count rate at largest excitation power is given.

When comparing brightness, the interesting figure of merit is the photon emission rate, which is the count rate divided by the collection and detection efficiency. The free

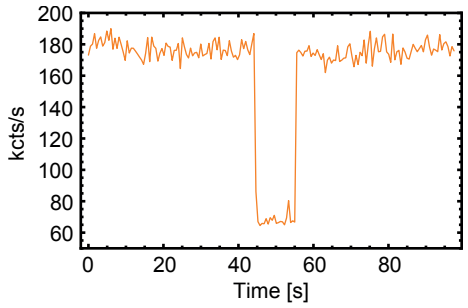

Figure 4.4.6.: Fluorescence time trace (count rate on detector) of a single emitter featuring blinking. [53]

space photon emission rate into 4π is given by

$$I_{\mathrm{fs}}^{\infty} = \frac{I_{\mathrm{m,fs}}^{\infty}}{\eta_{\mathrm{det}}\,\eta_{\mathrm{trans}}\,\eta_{\mathrm{coll}}\,\eta_{\mathrm{obj}}}, \tag{4.4.2}$$

where $I_{\mathrm{m,fs}}^{\infty}$ is the measured count rate, $\eta_{\mathrm{det}} = 70\%$ the detection efficiency, η_{trans} the transmission efficiency through the optics (including filters) from the first lens to the detector, η_{coll} the objective collection efficiency, and η_{obj} the transmission efficiency through the objective. η_{trans} was measured to be 64%. The manufacturer specification for the objective transmission for the fluorescence wavelength is $\eta_{\mathrm{obj}} = 80\%$. To obtain the objective collection efficiency, eq. 3.4.22 for the dipole radiation on a mirror needs to be integrated over the opening angle of the objective:

$$\eta_{\mathrm{coll}}(\theta) = \int_0^{\arcsin \mathrm{NA}} \int_0^{2\pi} P_{\mathrm{em}}(\alpha, \theta, \phi) \sin\alpha \,\mathrm{d}\phi \,\mathrm{d}\alpha \tag{4.4.3}$$

For a dipole oriented parallel to the mirror surface, one obtains $\eta_{\mathrm{coll}}(\pi/2) = 45\%$, for the perpendicular orientation $\eta_{\mathrm{coll}}(0) = 8\%$ for NA = 0.55. As very bright emitters are chosen for the cavity experiment, there is a bias towards those with optimal, i.e. parallel, dipole orientation. Therefore, $\eta_{\mathrm{coll}}(\pi/2)$ is used as a good estimate for the collection efficiency. This value carries an additional uncertainty, as one does not know the exact position of the dipole within the crystal. Again, one assumes that the diamonds in which the dipole resides close to the field maximum were preselected, as these diamonds will appear brighter. So the total collection and detection efficiency amounts to a maximum of 16.1%, meaning that the photon emission rate is up to a factor of 6.2 larger than the count rate.

4.4.5. Photostability

As previously observed [233, 295], the used sample contains a small fraction of photostable emitters, as well as emitters which feature blinking (see, e.g., Fig. 4.4.6) on different timescales (ranging from less than seconds to hours) and permanent photobleaching. The latter can occur after illumination times ranging from seconds to several

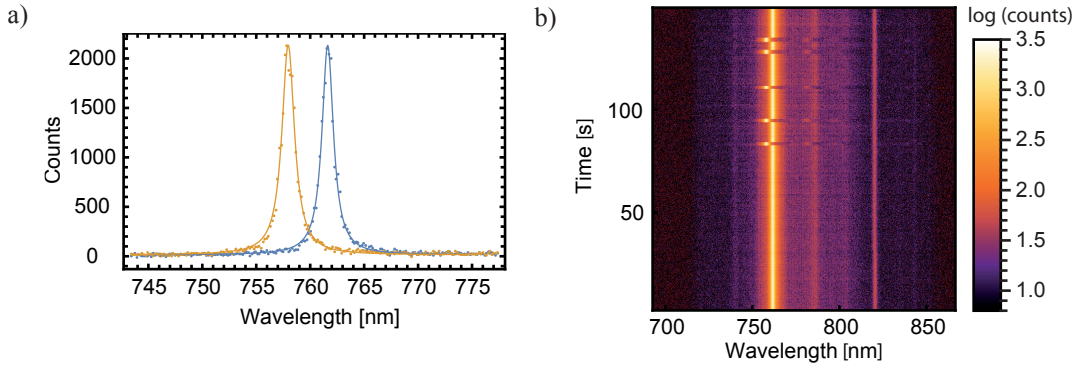

Figure 4.4.7.: (a) Free space spectra of emitter 4 (blue) and spectra of additional state it jumps to at high powers (yellow). (b) Logarithmic plot of spectra over time showing jumping line. Excitation power: 1 mW.

weeks and is more probable for higher excitation powers. This fact has prevented me from obtaining complete data sets for all emitters. New samples [285], however, promise better emitter photostability. Lindner et al. [295] attribute the observation of blinking to temporal ionisation resulting in an optically inactive charge state or in emission outside the detection window. They also find that narrow line, detuned emitters are far more likely to exhibit blinking as compared to broad line emitters. Blinking is thought to be the consequence of local crystal disorder, for example caused by a partially sp^2-hybridised carbon lattice, which is typical close to the surface, lattice dislocations or impurities [302]. Surface passivation in an oxygen atmosphere was shown to reduce the amount of sp^2-hybridised carbon [303, 304] and could therefore lead to better photostability.

It can even happen that the count rate does not go down to zero for a blinking emitter, but rather that it jumps between states of different brightness, which was also observed by Lindner et al. [295]. An especially peculiar behaviour was found for emitter 4: When excited at high powers, its line jumped between two spectral positions (see Fig. 4.4.7(a)) on a timescale of seconds. The position at larger wavelength is stably occupied for small powers and the fraction of time the system resides in the smaller wavelength position increases with increasing excitation power together with the frequency of such spectral jumps. The two states exhibit a slightly different brightness, but the most striking difference is that the bunching time constant a reaches values above eight for the smaller wavelength position as compared to values below two for the larger wavelength position. So the dynamics of the system drastically changes. As can be seen in the logarithmic spectra over time in Fig. 4.4.7(b), the phonon side band also jumps back and forth. An exception is the line at 820 nm, which stays constant. Neu et al. [278] report on a line at 822.7 nm, which they attribute to an additional electronic transition. The theoretical treatment by Gali and Maze [274] explains this line, which is mostly present in strained nanodiamonds, by a lattice distortion making a radiative de-shelving transition weakly allowed. While Siyushev et al. [298] and Tran et al. [299] also observe spectral jumps

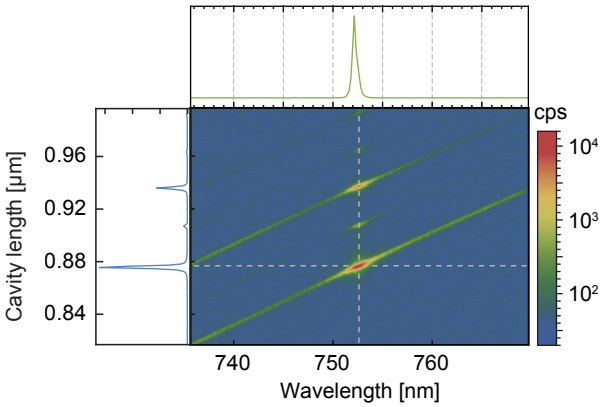

Figure 4.5.1.: Cavity fluorescence spectra of emitter 5 for different geometric cavity lengths (air gap). Logarithmic colour scale. Top panel: Linear-scale spectrum for $d = 0.875\,\text{nm}$, where maximal enhancement occurs. Left panel: Linear-scale plot of count rate for different lengths at the emission wavelength $\lambda = 752.4\,\text{nm}$. [53]

at increased powers for far detuned narrow line emitters, the side band was not studied. It remains unclear whether the constant line at 820 nm stems from another emitter or if it is just not affected by the mechanism causing the jumps.

4.5. Coupling single SiV centres to a microcavity

To achieve resonant coupling conditions with the SiV emission, one step-wise tunes the cavity length to shift a cavity resonance across the emission spectrum and record the fluorescence spectra on the spectrometer. On resonance, one observes enhanced emission into a single cavity resonance. Figure 4.5.1 shows fluorescence spectra for varying mirror separation for the 5th longitudinal mode order in a logarithmic colour scale to make the high signal-to-background level visible. Emission away from the cavity resonance is suppressed, and one detects only dark counts (in blue) mainly from the spectrometer CCD camera, indicating the high spectral purity of the single photon emission. The cavity resonance appears to be broadened due to the finite spectrometer resolution and some length jitter within the acquisition time of 1 s. The actual FWHM linewidth is 43 pm, or $\kappa = 21\,\text{GHz}$, as inferred from the quality factor. In addition to the fundamental mode, one can see the prominent second-order transverse mode, and in between the odd first-order mode, which couples weakly to the emitter. I shall now discuss the modified emission properties in the cavity closely following [53] (in parts identical).

4.5.1. Lifetime reduction

The Purcell enhancement of the spontaneous emission leads to a reduction of the excited-state lifetime. To quantify this effect, lifetime measurements were performed for the same emitters both in free space and in the cavity. In the latter case, the cavity is stabilised on

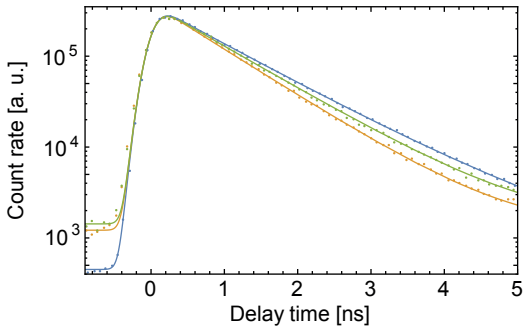

Figure 4.5.2.: Lifetime measurement for emitter 3. Data points (normalised to free space data for better comparison) and fit (the solid line) with an exponential function starting at $t = 0$ convoluted with the system response function. Blue: free space. Yellow: cavity, $q = 5$. Green: cavity, $q = 6$. [53]

resonance with the shear piezo stack the fibre is mounted to by maximising the count rate with a software algorithm. The polarisation of the excitation light is, in all cases, chosen to maximise the count rate, which implies matching it to the projection of the dipole orientation in the plane of the mirror. A lifetime reduction is observed in the cavity and the effect is larger for smaller mirror separation, i.e., smaller mode volume, which is visible in the exemplary lifetime traces in Fig. 4.5.2, where the situation in the cavity for the shortest (yellow) and next-shortest (green) accessible cavity length is compared to free space (blue). Table 4.5.1 summarises the lifetime measurements taken for three different emitters and shows that lifetime reductions $\Delta\tau/\tau_0$ between 17% and 31% can be observed. The values arise from applying different fitting methods to the data and

emitter	τ_0 [ns]	τ_c [ns]	$\tau_{c,2}$ [ns]	τ_0/τ_c
1	0.58 ± 0.02	0.46 ± 0.02	0.51 ± 0.02	1.28 ± 0.01
2	2.54 ± 0.24	1.75 ± 0.04	1.97 ± 0.10	1.45 ± 0.14
3	1.03 ± 0.01	0.85 ± 0.01	0.92 ± 0.01	1.21 ± 0.01

Table 4.5.1.: Measured lifetimes in free space (τ_0) and in the cavity (τ_c, lowest reachable order, $\tau_{c,2}$, following order). The error is obtained from different fitting methods. [53]

averaging them, where the half-min-max deviation is given as a conservative error of the fit. First, the whole trace is fitted, i.e. an exponential-decay function starting at delay time zero and including a constant background, convoluted with the system response function. For some emitters, a second exponential function has to be included to account for a fast-decaying background. This step is mostly necessary for the free-space time trace. Next, only the decay is fitted, to avoid systematic errors due to the positioning of the zero time delay. Last, only the section of exponential decay is fitted. The ratio of the lifetime in free space, τ_0, and in the cavity, τ_c, depends on the Purcell factor and the quantum efficiency as $\tau_0/\tau_c = C\,\mathrm{QE} + 1$ (see section 2.2.2.2). For an unknown $\mathrm{QE} < 1$,

it is therefore not possible to infer C directly from the lifetime reduction.

4.5.2. Enhanced spontaneous emission

Saturation measurements To quantify the cavity enhancement of the emission and to obtain an estimate for the achieved Purcell factor, the photon emission rate in free space is compared to the one in the cavity under saturation conditions. For this, saturation measurements were conducted on the same emitters in free space and in the cavity, where again the polarisation was optimised for maximal emission. In the cavity, the measurement took place at the shortest reachable axial mode order $q = 5$ and a software locking algorithm kept the length at the position of maximal count rate. The measured rate $I_m(P)$ was fit with the saturation function plus a linear background contribution $a_{\mathrm{bg}}P$:

$$I_m(P) = \frac{PI_m^\infty}{P + P_{\mathrm{sat}}} + a_{\mathrm{bg}}P \tag{4.5.1}$$

For emitter 4, one finds $a_{\mathrm{bg}} = 62\,(40) \times 10^3$ counts/(s mW) in free space (in the cavity). The background is dominated by broadband fluorescence from the crystal and greatly varies between crystals. In the cavity, the background is suppressed. The obtained values for I_m^∞ are given in table 4.5.2, where the errors are from the uncertainty of the fit. One observes saturation count rates at the detector of up to $I_{m,c}^\infty = 1.78 \times 10^6$ cps, corresponding to a peak spectral density of $2\,I_{m,c}^\infty/(\pi\kappa) = 54 \times 10^3$ counts/(s GHz). The spectral density is more than 20-fold larger than in earlier room-temperature experiments [46, 47, 50, 230, 305].

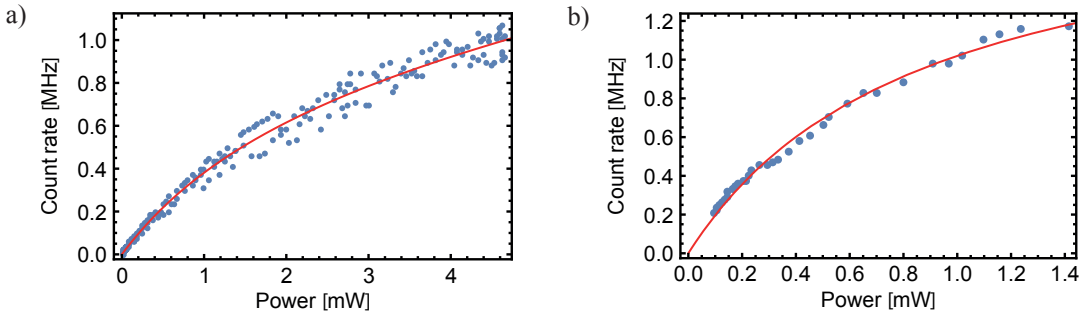

Figure 4.5.3.: Free space (a) and cavity (b) saturation measurement of emitter 4 showing the actually detected count rate. Blue: data. Red: fit. [53]

Calculation of photon emission rate from count rate To obtain the photon emission rates (the emission rate into a solid angle of 4π in free space, I_{fs}^∞, and into the cavity mode, I_c^∞) from measured count rates, one has to account for the collection and detection efficiency in both cases. The free space case is treated in section 4.4.4. In the cavity case, the photon emission rate can be calculated from the count rate as

$$I_c^\infty = \frac{I_{m,c}^\infty}{\eta_{\mathrm{det}}\,\eta_{\mathrm{trans}}\,\eta_c\,\eta_{\mathrm{fibre}}\,\epsilon}, \tag{4.5.2}$$

emitter	$I^{\infty}_{m,\mathrm{fs}}$	$I^{\infty}_{m,\mathrm{c}}$	I^{∞}_{fs}	I^{∞}_{c}	C_{th}	C_{exp}
1	0.092 ± 0.007	0.106 ± 0.009	0.57	2.64	9.1	4.6 ± 0.5
2	2.62 ± 0.34	1.21 ± 0.33	16.3	28.6	6.1	1.8 ± 0.5
4	1.07 ± 0.40	1.78 ± 0.13	6.6	25.3	9.9	3.8 ± 1.4
5	0.38 ± 0.04	1.65 ± 0.90	2.35	21.6	11.4	9.2 ± 5.1

Table 4.5.2.: Results of saturation measurements. $I^{\infty}_{m,\mathrm{fs}}$ ($I^{\infty}_{m,c}$): saturation count rate in free space (cavity). I^{∞}_{fs} (I^{∞}_{c}): photon emission rate in free space (cavity) calculated from count rates. All rates are in MHz. C_{th}: maximal theoretical Purcell factor. $C_{\mathrm{exp}} = I^{\infty}_{c}/I^{\infty}_{\mathrm{fs}}$. [53]

where $\eta_{\mathrm{det}} = 70\%$ is the detection efficiency, $\eta_{\mathrm{trans}} = 64\%$ the transmission through the optics including filters (as the optical path is the same in free space and for the cavity), η_c the cavity outcoupling efficiency, $\eta_{\mathrm{fibre}} = 96\%$ an additional factor accounting for the 4% lost at the glass-air interface at the outcoupling port of the fibre, and ϵ the mode matching. η_c is given by the transmission through the fibre mirror, which is the collection channel, divided by all losses:

$$\eta_c = \frac{T_f}{T_f + T_p + A + B} \tag{4.5.3}$$

T_f (T_p) is the transmittivity of the fibre (planar) mirror, A the absorption of both mirrors, and B the scattering and absorption loss introduced by the nanodiamond (see section 3.5). B can be calculated from the transmission normalised to the empty cavity transmission, T/T_0, via eq. 3.5.10. To obtain T/T_0, which is given for the considered emitters in table 4.5.3, the cavity transmission is measured and normalised to the transmission of the empty cavity. The values for η_c vary between 21% and 38% for the investigated emitters, limited by B. With an improved sample, this loss channel can be avoided. The mode matching evaluated according to eq. 2.1.41 amounts to $\epsilon = 46.6\%$. Note that this value is an upper boundary, as a slight misalignment of the fibre profile with respect to the fibre core can already significantly reduce the mode matching. Therefore, using ϵ for calculating the photon emission rate yields a conservative estimate. This factor could be avoided by collecting through the planar mirror, provided a suitable choice of mirror coatings is available. Because of the large uncertainties of some factors contributing to the photon emission rate, the resulting rates and Purcell factors are an estimate. In free space, one can infer a rate I^{∞}_{fs} of up to 16 MHz for emitter 2, while in the cavity, one finds a rate I^{∞}_{c} of more than 28 MHz.

Purcell enhancement The photon emission rates given include only the emission into the cavity mode, i.e. $I^{\infty}_{\mathrm{c}} = \beta I^{\infty}_{\mathrm{tot}}$, where $I^{\infty}_{\mathrm{tot}}$ would be the total rate into 4π. As $I^{\infty}_{\mathrm{tot}} = (C+1)\, I^{\infty}_{\mathrm{fs}}$, the ratio of the cavity and free-space emission rate yields C only:

$$I^{\infty}_{c} = \beta I^{\infty}_{\mathrm{tot}} = \beta\,(C+1)\, I^{\infty}_{\mathrm{fs}} = C I^{\infty}_{\mathrm{fs}} \tag{4.5.4}$$

emitter	T/T_0	η_c	C_{exp}	β	$\beta\eta_c$
1	0.25	0.21	4.2 ± 0.5	0.81	0.17
2	0.23	0.21	1.8 ± 0.5	0.64	0.13
5	0.45	0.35	3.8 ± 1.4	0.79	0.28
6	0.50	0.38	9.2 ± 5.1	0.90	0.34

Table 4.5.3.: T/T_0: transmission normalised to empty cavity transmission. η_c: outcoupling. C_{exp}: experimental Purcell factor. $\beta = C/(C+1)$: fraction of total emission into the cavity mode. $\beta\eta_c$: fraction of emission coupled out of the cavity.

In free space, the emission rate is given by $I_{\mathrm{fs}}^{\infty} = \gamma_r \rho_2^{\infty}$,were ρ_2^{∞} is the equilibrium population of the excited state. The emission rate into the cavity mode is $I_c^{\infty} = C\gamma_r\rho_2^{\infty}$, and the ration between the rates directly yields the Purcell factor, $C_{\mathrm{exp}} = I_c^{\infty}/I_{\mathrm{fs}}^{\infty}$, independent of the quantum efficiency.

The obtained Purcell factors are given in table 4.5.2. The stated errors stem from the uncertainties of the fit of the saturation curves, and they do not include further uncertainties. The largest value of $C_{\mathrm{exp}} = 9.2$ was obtained for emitter 5. One can also infer the enhancement of the spectral density compared to free-space emission, $C_{\mathrm{exp}}Q_c/Q_{\mathrm{em}}$, yielding a value of 237 for emitter 5.

Table 4.5.3 gives the efficiency $\beta = C/(C+1)$, which is the fraction of the total emission into the cavity mode. One obtains values up to 90%. The fraction of the light actually coupled out of the cavity, $\beta\eta_c$, is given in the last column. Note that this value could be significantly improved by choosing a sample with less extinction, i.e. smaller crystal size and better crystal quality.

Theoretical Purcell factor calculation One can compare C_{exp} to the expected maximal Purcell factor C_{th} as calculated from Q_c, Q_{em}, and V_m for the respective emitters:

$$C = \frac{3}{4\pi^2}\left(\frac{\lambda}{n}\right)^3 \frac{Q_{\mathrm{eff}}}{V_m}\zeta\left|\frac{\mathbf{d}\cdot\mathbf{E}}{dE_0}\right|^2 \tag{4.5.5}$$

$\zeta = 80\%$ is the branching ratio into the ZPL, and an ideal dipole orientation is assumed, i.e. $|\mathbf{d}\cdot\mathbf{E}/(dE_0)|^2 = 1$. The mode volume V_m is calculated using the effective cavity length and the optimised mode waist. Q_c is adjusted individually for all emitters as the additional extinction loss B alters the finesse on the emitter as compared to the bare cavity. This factor is, however, not very critical, as $Q_c \gg Q_{\mathrm{em}}$ still holds. The most important quantity is $Q_{\mathrm{em}} = \lambda/\delta\lambda$ and is obtained from the measured linewidth $\delta\lambda$. The resulting effective Purcell factors, as given in table 4.5.2, set an upper limit for the achievable experimental values for the case the dipole is oriented parallel to the mirror surface and resides in the maximum of the electric field. In reality, this does not have to be the case, and the effects on the Purcell factor shall now be discussed.

The planar mirror with a central wavelength of 780 nm is capped with a spacer layer of SiO_2, such that the field maximum for 780 nm lies 30 nm above the surface. Using the

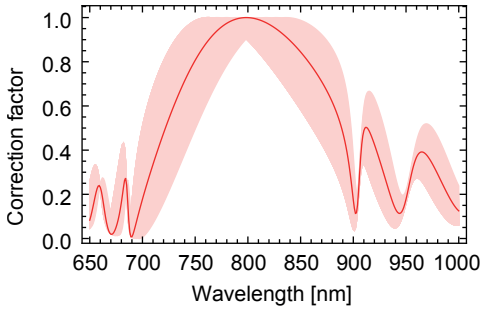

Figure 4.5.4.: Correction factor for the Purcell factor attributable to the emitter's position relative to the electric field maximum. The red line represents the colour centre residing in the middle of a 100 nm large diamond. The shaded area indicates the uncertainty of the correction factor resulting from the unknown position of the emitter. [53]

complex reflectivity r of the planar mirror, $|1+r|^2$ gives the field intensity normalised to the value without a mirror. Dividing this field intensity by the intensity maximum, one obtains a correction factor $|E/E_0|^2$ for the Purcell factor, which is plotted for different wavelengths in Fig. 4.5.4. The red line is computed assuming that the colour centre resides in the middle of a 100 nm large diamond. The shaded area gives the uncertainty of the correction factor due to the unknown position of the emitter. As an example, at a wavelength of 754 nm, the correction factor can range from 56% to almost 100%. Thus, an unfortunate position of the colour centre within the crystal can decrease the Purcell factor to half of its ideal value.

The second unknown quantity is the orientation of the dipole moment. Maximising the count rate means aligning the polarisation of the electric field with the in-plane component of the dipole moment. Therefore, only the out-of-plane component remains unknown, which can be characterised by an angle $\phi = \angle(\mathbf{d}, \mathbf{E})$. Considering eq. 4.5.5, one finds that $C \propto \sin^2\phi$. Therefore, the Purcell factor goes down to zero for $\mathbf{d} \perp \mathbf{E}$. However, as the excitation likewise goes down, emitters with an unfavourable orientation of $\mathbf{d}$ are not bright and are not likely to be preselected.

The ideal value for the Purcell factor is almost reached for emitter 5, but the experimental results stay well below the ideal enhancement for the other three emitters, which is explained by the above factors.

4.5.3. Quantum efficiency

From C_{exp} and the lifetime change τ_0/τ_c, one can coarsely estimate the quantum efficiency for emitter 1 and emitter 2, finding QE $\approx$ 7% and 25%, respectively. The former is comparable to previously published values [50, 233], the latter appears inconsistently high (see also the next paragraph). A low QE can also explain the low emission rate of emitter 1 despite its short lifetime. Notably, the Purcell effect leads to an increased QE (see eq. 2.2.44), such that, e.g. for emitter 1, the QE increases from 7% to 30% in the cavity. The overall device efficiency, which states the probability of obtaining a photon

in the fibre after excitation of the emitter (see section 4.1.2), is given by $\eta = \mathrm{QE}_c\,\beta\,\eta_c\,\epsilon$, yielding $\eta = \mathrm{QE}_c \times 16\%$ for emitter 5.

4.5.4. $g^{(2)}$-measurements and rate model

According to the discussion in section 4.2.2, the internal rate dynamics of the system can be investigated by measuring $g^{(2)}$-functions at different excitation powers. These measurements are conducted in free space and in the cavity for comparison. Figure 4.5.5 shows the free space $g^{(2)}$-measurement of emitter 1. One can see that the bunching increases for increasing powers at a decreased time constant, while the anti-bunching also decreases. To quantify this behaviour the traces are fitted as explained in section 4.4.2. The background parameter was kept constant at $p = 85\%$, which yielded the most accurate fit. The resulting fit parameters τ_1, τ_2, and a are given in Fig. 4.5.6(c) as functions of excitation power. As can be seen, the anti-bunching time constant τ_1 is smaller in the cavity, as expected. Note that $\tau_1\,(0)$ is equivalent to the spontaneous emission lifetime of the system being measured. One can observe a strong power dependence of the bunching time constant τ_2 [233], which is equally large in the cavity and in free space.

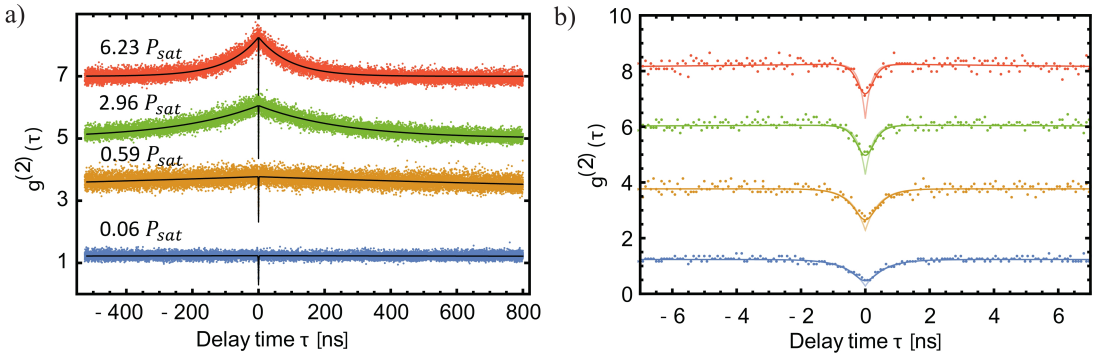

Figure 4.5.5.: (a) Free space $g^{(2)}$-measurement of emitter 1 for selected excitation powers. Black lines: fit. [53] (b) Close-up of (a). Solid lines: fit with $g^{(2)}$-function convoluted with system response function. Faint lines: $g^{(2)}$-function without convolution.

To analyse this data, the model introduced by Neu et al. [233] was applied to the data (see section 4.2.2). In contrast to the approach in this reference, a global fit (equations 4.2.10 and 4.2.13) of the six data sets was conducted ($\tau_{1,2}$ and a, each in the cavity and in free space) using all together 11 fit parameters – six fit parameters for cavity and free space, respectively: c, σ, τ_1^0, τ_2^0, τ_2^∞, and a^∞, where τ_2^0 is the same in both cases. The result is shown as dashed lines. The power dependence is well matched for τ_1 and a, but clearly, the model fails to fit τ_2.

To account for this, a modified rate model is introduced. According to the experimental observations, $\tau_2^\infty = 1/\left(k_{23}^\infty + k_{31}^\infty\right) = 0$, implying that rate k_{23} or k_{31} goes to infinity for large powers (see table 4.2.1). For $a^\infty = k_{23}^\infty / k_{31}^\infty$ to yield a finite value in agreement with the experimental findings, both rates must similarly depend on P. These

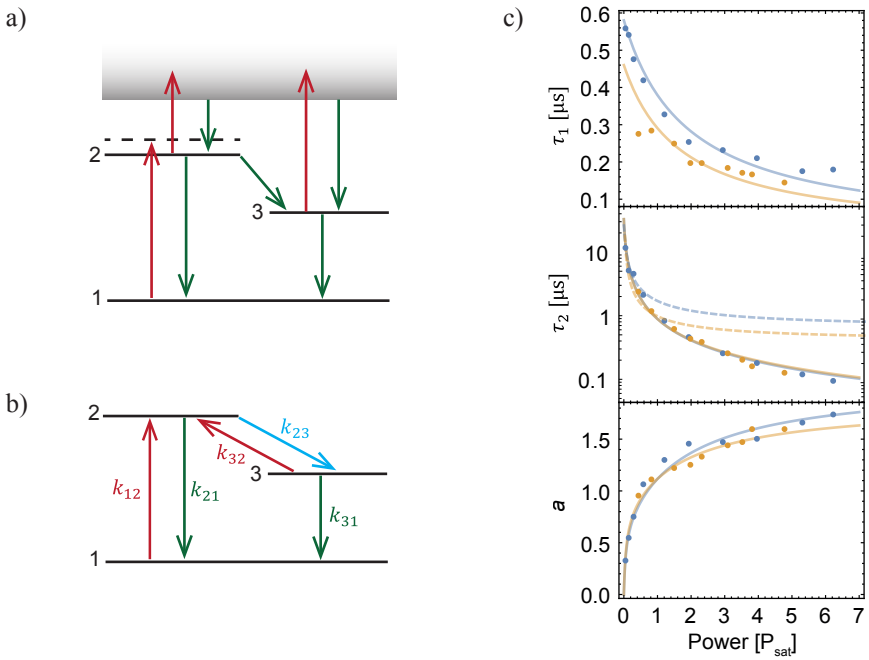

Figure 4.5.6.: (a) Proposed level scheme. Green arrows represent constant rates. Red arrows indicate linearly power dependent rates. (b) Equivalent three-level system. The Blue arrow shows a rate with a linear and constant term. (c) Fit parameters as a function of power and fit with power-dependent de-shelving model (the solid lines). Dashed lines: fit with model from [233]. [53]

requirements are fulfilled by the proposed level scheme shown in Fig. 4.5.6(a). It is assumed that both the excited state and the shelving state can be depopulated by further excitation to some higher-lying state or the valance band. An ionisation process could explain these dynamics. The excitation rates are assumed to be linearly dependent on power, like the excitation rate. All relaxation rates are constant. The cavity is resonant with transition $2 \rightarrow 1$. For easier mathematical treatment, an equivalent level scheme is presented in Fig. 4.5.6(b) leading to the same dynamics. Here, the green arrows indicate constant rates, the red arrows rates that are linearly dependent on power, and the blue rate k_{32} has both a linear and a constant term:

$$k_{12} = \sigma P \tag{4.5.6}$$
$$k_{32} = dP \tag{4.5.7}$$
$$k_{23} = eP + k_{23}^0 \tag{4.5.8}$$

σ, d, and e are proportionality constants. As we are still dealing with a three-level system, the $g^{(2)}$-function stays the same, where the constant rates can again be expressed by values for the parameters at zero power:

$$k_{21} = 1/\tau_1^0 - k_{23}^0 \equiv \gamma_\mathrm{r} + \gamma_\mathrm{nr} \tag{4.5.9}$$
$$k_{31} = 1/\tau_2^0 \tag{4.5.10}$$

In the limit of large powers, both time constants converge to zero. The bunching parameter a is zero for zero power and reaches a finite value a^∞ for large powers. One can use it for fitting instead of the proportionality constant e, as the starting value is easier to choose:

$$e = \frac{-a^\infty d^2 + a^\infty d\sigma}{a^\infty d + \sigma}. \tag{4.5.11}$$

One can now conduct a global fit of the data (solid lines in Fig. 4.5.6(c)) using eight free parameters altogether (d, d_c, σ, σ_c, a^∞, a_c^∞, τ_2^0, and k_{23}^0), as τ_2^0 and k_{23}^0 are the same in both cases. Clearly, the revised model fits the data well.

From the fit parameters, one can calculate the equilibrium population of the excited state, ρ_2^∞, and, finally, the total de-excitation rate Γ:

$$\rho_2 = \frac{k_{12}\,(k_{31} + k_{32})}{k_{23}k_{31} + k_{21}\,(k_{31} + k_{32}) + k_{12}\,(k_{23} + k_{31} + k_{32})} \tag{4.5.12}$$

$$\rho_2^\infty = \lim_{P\to\infty} \rho_2 = \frac{1}{1 + e/d} \tag{4.5.13}$$

$$\Gamma = \rho_2^\infty k_{21} \tag{4.5.14}$$

One obtains $\rho_2^\infty = 34\%$ for emitter 1. In free space (in the cavity), one gets $k_{21} = 1.7\,\mathrm{GHz}$ (2.2 GHz) and $\Gamma = 578\,\mathrm{MHz}$ (750 MHz), comparable to the values found by Neu et al. [233]. Γ includes non-radiative relaxation, such that it should be possible to extract the QE by a comparison with the measured photon emission rate I_{fs}^∞. This procedure yields a value for the QE of 0.1% to 0.5%, depending on the orientation of the dipole, significantly less than the 7% estimated from the experimental Purcell factor and the lifetime change. The origin of this discrepancy remains unclear. The emitter might show different levels of blinking at intermediate time scales or might have jumped into another state with a different emission rate between the measurements (see section 4.4.5). The short τ_2 at high power indicates the possibility of high repetition rates for pulsed excitation.

4.5.5. Potential of this approach

The presented experiments show significant Purcell enhancement of the single photon emission of SiV centres, achieving high efficiency ($\beta = 90\%$), a high photon rate coupled into a single-mode fibre (4.1 MHz), and a narrow linewidth (21 GHz) at room temperature. Several emitters show excited-state lifetimes below 1 ns and bunching time constants that decay quickly with excitation power, such that pulsed excitation at gigahertz rates is possible. The reported experiments are limited by properties of the sample, such as excessive scattering and absorption loss, photobleaching of the emitters after excitation times ranging from minutes to weeks, and a moderate quantum efficiency.

On the cavity side, a smaller mode volume and higher Q cavities have been fabricated. The following realistic scenario illustrates the high potential of the presented system. A readily produced fibre serves as an example: It has a radius of curvature $r_c = 11.6\,\mu\mathrm{m}$

at a depth of $t = 100\,\mathrm{nm}$. For a minimal cavity length $d = 4\,\lambda/2$, a mode volume of $V_m = 1.4\,\lambda^3$ is reached. These values yield an effective Purcell factor of $C_{\mathrm{eff}} = 38$ for an emitter with 1 nm linewidth. The combination of a fibre mirror with $T_f = 10\,\mathrm{ppm}$ with a planar mirror with $T_p = 1500\,\mathrm{ppm}$ would result in an outcoupling efficiency through the planar mirror of almost one, without further reduction due to mode coupling.

The large scattering and absorption losses reduce the number of useful emitters for investigation. It is therefore crucial to use smaller diamonds. Embedding the nanodiamonds in a layer of polymethyl methacrylate (PMMA, acrylic glass) would reduce the scattering loss due to a reduced refractive index contrast. Nanodiamonds with a diameter of 110 nm would then result in a normalised transmission of $T/T_0 = 80\%$, corresponding to an outcoupling efficiency of $\eta_c = 78\%$ for the mirrors in the experiment. Absorption can be caused by sp^2-hybridized carbon at surfaces, grain boundaries, and lattice defects. A higher crystal quality would thus reduce absorption and background fluorescence. It could be obtained, for example, by annealing of the nanodiamonds under an oxygen atmosphere. The fraction of the emission coupled out of the cavity would then be $\beta\eta_c = 76\%$. For a further reduction of scattering loss, diamond membranes could be applied [173, 306–308], possibly increasing $\beta\eta_c$ to over 95%.

Taking emitter 4 with $I_{\mathrm{fs}}^{\infty} = 6.6\,\mathrm{MHz}$ as an example for a reachable photon emission rate of a currently available sample, $C = 38$ and $\beta\eta_c = 76\%$ would yield an outcoupled photon rate of 190 MHz. For an improved SiV sample with QE = 30% [50], there is the prospect for a device efficiency $\eta = 90\%$ and single photon rates beyond 1 GHz. So far, photostable, bright single-SiV samples with high QE and small linewidth in small, high quality nanodiamonds are not available, but recent achievements on the sample side [285, 289] promise improvement.

4.6. Towards an indistinguishable single photon source

As has been seen in section 4.1.3, indistinguishability is required for many applications of SPS like all-optical quantum computation [309, 310]. Using a high-Q cavity, spectral purity can be improved to a level, where indistinguishable single photons could be produced under ambient conditions, which has been theoretically shown [54]. While a promising approach using a hybrid cavity system (Fabry-Pérot cavity and plasmonic antenna) and the SiV centre has been discussed [311], this section focuses on fibre-based microcavities. After having presented the general idea following Grange et al. [54], the feasibility for an efficient indistinguishable single photon source based on a SiV-microcavity system will be discussed.

4.6.1. Cavity funneling

A way of reaching indistinguishability for solid state emitters with the typical large ratio of $\gamma^\star/\gamma$ is spectral filtering of the emitted light resulting in a very low efficiency. A possibility to increase the indistinguishability $I = \gamma/(\gamma + \gamma^\star)$ without losing much light is strong Purcell enhancement such that $C\gamma \gg \gamma^\star$, which would require very high

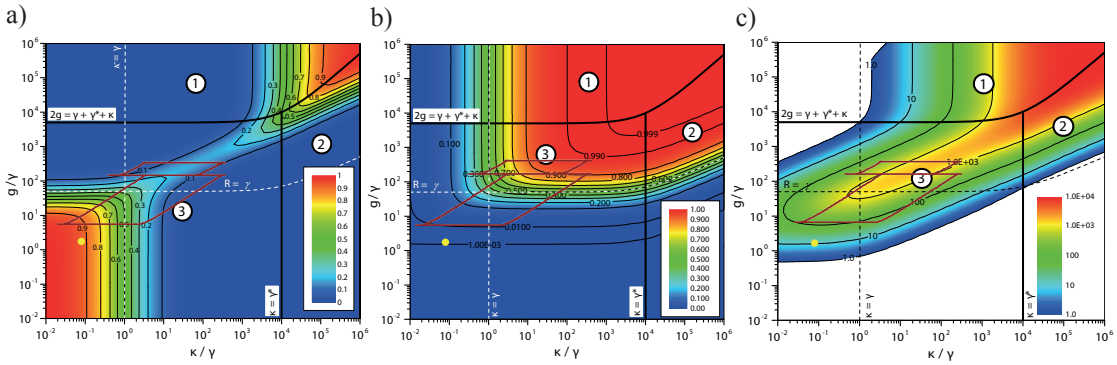

Figure 4.6.1.: Indistinguishability (a), efficiency (b) and funneling ratio $F = \beta I \gamma^\star/\gamma$ (c) as a function of cavity linewidth κ/γ and emitter-cavity coupling strength g/γ for $\gamma^\star/\gamma = 10^4$. Images taken from [54] and modified. The upper (lower) red framed area indicates the reachable parameter range for a microcavity with finesse $\mathcal{F} = 2000$ (200 000) and $r_C = 5$ (150) µm for cavity lengths in the range of $d = \lambda/2$ to $0.7\, r_C$. Yellow dot: parameters for high Q cavity described in sec. 3.3.3 at length of largest Q.

Purcell factors for room temperature solid state emitters as $\gamma^\star \approx 10^4\, \gamma$ in typical systems. Grange et al. [54] computed the indistinguishability for such a cavity-coupled system as a function of linewidth κ/γ and emitter-cavity coupling strength g/γ, shown in Fig. 4.6.1(a). One can see that apart from the region to the top right, which corresponds to large coupling and broad cavities and is difficult to be reached experimentally, there is another parameter range (bottom left) exhibiting good indistinguishability. The regions marked 2 and 3 are governed by incoherent dynamics with the effective transfer rate R (eq. 2.2.31) between emitter and cavity. Region 2 is the weak coupling regime (called 'bad cavity regime' in [54]) where re-absorption of an emitted photon by the emitter is negligible and one can describe the system as an emitter with a modified decay rate $\gamma + R$. In this week coupling regime, the indistinguishability is given by

$$I = \frac{\gamma + R}{\gamma + R + \gamma^\star}, \tag{4.6.1}$$

that is I can be increased by increasing R, which, however, requires $2g \gg \gamma^\star$, which is experimentally very challenging. Region 3 is referred to as the incoherent 'good cavity regime', where photons can be stored in the cavity longer than the emitter dephasing time meaning that the cavity is the effective emitter. The indistinguishability then reads

$$I = \frac{\gamma + R_{\text{eff}}}{\gamma + \kappa + 2R} \tag{4.6.2}$$

with $R_{\text{eff}} = \kappa R/(\kappa + R)$. Large indistinguishability is reached for $\kappa < \gamma$ and $R < \gamma$, which can be experimentally feasible.

Regarding the efficiency (plotted in Fig. 4.6.1(b)), which in this case is the probability to emit into the cavity mode upon excitation, high values are obtained in a different

parameter regime, namely for large g and κ. For the weak coupling regime, one gets

$$\beta = \frac{R_{\text{eff}}}{\gamma_0 + R_{\text{eff}}}, \tag{4.6.3}$$

which yields high values for $R > \gamma$ and $\kappa > R$, but is moderate in the 'good cavity regime'.

However, regarding the product of efficiency and indistinguishability, βI, it is still possible to achieve values larger than by spectral filtering, where the product cannot exceed $\beta_f I_f \leq \gamma/\gamma^\star$. The so-called 'cavity-funneling' factor

$$F = \frac{\gamma^\star}{\gamma}\beta I \tag{4.6.4}$$

compares βI to the best achievable value by spectral filtering – for $F > 1$ there is a spectral cavity-funneling effect, meaning that the broad emission spectrum of the emitter is 'funneled' into the narrow cavity line. The funneling factor does not yet take into account that the cavity mode can typically be collected more efficiently, which further increases the efficiency compared to spectral filtering. The parameter space for which $F > 1$ is shown in colour in Fig. 4.6.1(c). Clearly, even in the good cavity regime, funneling factors over 10^3 can be reached.

4.6.2. Requirements for the cavity system

For the SiV centre, $\gamma^\star/\gamma \approx 10^3 - 10^4$ is a typical value (e.g. $\gamma = 2\pi \times 160\,\text{MHz}$, $T_1 = 1\,\text{ns}$ and $\gamma^\star = 2\pi \times 3.3\,\text{THz}$ for a broad line emitter and $\gamma^\star = 2\pi \times 550\,\text{GHz}$ for a 1 nm narrow line emitter). If one wants to optimise for efficiency, a small radius of curvature and moderate finesse are desirable. The upper of the two red framed regions in Fig. 4.6.1 corresponds to the reachable parameter space for a cavity with $r_C = 5\,\mu\text{m}$ and $\mathcal{F} = 2000$ and cavity lengths from $d = \lambda/2$ to $0.7\,r_C$. It is visible that with such a cavity, efficiencies well larger than 0.9 are feasible. While the indistinguishability stays moderate, funneling factors over 10^3 show supremacy compared to spectral filtering.

Reaching the regime of high indistinguishability requires a high Q cavity, so a large cavity length and thus a large radius of curvature. The lower red framed region corresponds to a finesse of $\mathcal{F} = 200\,000$ and $r_C = 150\,\mu\text{m}$. Note that for large mirror separations, indistinguishabilities close to one can be achieved with funneling factors over 100, while a short cavity length results in a high efficiency > 0.8. This implies that tuning the system between high indistinguishability and high efficiency according to the needs of the current application is possible with one and the same cavity just by changing the mirror separation. As an example, the yellow dot in the plots indicates the parameters of the high Q cavity introduced in section 3.3.3 for the axial mode order $q = 589$ of maximal $Q = 3.2 \times 10^7$. The radius of curvature is 350 µm and the mode waist for this length $w_0 = 6.3\,\mu\text{m}$. This shows that fibre cavities allowing to create a single photon source with near unity indistinguishability at room temperature have already been produced.

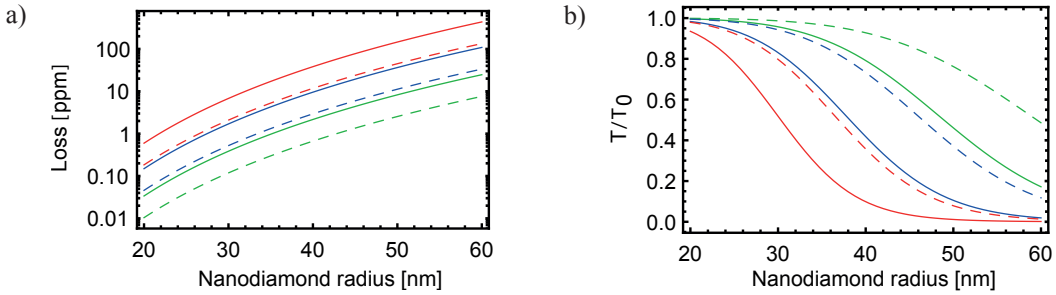

Figure 4.6.2.: (a) Scattering loss as a function of nanodiamond radius for crystals in air (solid line) and embedded into a layer of PMMA (dashed) in a cavity with $w_0 = 6.3\,\mu m$ (green), 3 µm (blue), and 1.5 µm (red). (b) Normalised transmission following for the situation in (a) assuming total cavity losses of 35 ppm.

On the experimental side, the challenge is to stabilise the mirror separation such that the cavity remains on resonance over long timescales. Notably, a quality factor of 3.2×10^7 corresponds to a linewidth of 13 MHz, which is $\delta\lambda$ =23 fm in units of wavelength. This corresponds to a difference of mirror separation of $\delta d = q/2 \cdot \delta\lambda = 6.8\,pm$. Locking such a cavity on resonance should be well feasible: Thomas Hümmer recently demonstrated root mean square (RMS) length jitters down to 100 fm with a monolithic, flexure-bearing-based cavity design [138]. So cavity systems allowing to reach the cavity-funneled high indistinguishability regime are already available, waiting for suitable samples to be tested.

4.6.3. Sample requirements

The general requirements for the SiV centres described in the above sections also apply here: The emitters should show clean single photon emission, be bright, narrow, photostable, and have a high quantum efficiency.

In contrast to an efficient (distinguishable) single photon source with a low Q cavity as was mostly treated in this chapter, the high Q cavity needed for indistinguishability sets much higher requirements for the diamond quality. If working with a nanodiamond sample, the crystal quality should be very good, ideally monocrystalline without much absorption. Assume a mirror transmittivity of 10 ppm per mirror and a total of 15 ppm mirror absorption (so total losses of 35 ppm) yielding a finesse of 180 000 as has been demonstrated for fibre cavities [134]. Any small additional loss would then already decrease the finesse substantially. The scattering loss introduced by a nanodiamond is plotted as a function of radius in Fig. 4.6.2(a) for a particle in air (solid lines) and embedded into a layer of PMMA (dashed lines) for different mode waists (green, blue, red corresponds to $w_0 = 6.3$, 5, 1.5 µm). So the diamond size should stay under a diameter of about 60 nm if one wants to maintain a high finesse even for small mode waists. Figure 4.6.2(b) shows the normalised transmission T/T_0 for the same values assuming total cavity losses of 35 ppm. Clearly, very small nanodiamonds are required to achieve a high outcoupling efficiency.

An alternative approach are diamond membranes [173, 306–308], which ideally should be monocrystalline and have to be optically contacted to the planar mirror. Depending on the thickness of the diamond layer, it acts like an additional weak resonator, such that a coupled resonator system needs to be considered. The resonances of the membrane, called 'diamond-like modes', and the resonances of the microcavity, called 'air-like modes' thereby feature the typical avoided crossing behaviour [173]. While the diamond-like modes are in principal advantageous for achieving highest Purcell factors, they exhibit a field antinode at the diamond surface such that low surface roughness is crucial in this case. Using a fibre machined for high finesse cavities for future SiV experiments in the course of this work (Fig. 3.1.5), Häußler et al. [308] integrated a 200 nm thin diamond membrane containing SiV centres into a fibre cavity and demonstrated that the cavity performance remained unaltered.

5. Towards cavity-enhanced single ion spectroscopy of $Eu^{3+} : Y_2O_3$

Rare-earth-ion-doped crystals are a promising candidate for quantum information applications and quantum networks in a solid state system [312]. Their large nuclear spin coherence times allow for storing quantum information. They also exhibit optical $4f - 4f$ transitions with exceptional coherence, which represent a photonic interface to the spin states [64–66]. The electric dipole interactions allow for an excitation blockade, which is similar to the case of Rydberg atoms and could be exploited for the implementation of quantum gates [78, 79]. But as the dipole-forbidden character of the transitions leads to a long excited-state lifetime, the resulting emission rates are very low. Coupling the optical transition to a microcavity leads to Purcell-enhanced rates and promises the possibility to address individual rare earth ions [76]. This chapter introduces the rare earths alluding to what makes them so suitable for quantum information applications and discusses single ion detection experiments. Then, the properties of europium ions shall be discussed in general and europium-doped yttria nanoparticles in particular. Next, sample preparation methods and a sample characterisation will be explained, showing an optical lifetime reduction by nanoparticle embedding. First spectroscopy results of a few-ion Eu-ensemble are presented, before giving an overview of the potential and challenges of this approach. Parts of the content of this chapter are published in [85] and are used under the Creative Commons Attribution 3.0 licence (CC BY 3.0).

5.1. Rare earths

5.1.1. Properties

The term rare earth metals describes the chemical elements with proton numbers 21 and 39 as well as 57 to 71, where the latter are also referred to as lanthanides. While the first rare earths yttrium and terbium were isolated in 1843 by the Swedish chemist Carl Gustav Mosander, only in 1949 the last element, promethium, was discovered. Due to the filled outer lying 5s, 5p, and 6s orbitals of the rare earth metals, they feature almost identical chemical properties, which is the reason why they typically appear together in nature and large efforts have to be taken to isolate the individual elements. While the applications of rare earths were sparse during the largest part of the 20th century, they have drastically risen in importance over the last 20 years and have become de rigeur in high-tech products, lighting, magnets, catalysts, and metallurgy. [313]

Rare earths typically exhibit the electron configuration $[Xe]\,4f^n6s^2$ meaning that the 5s, 5p, and 6s orbitals are closed and the inner lying 4f orbital is gradually filled from

element to element. Rare earth ions typically appear in the 3+ charge state having the electron configuration [Xe] $4f^m$ [314].

Rare earth metal ion (REI) dopants are a very promising solid state quantum system: Their nuclear spin coherence times are among the longest which can be found, up to six hours for europium ion dopants in yttrium orthosilicate [63], allowing for long term storage of photon states. They are not subject to spectral diffusion and exhibit very little vibronic coupling [84]. Together with the very narrow dipole-forbidden optical $4f - 4f$ transitions at low temperature the system is well suited for a photonic spin interface and quantum memory. Local host crystal fields make these transitions weakly allowed, while the outer lying orbitals effectively shield the 4f states from the environment. Even in nanocrystalline hosts, the good coherence properties were shown to be preserved [82]. Dipole interactions (interaction strengths on the order of GHz) between rare earth ions in the same host matrix promise a many qubit nuclear spin register and quantum logic gates between individual ions [78, 79]. At room temperature, the homogeneous linewidth is broadened by phononic processes and fluctuating spins [315], while linewidths as small as 73 Hz were observed in erbium-doped yttrium orthosilicate ($Er : Y_2SiO_5$) at liquid helium temperatures [316]. As each individual dopant ion is subject to a slightly different strain environment in the host crystal, the spectral line of an ensemble experiences inhomogeneous broadening many orders of magnitude larger than the homogeneous line, which can be exploited to spectrally address subgroups of the ensemble and apply spectral hole burning. [166, 312]

5.1.2. Rare earths as quantum memory

Rare earth quantum memories have been realised in ion ensembles using various techniques. Storage times of seconds have been achieved in praseodymium-doped orthosilicate ($Pr^{3+} : Y_2SiO_5$) by electromagnetically induced transparency, where characteristics of the light field are recorded as spin wave in a quantum ensemble [317]. The same REI system was used to demonstrate an optical gradient echo, where an external field gradient is used to more and more detune a spectrally sharp absorption feature (spectral hole burned into the inhomogeneous line) with increasing propagation depth into the material, thereby creating an effective broad line. Reversing the gradient retrieves an echo of the incoming pulse. A retrieval efficiency of over 60% at a storage time of 1.6 µs was reported [67]. The so-called atomic frequency comb is realised by periodic spectral hole burning into the broad inhomogeneous line leaving a series of narrow absorbing peaks with equal spacing. A photon can be stored delocalised over the peaks. After a rephasing time determined by the peak spacing, a photon echo is released [68, 69]. An atomic frequency comb was also realised in europium-doped yttrium orthosilicate ($Eu^{3+} : Y_2SiO_5$) [65]. The technique has also been applied to REI waveguide memories, where waveguides where written into $Pr^{3+} : Y_2SiO_5$ [70], made of thulium-doped lithium niobate [71], or coupled to a bulk $Pr^{3+} : Y_2SiO_5$ crystal [72]. A quantum memory at telecom wavelength has been demonstrated applying an erbium-doped optical fibre [73]. The controlled retrieval of pulses from a photonic crystal cavity written in a neodymium-doped yttrium orthovanadate ($Nd^{3+} : YVO_4$) crystal promises on-chip integration [74].

5.1.3. Single ion detection

Though challenging due to the low count rates of the weakly allowed optical transitions, individual rare earth ions have recently been detected: Kolesov et al. [318] performed upconversion spectroscopy on single praseodymium ions, which could also be detected in direct high-resolution spectroscopy of $4f-4f$ transitions [319, 320]. Furthermore, strong $5d-4f$ transitions were used to observe single cerium ions [64, 321], while the coherent $4f-4f$ transitions seem to be best suited for implementing a spin-photon interface. However, free-space single ion detection is challenging due to the very low emission rates of these transitions and in addition, the indistinguishability of the emitted photons gets deteriorated as the coherence time is typically much shorter than the excited state lifetime. These challenges can be resolved by coupling the ions to optical microcavites, which leads to an enhancement of the low emission rates and thereby greatly facilitates the read-out [85]. A Purcell factor of 111 was demonstrated for individual neodymium ions coupled to a photonic crystal nanobeam cavity [63, 77]. An enhancement by a factor of 650 for erbium ions coupled to a nanobeam cavity allows decay rates on the order of 10^4 photons/s in the telecom band [76]. Single europium ions have so far not been detected and their low branching ratio into the desired transition makes the observation challenging. This chapter will report on first steps towards single ion spectroscopy in europium-doped yttrium oxide ($Eu^{3+}:Y_2O_3$) [85].

5.2. Europium ions

5.2.1. Level scheme

The electron configuration of Eu^{3+} is $[Xe]\,4f^6$, where the partially filled 4f orbitals are shielded by closed $5s^2$ and $5p^6$ shells. Multiple degenerate states arise from the distribution of the six electrons into the seven 4f orbitals, where the degeneracy can be lifted by electron repulsion, spin-orbit coupling, the crystal-field perturbation, and the Zeeman effect. Electron repulsion leads to a splitting into 119 $^{2S+1}L\,(\tau)$ terms, where τ is a quantum number to differentiate between terms with identical S and L. The spectral separation of these terms is on the order of a few hundred THz. Each term has a degeneracy of $(2S+1)\,(2L+1)$,which is further lifted by spin-orbit coupling, yielding 295 $^{2S+1}L\,(\tau)_J$ levels with $J=L+S,...,|L-S|$, which still have a degeneracy of $(2J+1)$ and are split by a few tens of THz. The further level splitting due to the crystal field on the order of THz is dependent on the symmetry of the host crystal – the lower the symmetry, the more different energy levels and the more allowed transitions. Note that J is not well defined in low symmetry environment as J-mixing can occur. The Zeeman splitting in a strong magnetic field is typically no more than some tens of GHz. The ground state is $^7F_0$, since it is the largest L term with the highest spin multiplicity $2S+1=7$ and among these the lowest J value according to Hund's rules. The next higher lying term is ^5D_J with $^5D_0$ being the lowest energy level. A diagram of the relevant levels of $Eu^{3+}:Y_2O_3$ is shown in Fig. 5.2.1(a), showing the coherent $^5D_0-{}^7F_0$ transition at 580 nm and the strongest $^5D_0-{}^7F_2$ transition at 612 nm. A

detailed overview of the level scheme in different host materials is given in [322].

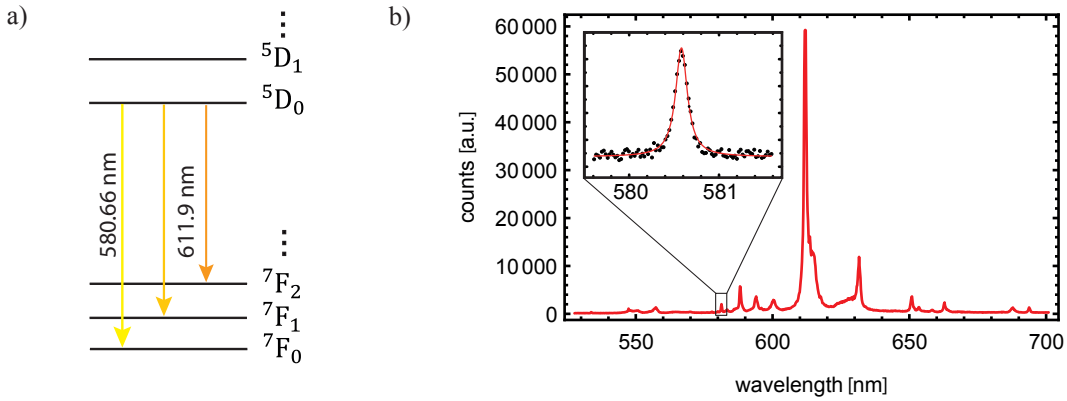

Figure 5.2.1.: (a) Relevant level diagram of $Eu^{3+} : Y_2O_3$,showing the coherent $^5D_0 - ^7F_0$ transition at 580 nm and the strongest $^5D_0 - ^7F_0$ transition at 612 nm. (b) Broadband fluorescence spectrum of single nanocrystal recorded by confocal microscopy. The inset shows the $^5D_0 - ^7F_0$ transition in high resolution together with a Voigt profile fit. Ions are off-resonantly excited using a laser at 532 nm. [85]

5.2.2. Yttria as a host matrix

Here, yttrium oxide or yttria (Y_2O_3) was used as a host matrix. Europium ions can replace yttrium in two different lattice sites belonging to the C_{3i} (or S_6) and C_2 point group, respectively. The C_{3i} group is centrosymmetric and belongs to the trigonal symmetry class, where the $^5D_0 - ^7F_0$ transition is not observed. In contrast, the C_2 group is non-centrosymmetric and belongs to the monoclinic symmetry class, where the degeneracy of all J levels is fully lifted (i.e. they split up into $2J+1$ sublevels each). In this case, the $^5D_0 - ^7F_0$ transition becomes weakly allowed [322, 323]. As this is the transition we are interested in, only the ions in C_2 sites are suited. Note that the transition only becomes weakly allowed in relatively low symmetry sites, which motivates the choice of yttria as host matrix. For a spectral study of the two sites, see [323]. The relative intensity of the $^5D_0 - ^7F_J$ transitions is strongly dependent on the site symmetry. A room temperature spectrum of $Eu^{3+} : Y_2O_3$ is shown in Fig. 5.2.1(b). The ions were excited off-resonantly with 532 nm light, which is close to the $^5D_1 - ^7F_1$ transition. Excitation works efficiently for this wavelength at room temperature as the $^7F_1$ level gets thermally populated. For excitation spectra around this wavelength, see the thesis of Tobias Krom [324]. At room temperature, phononic coupling allows for a fast non-radiative relaxation into the $^5D_0$ level, from which a decay into the ^7F_J multiplicity is observed. The most narrow $^5D_0 - ^7F_0$ transition is shown in the inset with higher resolution. The $^5D_0 - ^7F_2$ transition is called a 'hypersensitive transition' as it is most sensitive to the local symmetry [322]. In yttria it appears at about 612 nm, consists of 5 unresolved sublines (three for the S_6 site), and is the by far strongest transition. The $^5D_0 - ^7F_1$transition (in yttria consisting of three sublines for the C_2 site and two sublines for the S_6 site) sticks out by

being the only magnetic dipole transition. As such, it is largely insensitive to the local environment, which is why it can be used to compare and calibrate Eu^{3+} spectra [322]. The coherent $^5\mathrm{D}_0 - ^7\mathrm{F}_0$ transition features a low branching ratio of only $\zeta_{F_0} \approx 1/60$ ($\zeta_{F_0} = 1/63.2$ in Y_2SiO_5 [84]). Measurements by Tobias Krom [324] even suggest, that it could be lower by about a factor of two in an yttria nanoparticle sample. This also motivates Purcell enhancing this transition in order to obtain a larger branching ratio according to eq. 2.2.49.

5.2.3. Nuclear spin manipulation

For realising quantum gates or a quantum memory, the hyperfine states with their ultralong coherence time are applied, where photonic states can be mapped to the nuclear spin. There are two europium isotopes, ^{151}Eu and ^{153}Eu, which are about equally abundant and both feature a nuclear spin $I = 5/2$. Both ground ($^7F_0$) and excited state ($^5D_0$) feature six hyperfine sublevels with the states $\pm m_I$ being degenerate such that there are effectively three states each, with $m_I = \{1/2, 3/2, 5/2\}$. The lowest lying level in the excited state is $m_I = 1/2$ and $m_I = 5/2$ in the ground state. In the latter, the frequency spacing between the levels is 34 MHz and 29 MHz (88 MHz and 73 MHz), respectively, for ^{151}Eu (^{153}Eu) in Y_2O_3. For a spin-photon interface, two of the ground state hyperfine levels are chosen as qubits $|0\rangle$ and $|1\rangle$. Population can be transferred between them via the optical transition. Applying a Raman scheme with bi-chromatic pulses, coherence transfer has been demonstrated in a photon echo experiment [325]. This scheme has the potential for the realisation of universal single qubit gates on nuclear spin qubits [326].

5.2.4. Europium-doped yttria nanoparticles

In this work, Eu-doped yttria nanocrystals were studied, as they offer the best optical and spin coherence properties so far demonstrated for nanoparticles, featuring a homogeneous linewidth of $\gamma_h = \gamma/2 + \gamma^\star = 45$ kHz (at 1.5 K) [82–84] and a nuclear spin coherence time of 8 ms [81] observed in nanoparticle powders. The sample was synthesized by homogeneous precipitation [327] in the group of Philippe Goldner. The nanoparticles feature a dopant concentration of 0.5% and an average size of 60 nm. Figure 5.2.2(a) shows a scanning electron microscopy (SEM) image of the sample of nanoparticles spread out on a substrate and (b) a confocal microscope fluorescence image of individual nanoparticles, dispersed on a mirror by spin-coating. The inhomogeneous linewidth of the $^5\mathrm{D}_0 - ^7\mathrm{F}_0$ transition at room temperature as obtained from single nanoparticle spectra as shown in Fig. 5.2.1(b), was determined to be 80 GHz even for nanocrystals with very low count rate. This is as narrow as in bulk samples, thereby being an indicator of good crystal quality [85]. At liquid helium temperature, the inhomogeneous linewidth in bulk at 0.5% concentration is reported to be 23 GHz, with an optical lifetime $T_1 = 950$ µs [328, 329] and an optical coherence time $T_2 = 1.1$ ms [81], which would correspond to a homogeneous linewidth of $\gamma_h = 1/(\pi T_2) = 290$ Hz. Perturbations due to surface electric charges lead to a significant reduction of optical coherence in nanoparticles, where $T_2 = 7$ µs [83] corresponding to the above-mentioned $\gamma_h = 45$ kHz. However, the nuclear

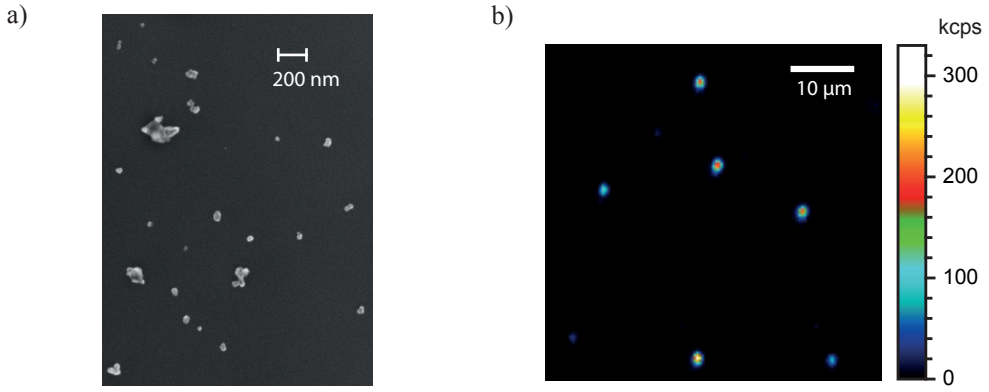

Figure 5.2.2.: (a) SEM image of isolated nanocrystals dispersed on a substrate. Measurement conducted in the group of Philippe Goldner. (b) Confocal fluorescence image of individual nanocrystals spin-coated onto a mirror. [85]

spin coherence is much less affected by surface charges as nuclear Stark coefficients are several orders of magnitude larger than their optical counterparts [330]. A nuclear spin coherence lifetime $T_2 = 12$ ms is reported in $Eu^{3+} : Y_2O_3$ bulk transparent ceramics [325] compared to $T_2 = 1.3$ ms in nanoparticles [81] showing a less dramatic difference. Applying spin echo and spin dynamical decoupling, the nuclear spin coherence time could be increased up to 8 ms, comparable to the bulk value [81].

Apart from the easy incorporation into microcavities, nanoparticles could potentially increase coherence by modification of the phonon density of states [327, 331, 332], provided the obstacle of surface charges gets resolved. A goal of the presented project is addressing single ions, which can be achieved by spectral selection in the small sized ensembles contained in nanoparticles: A crystal of 80 nm in diameter contains about 3×10^4 ions. The homogeneous lines of individual ions would not typically overlap, as shall be seen in section 5.5.2, allowing for individually addressing them. In bulk material, this would only be possible at the tail of the inhomogeneous line, which may not be optimal as these ions experience the largest crystal strain.

5.3. Optimised cavity coupling by thin film embedding

A novel method of sample preparation was applied were the yttria nanoparticles are embedded into a thin film of PMMA, which reduces scattering loss, increases the emission due to a modified density of states, and, with a correct choice of layer thickness, introduces an additional weak resonating structure. It could be shown that these effects lead to a lifetime reduction. Part of the discussion is adopted from [85] and is partially identical.

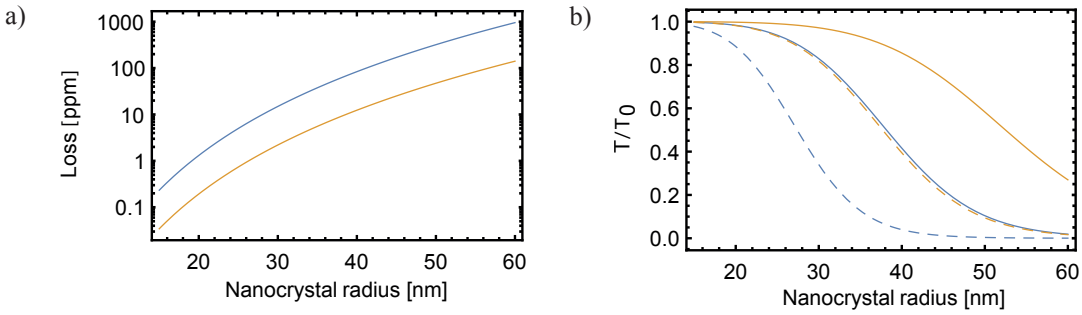

Figure 5.3.1.: (a) Scattering loss introduced by yttria nanoparticles for varying particle size for $w_0 = 1.3\,\mu\text{m}$ in free space (blue) and embedded in PMMA (yellow). (b) Transmission normalised to empty cavity transmission for a finesse of 20 000 (solid lines) and 150 000 (dashed lines).

5.3.1. Theoretical considerations

Two crucial aspects for the cavity experiment are the scattering loss introduced by the nanoparticle and the achievable ion–photon coupling strength, where the latter depends on the partially suppressed local electric field inside the particle. In fact, scattering loss and local field suppression both arise from the boundary condition introduced by the nanoparticle surface, and are related to modes outside or inside the crystal, respectively.

The additional scattering loss according to eq. 3.5.9 introduced by yttria nanoparticles ($n = 1.93$) of varying size is shown in Fig. 5.3.1(a) for a mode waist $w_0 = 1.3$ µm. The blue and yellow curves correspond to a particle in free space and embedded into a thin film of PMMA ($n = 1.49$), respectively. As the Clausius-Mossotti relation (eq. 3.5.3) yields a smaller polarisability for a decreased refractive index contrast, the scattering loss is reduced for the latter case. For a particle with a radius of 40 nm, the loss is reduced from 84 to 12 ppm, that is by a factor of seven. The resulting normalised transmission T/T_0 is shown in Fig. 5.3.1(b) for a finesse of 20 000 (solid lines) and 150 000 (dashed lines). So a particle with a radius of 40 nm would still allow for a transmission of almost 40% compared to the empty cavity transmission for high finesse in case of embedding.

Furthermore, the excited state lifetime of the ions is sensitively influenced by the host nanoparticle and the presence of the surrounding dielectric, which affect the light-matter coupling strength. For a nanocrystal far in the Rayleigh regime (diameter $\lesssim 20$ nm) embedded in a medium, the lifetime can be expressed as [333–336]

$$\tau(x) = \tau_0 n_r(x) \left(\frac{n_r(x)^2 + 2}{3} \right)^2, \tag{5.3.1}$$

where τ_0 is the lifetime in bulk Y_2O_3 and

$$n_r(x) = \frac{n}{x + (1-x)\, n_m} \tag{5.3.2}$$

is the relative refractive index. It includes an effective refractive index $x + (1-x)\, n_m$, where n_m belongs to the partially surrounding medium and x is the filling factor [336].

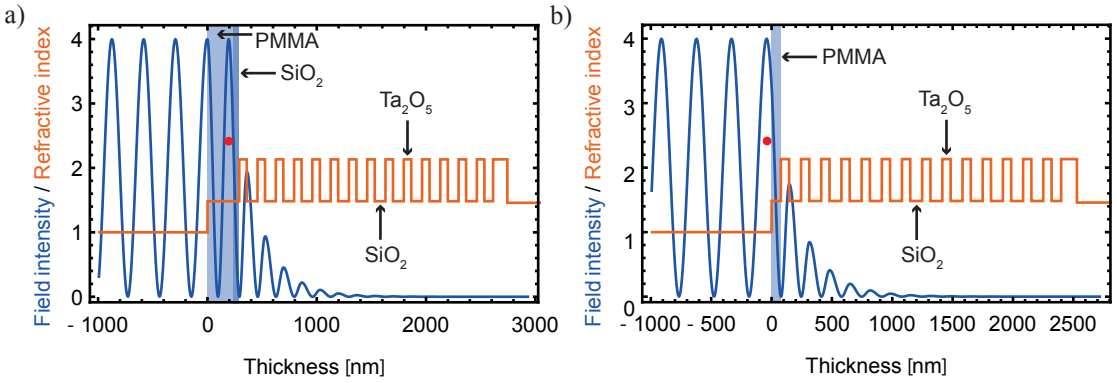

Figure 5.3.2.: (a) Refractive index profile (orange) of the mirror and electric field distribution (blue) for an embedded nanocrystal. The red dot marks the location and size of the nanocrystal. (b) Same as (a) for a nanocrystal on top of a spacer layer as used in the low temperature cavity experiment. [85]

The latter describes to which extent the particle is surrounded by the medium, which in this case would be the glass substrate, where $x = 1$ corresponds to a particle in vacuum and $x = 0$ to the fully embedded case. The resulting prolonged lifetime for small crystals is due to the boundary condition of the crystal-air interface, which makes the crystal act as an off-resonant cavity that suppresses the local field inside. According to eq. 5.3.1, ions in small Y_2O_3 nanocrystals in air should exhibit a lifetime $\tau_{\text{air}} = \tau(1) = 7.0\,\tau_0$. For larger nanoparticles, calculations [334, 336] and measurements [335, 336] illustrate a decrease of τ with increasing diameter, while the presence of a surrounding dielectric leads to a further reduction.

However, these calculations are not adequate for the situation discussed here, as the particles do not reside in a bulk medium but are embedded into a thin film on a mirror. Therefore, the effect of embedding is estimated by performing finite difference time domain simulations[1], where the spontaneous emission of a dipole located in an 80 nm cube of Y_2O_3 embedded into a thin film on a DBR mirror (see Fig. 5.3.2(a)) is analysed. One finds that the emission rate is increased by up to a factor of 3.8 as compared to a dipole in the same nanoparticle cube in free space. Compared to the case of a crystal on top of a spacer layer as shown in Fig. 5.3.2(b), one obtains a rate increased by a factor of 2.4. This evidences an increase of the local field strength within the crystal by embedding, where the coupling strength to the cavity field will be increased accordingly.

To keep the mode volume as small as possible, it seems obvious to keep the thin film at a minimal thickness, which still allows positioning the nanoparticle in the field maximum. However, in such a configuration the field intensity is reduced as compared to the case without embedding (Fig. 5.3.2(b)) as the PMMA layer acts as a non-resonant weak resonator. Increasing the layer thickness to $(3/4)\,\lambda/n_m$ (geometric length, for $\lambda = 580$ nm), a transfer matrix simulation shows that the field intensity is as large as in the vacuum part of the cavity, thereby maximising light-matter coupling (see

[1] Lumerical FDTD Solutions

Fig. 5.3.2(a)). It should be noted that the application of such a layer increases the transmittivity of the mirror, the more, the higher the field intensity inside the layer. For a $(3/4)\,\lambda/n_m$ film, the transmittivity is increased by a factor of two as compared to the naked mirror and by 30% as compared to the case where the particle resides on a spacer layer as shown in Fig. 5.3.2(b). In addition, the penetration depth increases from 859 nm (both mirrors) for the case in (b) to 1402 nm for the case in (a), which means that the length increase will be larger than the increase of spacer thickness.

In summary, when comparing the embedded case in (a) with the standard procedure (crystals on spacer layer) in (b), one gets the same field intensity, an emission rate increased by a factor of 2.4, and a scattering loss reduced by a factor of 7. However, this comes at the cost of an increased transmittivity of the planar mirror by 30% and a cavity length increase by at least 543 nm. As an example, assume a fibre with a radius of curvature $r_C = 20$ µm and a profile depth $t = 1.5$ µm. The particle diameter is 80 nm, the bare mirror transmission 95 ppm, and the total mirror absorption loss 40 ppm [85]. Due to the difference in penetration depth, one reaches $q = 9$ in case (b) and $q = 11$ in case (a) leading to different mode waists $w_0 = 1.12$ µm and 1.16 µm, respectively. The effective Purcell factors are 16.9 and 14.5. But even though the Purcell factor is significantly smaller in the embedded case, the ratio of the outcoupled rate to the free space emission rate,

$$\frac{\gamma_{\text{out}}}{\gamma_0} = C \cdot \beta \cdot \eta_c \cdot f, \tag{5.3.3}$$

is larger, where η_c is the outcoupling efficiency (containing scattering loss) and f the enhancement factor due to a different density of states. For (b), one obtains $\gamma_{\text{out}}/\gamma_0 = 11.7$ and 31.0 for (a); so the advantages of embedding outweigh the smaller Purcell factor.

5.3.2. Preparation

From the transfer matrix simulation shown in Fig. 5.3.2(a), one finds that the ideal layer thickness for a particle with a diameter of 80 nm is 290 nm. To ensure that the nanoparticle resides in a field maximum of the standing wave that will be formed in the cavity, a three-step preparation was used: First, a layer of 55 nm of SiO_2 was applied to the mirror by electron beam evaporation. Then, nanocrystals are deposited on this layer by spin-coating and are thus centred on an electric field maximum. Third, a 235 nm thick layer of PMMA is spin-coated to cover the particles. Coating a silicon test substrate with the same layers showed that this procedure results in the correct thickness up to about 5 nm according to ellipsometry measurements. The two materials feature a comparable refractive index $n_m = \{1.46, 1.49\}$. It remains unclear if the PMMA layer smoothly covers the nanoparticles or features bumps at these positions, which could introduce a further loss channel.

As for the spin-coating step, the following procedure was found to yield an even spread of particles without much agglomeration: First, the mirror surface was activated in an oxygen plasma to increase the hydrophilicity. The yttria powder is suspended in water (at a concentration of very roughly 1 µg per ml water). It was found that the particles have the tendency to form agglomerates, which is why 200 µg of the surfactant sodium

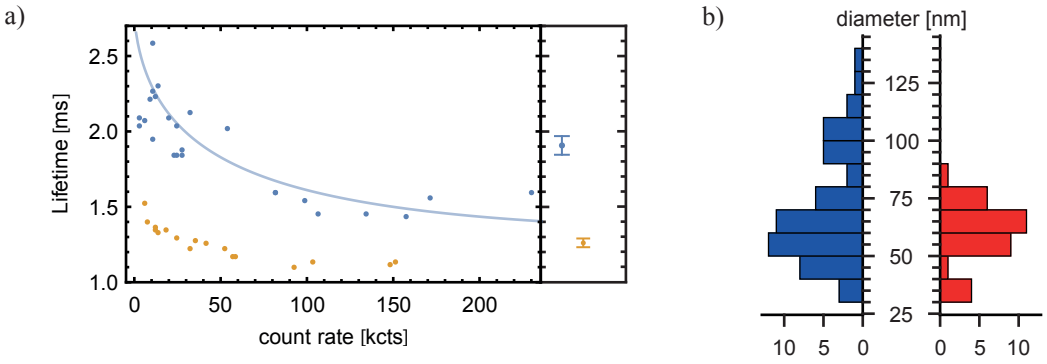

Figure 5.3.3.: (a) Fluorescence lifetime measurements as function of the photon count-rate. Each data point corresponds to a single measurement carried out on a randomly chosen crystal. Blue: crystals on silica slip. The blue solid line is a fit to a model. Orange: crystals embedded in a PMMA thin film on a mirror. The right panel shows the average lifetime and the standard deviation of the mean value for both cases. (b) Histogram of measured crystal sizes (right panel, red bars) and histogram of calculated crystal sizes from a measured fluorescence distribution (left panel, blue bars). [85]

dodecyl sulfate (SDS) per ml water was added. It is assumed that the agglomeration originates in a hydrophobic surface of the yttria particles, which then appear in bunches to reduce the surface to water. SDS has a hydrophobic and a hydrophilic end, such that the molecules cover the particles and help dissolving them in water. The sample was centrifuged to get rid of too large particles and agglomerates and treated in an ultrasonic bath to spread the particles. After having spin-coated the particles[2], the sample was again plasma-cleaned to remove the SDS.

5.3.3. Lifetime reduction and count rate estimate

To study the effect of embedding, the sample prepared on a mirror as described above was compared to a reference sample, where the nanoparticles are spin-coated onto a fused silica substrate. Both samples were examined in a confocal microscope (see exemplary scan in Fig. 5.2.2(b)) and lifetime measurements were conducted for all particles featuring the characteristic spectrum of Eu ions withing an area of $100 \times 100\,\mu m^2$. For the measurement, the ions were excited at 532 nm, where an acousto-optical modulator (AOM) was applied to generate 50 µs pulses at a repetition rate of 200 Hz. The whole spectral range above the excitation wavelength was collected. The obtained lifetime traces[3] were well fitted by an exponential decay and the resulting time constants are plotted in Fig. 5.3.3(a) as a function of count rate as detected on the APD[4] for cw excitation at 500 µW. The data shown in blue and yellow correspond to the particles on the fused silica substrate and embedded in PMMA on the mirror, respectively. Assum-

[2] 30 s at 50 rpm, then 60 s at 2000 rpm with an acceleration of 200 rpm/s
[3] TDC: qutools quTAU
[4] Laser Components Count-50

ing a homogeneous distribution of Eu ions and a linear relation between the count rate and the number if ions in the nanoparticle, one finds the expected correlation between lifetime and particle size.

Considering the count rate distribution and comparing it to a size distribution obtained from SEM images like the one in Fig. 5.2.2(a), one can get an order of magnitude estimate for the typical count rate per single ion. Figure 5.3.3(b) shows a histogram of the measured nanoparticle size (red, right) and the expected size distribution calculated from the measured fluorescence count rates (blue, left). For the calculation, it is assumed that the count rate I and the particle radius are directly related via $I = NI_0 = (4\pi/3)\, n_0 r^2 I_0$, where I_0 is the single ion count rate and N the number of ions. From the size and doping concentration, and with the known yttrium concentration in the C_2 site of $n_0 = 1.6 \times 10^{22}\,\mathrm{cm}^{-3}$, one can deduce that single crystals of e.g. 60 nm diameter contain $N \sim 10^4$ ions. The two distributions match if assuming an excited state population of 20% (several ground state levels are thermally populated, but only one is excited at about one saturation intensity) and an overall fluorescence detection efficiency of 1.5%. This value is smaller than the expected maximally achievable detection efficiency of 20% for the setup, which can be calculated by spatially integrating over the dipole emission on the mirror averaged over dipole orientations (see section 3.4.5), the angular collection efficiency of the microscope objective, the maximal transmission through the optics, and the detector quantum efficiency, in analogy to the discussion in section 4.4.4. The smaller experimental value is ascribed to suboptimal collection and transmission efficiency and a potential overestimation of the excited state population. From this analysis, it can be deduced that about 2 photons per second per ion are detected, which could be increased to 100 photons s^{-1} under ideal conditions. This discussion shows that a free space experiment is not well suited for efficient single ion read-out.

According to Le Kien et al. [334], the size-dependent lifetime of a dipole in the centre of a dielectric sphere is given by

$$\tau\,(r,x) = \tau_0\, n_r\,(x)\, U\,(r) \tag{5.3.4}$$

with $n_r\,(x)$ as given in eq. 5.3.2 and

$$\begin{aligned}
U\,(r) &= \frac{1}{2\epsilon^3 z^6}\left(K + B\cos\left(2\sqrt{\epsilon}z\right) + C\sin\left(2\sqrt{\epsilon}z\right)\right) && (5.3.5)\\
K &= \epsilon^2\,(\epsilon+1)\,z^6 - (\epsilon-1)^2\left[\epsilon z^4 - (\epsilon+1)\,z^2 - 1\right] && (5.3.6)\\
B &= (\epsilon-1)\left[\epsilon^2 z^6 - \epsilon\,(\epsilon+3)\,z^4 + (\epsilon-1)^2\,z^2 - (\epsilon-1)\right] && (5.3.7)\\
C &= -2\,(\epsilon-1)\,\sqrt{\epsilon}z\left(\epsilon z^4 - z^2 + \epsilon - 1\right) && (5.3.8)
\end{aligned}$$

$z = kr$ is the wave number multiplied with the radius and $\epsilon = n_r\,(x)^2$ is the relative permittivity. The expression converges to eq. 5.3.1 for $r \to 0$. It is assumed that a single central dipole reasonably approximates the continuous ion distribution in the nanocrystals as long as $r < \lambda/\,(2\pi n) \approx 50$ nm. To fit eq. 5.3.4 to the data, the wavelength of the strongest transition, $\lambda = 612$ nm, is chosen; the wavelength in bulk is

$\tau_0 = 0.94$ ms; and the radius is expressed with respect to the count rate as

$$r = \sqrt[3]{\frac{3I\tau\,(r)}{2\pi\, n_0\, c_{\mathrm{dop}}\, \eta_{\mathrm{col}}}}, \tag{5.3.9}$$

where I is the count rate, c_{dop} the doping concentration, and η_{col} the collection efficiency obtained from the histogram comparison discussed above. Note that the resulting relation is recursive as it contains the lifetime $\tau(r)$. It was found that the expression has well converged after 10 iterations starting with $\tau\,(r) = \tau_0$, and the result is taken as a fit function with the filling factor x as sole fit parameter. The best agreement was achieved for $x = 0.30$ (solid line in Fig. 5.3.3(a)), which is smaller than expected, such that other factors that reduce the lifetime in addition to the presence of the substrate cannot be excluded.

Regarding the data set corresponding to the embedded particles (yellow), one can observe a significant lifetime reduction [337] as compared to the particles on fused silica. The right panel of Fig. 5.3.3(a) shows the lifetime for the two cases averaged over all crystals – one observes an averaged lifetime reduction by a factor of 1.5 for the embedded sample, which features a lifetime of $\tau_{\mathrm{emb}} = (1.26 \pm 0.03)$ ms as compared to $\tau_{\mathrm{sub}} = (1.91 \pm 0.06)$ ms for the sample on silica. The observed average lifetime reduction is in agreement with the FDTD simulation when considering that the simulation compares a crystal in free space with an embedded one, while the measurement compares crystals on a substrate with embedded ones. If relying on the model used for the fit of the lifetime data, one can use the ratio $\tau\,(x = 1)\,/\tau\,(x = 0.3) = 2.66$ to calculate the expected lifetime in air for the measured data. With this, one obtains an overall lifetime reduction compared to a crystal in air of

$$\frac{\tau_{\mathrm{air}}}{\tau_{\mathrm{emb}}} = \frac{\tau_{\mathrm{air}}}{\tau_{\mathrm{sub}}}\frac{\tau_{\mathrm{sub}}}{\tau_{\mathrm{emb}}} = \frac{\tau\,(x=1)}{\tau\,(x=0.3)}\frac{\tau_{\mathrm{sub}}}{\tau_{\mathrm{emb}}} = 2.66 \times 1.52 = 4.0, \tag{5.3.10}$$

close to the FDTD prediction of 3.8. Note that this estimate makes the assumption that the ratio $\tau_{\mathrm{air}}/\tau_{\mathrm{sub}}$ is the same for larger crystals as in the limit $r \to 0$, which is but an approximation.

5.3.4. Embedding in yttria

To further reduce scattering loss, it could be useful to consider an yttria thin film on the mirror. As additional dephasing in nanostructures was shown to be reduced by embedding them into bulk [338, 339], which could even increase coherence. However, annealing such a thin film, which is needed to get good coherence properties, would require higher temperature than a dielectric mirror can bear. Furthermore, nanocrystals comprising only a small number of ions make it easier to spectrally select single ions, even in the centre of the inhomogeneous line. These considerations led to the idea to embed annealed yttria nanoparticles into a non-annealed yttria thin film. In analogy to the procedure described in section 5.3.2, a spacer layer of yttria would be deposited on the mirror to shift the nanoparticles into the field maximum. After spin coating

the nanoparticles, a second layer of yttria would be applied. Again, it can be shown that the emission rate is largest for a geometric layer thickness $(3/4)\,\lambda/n$, which would correspond to 225 nm of yttria. This would increase the mirror transmittivity by a factor of 3.5 and the total penetration depth would be about 2 µm. Nevertheless, this approach would result in a higher emission rate into the collection channel, as can be seen when computing the numbers for the same example cavity as in section 5.3.1: The smallest accessible mode order is $q = 13$ leading to $w_0 = 1.2$ µm and a Purcell factor of 9.5. As there is no scattering loss, 73% of the light emitted into the cavity mode is coupled out through the planar mirror. Together with an enhancement factor of 7 compared to a nanoparticle in air, one obtains $\gamma_{\text{out}}/\gamma_0 = 43.7$, which is over 40% more than for the nanoparticles embedded into PMMA.

First confocal fluorescence measurements of a non-annealed yttria film, deposited on a fused silica substrate in the group of Alban Ferrier, did not show any material fluorescence in the important spectral window. At this stage, it is not known if the surface roughness will be small enough for cavity experiments, but this approach is certainly worth to be further pursued. A practical challenge could be to laterally locate the nanoparticles in the cavity as absorption scans would probably no longer reveal them.

5.4. Experimental setup and specifications

This section describes the setup used for the few ion spectroscopy in [85] and explains the potential Purcell enhancement in this system and the detection scheme. A detailed description of the setup can also be found in [166].

5.4.1. Cavity

The cavity consists of two mirrors with a dielectric coating with a specified transmission of 100 ppm at 580 nm each. Finesse measurements at different longitudinal mode orders yield an average value of $\mathcal{F} = 17\,000$, which varies by about 5000 due to transverse mode coupling losses at particular mode orders. As the cavity experiment was conducted while the embedded sample discussed in the previous section was being prepared, an earlier sample preparation method was applied: The nanoparticles are spin-coated onto a PMMA spacer layer (Fig. 5.3.2(b)) to shift the centre of nanoparticles with a diameter of 80 nm into the field maximum. This requires a geometric layer thickness of 77 nm leading to an enhanced transmittivity of 190 ppm. Having measured the finesse and knowing the mirror transmission, the residual scattering and absorption losses can be calculated to be 30 ppm for each mirror [85].

The radius of curvature of the fibre profile is 20 µm with a depth of 1.5 µm. The specifications of the used cavity can also be found in appendix A (fibre C). The smallest accessible axial mode order is $q = 9$ (total penetration depth $d_{\text{pen}} = 860$ nm) leading to a mode waist $w_0 = 1.1$ µm and mode volume $V_m = 2.6\,\lambda^3$.

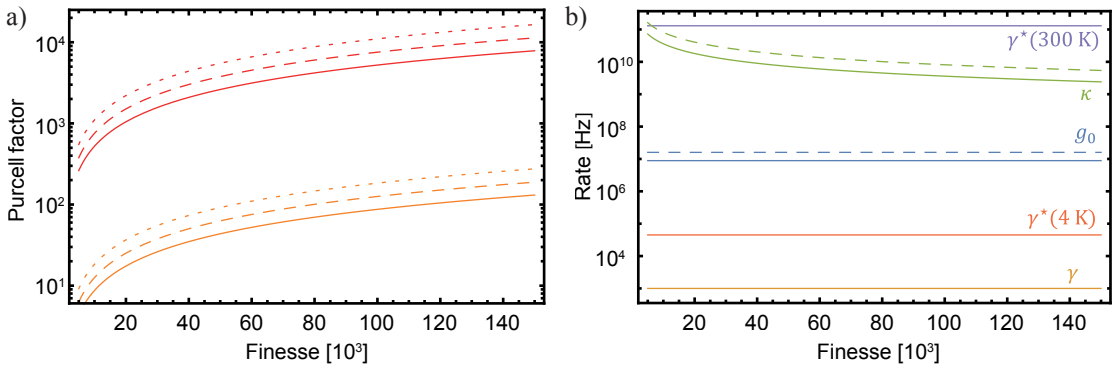

Figure 5.4.1.: (a) Calculated ideal (red) and effective (orange) Purcell factor as a function of finesse. Solid lines: $q = 9$, $r_C = 20$ µm. Dashed lines: $q = 4$, $r_C = 20$ µm. Dotted lines: $q = 4$, $r_C = 10$ µm. (b) Cavity QED parameters as a function of finesse for $r_C = 20$ µm and $q = 9$ (4) (solid (dashed)). $\gamma^\star$ taken from [83] and $\gamma^\star\,(300\,\mathrm{K}) \approx 130$ GHz. $g_0 = \sqrt{\zeta} g_{\mathrm{all}}$.

5.4.2. Expected Purcell enhancement

The above named values lead to an ideal Purcell factor $C_0 = 950$ and an effective Purcell factor including the branching ratio of $C_{\mathrm{eff}} = \zeta C_0 = 16$. Figure 5.4.1(a) shows the ideal (red) and effective (orange) Purcell factor as a function of finesse, where the solid lines correspond to the cavity in the experiment ($q = 9$, $r_C = 20$ µm). The dashed lines are for the same radius of curvature reaching a smaller axial mode order $q = 4$, which is reasonable for a more shallow profile. The Purcell factor for a cavity with a smaller radius of curvature $r_C = 10$ µm is shown as dotted lines. For an envisaged finesse of 150 000, effective Purcell factors of more than 100 are reached with realistic cavity geometries.

Regarding the cavity QED parameters, which are shown as a function of finesse in Fig. 5.4.1(b), there is a clear distinction between room temperature and liquid helium temperature regarding the pure dephasing rate $\gamma^\star$. Note that $g_0 = \sqrt{\zeta} g_{\mathrm{all}}$ includes the branching ratio. The strong coupling regime, for which $2g > |\gamma + \gamma^\star - \kappa|$ must hold, is reached in neither case. At room temperature, $\gamma + \gamma^\star \gg \kappa \gg 2g_0$, that is the system is in the bad emitter regime of the weak coupling regime. Even at cold temperature, $\kappa > R$ holds for all finesse values, such that the good cavity regime cannot be reached, meaning that the photon leaves the cavity directly upon emission [147]. With $\kappa \gg 2g_0 \gg \gamma + \gamma^\star$, the system is not in the classical bad cavity regime (with $\kappa \gg \gamma + \gamma^\star \gg 2g_0$), but the cavity-emitter coupling dominates over the total emitter dephasing. It was theoretically shown [84] that the reversible transfer of quantum states between ions in separate cavities is possible in this regime, which is important when using such a system as node in a quantum network.

5.4.3. Optics

The optical setup is shown in a schematic drawing in Fig. 5.4.2. There are three laser sources available: The laser for the Eu spectroscopy is a commercial Toptica DL pro ECDL at 1160 nm[5]. The 580 nm light for resonant excitation of the $^5D_0 - ^7F_0$ transition is generated in a temperature-stabilised[6] fibre-coupled second-harmonics generation (SHG) stage based on a periodically poled lithium niobate (PPLN) waveguide[7]. The laser offers mode-hop free scanning over 1 GHz and a narrow linewidth of around 100 kHz. It is tuned to the correct wavelength with the help of an optical spectrum analyser[8], which has a resolution of 60 MHz. For maximum conversion efficiency (about 8% of the original power), the temperature of the SHG needs to be well adjusted for each wavelength setting as the optimal temperature varies with 2.23 K/0.1 nm [166]. To generate pulses and, perspectively, to individually address the hyperfine states of the Eu ions, an AOM[9] is used in a double-pass configuration, where the first diffraction order is selected by an iris aperture and reflected back into the AOM such that it retraces the light path of the incoming light, making the further beam path independent of the deflection angle. The beam is coupled out of the AOM arm by polarisation optics[10]. To address a single polarisation mode of the cavity (see eq. 2.1.33), the polarisation can be tuned by a half-wave plate and a quarter-wave plate in the 580 nm beam path. An optical chopper wheel can be used in addition to the AOM to periodically chop the beam for resonant excitation and thus fully block residual resonant excitation light.

The light of a home-built ECDL at 640 nm[11] is overlapped with the 580 nm beam path via a dichroic mirror[12]. Its light is phase-modulated in a fibre-coupled electro-optical modulator[13] (EOM) to generate an error signal for Pound-Drever-Hall locking (see chapter 6).

Light from a 532 nm laser[14] is also overlapped with the general beam path via a dichroic mirror[15]. As 532 nm lies on the edge of the cavity mirror stop-band, it leads to a low finesse ($\sim 10^2$) making the green light well suited to align the cavity and the collection beam path. Furthermore, it can be used for room temperature off-resonant excitation of the Eu ions and analysing the noise spectrum of an unstabilised cavity.

All colours can be simultaneously coupled into the cavity fibre[16], which enters the

[5] with a Toptica DLC pro Digital Laser Controller
[6] Meerstetter TEC-1091 controller
[7] NTT Electronics WH-0580-000-A-B-C
[8] Bristol Instruments 771A
[9] Gooch & Housego 3350-199
[10] A quarter-wave plate turns the linearly polarised light into circularly polarised light, whose handedness is inverted on the mirror. When it passes the quarter-wave plate on the way back, it is therefore converted to linearly polarised light whose polarisation is perpendicular of the incoming light, such that it can be coupled out with a polarising beam splitter.
[11] Laser diode: Ushio HL63142DG, 637 nm, 120 mW
[12] Semrock FF635-DI01
[13] Jenoptik PM635
[14] Cobolt Samba, 150 mW
[15] Semrock FF552-DI02
[16] IVG Fiber Cu450

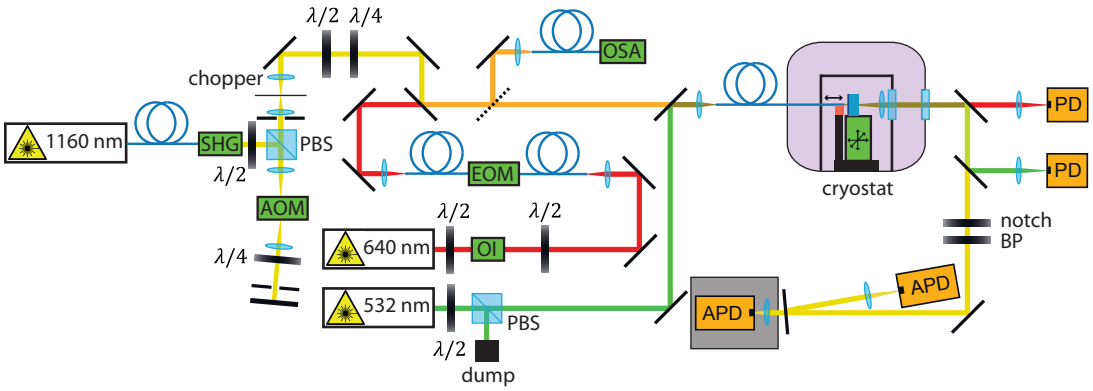

Figure 5.4.2.: Schematic drawing of the optical setup. SHG: second-harmonics generation stage. BP: band pass filter. PD: photo diode. PBS: polarising beam splitter. OSA: optical spectrum analyser. EOM: electro-optical modulator. OI: optical isolator.

cryostat through a vacuum-tight fibre feed-through. The light coupled out of the cavity through the planar mirror is collimated by an aspheric lens and leaves the cryostat radiation shield and sample chamber through two windows. With a dichroic mirror each, the red and the green light can be split off and individually detected. Depending on the wavelength or wavelength range one wants to detect, a range of band pass[17], short[18] and long pass[19], and notch[20] filters is available. When detecting non-resonant fluorescence upon excitation with 580 nm, a pellicle beam splitter can be used to reflect off a small fraction of the light in a steep angle to the beam (to keep the losses low) such that the transmitted 580 nm light can be monitored with an APD[21] in addition to the fluorescence light. In this case the excitation light would be filtered out after the pellicle beam splitter. The fluorescence light is detected by a photon counting APD[22] in a light-tight box, which has a measured dark count rate of about 35 cps.

5.4.4. Cryostat and nanopositioner

For cooling the cavity to liquid helium temperature, a cold finger cryostat, the Montana Instruments Cryostation, is used. It is a closed-cycle helium system with a two-stage Gifford-McMahon cooler [340, 341]. The second stage is connected via a thermal link to the sample platform, which reaches a temperature of 3.2 K without thermal load. A metallic radiation shield (with windows for optical access) mounted to a ring thermally linked to the first stage (27 K) shields the sample from thermal radiation, which is negligible at this temperature as it scales as ΔT^4. An outer metallic housing with windows closes the sample space and is evacuated before cool-down.

[17] 610 nm (Semrock FF01-610/5-25), 580 nm (FF01-580/14-25)
[18] 650 nm (FF01-650/SP-25)
[19] 594 nm (BLP01-594R)
[20] 580 nm (NF03-577E), 532 nm (NF03-532E-25)
[21] Thorlabs APD120A/M
[22] Laser Components Count-100C

The planar mirror is mounted to a stack of three closed-loop stepper positioning stages[23] for displacement in all three directions, which constitutes the first version of the cryogenic scanning cavity setup (for the second version, see chapter 6). The positioner stack is connected via a copper block to the cold platform. Additional thermal bridges (braided copper wires) thermally connect the mirror holder to the copper block to allow a heat flow to the cold base. With this setting, a sample temperature of 8.5 K could be reached. The fibre is glued into a syringe needle for stiffness and robustness, which in turn is glued to a shear piezo stack for fine tuning of the cavity length. The vibrations introduced by the piezo movement can be compensated for by an identical dummy piezo stack. The fibre side is rigidly connected to the base copper block by a tapered aluminium piece. An aspheric lens mounted behind the mirror and not touching the positioning stages, collimates the light before it leaves the cryostat through two windows. A detailed description of the mechanics and thermalisation can be found in the thesis of Franziska Beck [166], who designed this setup.

Although the mechanical setup was designed for high stiffness, i.e. high mechanical resonance frequencies, it was found that the vibrations introduced by the cryostat were too large to actively lock the cavity on resonance. Note that a special spring suspension of the cold head and a floppy thermal link already make the Cryostation far less noisy than comparable cryostats. However, the specified vibrations are still 5 nm peak to peak. The relative length jitter between the two mirrors along the cavity axis is considerably lower, but to keep the cavity on resonance, the length jitter must be on the pm level. Introducing a screw forming a rigid connection between the fibre holder and the mirror, reduced the jitter by an order of magnitude, however still not sufficient. This is why the measurements discussed here are conducted while modulating the cavity length over resonance with the shear piezo. A new cryopositioner design allowing for higher stability is presented in the next chapter.

5.4.5. Detection scheme

To spatially locate a crystal of suitable size, scanning cavity microscopy is performed. The measurements presented in this section were performed by Bernardo Casabone. The discussion is partially identical to [85]. From eq. 3.5.10, the scattering loss introduced by the particle can be obtained. A nanoparticle is selected for further investigation, when it is large enough to contain a suitable ion ensemble for fluorescence measurements, but small enough that the scattering loss does not largely deteriorate the outcoupling efficiency of the fluorescence light from the cavity. Figure 5.4.3(a) shows the scattering loss of a single crystal deduced from an SCM scan at a cavity length $d = 5.5$ µm. The shape represents the point spread function defined by the cavity mode, while the asymmetry is due to a miscalibration of the nanopositioning stage at short length scales. From the peak loss $B = 203 \pm 20$ ppm observed for perfect spatial alignment, for which the outcoupling efficiency is $\eta_c = 0.26$, one can calculate the crystal diameter to be 91 ± 3 nm. Together with the doping concentration of 0.5%, this allows to estimate the

[23] Attocube ANPx311 for both horizontal directions, ANPz51 for vertical direction, ANC300 controller

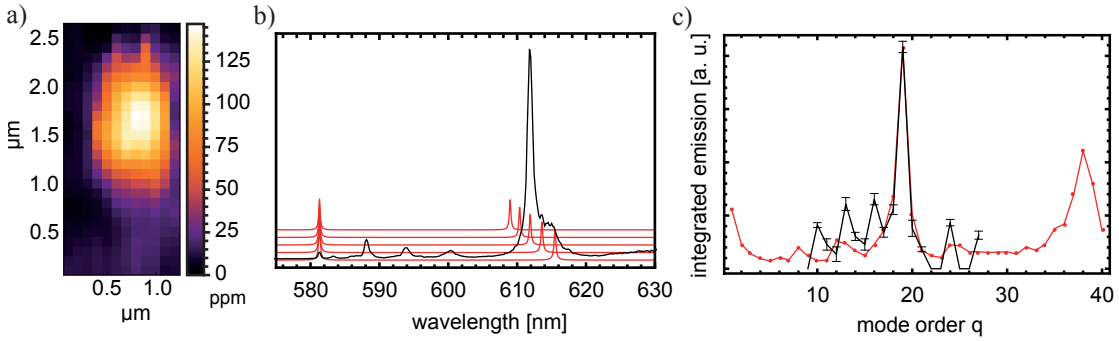

Figure 5.4.3.: (a) Map of scattering loss introduced by a single crystal when scanning the cavity mode across it. (b) Eu^{3+} spectrum (black) overlapped with the cavity spectrum (red) with resonances at 580 nm and around 612 nm for longitudinal cavity mode orders $q = 17, ..., 21$ (resonance linewidth not to scale). (c) Calculation (red line) and measurement (black) of the count rate as a function of mode order q. Measurements performed by Bernardo Casabone. [85]

number of ions contained in the crystal, yielding $N = 3 \times 10^4$ ions in this case. [85]

At room temperature, it can be easily verified if the loss is caused by a Eu-doped crystal by coupling 532 nm light into the cavity. Due to the low finesse at this wavelength, meeting the resonance condition is not so critical for the excitation light. Modulating the cavity length, one can find mirror separations where the cavity is resonant with the strong transition around 612 nm, whose fluorescence can be detected. At cryogenic temperature, excitation with 532 nm is no longer possible as it requires phononic relaxation, such that resonant excitation at 580 nm must be used. For studying the $^5D_0 - ^7F_0$ transition, a pulsed excitation scheme is applied where pulses with a duration of $\sim$ 100 µs are generated with the AOM and/or the chopper wheel. The photon counting APD is gated such that it only detects photons while the excitation light is off. A small temporal delay of a few µs between the excitation and detection window temporally filters out background fluorescence. However, as locking was not possible, the fraction of time on resonance was not sufficient to observe fluorescence from this weak transition.

Therefore, one takes advantage of the brightest emission line, the $^5D_0 - ^7F_2$ transition at 612 nm, such that the fluorescence can be well detected also for an unstabilised cavity. Exciting at 580 nm and detecting at 612 nm requires having the cavity resonant with both wavelengths. Figure 5.4.3(b) shows the Eu^{3+} spectrum overlapped with the cavity resonances at 580 and 612 nm, where the longitudinal mode order is varied from $q = 17$ to $q = 21$ for 580 nm. This illustrates that for $q = 19$, both 580 and 612 nm light is resonant, such that this mode order is used for the introduced excitation and detection scheme. Figure 5.4.3(c) shows a calculation and a measurement of the count rate as a function of mode order q for 580 nm cavity excitation. For this measurement, the cavity length was tuned to a particular mode order q and modulated with a rate of 10 Hz and an amplitude of about 4 nm around the set value, corresponding to an amplitude of more than 250 cavity linewidths (1.3 GHz at 580 nm). The data acquisition with the

APD is synchronised with this modulation to obtain a time-resolved photon counting signal. The detected counts are summarised in a histogram with a bin size corresponding to about two cavity linewidths and the averaged peak count rate per bin after several seconds of data acquisition is evaluated. [85]

5.5. Few ion spectroscopy

While it should be possible to talk to individual Eu^{3+} ions in a stabilised cavity, first measurements conducted by Bernardo Casabone with an unstabilised cavity already show spectroscopy of a small ion ensemble. The discussion is adopted from and partially identical to [85].

5.5.1. Measurement of the inhomogeneous line

To perform spectroscopy of the ${}^5D_0 - {}^7F_0$ transition, the cavity length is set to $q = 19$ and the laser frequency is tuned across the inhomogeneous line, while the count rate is measured. Figure 5.5.1 shows the obtained spectrum. Due to the limited tuning range with the inbuilt piezo, the whole line is covered by manually setting the laser frequency to three different values and scanning around them. The Gaussian fit to the data yields a FWHM linewidth of 22 GHz and a centre wavelength of 580.866 nm, which agrees very well with the linewidth in bulk samples at this doping concentration, thereby confirming the high crystal quality [342]. This measurement represents the first low-temperature spectroscopy of a single $Eu^{3+} : Y_2O_3$ nanocrystal of such a small size.

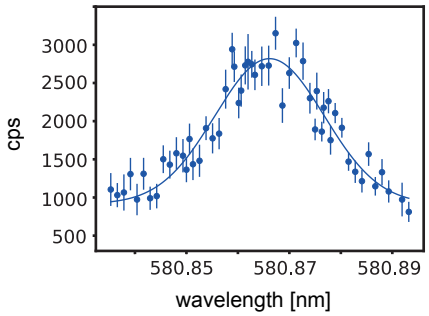

Figure 5.5.1.: Measurement (performed by Bernardo Casabone) of the inhomogeneous line of the ${}^5D_0 - {}^7F_0$ transition. The solid line is a Gaussian fit, yielding a full-width-half-maximum linewidth of 22 GHz. [85]

5.5.2. Estimation of ensemble size

To gain insight in the spectral distribution of the ions in a single nanoparticle, the number of ions within the frequency interval of the homogeneous linewidth of a single ion is estimated, assuming a Gaussian spectral ion density and neglecting the hyperfine structure.

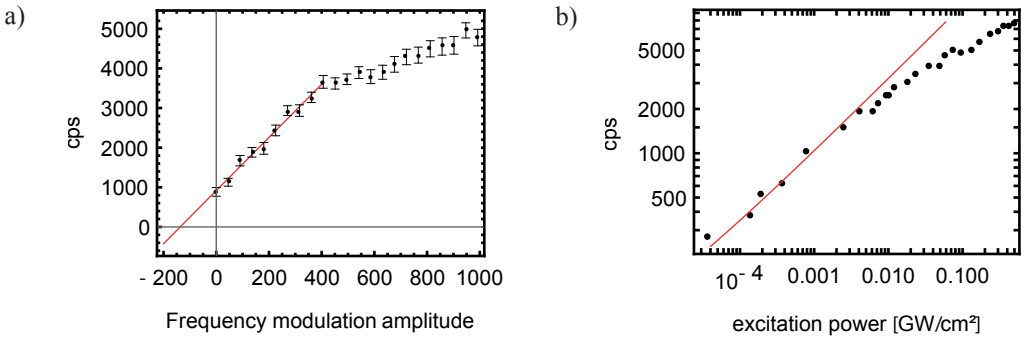

Figure 5.5.2.: (a) Calibration of the power broadening by laser frequency modulation. The count rate as a function of modulation amplitude (black data points) shows a linear dependence (red line: fit). From the extrapolation to zero count rate, one can estimate the power broadening, yielding 140 MHz in this case. (b) Count rate as a function of intra-cavity power. The solid line is a fit to the data for low power. Measurements performed by Bernardo Casabone. [85]

An estimated number of $N \approx 3 \times 10^4$ ions in the crystal with an expected homogeneous linewidth of about $\gamma_h = 200$ kHz at 10 K [83] are spread over an inhomogeneous linewidth of $\gamma_{\text{inh}} = 22$ GHz. This leads to a peak density $n = 2\sqrt{\ln 2/\pi} N\gamma_h/\gamma_{\text{inh}} = 0.27$, i.e. in the centre of the line, the ion transitions are spaced by about four linewidths, and low power spectroscopy would in most cases address no or at most a single ion. An overview of the relevant frequency scales of the experiment is given in appendix E.

To obtain the observed signal, a very high excitation intensity of several $\text{GW}\,\text{cm}^{-2}$ is used, which leads to strong power broadening and thus off-resonant excitation of small ion ensembles. To calibrate the amount of power broadening, the frequency of the excitation laser is modulated and the count rate is measured as a function of the modulation amplitude (see Fig. 5.5.2(a)). One can observe a linear signal increase up to an amplitude that approximately corresponds to the cavity linewidth. The slope then levels off as the excitation light is no longer on resonance with the cavity. Extrapolating the linear dependence to zero count rate, gives an estimate of the power broadening. For the presented measurement, this amounts to 140 MHz, taken at an intra-cavity power of ~ 53 mW and an intensity of $\sim 3.5\,\text{GW}\,\text{cm}^{-2}$ (see eq. 2.1.14).

In Fig. 5.5.2(b), the count rate on resonance (without frequency modulation) is shown as a function of excitation power. The power-broadened linewidth scales with $\sqrt{S_0} = \Omega\sqrt{2}/\gamma$, where S_0 is the saturation parameter, Ω the Rabi frequency, and γ the excited state decay rate. The observed power dependence follows the expected $\sqrt{S_0}$ relation over a large range (red solid line). For the weakest accessible excitation power of 0.15 mW, where there is still a significant signal to background ratio of 2, the excitation is a factor 400 weaker than for the value used for the calibration. This means that the broadening is a factor of 20 smaller, i.e. ~ 7 MHz. With an average spectral ion separation of $\delta = 750$ kHz, this corresponds to probing ~ 10 ions. At this power level, a count rate of 300 cps is detected on resonance, such that a single ion count rate of approximately

30 cps can be deduced. This value is already larger than the estimated single ion count rate for confocal detection, despite the fact that only a single transition is detected and that the cavity is only resonant during a small fraction of time.

In the revised second version of the setup, which should allow cavity locking in the near future, the cavity would be continuously coupled to the $^5\mathrm{D}_0 - ^7\mathrm{F}_0$ transition for both excitation and detection, such that much larger count rates are expected. Without the need for the double resonance scheme, shorter cavity lengths are possible, corresponding to larger enhancement. For a realistic cavity with $\mathcal{F} = 10^5$ and $d = 2$ µm, $C = 100$ is expected, such that up to 10^5 photons per second can be scattered into the cavity, enabling efficient single ion readout. As shall be further discussed in the following chapter, a stable cryocompatible nanopositioning stage has already been implemented. While active cavity stabilisation at cold temperature still faces some issues, it has already been possible to image the yttria nanoparticles via SCM and detect fluorescence from the dominant $^5\mathrm{D}_0 - ^7\mathrm{F}_2$ transition following the same scheme as has been introduced above. This implies that reproducing the presented spectroscopy is readily possible with the revised setup.

6. A low noise nanopositioning stage for a cryogenic environment

Low temperature fibre-cavity applications which require high finesse but still rely on tunability, face the problem that the mirror separation needs to very precisely stabilised in a noisy and potentially not very well controllable environment. This chapter first focuses on the challenges arising in the cryostat used for the Eu experiment and discusses active stabilisation and passive stiffness. Next, a home-built lever-based positioning stage is introduced, alluding to the necessary adaptions for cryogenic use. After discussing the obtained stability and remaining challenges, a short outlook is given.

6.1. Noise and active stabilisation

To keep the cavity on resonance on long time scales, the relative position of the mirrors to each other must be kept constant. Noise from the environment coupling to the system typically leads to a jitter of the mirror separation much larger than required for this goal. Therefore, the mechanical design needs to be as stiff as possible to be less susceptible to low frequency noise; the system needs to be passively vibration isolated to damp out high frequencies, and an active stabilisation of the mirror separation is necessary to correct for residual low frequency noise and drifts. These three measures shall here be discussed in more detail.

6.1.1. Required stability

To estimate the required relative length stability, one must regard the resonance linewidth (FWHM) as a function of cavity length change, which is given by [138]

$$\delta d = \frac{\lambda/2}{\mathcal{F}}, \tag{6.1.1}$$

which means that it is independent of the cavity length. At first glance, this seems counter-intuitive as the linewidth as a function of wavelength is inversely proportional to the mirror separation,

$$\delta\lambda = \frac{\lambda}{\mathcal{F}q}, \tag{6.1.2}$$

directly following from $Q = \mathcal{F}q = \nu/\delta\nu$, such that $\delta d = (q/2)\,\delta\lambda$. To understand this, one can picture the $q = d/(\lambda/2)$ field antinodes between the mirrors. A small change in λ accumulates for all antinodes making longer cavities more sensitive to wavelength/frequency changes, whereas the number of antinodes does not matter for the

response upon a small change in d. Assuming a finesse $\mathcal{F} = 20\,000$, the length-change linewidth for $\lambda = 580$ nm is $\delta d = 14.5$ pm, and for $\mathcal{F} = 150\,000$, one gets $\delta d = 1.9$ pm. To keep the transmission above 90% of the centre resonance transmission, the mirror separation must not change more than $\delta d/3 = 4.8$ pm or 0.6 pm, respectively. Assuming these values as allowed peak to peak amplitude of the length jitter, the allowed RMS values can be estimated: $4.8\,\mathrm{pm}/\left(2\sqrt{2}\right) = 1.7$ pm for the low and 0.2 pm for the high finesse. The cavity should remain on resonance for at least the optical lifetime, so more than 1 ms.

These values sound particularly challenging, when noting that the Cryostation has a specified peak to peak jitter of 5 nm. With the setup described in the previous chapter, one could achieve an RMS length jitter of 100 to 200 pm[1], which clearly is not sufficient. With another commercial cryo three-axis positioning stage[2], Franziska Beck reports 1.4 nm RMS with the Cryostation running [166]. The cryocooler has a cycle frequency of about 1 Hz, whereof an interval of about 300 ms is relatively quiet such that it should be sufficient to trigger on the cooler cycle and have the cavity locked on resonance only during this less noisy fraction of time.

6.1.2. Pound-Drever-Hall locking

The 580 nm light is perspectively to be used in pulsed excitation mode, which means that the cavity needs to be held on resonance with the 580 nm line even in time intervals of a few hundred µs length where the excitation light is off. This scheme requires a second 'locking' laser for active stabilisation. As the system will be subject to large vibrations during the noisier part of the cryostat cycle, which could result in cavity length jitter amplitudes larger than the 580 nm length-change linewidth, it is useful to use a locking laser at a wavelength, which experiences a smaller finesse. Here, a wavelength of 640 nm is chosen, corresponding to $\mathcal{F} \approx 2000$. The different wavelength light can be easily split off after the cavity by a dichroic mirror and individually detected. The drawback of this method is that both wavelengths need to be simultaneously resonant. The resonances come close to each other periodically with increasing cavity length, where the distance of such encounters is the beating length

$$d_B = \frac{\lambda_1 \lambda_2}{2\,(\lambda_2 - \lambda_1)}, \tag{6.1.3}$$

which is 3.1 µm or 11 orders of the 580 nm light for $\lambda_1 = 580.87$ and $\lambda_2 = 640.4$. With a bare mirror, a simultaneous resonance happens at the second shortest accessible axial mode order. However, when using the specially prepared mirror with a 290 nm layer with embedded nanoparticles as described in section 5.3, this order is no longer accessible (could potentially be possible with a more shallow fibre profile). In this case, the first double resonance appears at a geometric cavity length of 1.9 µm [3]. Together with a total penetration depth of 1.4 µm, this corresponds to $q = 12$.

[1] value taken from slides by Bernardo Casabone
[2] JPE IM-CPSHR-COE
[3] value obtained from transfer matrix simulation

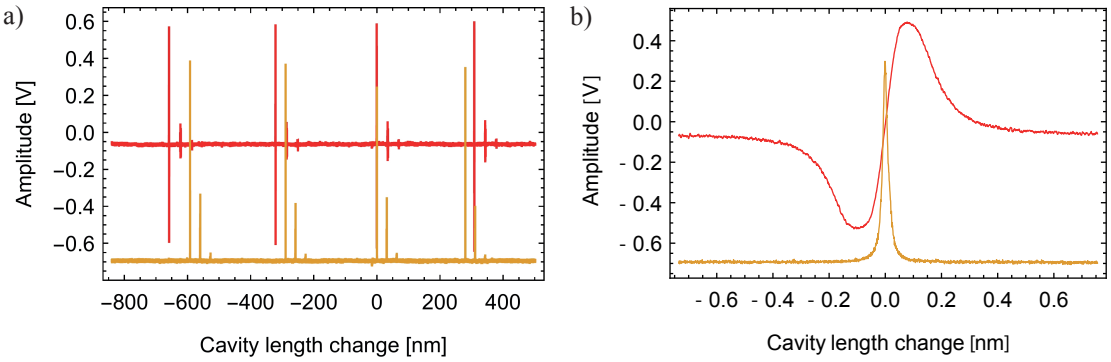

Figure 6.1.1.: (a) 580 nm transmission trace as a function of cavity length change (yellow) and error signal generated with 640 nm light (red). Yellow trace shifted downwards for clarity. (b) Close-up of double resonance.

To stabilise the cavity length on centre of the resonance, Pound-Drever-Hall (PDH) locking is applied [343, 344]. To create an error signal, the 640 nm light is phase-modulated with an EOM[4], which is driven with a 4 GHz signal[5]. The cavity transmission is detected with an amplified photo diode[6] and mixed with the amplified[7] oscillator signal, which, after low pass filtering with a cut-off frequency of 1.9 MHz, results in a trace as shown in Fig. 6.1.1(b) (red). Note that the modulated sidebands reside within the cavity resonance, which has a width of about 20 GHz. The laser is frequency tuned such that, for the axial order exhibiting the double resonance, the 580 nm resonance line (yellow) resides within the near-linear part of the error signal, close to its zero crossing. Figure 6.1.1(a) shows the 580 nm transmission as a function of cavity length recorded for several free spectral ranges together with the 640 nm error signal, including the double resonance at zero length change. As the error signal is linear and in particular inversion symmetric around the origin, its value marks the position on the line, allowing for correcting the cavity length accordingly by applying a voltage to a piezo actuator. However, a voltage proportional to the error signal is not sufficient as it would be zero when the resonance condition is perfectly fulfilled, thereby not accounting for a constant offset and slow drifts. This explains the necessity for an integrative (I) or proportional-integrative (PI) controller. As the integrative part integrates the signal with respect to time, its history and therefore the slowly varying offset is accounted for. Another way of seeing it is regarding the integrator gain profile, which is largest at zero frequency and exponentially decreasing with frequency, whereas the proportional part, which just multiplies the signal with a constant, has a gain profile constant with frequency. The centre of the 580 nm resonance is in general not perfectly positioned at the zero crossing of the error signal, which can be accounted for by adding an adjustable offset (set point).

[4] Jenoptik PM635
[5] DS Instruments SG4400L RF signal generator
[6] see Brachmann et al. [134] and the cavity lock report [345]: Hamamatsu G4176 photo diode, Minicircuits ZX86-12G-S+ Bias-Tee, Miteq AMFW-8S-03700420-28 amplifier (70 dB gain)
[7] Microwave Solutions MSH-5556603, 35 dB gain

The output signal of the I/PI controller is low pass filtered and fed back to a piezo crystal, which adjusts the cavity length accordingly, thereby closing the active feedback loop. A schematic overview is presented in Fig. 6.3.1.

Low pass filtering is crucial as the response of the system to external driving undergoes a π phase shift at the first mechanical resonance. That is, while the length jitter is compensated by the lock for frequencies well below the first eigenfrequency of the system, it even gets enhanced for frequencies above. This implies that the gain needs to fade out before the first mechanical resonance, which can be achieved by low pass filtering. Note that a filter, be it analog or digital, also evokes a phase shift, which is why the choice of cut-off frequency is always a trade-off.

Successful locking schemes for fibre cavities have been demonstrated by Brachmann et al. [134], who achieved a remaining length jitter of 153 fm RMS in a stiff mechanical design. Janitz et al. [346] realised a locking scheme with a large bandwidth of 44 kHz in a monolithic, miniaturised design. However, both approaches have a limited tunability and were not tested in a cryogenic environment.

6.1.3. Passive stability, damping, and active stabilisation

As locking is only an option below the first mechanical eigenfrequency, it is crucial to shift its occurrence to as high frequency as possible. This can be achieved by a monolithic design with rigid, compact parts [347, 348], thereby setting on a high passive stability of the system. Moving parts are clearly counteracting this goal and especially positioning stages stacked in series are prone to low resonance frequencies and a build-up of oscillations. Piezo-steered flexure bearings allow for fast and precise nanopositioning, at the same time keeping a monolithic design and the possibility of small load masses, thereby offering high stiffness. The down-side is the limited traveling range, especially at cryogenic temperature, where the piezo traveling range is reduced by about a factor of 5-10 [349]. A summary of nanopositioners arranged by their range and resonance frequency can be found in [350], clearly showing that a larger traveling range comes at the expense of a lower resonance frequency. When several degrees of freedom are required, stacking the individual piezo-based flexures in series lowers the resonance frequency, which is why a parallel design should be chosen for highest mechanical stiffness, meaning that each stage individually acts on the target [350].

External higher frequency noise, for instance from the cryostat, should be well decoupled from the positioning stage, which can be accomplished by passive damping. Possible solutions are suspensions on springs or flexible materials like teflon (polytetrafluoroethylene, PTFE). Springs convert a high frequency external drive to a low frequency motion, which can be dealt with by active locking, whereas suspension on soft materials rather has a damping effect, taking out mechanical energy and converting it to heat. A large suspended mass having large inertia is beneficial here.

Having well decoupled the high frequency noise, what remains should mostly be low frequency contributions and drifts well below the resonance frequency of the rigid system. These can be compensated for with a low bandwidth active cavity stabilisation or even just a drift compensation [138].

a) b)

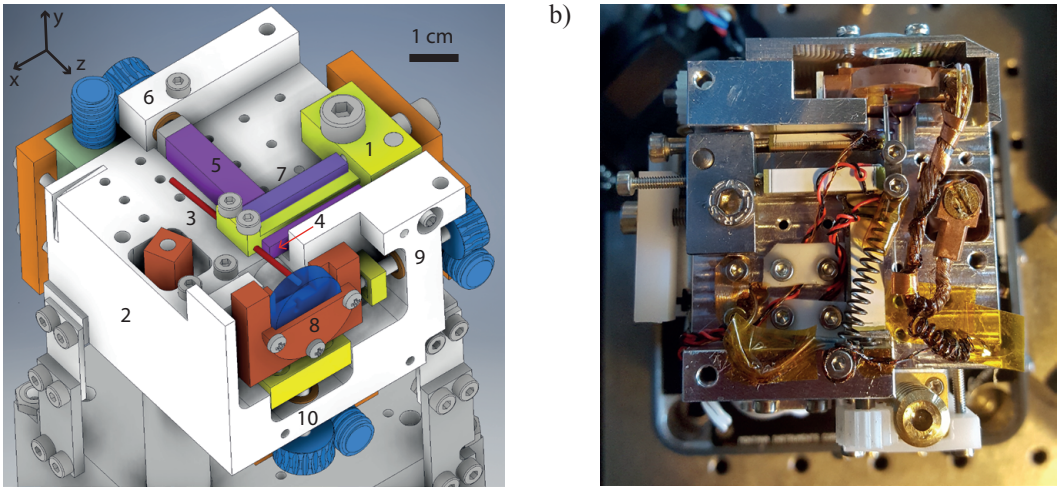

Figure 6.2.1.: (a) Technical drawing of flexure-based nanopositioning stage. (1) Flexible lever, attached to base block (2) via a dowel pin and fixed by a screw. (3) Syringe needle (red) to which fibre is glued. (4) Length tuning piezo. (5) y-axis piezo. (6) x-axis piezo. (7) Copper mirror holder on ball bearing. (8) Screw for coarse length adjustment. (9, 10) Coarse positioning screws for lateral displacement of mirror. (b) Top view photograph (without top radiation shield) of cryo positioning stage. The planar mirror is facing the top of the image.

6.2. A cryocompatible stiff positioning stage

A rigid flexure-based cryocompatible nanopositioning stage was designed for the europium project based on a highly stable room temperature design by Thomas Hümmer [138]. The stage has the potential to allow for locking a high finesse fibre-based cavity at liquid helium temperature in a noisy environment. This section explains the basic ideas and the adaptions for cryogenic use.

6.2.1. The Hümmer design

The major parts of the design are shown in Fig. 6.2.1(a), which is a technical drawing already adapted to the use in the cryostat. Figure 6.2.1(b) is a top view of the cryocompatible positioning stage. The core part is a free standing lever (1, yellow) made of titanium for a low thermal expansion coefficient, which is hinged to a massive aluminium base block (2) with a dowel pin and can be fixed with a screw. The two small screws on the left hold a steel syringe needle (3, red), to which the cavity fibre is glued. The bore for the needle has a slight inclination to the top right to allow for angular alignment of the cavity: For the vertical angle, the needle is first secured at the correct position with the back screw, while the front screw is screwed down until the correct angle is reached. To set the horizontal angle, a stack piezo actuator[8] (4) is pressed onto the needle from

[8]Piezomechanik PSt 150/2x3/20, 460 nF measured capacitance, 18 mm length, $\sim$ 130 nm/V (RT)

the right. Note that the necessary displacement is not performed by piezoelectric motion, but rather the piezo stack is held from the back by an adjustment fine thread screw mounted to the lever base. This piezo actuator is used to scan the fibre in horizontal (x) direction by slightly bending the fibre back and forth. Another piezo stack[9] (5) is clamped in between the lever and a micrometer screw[10] (6), whose bushing is slip fitted to the base block. This screw allows moving the piezo and with it the lever in both directions, thereby coarsely setting the cavity length (z direction). The restoring force is hereby applied by a spring (see Fig. 6.2.1(b)) pulling the tip of the lever towards the z piezo, which is used for precise modulation of the cavity length. A second small piezo actuator[11] with less stroke can be stacked between the lever and the modulation piezo (see Fig. 6.2.1(b)) for active length stabilisation. In z direction, the lever has a width of 6.5 mm and a free standing length in x direction of 22 mm, which makes it rather stiff: A finite element simulation[12] yields a resonance frequency of 5.8 kHz. For vertical scanning, another piezo stack[13] (7) is clamped between the lever base and an extrusion at the lever tip. The lever has an overall thickness of 3 mm, but a 1 mm wide notch at the connection to the base thins it to 1 mm, which allows for an easy downwards bending when the piezo expands. In this direction, the simulation yields a resonance frequency of 1.7 kHz. Note that the y axis does not require the same high stiffness as the z direction as it should ideally leave the cavity length unaltered. The three axes act in parallel as all three piezos have either the base block or the lever base as their reference. Retracting the fibre by turning the z micrometer screw is possible without losing the angular alignment as the whole lever including the lateral piezos can be loosened and rotated around the dowel pin connecting it to the base block. The planar mirror is clamped into a copper mirror holder (8), which can slip in lateral direction on three glass spheres lowered into the base block and arranged in a triangle. A spring is attached to the mirror holder, which goes through a borehole (7 mm diameter), is tightened and fixed at the back of the base block. Due to an inclination of the hole, the spring does not only push the mirror holder backwards onto the ball bearing, but also in negative y and negative x direction (as defined in Fig. 6.2.1(a)). This force can be counteracted by two micrometer screws, acting on the mirror holder from the side and from the bottom. Adjusting these screws allows for coarse positioning of the mirror.

The lever design combines fast scanning with high stability. Thomas Hümmer reports on 'real time' scanning cavity microscopy, capturing more than one 30 µm×20 µm image per second or up to 10 000 points per second. A modulation bandwidth of 500 kHz was demonstrated. The achieved cavity length jitter was down to 100 fm RMS with a software-based active drift compensation only [138].

The necessary trade-off between stiffness and traveling range can be defined by choosing the length of the lever and the point where the z piezo acts upon it: The longer the lever, the easier it can be bent, but also the lower the resonance frequency. The

[9] Piezomechanik PSt 150/5x5/20, 1.7 µF measured capacitance, 18 mm length, ∼ 130 nm/V (RT)
[10] Thorlabs F3ES15 hex adjuster with phosphor bronze threaded bushing F3ESN1P
[11] Thorlabs PA4FEW, 160 nF measured capacitance, 2 mm length, ∼ 17 nm/V (RT)
[12] Autodesk Inventor
[13] Piezomechanik PSt 150/3.5x3.5/20, 860 nF measured capacitance, 18 mm length, ∼ 130 nm/V (RT)

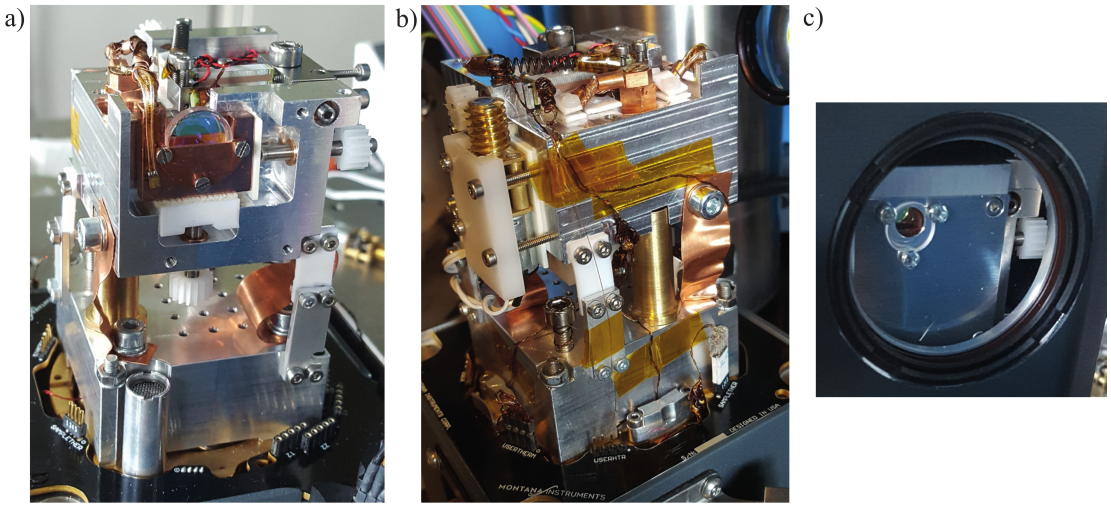

Figure 6.2.2.: (a) Nanopositioning stage, front view. Motors not yet installed. (b) Side view. (c) Stage with radiation shield viewed through the collection window of the sample chamber.

larger the displacement between the point of action of the piezo and the lever tip with the needle, the larger the mechanical amplification. Taking the cryo positioning stage shown in Fig. 6.2.1 as an example, the length modulation piezo has a specified stroke of 130 nm/V. However, when modulating the cavity length in the lever setup, about six FSR can be scanned with a voltage difference of just 10 V, corresponding to a stroke of approximately 350 nm/V at room temperature.

6.2.2. Adaption to low temperature

For making the positioning stage (which is shown in different views in Fig. 6.2.2) cryocompatible, the following points need to be considered:

Cooling the sample The only part of the setup, which necessarily must reach the lowest possible temperature, are the Eu-doped nanoparticles on the planar mirror. As they cannot be directly cooled, the mirror needs to be cooled down. As fused silica has a rather low thermal conduction coefficient (for an overview of material parameters, see appendix F), it is important that it connects well to a cold surface on a large area. To achieve this, the mirror is clamped into a massive copper mirror holder covering about half its surface. A flexible copper braided wire is soldered to the mirror holder for good thermal contact (see 6.2.1(b), on the right). It serves as a thermal bridge between the mirror holder and a cold copper finger, which is mounted onto the cold platform of the sample chamber. Thereby, a copper connection is formed between the mirror and the cold platform allowing a heat flow from the mirror. Copper is used as it is among the materials with the highest thermal conductivity. For the two screw joints (braided wire to copper finger and copper finger to cold platform), brass screws are used

as they undergo a larger thermal contraction than copper thereby pressing the parts together when cooled down, which would not be the case for steel screws. A measured temperature difference of only 0.8 K between the cold platform and the mirror holder at cold temperature evidences the high quality of the thermal bridge.

For an easier cool-down and more convenient handling, the mirror holder is the only part in the setup, which is intended to be cooled to liquid helium temperature. In particular, the base block of the positioning stage is thermally connected to the first stage of the cryostat, which is at 27 K. A hollow aluminium block (see 6.2.2(a)) is connected to the ring on the bottom of the sample chamber, which is connected to the first stage and is originally meant for mounting the radiation shield. This lower block shields the cold platform from thermal radiation and is thermally connected to the upper base block by three S-shaped copper sheets, where the shape is to reduce the conduction of vibrations to a minimum. Keeping the base block at tens of Kelvin has the charm that it does not need to be shielded from radiation, not so much care needs to be taken regarding cryomaterials and well conducting joints, the contraction is not quite as large, the piezo actuators retain a larger traveling range, and one can avoid cryocooling a large heat reservoir.

Thermal insulation As thermal radiation does not play a role at cryogenic temperature, thermal conductance is the only relevant mechanism of heat transfer. Due to the large temperature gradient between the mirror holder and the base block, good thermal insulation is crucial. However, the mirror holder must be at the same time very rigidly connected to the base block in z direction and be movable in lateral direction in a well-defined manner. This is achieved by the glass ball bearing: The three point bearing keeps the mirror holder accurately at a distance of 0.7 mm from the base block, at the same time allowing for a free movement in lateral direction. The thermal insulation is two-fold: Glass is a good heat insulator and the contact area between base block and glass ball and glass ball and mirror holder, respectively, is minimal. Thermal insulation between the mirror holder and the lateral adjustment screws is ensured by a sheet of roughened fibre glass each, where the roughening is again for a reduction of contact area, and an additional teflon block in y direction (see Fig. 6.2.2(a)). The restoring spring (hooked to the mirror holder) does not touch the base block – the hole drilled through the base block is large enough to allow for a few mm movement of the mirror holder before the spring hits the wall. The back end of the spring is hooked to a metal pin held by a polyoxymethylene (POM) disc, which is in turn inserted into a pit on the back side of the base block, thermally insulating the spring from the base block.

Apart from the mirror holder, also all other parts of the thermal link to the cold platform must not come in contact with the base block. The braided copper wire can either be left free-standing (like in Fig. 6.2.1(b)) or clamped to the base block with teflon sheets and nylon screws, where teflon sheets are taken as a heat insulating spacer (like in Fig. 6.2.2(b)). The copper finger is guided through a broad hole in the base block and the lower block, not touching either of them. It is shielded from thermal radiation by a brass pipe rigidly screwed to the lower block. The pipe overlaps with the hole in

the upper base block, however does not touch the wall to prevent vibrations from the bottom to be coupled to the base block (see Fig. 6.2.2(b)).

For thermal insulation from the room temperature wall of the sample chamber, it is crucial that no part of the stage comes in contact with it.

The electric connection of the piezo actuators to the electric feed-through pins of the sample chamber, which are at room temperature, is realised with phosphor bronze cables. They have an approximately six-fold lower thermal conductivity compared to copper wires of the same diameter[14], effectively reducing the heat flux towards the piezos.

Radiation shield As already mentioned, the parts thermally connected to the cold platform need to be shielded from thermal radiation by completely surrounding them by parts set to stage 1 temperature, i.e. a few tens of Kelvin, where thermal radiation is negligible. To the front side, the mirror holder is shielded by an aluminium cover screwed to the base block, which has a window with an anti-reflective (AR) coating such that the light from the cavity can be collected without much loss. A further aluminium lid, screwed to the base block from the top, completely covers all relevant parts. Figure 6.2.2(c) shows the setup with all radiation shields installed through the collection window of the sample chamber. The dimensions of the setup are chosen such that it fits well into the sample chamber, which has a diameter of about 70 mm and a height of 100 mm, and that the outcoupled light leaves the sample chamber at a central point of the collection window such that a small misalignment does not reduce the collection.

Coarse positioning For turning the three coarse positioning micrometer screws, small geared motors[15] are used as available for hobby model building. The reason is a lack of small-scale cryocompatible motors, which can apply enough force, and the idea to make the positioning stage low cost (compare to 'bill of materials' in [117]). As the motors are not cryocompatible, they are thermally insulated from the base block and kept rather warm by linking them to room temperature via their copper cables. Thermal insulation is granted by a fibre glass spacer between the motors and the base block and a motor holder made of POM. The torque is translated by a worm gear[16] to a gear wheel[17] glued to the screw (see rear motor in Fig. 6.2.2(b) and Fig. 6.2.1(b)). The latter is made of plastic (not clear which kind) for thermal insulation. As it turns out, the motors can be used down to the lowest possible sample temperature in this configuration.

Temperature measurement In total, five thermometers are available to monitor various temperatures: Three of them are pre-mounted and measure the temperatures of

[14] Note that in metals the thermal conductivity is proportional to the electric conductivity (Wiedemann-Franz law), which is why the resistance (inversely proportional to conductivity) of phosphor bronze cables is larger, accordingly. For details, see [351].

[15] Eckstein Komponente, V-TEC 6V Micro 10x12 mm DC motor with spur gearing, 54 rpm, cost < 8 €

[16] Lemo-Solar SCR05 worm gear, modulus 0.5, brass, inner hole bored up to fit motor shaft

[17] from plastic gear kit from ebay

stage 1 and 2 and of the cold platform. With the two available user thermometers[18], the temperature of the mirror holder and the base block are monitored. The sensor is glued[19] to the front of the mirror holder (see Fig. 6.2.2(a), from now on called sample thermometer) and its phosphor bronze cables are guided along and glued to the braided wire for thermal lagging. Before the cables get in touch with the base block, a few cm long coiled part is left loose to leave a long way between the two temperature stages (see Fig 6.2.1(b)). The same is done for the transition from radiation shield temperature to room temperature: The cable is clamped to radiation shield temperature and then left loose for several cm before it is plugged into the electric connector at room temperature. The base block thermometer is clamped under a copper sheet on top of the base block (see Fig. 6.2.1(b) on the bottom left) and thermally lagged in the same manner. It may exhibit a systematic error of up to 3 K as it was manually calibrated[20] to the other user thermometer.

Without thermal load, stage 1 temperature is 27 K, stage 2 is at 2.4 to 2.7 K, and the cold platform at 2.7 to 3.0 K. These temperatures rise respectively when either stage experiences a heat load[21]. When the stages are not perfectly thermally decoupled from one another, all parts linked to stage 2 show a higher temperature whereas the stage 1 temperature is lowered, trying to compensate the rise.

With the positioning stage completely mounted, but without electrical connections, the mirror holder reaches a temperature of 6.8 K, with 6.0 K for the platform and 5.1 K for stage 2. The rather small gradient between the parts shows that the thermal connection is good, however, the increased temperature points at an introduced heat load. Taken, the stage 1 temperature is only 26.6 K, it seems clear that the insulation between the stages is not perfect. This is not surprising with the cold mirror holder in close proximity to the base block being at a temperature of 46 K. In a future revised setup, one could try to better cool down the base block or add insulation layers between base block and mirror holder.

With all electric connections plugged in, in particular the three motors, the coldest reached temperatures are as follows: 7.6 K for the sample, 6.4 K for the platform, and 5.7 K for stage 2. This evidences an additional heat load by the motors, increasing the base block temperature to 59 K. According to a chart[22] from the manufacturer, one experiences a heat load of around 0.45 W. However, note that the reached sample temperature is still smaller than the best achieved with the commercial positioner setup described in the previous chapter and would be acceptable for experiments with europium ions (homogeneous linewidth below 200 kHz [82]).

[18] Lakeshore Cernox CX-1050-SD-HT-1.4L-QT resistance thermometer
[19] using GE-varnish and applying pressure while curing
[20] They were both glued to a copper piece directly mounted to the cold platform. The resistance was measured for both of them and compared to the temperature scale of the readily calibrated sensor. The potential error arises due to the imperfect thermal contact.
[21] temperature as a function of heat load: https://www.montanainstruments.com/help/Heat-Load/
[22] https://www.montanainstruments.com/help/Heat-Load/

Cool-down time The cool-down time depends on the amount of material to be cooled and the possible thermal flux. In the empty sample chamber, the target temperature is reached after about two hours. The nanopositioning stage is cooled in 4 h 20 min. The longer cooling time can be explained by the large heat reservoir represented by the massive base block, where the thermal linkage to the lower block is realised by three copper bridges. In a first attempt, only two of them were in place, leading to a cool-down time of over six hours. So clearly, further thermal links could further lower the cool-down time. Furthermore, one could think of caving the base block by removing material from its bottom.

Cryocompatible choice of materials As the sample is coldest, gases would first condense there, leading to increased losses, as could be observed in case of a vacuum leak in the sample chamber. It is therefore important to use materials, which do not outgas much, such as metals, teflon, and cryocompatible glue. Furthermore, all parts should be thoroughly cleaned. However, it was found that small amounts of plastics and epoxy glue designed for an ambient environment did not deteriorate the performance of the cavity. For instance, cables with plastic cladding and other plastic parts in the setup were not found to cause a reduced finesse.

As already mentioned, one needs to take great care to thermal conductance and thermal expansion coefficients of the applied materials. Aluminium was mainly chosen for the base block due to convenient fabrication. It would be worth considering replacing it by titanium, whose thermal expansion coefficient is lower by about a factor of two. On the other hand, titanium has a much lower thermal conduction, which would probably call for additional heat bridges.

What the use of plastics is concerned, one needs to keep in mind, that they can quite drastically change their behaviour below their so-called glass transition temperature, a phase transition of amorphous materials, below which flexible, viscous materials become rigid and brittle [352]. Nylon, for example, is already below its glass transition temperature at room temperature, which explains its hard character (screws are made from it).

Vibration isolation Vibration absorbing polymers, as typically used at ambient conditions, are no longer suitable at cryogenic temperature as they fall below their glass transition temperature and become rigid. The semi-crystalline teflon is a special case as it allows for elastic deformation even though its glass transition temperature lies above room temperature. In contrast to most other polymers, it maintains some flexibility down to 5 K [353–355]. In the cryopositioner setup, the base block is mounted on three 1 mm thick teflon sheets (see Fig. 6.2.2) for mechanical decoupling from the sample chamber.

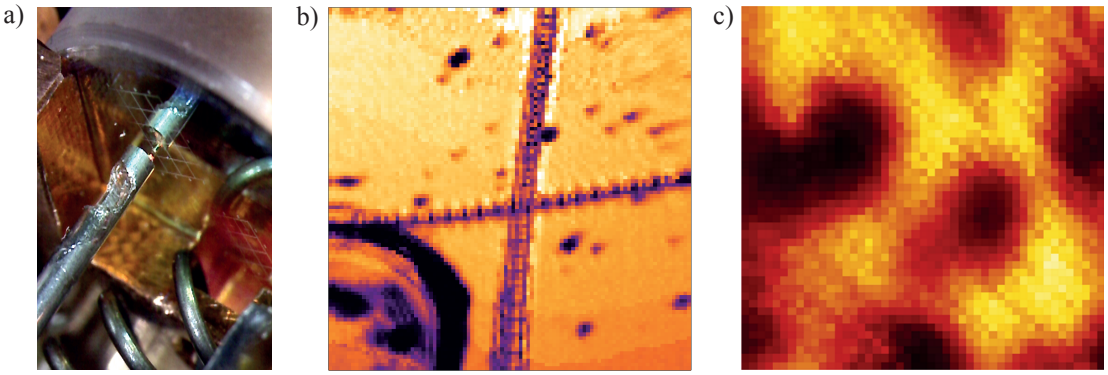

Figure 6.2.3.: (a) Syringe needle with fibre glued to it and its mirror image in planar mirror. Mirror is marked with 'battleships' pattern. In the bottom, the spring pulling the mirror towards the base block is visible. (b) Scanning cavity transmission image (arbitrary colour scale with white corresponding to highest and black to lowest transmission) of mirror mark at room temperature. Dark spots are yttria particles. Black circular feature in the bottom left is an imprint of the fibre. The lateral extent is on the order of 100 µm. (c) Scanning cavity transmission image off yttria particles at 8 K (arbitrary colour scale). The scanning range is on the order of 10 to 20 µm.

6.2.3. Coarse and fine positioning

At room temperature For easier position referencing, the planar mirror was marked with a 'battleships' style grid of five times five squares with an edge length of 525 µm each by writing thick lines into the mirror coating with the CO_2 laser. As can be seen in Fig. 6.2.3(a), the mark is visible with the bare eye and allows for coarse positioning. In each of the squares, a cross is written, whose vertical line starts at the upper edge of the square, such that it can be easily found in scanning cavity microscopy. The cross consists of fainter lines, where the mirror coating is slightly bulged by the heat of the CO_2 laser pulse, not visible to the bare eye. The lines have a thickness of approximately 10 to 20 µm.

For a fast detection of the cavity transmission, the cavity length is modulated over several free spectral ranges and the transmission trace is detected. An algorithm by Thomas Hümmer [138] run on an FPGA module[23] returns the maximum value of each trace, which is then fed to an analog input port of a data acquisition card[24] allowing to display the transmission data with software[25].

For lateral scanning, a voltage ramp is output via the data acquisition card and fed to the x and y piezo actuators, where x was chosen to be the fast and y the slow axis. The signal is low-pass-filtered and amplified[26], such that the whole allowed voltage range of the piezos (-30 to 150 V) is exploited. Note that the voltage amplifier for the fast axis

[23] Red Pitaya StemLab 125-14
[24] National Instruments NI 6323, 250 kS/s
[25] scanning routine programmed in Python by Thomas Hümmer [138]
[26] fast axis: MPQ design high voltage amplifier, gain 40; slow axis: Falco Systems WMA-02, gain 20

must have a considerably larger bandwidth than the frequency of the ramp such that the edges are well resolved.

Figure 6.2.3(b) shows a transmission scan of the cross mark written into the mirror. It is surrounded by dark spots stemming from scattering loss by Eu-doped yttria particles as can be confirmed by a fluorescence measurement. The dark circular feature in the bottom left of the image indicates damage of the mirror coating caused by a touch-down of the fibre tip. This particular scan was chosen here, as the diameter of the cross lines and the fibre imprint reveal the approximate scanning range, which should be more than 100 µm. Notably, the maximal stroke of the piezos is only 28 µm, nicely showing the mechanical amplification by the lever design.

Note that the transmission values seem to undergo discrete changes (different shades of orange). The reason is that the cavity length slightly changes for different lateral positions due to non-perfect angular alignment. As not all axial mode orders show exactly the same transmission due to transverse mode coupling losses, a different maximal transmission value is recorded when different axial mode orders are within the cavity length modulation range. This can be avoided by using a feed-forward algorithm to correct for the change of cavity length by applying an additional voltage to the z piezo, whose magnitude is linearly dependent on the lateral position. The feed-forward signal and length modulation signal are added up by a voltage adder and fed to the piezo stack. However, this method turned out to be most suitable for smaller scanning ranges and reached its limits for larger areas due to the piezo non-linearity and its limited traveling range.

Taken no length calibration or image post-processing was conducted, the linearity is quite remarkable. Nevertheless, one can observe certain image defects like a non-linearity towards the edges, which can be explained by the piezo non-linearity. Moreover, there is a certain cross-coupling between the two lateral scanning axes [350], meaning that a movement in x direction also causes a slight movement in y direction and vice versa, which manifests itself in a non-perpendicular angle of the cross mark lines and the discrete changes in transmission not forming straight parallel lines. Nevertheless, the images are highly reproducible and fast scanning allows almost real time imaging of nanoscaled samples.

For coarse positioning, the three motors are controlled by H-bridge-based motor drivers[27], such that the three motors can be moved back and forth with six digital output channels (one for each direction). Typical applied voltages range from 1.5 V to 5 V depending on how large the movement is supposed to be. For small steps corresponding to about 100 nm cavity length change, pulses of 10 ms length were applied; for coarsely moving the mirror by tens of µm, up to 200 ms long pulses can be useful. There is some clearance in the translation, such that returning to the original position requires more pulses than had to be spent for the first way, rendering absolute positioning impossible without installing some position readout scheme. However, the fast scanning images and a marked mirror make directed movements quite easy.

[27] x and y axis: Pololu DRV8833 dual motor driver, 2 A maximum output current; z axis: ST L293B push-pull four channel driver, 2 A maximum output current

During cool-down As contraction of relevant parts during cool-down leads to a quite drastic reduction of the cavity length on the order of 100 µm, continuously scanning turned out to be challenging. This is why, during cool-down, only the cavity length was modulated over several FSR to monitor the change and compensate for it by gradually retracting the z screw. Before the cool-down, the lever needed to be tightly prestressed such that the modulation piezo would not become loose rendering length modulation impossible.

To maintain motor functionality down to target temperature, all lubricant is removed from the motors by thoroughly rinsing them in acetone. Also, the micrometer screws need to be cleaned as they can get stuck otherwise. Next, motors, gears, and micrometer screws are lubricated with teflon spray[28]. As the electrical resistance of the motors decreases with temperature by up to a factor of five, a voltage source for the motor drivers allowing currents up to 1 or 2 A needs to used.

In consequence, an electrical power on the order of 1 W is applied, leading to significant heating of the motors. The fact that the base block and sample temperatures only slightly rise by a few degrees when applying a voltage to the motors for minutes, evidences the good thermal insulation to the base block.

Observing the position of the fibre on the grid mark through the collection window, showed that a lateral displacement of several 100 µm took place in negative y and positive x direction. The likely reason is that the metal parts contract more than the piezo ceramics such that the fibre is pushed to the side and down.

At low temperature Due to the reduced traveling range of the piezos at low temperature, voltage amplification[29] is now also applied to the z piezo to be able to modulate over a few free spectral ranges. A transmission scan at low temperature can be seen in Fig. 6.2.3(c) showing Eu-doped nanoparticles (confirmed by a fluorescence measurement). Judging from the relative size of the spots, the estimated scanning range is about 10 to 20 µm, as expected. It is possible to move the mirror around with the motors while scanning to search for suitable particles. No relevant drift has been observed and the position does not have to be readjusted over minutes. This will allow for long term experiments with one and the same nanoparticle.

6.3. Achieved Stability

This section discusses locking schemes and their application, presents noise spectra of the setup, and describes the challenges of cavity length stabilisation at cold temperature.

[28] It was observed that some motors got stuck when cooled down, while others worked fine; so having some in stock can be useful.

[29] Falco Systems WMA-300 high speed high voltage amplifier, 5 MHz bandwidth

6.3.1. Locking schemes

Side of fringe locking For first testing, side of fringe locking was applied using either the 640 nm or the 580 nm light. This means that the fringe of the cavity resonance is directly used as an error signal. Clearly, this method does not allow locking on top of the resonance as a decreasing signal does not contain information on the sign of the necessary compensation. Locking can only be realised on one of the two sides of the resonance, where the polarity of the feedback signal chooses one side. This implies that the lock can only be maintained as long as the length jitter is not large enough to cause a shift over the resonance tip, resulting in the system being driven away from resonance. So the setpoint (being the level to be stabilised to) must be chosen such that the system remains on the fringe. The smaller the jitter, the higher the setpoint can be.

Side of fringe locking is not very well suited while the cryostat is running due to the large amplitude of the length jitter during the noisy phase of the cryostat cycle, where the larger capture range of the PDH lock is beneficial. If a side of fringe lock were to be implemented, it would be conducted on the red locking laser, which would be tuned such that the tip of the 580 nm resonance overlaps with the centre of its fringe, thereby allowing for permanent locking during pulsed excitation.

In practice, the side of fringe lock is frequently used for analysing the system's length jitter and recording noise spectra. The reason is that a recorded voltage timetrace can easily be converted into units of cavity length change: Knowing the finesse gives the cavity length change linewidth δd according to eq. 6.1.1. The maximum voltage on top of the resonance together with δd completely defines the Lorentzian line shape. The derivative of this Lorentzian evaluated at the setpoint constitutes a conversion factor K from voltage to length scale. The RMS length jitter can then be determined by multiplying K to the voltage jitter, which can be directly read out from the oscilloscope[30]. For noise spectra, the voltage timetrace is Fourier transformed by the oscilloscope. The power spectrum in dBm can then be converted to V via

$$[\mathrm{V}] = \sqrt{50\Omega \times 1\mathrm{mW} \times 10^{[\mathrm{dBm}]/10}}. \tag{6.3.1}$$

The RMS noise can be obtained by integrating the power spectral density, PSD, and taking the square root:

$$\mathrm{RMS} = \sqrt{\int \mathrm{PSD}\,\mathrm{d}\nu} \tag{6.3.2}$$

For discrete normalised Fourier components $\hat{x}_i$ and $\mathrm{PSD_i} = \hat{x}_i^2/\Delta\nu$, this yields[31]

$$\mathrm{RMS} = \sqrt{\sum_{i=1}^{N} \frac{\hat{x}_i^2}{\Delta\nu}\Delta\nu} = \sqrt{\sum_{i=1}^{N} \hat{x}_i^2}. \tag{6.3.3}$$

[30] LeCroy WaveRunner HRO 64Zi 400 MHz 12-bit oscilloscope, 2 GS/s

[31] The Fourier components $\hat{x}_i$ are not equivalent to the raw FFT components, as $\hat{x}_i = \mathrm{FFT}\,(x_i)\,/N$ with N being the number of sample points [356]. However, what the oscilloscope calls 'FFT' is in fact already normalised, which is somewhat misleading. This implies that eq. 6.3.3 holds for the oscilloscope data. In case of 'real' FFT data, an additional factor $1/N$ would be needed. For details, see [138].

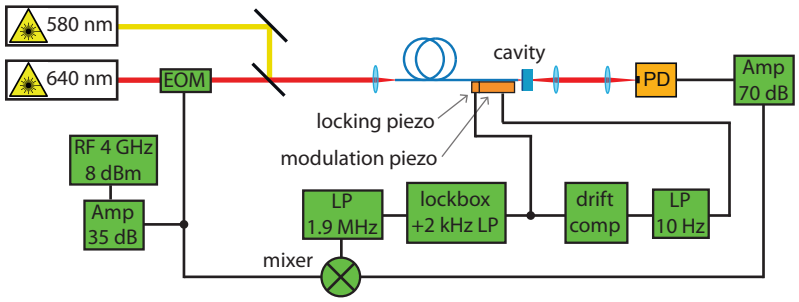

Figure 6.3.1.: Schematic drawing of PDH feedback loop. Amp: amplifier with gain in dB. LP: low pass with cutoff frequency. RF: radio frequency source with oscillation frequency and amplitude.

Note that the power spectrum provided by the oscilloscope is not a power spectral density (in units of dBm/Hz), meaning that changing the sampling rate and therefore the frequency resolution changes the amplitude values x_i. For proper comparability of several noise spectra, it is therefore important to either convert them to a spectral density or always choose the same sampling rate (the latter is done here). Converting the RMS voltage noise to RMS length noise by multiplying it with the conversion factor K allows for a comparison with the value directly obtained from the time trace. The two values being approximately the same ensures that the spectrum was correctly converted.

Clearly, a lower finesse can be more easily locked due to the larger length change linewidth. This is why, in practice, one starts optimising the mechanical setup while locking on the 640 nm resonance. However, the higher the finesse, the more accurate the noise spectrum, due to the smaller relative contribution of the detector noise. The reason is that the voltage change of the signal per change of cavity length (conversion factor K) is larger. So for highest sensitivity, the largest slope should be chosen, i.e. a high finesse (in this case the 580 nm light) and a setpoint around the inflection point of the fringe.

Passive stability tests with drift compensation Optimising both the lock parameters and the mechanical system at the same time can be challenging because noise within the locking bandwidth is compensated. If this noise could, however, be reduced by mechanical optimisation, the gain could be set lower allowing for a higher bandwidth. It is therefore useful to decouple the mechanical optimisation from finding good locking parameters. However, without any active stabilisation, drifts cause the system to fall off the resonance, which renders the recording of meaningful noise spectra impossible. To solve this, a software-based drift compensation (integrative controller, see [138]) with a bandwidth of 10 Hz is applied. The feedback signal from the digital-to-analog converter (data acquisition card) was strongly low-pass filtered such that its noise contribution was negligible. Being able to lock a finesse of 17 000 merely with this drift compensation evidences the good passive stability of the system.

PDH lock with analog lockbox Once good passive stability at high frequencies is achieved, a modified analog lockbox was used to compensate low frequency noise. The lockbox consists of an I^2 controller and an integrated low pass filter with variable cut-off frequency, where the bandwidth was typically limited to around 2 kHz in this case. The required gain drastically varies from compensation of slow drifts up to micrometer scale, to sub-pm stabilisation at moderate frequencies, which is why a two-stage approach is applied, depicted schematically in Fig. 6.3.1 for the PDH lock. The low-pass-filtered error signal is fed to the lockbox, whose output signal is applied to the small locking piezo and, in addition, is used as an input signal for the software-based drift compensation. The heavily low-pass-filtered output of the digital to analog converter is fed to the large length modulation piezo for a coarse offset and drift compensation. Note that the capacitance of the locking piezo (160 nF) together with the output resistance of the lockbox (100 Ω) results in an additional effective low pass filter with a cutoff frequency of about 10 kHz. In this case, this is not limiting the bandwidth, but one should keep in mind not to use piezos with too high capacitance. The described setting can very similarly be used for side of fringe locking, where the detected transmission signal is directly fed to the lockbox. The gain must then be adjusted due to the different slope K.

Optimisation of the locking parameters is conducted according to the following procedure: One starts with the lockbox only, while manually correcting for drifts. The gain of the analog lockbox is increased until the onset of ringing, then slightly reduced again such that the ringing stops. This is repeated for different cutoff frequencies while observing the noise spectrum to find a good trade-off between locking bandwidth and good suppression of small frequency noise. The higher the bandwidth, the lower the gain must be set to avoid exciting mechanical resonances. Typically, an additional attenuator (6 dB) was used at the lockbox input, as the lowest possible gain already causes ringing otherwise, which can be explained by the rather large stroke of the piezo. Once the moderate frequency noise is well suppressed, the drift compensation is switched on while already in lock. It tends to be rather uncritical concerning its settings and includes a recapture scheme in case the system falls out of lock.

Digital lock To avoid the rather noisy lockbox and to be able to implement more flexible and demand-oriented locking schemes in future, an FPGA-based digital lock was investigated in collaboration with the group of Nestor Oliverio at Keysight Technologies. The FPGA board comprises a digitizer and arbitrary waveform generator[32] and can be freely programmed using a Vivado-based software[33] provided by Keysight. The status of the project is a working PID controller with in situ tunable parameters and setpoint, which has been successfully tested for cavity stabilisation.

[32] Keysight M3300A PXIe AWG and Digitizer Combination, 500 MSa/s, 16 bit, 200 MHz bandwidth and 100 MSa/s, 14 bit, 100 MHz bandwidth

[33] Keysight M3602A

6.3.2. Noise spectra

Without active stabilisation Before discussing cavity stabilisation, let us consider the free running system without active locking. For measuring the RMS length jitter, the cavity length was swept over resonance, while the transmission was detected. From a single sweep, one recovers the expected length change linewidth of 17 pm. For longer integration times, averaging over many sweeps, the noise broadens the line. The yellow trace in Fig. 6.3.2 was recorded by averaging 1000 sweeps over 1.5 min. A Gaussian fit to this length jitter distribution yields a standard deviation of 890 pm. When the cryostat is switched on, the additional noise further broadens the distribution (blue trace). Fitting a Gaussian gives a standard deviation of 2.6 nm. However, the fit to the data is not very accurate as the noise is overlain by a slow uni-directional drift, which means that the real noise is somewhat smaller. Nevertheless, even without the cryostat running, the jitter is about two orders of magnitude too large to stay on resonance, motivating the need for active stabilisation.

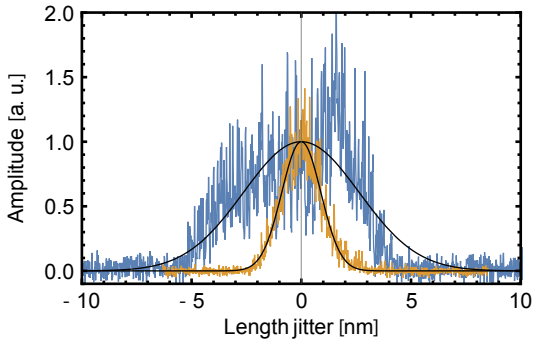

Figure 6.3.2.: Length jitter recorded by modulating cavity length over resonance and averaging over 1000 sweeps (1.5 min). Amplitude normalised. Blue: cryostat on. Yellow: cryostat off. Black: Gaussian fit.

Mechanical and electric optimisation Using the software drift compensation only, the mechanical system was optimised. The best value achieved for the RMS length jitter in this case were 2 pm, which evidences a high passive stability, taken the bandwidth of the drift compensation of only about 10 Hz. Moreover, the remaining noise is largely concentrated in the low frequency band: Integrating the noise spectrum starting from 150 Hz, one obtains an RMS value of only 0.6 pm. Frequencies lower than that are not so critical as they can be compensated for.

To achieve this passive stability, several measures were found to be useful. Before optimising the mechanical components, electronic noise should minimised. It is typically characterised by sharp spikes in the noise spectra. Apart from filtering, avoiding ground loops is crucial, which is why all cables going to the setup where electrically isolated from one another. Wherever possible, coaxial cables are applied and otherwise, the individual strands are well twisted to reduce the impact of external fields. On the mechanical side, a very important point is affixing the piezo cables to the base block with teflon

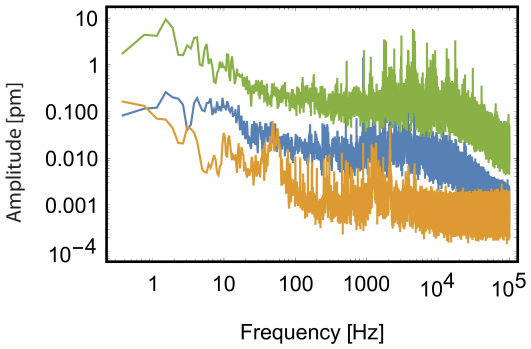

Figure 6.3.3.: Noise spectra for PDH lock with cryostat switched off (yellow), with cryostat running at room temperature (blue), and side of fringe lock at 12 K (green).

sheets (see Fig. 6.2.1(b)), which greatly reduces noise. A rigid connection between the mirror mount and base block prohibits a relative movement along the cavity axis. This is why the connection point of the restraint spring must lie in the middle of the triangle spanned by the three glass balls. Care must be taken that the copper finger, which serves as thermal connection to the cold platform, does not touch the base block to prevent the transfer of vibrations. Closing the sample chamber further reduces the noise, meaning that acoustic noise also plays a role. Interestingly, evacuating the sample chamber does not bring further improvement. Moreover, it does not matter whether the vacuum pump is running. Once the sample chamber is closed, acoustic noise is largely uncritical, which implies an efficient decoupling from the table and the housing. It was observed that the braided wire thermal bridge is not yet flexible enough and vibrations can be transferred to the mirror. To avoid this, the wire is clamped to the base block using teflon sheets and nylon screws (see Fig. 6.2.2(b)), which unfortunately leads to a temperature rise by a few K. In a revised setup, a more flexible solution needs to be found for the thermal bridge.

Analog lock A fibre modulation measurement showed that the first mechanical resonance on the fibre side occurs at 3.3 kHz. This value was obtained by applying a sine voltage to the locking piezo, sweeping the frequency, and observing the transmission on the fringe of a 532 nm resonance, which is broad enough ($\mathcal{F} = 52$) to passively remain there for minutes. Recording amplitude and phase of the transmission timetrace revealed the first resonance frequency, which comes with a π phase shift. This means that locking with a bandwidth of 2 kHz is reasonable.

The yellow trace in Fig. 6.3.3 shows a noise spectrum taken at room temperature using the analog lockbox and PDH locking (for a linear plot, see Fig. 6.3.5, blue trace). Length jitters on the order of 0.4 pm RMS can be achieved, already limited by the detector noise floor. Below about 1 kHz, the noise is reliably compensated, and above 2 kHz, hardly any noise is visible. Between 1 and 2 kHz, some spikes remain, which could be further suppressed with a sharper gain profile.

Switching on the cryostat, the cavity stays locked over the entire cryostat cooling cycle,

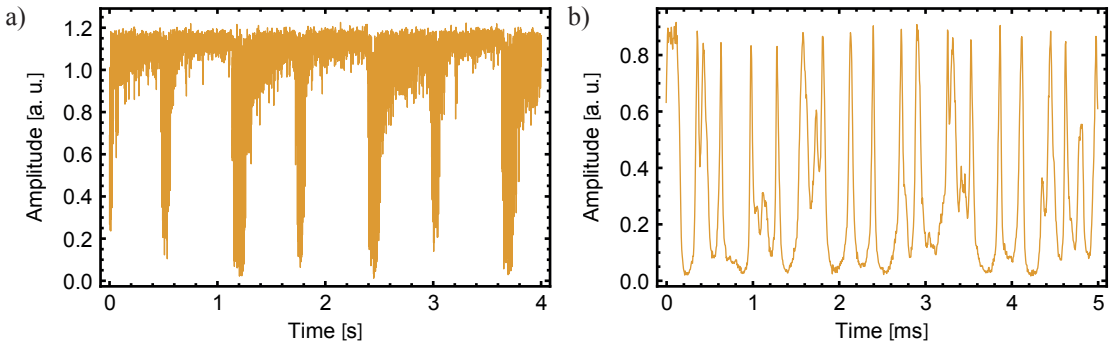

Figure 6.3.4.: (a) Transmission timetrace of 580 nm light while PDH locking at room temperature with running cryostat. (b) Transmission timetrace of 580 nm light while PDH locking at 12 K; close-up of the most quiet part of the cryostat cycle.

with a reliable PDH lock on top of the 580 nm resonance still being possible during the quiet phase of the cryostat cycle, which can be seen in a 580 nm transmission timetrace in Fig. 6.3.4(a). The corresponding noise spectrum is shown in blue in Fig. 6.3.3. The length jitter amounts to about 4 pm RMS, averaged over the whole cooling cycle. The noise below 1 kHz is still well compensated for, while multiple higher frequency noise components in the range of 1 to 6 kHz accrue.

Surprisingly, at low sample temperature, one observes a significant increase in mechanical noise by more than a factor of 10. The integrated noise level is then 60 pm, which is already larger than the cavity linewidth. This can be seen in the timetrace in Fig. 6.3.4(b), which is a close-up of the most quiet part of the cooling cycle. Clearly, the cavity does not remain in lock long enough to perform experiments. Regarding the noise spectrum (green trace in Fig. 6.3.3), which is recorded while performing side of fringe locking on the 640 nm resonance, it is apparent that the noise level is increased throughout the spectrum, in particular also at high frequencies up to several tens of kHz. It should be noted that the gain settings must be chosen differently at cold temperatures as the piezos have a smaller traveling range. The gain can be adjusted most accurately, if the cryostat is switched off during the process for a short period of time (seconds). It is not readily clear what causes the drastic increase of vibrations upon cool-down. Stepwise increasing the temperature while successively locking and taking noise spectra, showed that the noise gradually decreases with rising temperature. It appears most likely that either thermal contraction makes parts of the upper and lower part of the setup touch each other thereby transferring vibrations or that the teflon sheets become too rigid to effectively damp out high frequency vibrations. This would then also be a natural starting point for revising the current setup.

Digital lock As the digital lock implemented on the Keysight FPGA system does not yet include filters, a simple analog low pass filter (2 kHz cutoff frequency) was added at the output. The achieved noise spectrum at room temperature is shown as yellow trace in Fig. 6.3.5 and can be compared to using the analog lockbox (blue trace). The achieved

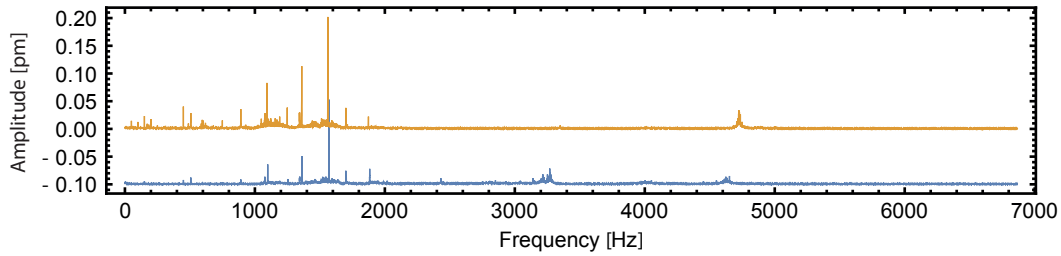

Figure 6.3.5.: Noise spectra for PDH lock at room temperature, using analog lockbox (blue) and digital lock (yellow).

length jitter is 0.6 pm RMS, only slightly worse than the analog lock, in particular for the low frequencies. As soon as the filters are implemented, it should be possible to further increase the gain and beat the analog lock. In the spectral region above 2 kHz, the digital lock (PI controller) is already superior.

6.4. Outlook

A rigid, low-cost, and fast cryocompatible positioning stage was presented, demonstrating SCM imaging at cryogenic temperature. A remaining length jitter of 4 pm averaged over the cooling cycle of the cryostat evidences a high stability of the system, which would be sufficient for spectroscopy of Eu ions with the described cavity system. However, the drastic increase of vibrations at low temperatures still hampers this endeavor. This calls for a revised version of the positioning stage. Especially, the teflon sheets, which apparently become too stiff when cold, should be replaced by soft springs, which should reliably cushion high frequencies. Furthermore, the copper thermal bridge must become more flexible: Instead of using the copper finger, whose unfavourable geometry could enhance vibrations, the whole thermal bridge from the cold platform to the mirror holder should be a flexible braided wire, thermally insulated from the base block and the lower pipe with teflon rings. These measures hopefully resolve the vibrations issue.

To mitigate the issue of large deformations due to thermal contraction, the main parts of the setup should be fabricated from titanium instead of aluminium. However, due to the much lower thermal conductivity of titanium, more thermal bridges are needed. The thermal connections between the lower block and the base block should be replaced by more flexible copper sheets or braided wires.

In case even higher stability is required, one can think of establishing a rigid connection between fibre and mirror. A certain tunability could be maintained by making use of a piezo tube scanner. To motivate the idea of establishing contact between the two mirrors, noise spectra were taken while the fibre tip was pushed to the planar mirror (Fig. 6.4.1) at cryogenic temperature. The yellow trace is taken at 12 K with the cryostat running, while the blue trace is taken shortly after the cryostat is switched off, at a temperature of about 15 K. Comparing to the green trace in Fig. 6.3.3, the drastically enhanced stability is striking. Regarding the length jitter, a value of 7 pm was measured for the

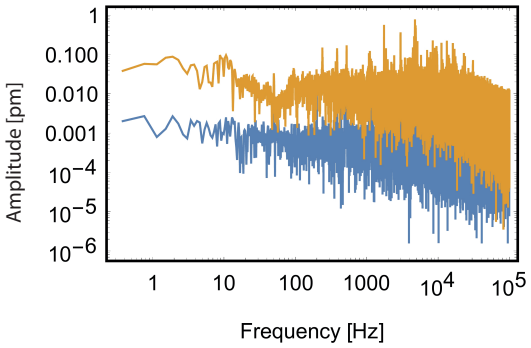

Figure 6.4.1.: Noise spectra for side of fringe lock on 580 nm resonance with fibre being in contact with the mirror. Blue: cryostat off (about 15 K). Yellow: Cryostat on (12 K).

case where the cryostat was running (compared to 60 pm without contact) and 0.3 pm with the cryostat switched off, where the latter is limited by the detector noise. Hence, a combination of better vibrational decoupling and establishing a contact between the two mirrors has the potential to allow for successfully locking a much higher finesse cavity.

7. Conclusion

This work has treated cavity enhanced light matter interaction applying fibre-based microcavities. After discussing technical aspects of such microcavities, in particular transverse-mode coupling, cavity coupling of two different solid state quantum systems was presented: The demonstration of significantly enhanced single-photon emission from SiV centres guides the way towards an efficient, bright single photon source at room temperature. Furthermore, first cavity enhanced measurements on a small ensemble of europium ions were conducted, where the presented home-built nanopositioning stage promises to enable single ion addressing in the near future. This chapter gives a recapitulation of some central aspects of this work as well as an outlook.

Avoiding or harnessing transverse-mode coupling It was shown that additional diffraction losses at specific, reproducible axial mode orders are evoked by transverse-mode coupling, which leads to a finesse reduction, frequency shifts, and a distorted mode. An imperfect mirror geometry and a finite mirror size were found to be the cause of this coupling, for which an accurate numeric simulation was presented. With this model, it becomes possible to predict the performance of a cavity, which is helpful for optimising the geometry and predict suitable axial mode orders for a reliable behaviour. One could also think of harnessing the knowledge about transverse-mode coupling for non-trivial novel cavity design and individual mode tailoring, such as single-transverse-mode operation [357, 358]. With mode tailoring, higher order modes can be suppressed without significantly affecting the fundamental mode, for example to improve spectral filtering or mode imaging [359], where a specifically designed cavity mode can avoid scatterers in the cavity, thereby reducing loss. [94]

In scanning cavity microscopy, near-resonant transverse-mode coupling was shown to cause two kinds of artefacts: Sharp ring-like features could be traced back to the surface topography of the planar mirror, while weak periodic background patterns are caused by microscopic surface roughness. The variation of the effective radius of curvature due to the local surface angle of the planar mirror leads to line shift variations on the order of GHz, even for super-polished mirrors. This high sensitivity to local surface inclination can be relevant for cavity QED experiments with solid state emitters. When for example integrating thin diamond membranes into a scanning cavity geometry [173, 306–308], slight imperfections of the membrane surface together with mode coupling can lead to further modifications of the non-trivial mode structure present in such systems. Resonant mode coupling could potentially be harnessed to sensitively characterise mirrors for high precision applications like laser gyroscopes, high-finesse reference cavities, or gravitational wave detectors. [95]

Generally, mode coupling is minimised for mirror geometries approaching a sphere. Such optimised mirror profiles could be achieved by multi-shot laser machining [137] or precise focused-ion-beam milling [162], where the latter might profit from CO_2 post-treatment to obtain better surface smoothness [360]. [95]

Towards an indistinguishable single photon source at room temperature Single silicon vacancy centres in diamond coupled to a microcavity offer the prerequisites for an efficient, bright single photon source at room temperature. Their narrow, prominent zero phonon line allows for high Purcell factors and a narrow-band emission. In this work, a significant Purcell enhancement was demonstrated for narrow line single SiV centres, reaching photon emission rates over 20 MHz into a well-collectible cavity mode at a linewidth of around 20 GHz. A revised rate model for the SiV was introduced, which accurately reflects the observed power-dependent dynamics. [53]

The potential of the presented approach could not be fully exploited with the available sample: The nanoparticles introduced large scattering and absorption losses; they did not contain single SiV centres but ensembles, such that strongly spectrally shifted lines with largely unknown properties had to be chosen; the quantum efficiency was moderate and many emitters lacked permanent photo-stability. Small nanodiamonds containing one single bright and narrow line SiV centre with high quantum efficiency and featuring a good crystal quality are currently not available, although recent efforts on the material side [285, 289] seem promising. With a quantum efficiency of 30%, which seems in reach [50], the presented cavity coupling scheme could reach single photon rates on the order of GHz and device efficiencies close to unity, unprecedented for a solid state system at ambient conditions. Such a system would allow high bandwidth quantum key distribution and open the path for efficient shot-noise-unlimited sensing applications.

Integrating such an improved sample into a high Q microcavity, as was machined and tested in the course of this work, the emission spectrum could be compressed to the level where indistinguishable single photon emission is possible at room temperature. The achievable efficiencies are predicted to be orders of magnitude better than with spectral filtering [54]. Such an indistinguishable single photon source could be beneficial for various quantum information applications: They could enhance the entanglement distribution rate in memory-based quantum repeaters [30, 31] or could potentially meet the requirements for all-optical quantum simulation [39–41] and computation schemes [35, 36, 38]. Additionally making use of the spin degree of freedom, for which a coherence time of 13 ms was recently demonstrated [361], the system could be used to establish an efficient spin-photon interface in a future quantum network and interactions between several SiV centres could be realised by coupling them to one and the same cavity mode [362].

Addressing single europium ions I outlined first steps towards the detection of single europium ions in yttrium oxide nanoparticles. In a first cavity coupling experiment at cryogenic temperature, it was possible to address a small ensemble of on the order of 10 ions in a single nanocrystal. The estimated single ion photon count rate of 30 cps from

the cavity-coupled $^5D_0 - ^7F_2$ transition already evidences an enhancement compared to the expected count rate for confocal detection of the whole emission spectrum. In this experiment, the cavity was on resonance only during a small fraction of time, such that active cavity locking holds the prospect of much larger rates, then also being able to cavity couple the coherent $^5D_0 - ^7F_0$ transition. [85]

For this goal, a novel cryocompatible nanopositioning stage was developed and tested, based on a rigid flexure bearing design. It features full tunability and fast scanning cavity imaging, while offering a high passive stability over a large frequency range. Applying an active length stabilisation scheme, the cavity could be successfully locked on resonance during the entire cryostat cooling cycle with a length jitter on the order of pm, exceeding commercially available solutions. Both fast scanning and coarse positioning could be successfully operated at cryogenic temperature. A remaining obstacle is the drastically increased noise transfer to the stage at cold temperature, having prevented reliable locking. A spring bearing in a revised setup should be able to damp out this high frequency noise such that locking of a high finesse cavity at cryogenic temperature in a noisy environment is in reach.

To reduce scattering loss and enhance the emission rate, a new sample preparation method was devised and implemented: Embedding the Eu-doped yttria nanoparticles into a thin film of PMMA, whose thickness is chosen to maximise the field intensity, a significant reduction of the excited state lifetime could be observed. Calculations predict about a threefold enhancement of the detected emission rate compared to the traditional sample preparation method, where the nanoparticles reside on a spacer layer. Embedding the particles into a thin film of yttria could even lead to a fourfold increase compared to the traditional method.

Using this new sample and operating a locked high finesse cavity with a realistic geometry, emission rates from the desired $^5D_0 - ^7F_0$ transition into the cavity mode could reach 10^5 photons s^{-1} per ion, such that single ions could be efficiently detected. The extraordinary nuclear spin coherence makes this system a promising candidate for a node in a large scale quantum network [14, 15], being used as single qubit quantum memory and for the implementation of quantum logic, where individually addressing single europium ions and harnessing the large dipole interactions bears the prospect of realising a multi-qubit register.

A. Overview of cavity parameters

This section contains a look-up table of all important cavity parameters used for the experiments in this work. If not otherwise stated, the coatings were applied by Laseroptik GmbH.

	A	B	C	D
used in chap.	3.2	4	5	3.3.3
fibre name	?	9A	23F	29A
machined by	D. Hunger	B. Schlederer	F. Oehl	J. B.
λ_0 of fibre mirror (nm)	780 (ATF)	740	585	740
T at λ_0 (ppm)	10	1500	100	10
absorption loss (ppm)	12	20	30†	10
λ_0 of planar mirror	780 (Layertec)	780	585	740
T at λ_0 (ppm)	60	60	190	10
absorption loss (ppm)	34	20	30†	10
spacer layer?	$\lambda/4$ SiO_2	20 nm SiO_2	80 nm PMMA	no
$\mathcal{F}$	60 000	3750	17 000	57 500 at 786 nm
shortest d ($\lambda/2$)	9	5	9	14
largest Q_c	10^7	$19 \times 10^{3\star}$	$1.3 \times 10^{5\star}$	2×10^7 at 786 nm
w_0 (µm)*	2.5	1.0	1.1	3.3
r_C (µm)	161 (x), 201 (y)	25.1 (x), 27.0 (y)	20	350
profile depth t (µm)	2.2	0.3	1.5	3.0
profile radius a (µm)	26 (x), 29 (y)	3.5	7.6	43
smallest V_m (λ^3)	36	3.4	2.6	97
outcoupling efficiency	52%	90% at 740 nm	54%	41% at 786 nm
MFD of fibre (µm)	7	5	4	5

Table A.1.: Overview of fibre parameters. *for smallest mirror separation. †Estimated from finesse.

B. Transverse mode coupling scans

B.1. Selected scans with Fourier transform

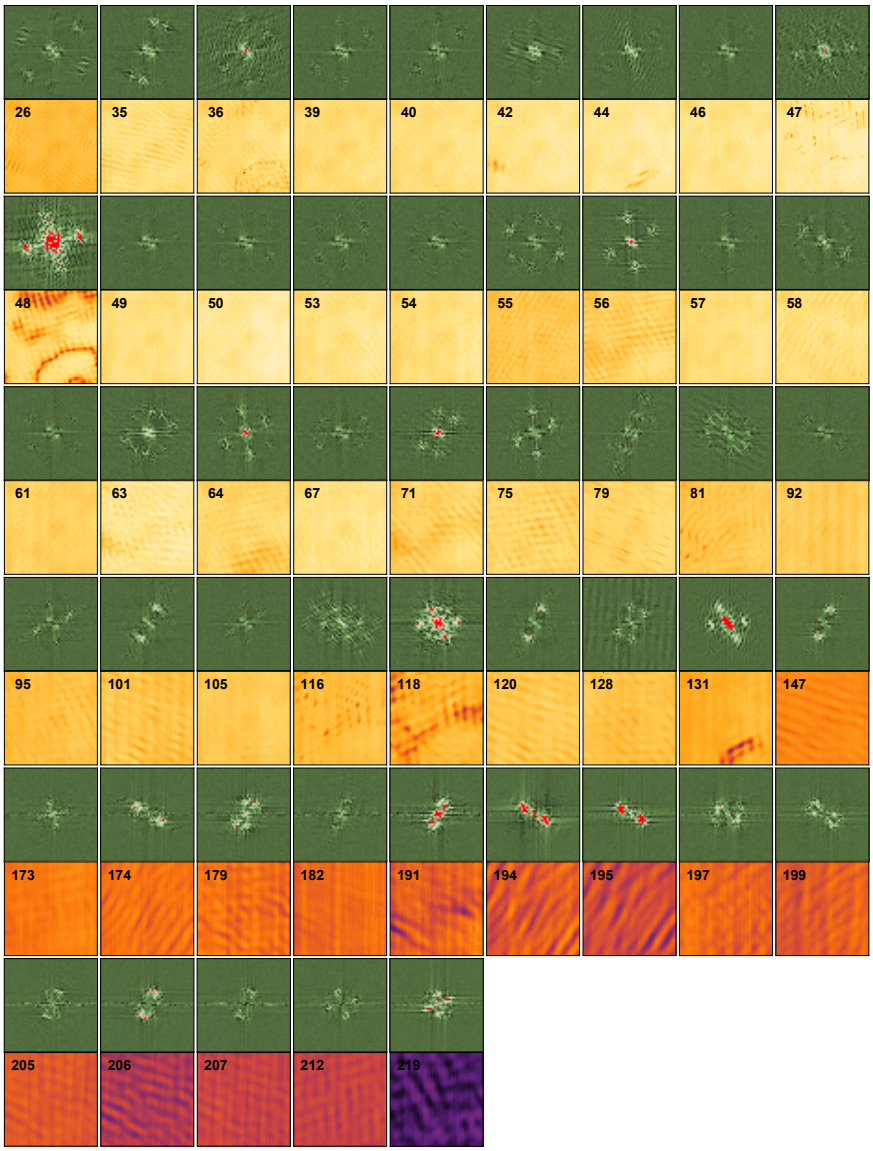

B.2. Transmission scans for all axial mode orders

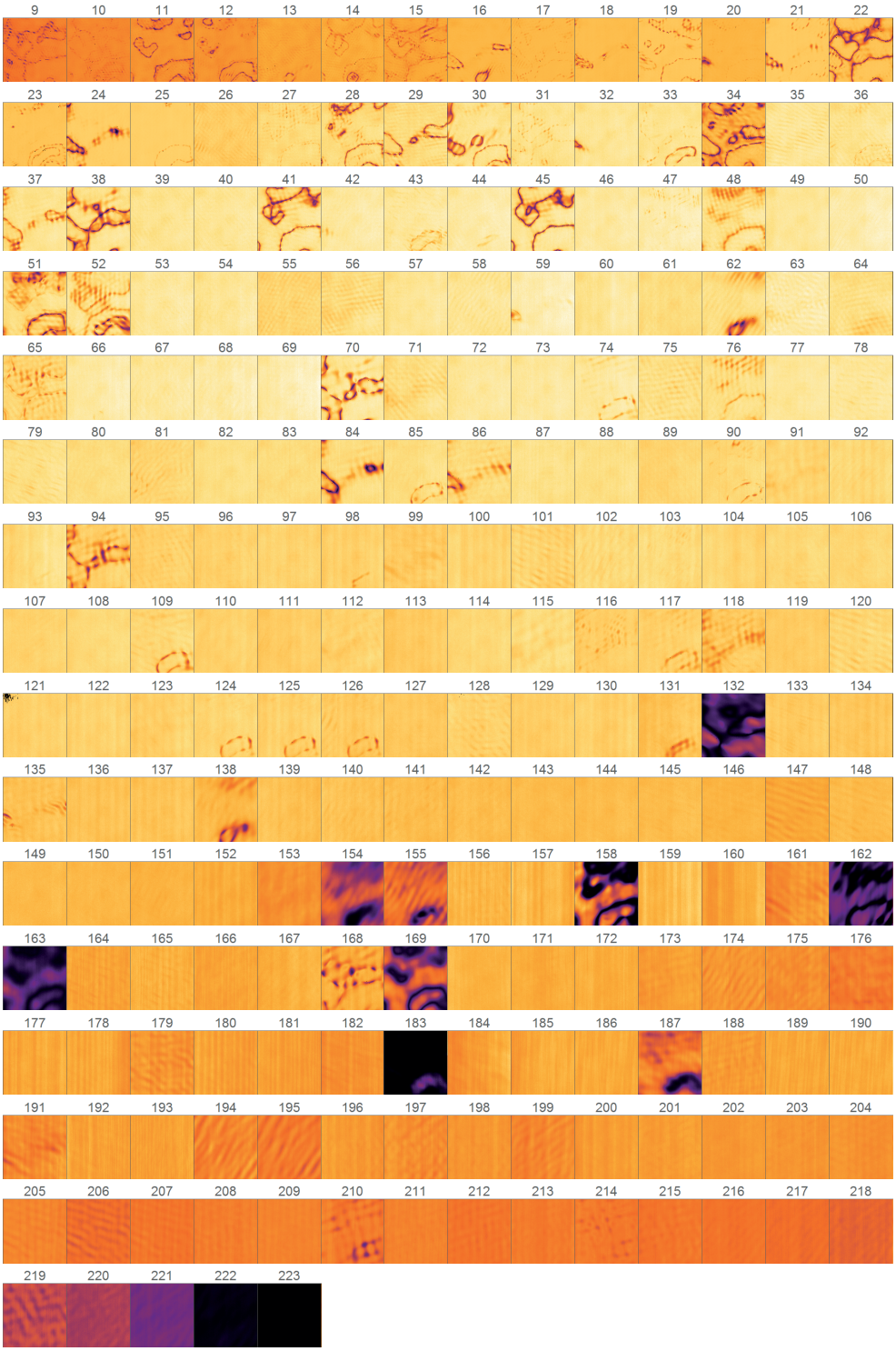

C. Calibration of two-in-one setup

For calibrating the offset between the objective and the fibre cavity, the mirror was marked with a standard permanent marker. Care was taken to make the dot quite small. Figure C.1(a) shows a fluorescence image of the dot taken with the objective. As the dot is visible with the bare eye, it was possible to coarsely move it into the objective focus or into the cavity mode. The absolute position of a sharp feature (white circle) was noted; then an SCM scan was taken in the fibre cavity (Fig. C.1(b)). The pointed feature is also clearly visible here. The vertical and horizontal offset between the two positions is saved in the measurement software such that fast switching between the two modes becomes possible. After this coarse calibration, a fine adjustment using SiV nanodiamonds (see Fig. 4.3.5) was conducted. It was found that the coarse alignment was correct with a tolerance of less than 10 µm.

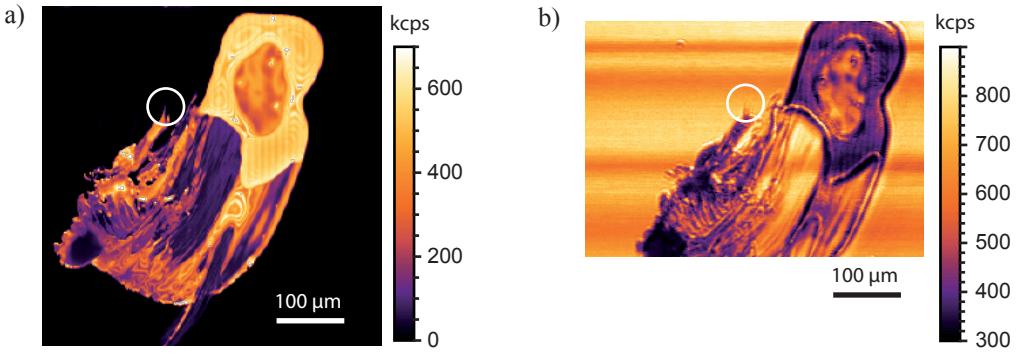

Figure C.1.: Dot on mirror made with an ordinary permanent marker. (a) Fluorescence confocal microscope image. (b) SCM image. The pointed feature in the white circle was used for calibration.

D. Determining the timing jitter for $g^{(2)}$ lifetime measurements

The total $1/e^2$-width of the system response function is given by

$$\sigma = \sqrt{\sigma_{\mathrm{APD1}}^2 + \sigma_{\mathrm{APD2}}^2 + \sigma_{\mathrm{TDC}}^2 + \sigma_{\mathrm{laser}}^2} \tag{D.1}$$

as the convolution of Gaussian functions is again a Gaussian with the widths adding up quadratically. The broadening due to the laser is given by its pulse length (50 ps FWHM), so

$$\sigma_{\mathrm{laser}} = \frac{50\,\mathrm{ps}}{2\sqrt{2\ln 2}} = 21.2\,\mathrm{ps}. \tag{D.2}$$

There were two TDCs available, the quTAU from qutools and the PicoHarp 300 from PicoQuant. The former was predominantly used for the measurements as it allows for larger delay times. However, the PicoHarp has a higher resolution of 4 ps (compared to 81 ps of the quTAU), which is much smaller than the timing jitter considered here, such that it is taken as negligible here. The timing jitter of the two APDs was measured individually by a start-stop measurement, where a trigger pulse from the supercontinuum laser was taken as start and the APD pulses as stop signal. The measurement was conducted with both TDCs. The results given in table D.1 were obtained by Gaussian fits. Note that the laser jitter is already included here. The resulting value for $\sqrt{\sigma_{\mathrm{APD1}}^2 + \sigma_{\mathrm{APD2}}^2}$ is found to be much too large to fit the $g^{(2)}$-measurements. In addition, the values for the individual APDs are larger than the manufacturer specifications, which are 102 ps for APD1 and 105 ps for APD2. So there is some additional unknown broadening mechanism. However, even though the measurement does not yield meaningful results for the APDs, a comparison of the values for both TDCs gives an estimate for the jitter of the quTAU. As its jitter is convoluted with the detection jitter, it can

σ [ps]	quTAU	PicoHarp	$\sqrt{\mathrm{quTAU}^2 - \mathrm{PicoHarp}^2}$
APD1	164	126	105
APD2	219	174	133
$\sqrt{\sigma_{\mathrm{APD1}}^2 + \sigma_{\mathrm{APD2}}^2}$	274	215	

Table D.1.: Timing jitter obtained from Gaussian fit to start-stop measurement with both TDCs. Rightmost column: From the quadratic difference follows the jitter of the quTAU if the jitter of the PicoHarp is assumed to be negligible.

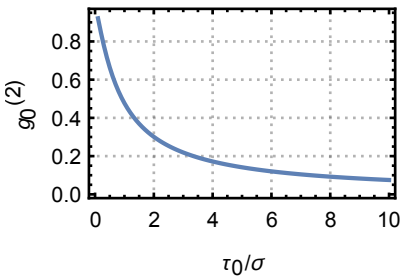

Figure D.1.: The minimal $g^{(2)}$-value for different ratios of lifetime to timing jitter.

be determined by the quadratic difference between the two values as given in the rightmost column with a mean value of 119 ps. Inserting this into eq. D.1 together with the manufacturer values yields $\sigma = 190\,\text{ps}$. A theoretical consideration taking into account the bin width of the quTAU of 81 ps with $\sigma_{TDC} = \frac{81\,\text{ps}}{\sqrt{2}} = 57\,\text{ps}$, results in $\sigma = 151\,\text{ps}$. The mean value of 170 ps between experimental and theoretical value was found to fit the measurements well.

Figure D.1 shows the minimal $g^{(2)}$-value, which can be ideally reached (i.e. without uncorrelated background light) for a given ratio of the lifetime to the timing jitter width. To get $g^{(2)}(0) < 0.5$, $\tau_0 > \sigma$ is necessary.

E. Frequency scales of Eu experiment

As the various linewidths relevant in the europium experiment might lead to confusion, the following table gives an overview:

inhomogeneous linewidth	22 GHz
homogeneous linewidth	200 kHz at 10 K
mean distance of homogeneous lines	750 kHz
laser linewidth	$\sim$ 100 kHz
laser modulation amplitude	few 100 MHz
cavity linewidth at 580 nm	1.6 GHz
cavity linewidth at 612 nm	5 GHz

F. Cryomaterial parameters

Note that the values of both thermal conductivity and thermal expansion coefficients are given at room temperature, but decrease significantly for lower temperatures. However, their ordering typically stays the same. For example, aluminium still has a larger thermal expansion coefficient than titanium at cryogenic temperature, only the absolute values differ. For graphs showing the temperature dependence of both coefficients for important materials down to 0 K, consult [363, 364].

Material	Th. conductivity [W/ (m K)]	Th. expansion [10^{-6}K^{-1}]
copper	$240 - 380^{(a)}$ [365]	16.5 [366]
aluminium	236	23.1 [366]
titanium	22	8.6 [366]
steel	$20 - 50$	$11 - 13$
brass	120	19
phosphor bronze	$62^{(b)}$	$18.2^{(b)}$
fused silica	$1.38^{(c)}$	$0.51^{(c)}$
teflon (PTFE)	0.25	$200^{(d)}$ [367]
fibre glass	$0.2 - 0.3^{(e)}$	$7^{(e)}$
nylon (polyamide)	$0.25 - 0.35$[368]	$90 - 95^{(f)}$
polyoxymethylene (POM)	0.31 [369]	110 [369]
Kapton	0.12 [370]	20 [370]

Table F.1.: Thermal conductivity and thermal expansion coefficients at room temperature for the main materials used for the nanopositioning stage. [(a)]401 for pure copper. [(b)]Taken from Elgin Fastener Group LLC. [(c)]Taken from Heraeus Quarzglas GmbH. [(d)]Average of 86 from 83 K to 298 K.[(e)]Taken from P+H Plüss AG. [(f)]Taken from Professional Plastics, Inc. For temperature dependence graph, see [351].

Nomenclature

Abbreviations

AFM atomic force microscope

AOM acousto-optical modulator

AOTF acousto-optic tunable filter

APD avalanche photo detector

AR anti-reflective

cps counts per second

CQED cavity quantum electrodynamics

CVD chemical vapour deposition

cw continuous wave

DBR distrubuted Bragg reflector

EOM electro-optical modulator

FSR free spectral range

FWHM full width at half maximum

HBT Hanbury-Brown-Twiss

HG Hermite-Gaussian

HPHT high-pressure high-temperature

IBS ion beam sputtering

PMMA polymethyl methacrylate

POM polyoxymethylene

QKD quantum key distribution

REI rare earth ions

RMS root mean square

SCM scanning cavity microscopy

SDS sodium dodecyl sulfate

SEM scanning electon microscopy

SHG second-harmonics generation

SPS single photon source

TDC time-to-digital converter

WGM whispering galery mode

WLI white light interferometer

ZPL zero phonon line

Symbols

β efficiency factor (fraction of emission coupled to cavity mode)

C Purcell factor

C_0 ideal Purcell factor

$\mathbf{d}$ electric dipole

d mirror separation

$\Delta\nu$ free spectral range

$\delta\nu$ cavity linewidth

$\delta\nu_{em}$ emitter linewidth

d_{pen} penetration depth into dielectric mirror stack

ϵ mode matching

η efficiency

η_c outcoupling efficiency

$\mathcal{F}$ finesse

F cavity-funneling factor

g_0 cavity-emitter coupling strength

γ spontaneous emission rate

γ_h	homogeneous linewidth
$\gamma^\star$	pure dephasing rate
I	indistinguishability
I^∞	saturation photon emission rate
κ	cavity decay rate
λ	wavelength
μ_{12}	electric dipole transition matrix element
n	refractive index
ν_{qmn}	resonance frequency of mode with longitudinal mode order q and transverse mode order (m, n)
P_{sat}	saturation power
Q	quality factor
q	longitudinal mode order
QE	quantum efficiency
R	effective emitter-cavity coupling rate
r_C	radius of curvature
τ_0	lifetime in free space
τ_c	lifetime in the cavity
τ_r	radiative lifetime
θ	Gouy-phase
V_m	mode volume
w	1/e radius of the Gaussian beam
w_0	beam waist
w_c	mode radius on curved mirror
w_f	mode field diameter of optical fibres
ξ	dipole orientation with respect to electric field
ζ	branching ratio

Bibliography

[1] S. Haroche and J.-M. Raimond, *Exploring the Quantum: Atoms, Cavities, and Photons* (Paperbackshop UK Import, 19th May 2013), 616 pp.

[2] C. Monroe, D. M. Meekhof, B. E. King, W. M. Itano and D. J. Wineland, "Demonstration of a Fundamental Quantum Logic Gate", Physical Review Letters **75**, 4714–4717 (1995).

[3] A. Steane, "Quantum computing", Reports on Progress in Physics **61**, 117–173 (1998).

[4] C. H. Bennett and D. P. DiVincenzo, "Quantum information and computation", Nature **404**, 247–255 (2000).

[5] P. W. Shor, "Polynomial-Time Algorithms for Prime Factorization and Discrete Logarithms on a Quantum Computer", SIAM Journal on Computing **26**, 1484–1509 (1997).

[6] A. Ekert and R. Jozsa, "Quantum computation and shor's factoring algorithm", Reviews of Modern Physics **68**, 733–753 (1996).

[7] S. Lloyd, "Universal Quantum Simulators", Science **273**, 1073–1078 (1996).

[8] H. Bernien et al., "Probing many-body dynamics on a 51-atom quantum simulator", Nature **551**, 579–584 (2017).

[9] T. D. Ladd, F. Jelezko, R. Laflamme, Y. Nakamura, C. Monroe and J. L. O'Brien, "Quantum computers", Nature **464**, 45–53 (2010).

[10] J. P. Dowling and G. J. Milburn, "Quantum technology: the second quantum revolution", Philosophical Transactions of the Royal Society of London. Series A: Mathematical, Physical and Engineering Sciences **361**, edited by A. G. J. MacFarlane, 1655–1674 (2003).

[11] P. W. Shor, "Scheme for reducing decoherence in quantum computer memory", Physical Review A **52**, R2493–R2496 (1995).

[12] N. Ofek et al., "Extending the lifetime of a quantum bit with error correction in superconducting circuits", Nature **536**, 441–445 (2016).

[13] K. L. Brown, A. Daskin, S. Kais and J. P. Dowling, "Reducing the number of ancilla qubits and the gate count required for creating large controlled operations", Quantum Information Processing **14**, 891–899 (2014).

[14] H. J. Kimble, "The quantum internet", Nature **453**, 1023–1030 (2008).

[15] S. Wehner, D. Elkouss and R. Hanson, "Quantum internet: A vision for the road ahead", Science **362**, eaam9288 (2018).

[16] J. I. Cirac, A. K. Ekert, S. F. Huelga and C. Macchiavello, “Distributed quantum computation over noisy channels”, Physical Review A **59**, 4249–4254 (1999).

[17] R. V. Meter, W. J. Munro, K. Nemoto and K. M. Itoh, “Arithmetic on a distributed-memory quantum multicomputer”, ACM Journal on Emerging Technologies in Computing Systems **3**, 1–23 (2008).

[18] R. Beals, S. Brierley, O. Gray, A. W. Harrow, S. Kutin, N. Linden, D. Shepherd and M. Stather, “Efficient distributed quantum computing”, Proceedings of the Royal Society A: Mathematical, Physical and Engineering Sciences **469**, 20120686–20120686 (2013).

[19] P. W. Shor and J. Preskill, “Simple Proof of Security of the BB84 Quantum Key Distribution Protocol”, Physical Review Letters **85**, 441–444 (2000).

[20] C. H. Bennett and G. Brassard, “Quantum cryptography: Public key distribution and coin tossing”, Theoretical Computer Science **560**, 7–11 (2014).

[21] S.-K. Liao et al., “Satellite-to-ground quantum key distribution”, Nature **549**, 43–47 (2017).

[22] X.-B. Wang, “Beating the Photon-Number-Splitting Attack in Practical Quantum Cryptography”, Physical Review Letters **94** (2005).

[23] H.-K. Lo, X. Ma and K. Chen, “Decoy State Quantum Key Distribution”, Physical Review Letters **94** (2005).

[24] C.-Z. Peng et al., “Experimental Long-Distance Decoy-State Quantum Key Distribution Based on Polarization Encoding”, Physical Review Letters **98** (2007).

[25] H.-K. Lo, M. Curty and K. Tamaki, “Secure quantum key distribution”, Nature Photonics **8**, 595–604 (2014).

[26] I. Aharonovich, D. Englund and M. Toth, “Solid-state single-photon emitters”, Nature Photonics **10**, 631–641 (2016).

[27] L.-M. Duan, M. D. Lukin, J. I. Cirac and P. Zoller, “Long-distance quantum communication with atomic ensembles and linear optics”, Nature **414**, 413–418 (2001).

[28] C. Simon, H. de Riedmatten, M. Afzelius, N. Sangouard, H. Zbinden and N. Gisin, “Quantum Repeaters with Photon Pair Sources and Multimode Memories”, Physical Review Letters **98** (2007).

[29] N. Sangouard, C. Simon, H. de Riedmatten and N. Gisin, “Quantum repeaters based on atomic ensembles and linear optics”, Reviews of Modern Physics **83**, 33–80 (2011).

[30] N. Sangouard, C. Simon, J. Minář, H. Zbinden, H. de Riedmatten and N. Gisin, “Long-distance entanglement distribution with single-photon sources”, Physical Review A **76** (2007).

[31] S. Guha, H. Krovi, C. A. Fuchs, Z. Dutton, J. A. Slater, C. Simon and W. Tittel, "Rate-loss analysis of an efficient quantum repeater architecture", Physical Review A **92** (2015).

[32] K. Azuma, K. Tamaki and H.-K. Lo, "All-photonic quantum repeaters", Nature Communications **6** (2015).

[33] M. Pant, H. Krovi, D. Englund and S. Guha, "Rate-distance tradeoff and resource costs for all-optical quantum repeaters", Physical Review A **95** (2017).

[34] N. H. Lindner and T. Rudolph, "Proposal for Pulsed On-Demand Sources of Photonic Cluster State Strings", Physical Review Letters **103** (2009).

[35] F. Flamini, N. Spagnolo and F. Sciarrino, "Photonic quantum information processing: a review", Reports on Progress in Physics **82**, 016001 (2018).

[36] J. L. O'Brien, A. Furusawa and J. Vučković, "Photonic quantum technologies", Nature Photonics **3**, 687–695 (2009).

[37] J. L. O'Brien, "Optical Quantum Computing", Science **318**, 1567–1570 (2007).

[38] Y. Li, P. C. Humphreys, G. J. Mendoza and S. C. Benjamin, "Resource Costs for Fault-Tolerant Linear Optical Quantum Computing", Physical Review X **5** (2015).

[39] A. Aspuru-Guzik and P. Walther, "Photonic quantum simulators", Nature Physics **8**, 285–291 (2012).

[40] A. Peruzzo et al., "Quantum Walks of Correlated Photons", Science **329**, 1500–1503 (2010).

[41] P. P. Rohde, "Boson sampling with photons of arbitrary spectral structure", Physical Review A **91** (2015).

[42] Z. Yuan, B. E. Kardynal, R. M. Stevenson, A. J. Shields, C. J. Lobo, K. Cooper, N. S. Beattie, D. A. Ritchie and M. Pepper, "Electrically Driven Single-Photon Source", Science **295**, 102–105 (2001).

[43] C. Santori, D. Fattal, J. Vučković, G. S. Solomon and Y. Yamamoto, "Indistinguishable photons from a single-photon device", Nature **419**, 594–597 (2002).

[44] N. Somaschi et al., "Near-optimal single-photon sources in the solid state", Nature Photonics **10**, 340–345 (2016).

[45] S. Schietinger, M. Barth, T. Aichele and O. Benson, "Plasmon-Enhanced Single Photon Emission from a Nanoassembled Metal-Diamond Hybrid Structure at Room Temperature", Nano Letters **9**, 1694–1698 (2009).

[46] H. Kaupp et al., "Purcell-Enhanced Single-Photon Emission from Nitrogen-Vacancy Centers Coupled to a Tunable Microcavity", Physical Review Applied **6** (2016).

[47] R. Albrecht, A. Bommer, C. Deutsch, J. Reichel and C. Becher, "Coupling of a Single Nitrogen-Vacancy Center in Diamond to a Fiber-Based Microcavity", Physical Review Letters **110** (2013).

[48] P. R. Dolan et al., “Robust, tunable, and high purity triggered single photon source at room temperature using a nitrogen-vacancy defect in diamond in an open microcavity”, Optics Express **26**, 7056 (2018).

[49] E. Neu et al., “Narrowband fluorescent nanodiamonds produced from chemical vapor deposition films”, Applied Physics Letters **98**, 243107 (2011).

[50] J. Riedrich-Möller, C. Arend, C. Pauly, F. Mücklich, M. Fischer, S. Gsell, M. Schreck and C. Becher, “Deterministic Coupling of a Single Silicon-Vacancy Color Center to a Photonic Crystal Cavity in Diamond”, Nano Letters **14**, 5281–5287 (2014).

[51] J. L. Zhang et al., “Strongly Cavity-Enhanced Spontaneous Emission from Silicon-Vacancy Centers in Diamond”, Nano Letters **18**, 1360–1365 (2018).

[52] D. Hunger, T. Steinmetz, Y. Colombe, C. Deutsch, T. W. Hänsch and J. Reichel, “A fiber Fabry–Perot cavity with high finesse”, New Journal of Physics **12**, 065038 (2010).

[53] J. Benedikter et al., “Cavity-Enhanced Single-Photon Source Based on the Silicon-Vacancy Center in Diamond”, Physical Review Applied **7** (2017).

[54] T. Grange, G. Hornecker, D. Hunger, J.-P. Poizat, J.-M. Gérard, P. Senellart and A. Auffèves, “Cavity-Funneled Generation of Indistinguishable Single Photons from Strongly Dissipative Quantum Emitters”, Physical Review Letters **114** (2015).

[55] M. Peev et al., “The SECOQC quantum key distribution network in Vienna”, New Journal of Physics **11**, 075001 (2009).

[56] M. Sasaki et al., “Field test of quantum key distribution in the Tokyo QKD Network”, Optics Express **19**, 10387 (2011).

[57] H.-J. Briegel, W. Dür, J. I. Cirac and P. Zoller, “Quantum Repeaters: The Role of Imperfect Local Operations in Quantum Communication”, Physical Review Letters **81**, 5932–5935 (1998).

[58] W. J. Munro, K. Azuma, K. Tamaki and K. Nemoto, “Inside Quantum Repeaters”, IEEE Journal of Selected Topics in Quantum Electronics **21**, 78–90 (2015).

[59] Z.-S. Yuan, Y.-A. Chen, B. Zhao, S. Chen, J. Schmiedmayer and J.-W. Pan, “Experimental demonstration of a BDCZ quantum repeater node”, Nature **454**, 1098–1101 (2008).

[60] C. H. Bennett, G. Brassard, C. Crépeau, R. Jozsa, A. Peres and W. K. Wootters, “Teleporting an unknown quantum state via dual classical and Einstein-Podolsky-Rosen channels”, Physical Review Letters **70**, 1895–1899 (1993).

[61] L. V. Hau, S. E. Harris, Z. Dutton and C. H. Behroozi, “Light speed reduction to 17 metres per second in an ultracold atomic gas”, Nature **397**, 594–598 (1999).

[62] J. Nunn, I. A. Walmsley, M. G. Raymer, K. Surmacz, F. C. Waldermann, Z. Wang and D. Jaksch, “Mapping broadband single-photon wave packets into an atomic memory”, Physical Review A **75** (2007).

[63] M. Zhong, M. P. Hedges, R. L. Ahlefeldt, J. G. Bartholomew, S. E. Beavan, S. M. Wittig, J. J. Longdell and M. J. Sellars, "Optically addressable nuclear spins in a solid with a six-hour coherence time", Nature **517**, 177–180 (2015).

[64] R. Kolesov, K. Xia, R. Reuter, M. Jamali, R. Stöhr, T. Inal, P. Siyushev and J. Wrachtrup, "Mapping Spin Coherence of a Single Rare-Earth Ion in a Crystal onto a Single Photon Polarization State", Physical Review Letters **111** (2013).

[65] C. Laplane, P. Jobez, J. Etesse, N. Timoney, N. Gisin and M. Afzelius, "Multiplexed on-demand storage of polarization qubits in a crystal", New Journal of Physics **18**, 013006 (2015).

[66] M. Gündoğan, P. M. Ledingham, K. Kutluer, M. Mazzera and H. de Riedmatten, "Solid State Spin-Wave Quantum Memory for Time-Bin Qubits", Physical Review Letters **114** (2015).

[67] M. P. Hedges, J. J. Longdell, Y. Li and M. J. Sellars, "Efficient quantum memory for light", Nature **465**, 1052–1056 (2010).

[68] H. de Riedmatten, M. Afzelius, M. U. Staudt, C. Simon and N. Gisin, "A solid-state light–matter interface at the single-photon level", Nature **456**, 773–777 (2008).

[69] M. Afzelius et al., "Demonstration of Atomic Frequency Comb Memory for Light with Spin-Wave Storage", Physical Review Letters **104** (2010).

[70] G. Corrielli, A. Seri, M. Mazzera, R. Osellame and H. de Riedmatten, "Integrated Optical Memory Based on Laser-Written Waveguides", Physical Review Applied **5** (2016).

[71] E. Saglamyurek et al., "Broadband waveguide quantum memory for entangled photons", Nature **469**, 512–515 (2011).

[72] S. Marzban, J. G. Bartholomew, S. Madden, K. Vu and M. J. Sellars, "Observation of Photon Echoes From Evanescently Coupled Rare-Earth Ions in a Planar Waveguide", Physical Review Letters **115** (2015).

[73] E. Saglamyurek, J. Jin, V. B. Verma, M. D. Shaw, F. Marsili, S. W. Nam, D. Oblak and W. Tittel, "Quantum storage of entangled telecom-wavelength photons in an erbium-doped optical fibre", Nature Photonics **9**, 83–87 (2015).

[74] T. Zhong et al., "Nanophotonic rare-earth quantum memory with optically controlled retrieval", Science **357**, 1392–1395 (2017).

[75] G. Heinze, C. Hubrich and T. Halfmann, "Stopped Light and Image Storage by Electromagnetically Induced Transparency up to the Regime of One Minute", Physical Review Letters **111** (2013).

[76] A. M. Dibos, M. Raha, C. M. Phenicie and J. D. Thompson, "Atomic Source of Single Photons in the Telecom Band", Physical Review Letters **120** (2018).

[77] T. Zhong et al., "Optically Addressing Single Rare-Earth Ions in a Nanophotonic Cavity", Physical Review Letters **121** (2018).

[78] N. Ohlsson, R. K. Mohan and S. Kröll, "Quantum computer hardware based on rare-earth-ion-doped inorganic crystals", Optics Communications **201**, 71–77 (2002).

[79] J. J. Longdell, M. J. Sellars and N. B. Manson, "Demonstration of Conditional Quantum Phase Shift Between Ions in a Solid", Physical Review Letters **93** (2004).

[80] D. Schrader, I. Dotsenko, M. Khudaverdyan, Y. Miroshnychenko, A. Rauschenbeutel and D. Meschede, "Neutral Atom Quantum Register", Physical Review Letters **93** (2004).

[81] D. Serrano, J. Karlsson, A. Fossati, A. Ferrier and P. Goldner, "All-optical control of long-lived nuclear spins in rare-earth doped nanoparticles", Nature Communications **9** (2018).

[82] A. Perrot, P. Goldner, D. Giaume, M. Lovrić, C. Andriamiadamanana, R. R. Gonçalves and A. Ferrier, "Narrow Optical Homogeneous Linewidths in Rare Earth Doped Nanocrystals", Physical Review Letters **111** (2013).

[83] J. G. Bartholomew, K. de Oliveira Lima, A. Ferrier and P. Goldner, "Optical Line Width Broadening Mechanisms at the 10 kHz Level in $Eu^{3+} : Y_2O_3$ Nanoparticles", Nano Letters **17**, 778–787 (2017).

[84] D. L. McAuslan, J. J. Longdell and M. J. Sellars, "Strong-coupling cavity QED using rare-earth-metal-ion dopants in monolithic resonators: What you can do with a weak oscillator", Physical Review A **80** (2009).

[85] B. Casabone et al., "Cavity-enhanced spectroscopy of a few-ion ensemble in Eu^{3+}:Y_2O_3", New Journal of Physics **20**, 095006 (2018).

[86] T. Yoshie, A. Scherer, J. Hendrickson, G. Khitrova, H. M. Gibbs, G. Rupper, C. Ell, O. B. Shchekin and D. G. Deppe, "Vacuum Rabi splitting with a single quantum dot in a photonic crystal nanocavity", Nature **432**, 200–203 (2004).

[87] A. Faraon, C. Santori, Z. Huang, V. M. Acosta and R. G. Beausoleil, "Coupling of Nitrogen-Vacancy Centers to Photonic Crystal Cavities in Monocrystalline Diamond", Physical Review Letters **109** (2012).

[88] B. J. M. Hausmann et al., "Coupling of NV Centers to Photonic Crystal Nanobeams in Diamond", Nano Letters **13**, 5791–5796 (2013).

[89] S. Reitzenstein et al., "AlAs/GaAs micropillar cavities with quality factors exceeding 150.000", Applied Physics Letters **90**, 251109 (2007).

[90] X. Ding et al., "On-Demand Single Photons with High Extraction Efficiency and Near-Unity Indistinguishability from a Resonantly Driven Quantum Dot in a Micropillar", Physical Review Letters **116** (2016).

[91] D. Hunger, C. Deutsch, R. J. Barbour, R. J. Warburton and J. Reichel, "Laser micro-fabrication of concave, low-roughness features in silica", AIP Advances **2**, 012119 (2012).

[92] M. Mader, J. Reichel, T. W. Hänsch and D. Hunger, "A scanning cavity microscope", Nature Communications **6** (2015).

[93] M. Mader, "A Scanning Cavity Microscope", PhD thesis (Ludwig-Maximilians-Universität München, 2018).

[94] J. Benedikter, T. Hümmer, M. Mader, B. Schlederer, J. Reichel, T. W. Hänsch and D. Hunger, "Transverse-mode coupling and diffraction loss in tunable Fabry–Pérot microcavities", New Journal of Physics **17**, 053051 (2015).

[95] J. Benedikter, T. Moosmayer, M. Mader, T. Hümmer and D. Hunger, "Transverse-mode coupling effects in scanning cavity microscopy", submitted (2019).

[96] C. Fabry and A. Pérot, "Theorie et applications d'une nouvelle methode de spectroscopie interferentielle", Ann. Chim. Phys. **16** (1899).

[97] C. Fabry and A. Pérot, "On a New Form of Interferometer", Astrophysical Journal, 265–272 (1901).

[98] E. M. Purcell, "Spontaneous Emission Probabilities at Radio Frequencies", Physical Review **69** (1946).

[99] J. P. Gordon, H. J. Zeiger and C. H. Townes, "The Maser—New Type of Microwave Amplifier, Frequency Standard, and Spectrometer", Physical Review **99**, 1264–1274 (1955).

[100] T. H. Maiman, "Stimulated Optical Radiation in Ruby", Nature **187**, 493–494 (1960).

[101] P. Goy, J. M. Raimond, M. Gross and S. Haroche, "Observation of Cavity-Enhanced Single-Atom Spontaneous Emission", PRL **50**, 1903–1906 (1983).

[102] R. G. Hulet, E. S. Hilfer and D. Kleppner, "Inhibited Spontaneous Emission by a Rydberg Atom", PRL **55**, 2137–2140 (1985).

[103] D. J. Heinzen, J. J. Childs, J. E. Thomas and M. S. Feld, "Enhanced and inhibited visible spontaneous emission by atoms in a confocal resonator", PRL **58**, 1320–1323 (1987).

[104] K. J. Vahala, "Optical microcavities", Nature **424**, 839–846 (2003).

[105] A. Kuhn, M. Hennrich and G. Rempe, "Deterministic Single-Photon Source for Distributed Quantum Networking", Physical Review Letters **89** (2002).

[106] R. J. Thompson, G. Rempe and H. J. Kimble, "Observation of normal-mode splitting for an atom in an optical cavity", Physical Review Letters **68**, 1132–1135 (1992).

[107] D. W. Vernooy, V. S. Ilchenko, H. Mabuchi, E. W. Streed and H. J. Kimble, "High-Q measurements of fused-silica microspheres in the near infrared", Optics Letters **23**, 247 (1998).

[108] T. J. Kippenberg, S. M. Spillane and K. J. Vahala, "Demonstration of ultra-high-Q small mode volume toroid microcavities on a chip", Applied Physics Letters **85**, 6113–6115 (2004).

[109] Y. Louyer, D. Meschede and A. Rauschenbeutel, “Tunable whispering-gallery-mode resonators for cavity quantum electrodynamics”, Physical Review A **72** (2005).

[110] C. Junge, D. O’Shea, J. Volz and A. Rauschenbeutel, “Strong Coupling between Single Atoms and Nontransversal Photons”, Physical Review Letters **110** (2013).

[111] F. Vollmer and S. Arnold, “Whispering-gallery-mode biosensing: label-free detection down to single molecules”, Nature Methods **5**, 591–596 (2008).

[112] F. Vollmer and L. Yang, “Review Label-free detection with high-Q microcavities: a review of biosensing mechanisms for integrated devices”, Nanophotonics **1** (2012).

[113] M. R. Foreman, J. D. Swaim and F. Vollmer, “Whispering gallery mode sensors”, Advances in Optics and Photonics **7**, 168 (2015).

[114] N. E. Flowers-Jacobs, S. W. Hoch, J. C. Sankey, A. Kashkanova, A. M. Jayich, C. Deutsch, J. Reichel and J. G. E. Harris, “Fiber-cavity-based optomechanical device”, Applied Physics Letters **101**, 221109 (2012).

[115] A. B. Shkarin, N. E. Flowers-Jacobs, S. W. Hoch, A. D. Kashkanova, C. Deutsch, J. Reichel and J. G. E. Harris, “Optically Mediated Hybridization between Two Mechanical Modes”, Physical Review Letters **112** (2014).

[116] S. Stapfner, L. Ost, D. Hunger, J. Reichel, I. Favero and E. M. Weig, “Cavity-enhanced optical detection of carbon nanotube Brownian motion”, Applied Physics Letters **102**, 151910 (2013).

[117] T. Hümmer, J. Noe, M. S. Hofmann, T. W. Hänsch, A. Högele and D. Hunger, “Cavity-enhanced Raman microscopy of individual carbon nanotubes”, Nature Communications **7** (2016).

[118] Y. Colombe, T. Steinmetz, G. Dubois, F. Linke, D. Hunger and J. Reichel, “Strong atom–field coupling for Bose–Einstein condensates in an optical cavity on a chip”, Nature **450**, 272–276 (2007).

[119] R. Gehr, J. Volz, G. Dubois, T. Steinmetz, Y. Colombe, B. L. Lev, R. Long, J. Estève and J. Reichel, “Cavity-Based Single Atom Preparation and High-Fidelity Hyperfine State Readout”, Physical Review Letters **104** (2010).

[120] F. Haas, J. Volz, R. Gehr, J. Reichel and J. Esteve, “Entangled States of More Than 40 Atoms in an Optical Fiber Cavity”, Science **344**, 180–183 (2014).

[121] B. Brandstätter et al., “Integrated fiber-mirror ion trap for strong ion-cavity coupling”, Review of Scientific Instruments **84**, 123104 (2013).

[122] H. Takahashi, A. Wilson, A. Riley-Watson, F. Oručević, N. Seymour-Smith, M. Keller and W. Lange, “An integrated fiber trap for single-ion photonics”, New Journal of Physics **15**, 053011 (2013).

[123] T. G. Ballance, H. M. Meyer, P. Kobel, K. Ott, J. Reichel and M. Köhl, “Cavity-induced backaction in Purcell-enhanced photon emission of a single ion in an ultraviolet fiber cavity”, Physical Review A **95** (2017).

[124] H. Kaupp, C. Deutsch, H.-C. Chang, J. Reichel, T. W. Hänsch and D. Hunger, "Scaling laws of the cavity enhancement for nitrogen-vacancy centers in diamond", Physical Review A **88** (2013).

[125] R. Albrecht et al., "Narrow-band single photon emission at room temperature based on a single nitrogen-vacancy center coupled to an all-fiber-cavity", Applied Physics Letters **105**, 073113 (2014).

[126] H. Kaupp, "Coupling Nitrogen-Vacancy Centers in Diamond to Fiber-based Fabry-Pérot Microcavities", PhD thesis (Ludwig-Maximilians-Universität München, 2017).

[127] M. Förg, L. Colombier, R. K. Patel, J. Lindlau, A. D. Mohite, H. Yamaguchi, D. Hunger and A. Högele, "Cavity-control of bright and dark interlayer excitons in van der Waals heterostructures", arXiv:1710.00990v2 (2017).

[128] C. Gebhardt et al., "Polariton hyperspectral imaging of two-dimensional semiconductor crystals", arXiv:1803.08690 (2018).

[129] A. Muller, E. B. Flagg, M. Metcalfe, J. Lawall and G. S. Solomon, "Coupling an epitaxial quantum dot to a fiber-based external-mirror microcavity", Applied Physics Letters **95**, 173101 (2009).

[130] J. Miguel-Sánchez, A. Reinhard, E. Togan, T. Volz, A. Imamoglu, B. Besga, J. Reichel and J. Estève, "Cavity quantum electrodynamics with charge-controlled quantum dots coupled to a fiber Fabry–Perot cavity", New Journal of Physics **15**, 045002 (2013).

[131] B. E. A. Saleh and M. C. Teich, *Fundamentals of Photonics* (John Wiley & Sons, Inc., Aug. 1991).

[132] N. Hodgson and H. Weber, *Optical Resonators* (Springer London, 1997).

[133] W. Zinth and U. Zinth, *Optik: Lichtstrahlen - Wellen - Photonen* (Oldenbourg, 2008).

[134] J. F. S. Brachmann, H. Kaupp, T. W. Hänsch and D. Hunger, "Photothermal effects in ultra-precisely stabilized tunable microcavities", Optics Express **24**, 21205 (2016).

[135] J. Benedikter, "Transverse-Mode Coupling and Diffraction Loss in Fibre-Based Optical Microcavities", MA thesis (Ludwig-Maximilians-Universität München, 2014).

[136] M. Uphoff, M. Brekenfeld, G. Rempe and S. Ritter, "Frequency splitting of polarization eigenmodes in microscopic Fabry–Perot cavities", New Journal of Physics **17**, 013053 (2015).

[137] K. Ott, S. Garcia, R. Kohlhaas, K. Schüppert, P. Rosenbusch, R. Long and J. Reichel, "Millimeter-long fiber Fabry-Perot cavities", Optics Express **24**, 9839 (2016).

[138] T. Hümmer, "Micro-cavity enhanced Raman and Absorption Microscopy for Nanoscale Solid State Systems", PhD thesis (Ludwig-Maximilians-Universität München, 2019).

[139] H. Kogelnik and T. Li, "Laser Beams and Resonators", Applied Optics **5**, 1550 (1966).

[140] H. Laabs and A. T. Friberg, "Nonparaxial eigenmodes of stable resonators", IEEE Journal of Quantum Electronics **35**, 198–207 (1999).

[141] M. Lax, W. H. Louisell and W. B. McKnight, "From Maxwell to paraxial wave optics", Physical Review A **11**, 1365–1370 (1975).

[142] M. B. Doost, W. Langbein and E. A. Muljarov, "Resonant state expansion applied to two-dimensional open optical systems", Physical Review A **87** (2013).

[143] W. B. Joyce and B. C. DeLoach, "Alignment of Gaussian beams", Applied Optics **23**, 4187 (1984).

[144] M. Fox, *Quantum Optics* (Oxford University Press, 11th Apr. 2006), 384 pp.

[145] J. Bylander, I. Robert-Philip and I. Abram, "Interference and correlation of two independent photons", The European Physical Journal D **22**, 295–301 (2003).

[146] A. Auffèves, J.-M. Gérard and J.-P. Poizat, "Pure emitter dephasing: A resource for advanced solid-state single-photon sources", Physical Review A **79** (2009).

[147] A. Auffèves, D. Gerace, J.-M. Gérard, M. F. Santos, L. C. Andreani and J.-P. Poizat, "Controlling the dynamics of a coupled atom-cavity system by pure dephasing", Physical Review B **81** (2010).

[148] E. T. Jaynes and F. W. Cummings, "Comparison of quantum and semiclassical radiation theories with application to the beam maser", Proceedings of the IEEE **51**, 89–109 (1963).

[149] D. Meschede, H. Walther and G. Müller, "One-Atom Maser", Physical Review Letters **54**, 551–554 (1985).

[150] G. Rempe, H. Walther and N. Klein, "Observation of quantum collapse and revival in a one-atom maser", Physical Review Letters **58**, 353–356 (1987).

[151] M. G. Raizen, R. J. Thompson, R. J. Brecha, H. J. Kimble and H. J. Carmichael, "Normal-mode splitting and linewidth averaging for two-state atoms in an optical cavity", Physical Review Letters **63**, 240–243 (1989).

[152] L. C. Flatten, Z. He, D. M. Coles, A. A. P. Trichet, A. W. Powell, R. A. Taylor, J. H. Warner and J. M. Smith, "Room-temperature exciton-polaritons with two-dimensional WS_2", Scientific Reports **6** (2016).

[153] B. H. Lukas Novotny, *Principles of Nano-Optics* (Cambridge University Press, 11th Sept. 2012).

[154] A. Meldrum, P. Bianucci and F. Marsiglio, "Modification of ensemble emission rates and luminescence spectra for inhomogeneously broadened distributions of quantum dots coupled to optical microcavities", Optics Express **18**, 10230 (2010).

[155] M. Motsch, M. Zeppenfeld, P. W. H. Pinkse and G. Rempe, "Cavity-enhanced Rayleigh scattering", New Journal of Physics **12**, 063022 (2010).

[156] H. Tanji-Suzuki, I. D. Leroux, M. H. Schleier-Smith, M. Cetina, A. T. Grier, J. Simon and V. Vuletić, "Interaction between Atomic Ensembles and Optical Resonators", in *Advances in atomic, molecular, and optical physics* (Elsevier, 2011), pp. 201–237.

[157] E. A. Hinds, "Cavity Quantum Electrodynamics", in *Advances in atomic, molecular, and optical physics* (Elsevier, 1990), pp. 237–289.

[158] L. Greuter, S. Starosielec, D. Najer, A. Ludwig, L. Duempelmann, D. Rohner and R. J. Warburton, "A small mode volume tunable microcavity: Development and characterization", Applied Physics Letters **105**, 121105 (2014).

[159] B. Schlederer, "Development of a CO_2 laser setup for fiber end facet machining and characterization", MA thesis (Ludwig-Maximilians-Universität München, 2014).

[160] D. Kleckner, W. T. M. Irvine, S. S. R. Oemrawsingh and D. Bouwmeester, "Diffraction-limited high-finesse optical cavities", Physical Review A **81** (2010).

[161] L. R. Brovelli and U. Keller, "Simple analytical expressions for the reflectivity and the penetration depth of a Bragg mirror between arbitrary media", Optics Communications **116**, 343–350 (1995).

[162] A. A. P. Trichet, P. R. Dolan, D. M. Coles, G. M. Hughes and J. M. Smith, "Topographic control of open-access microcavities at the nanometer scale", Optics Express **23**, 17205 (2015).

[163] T. Moosmayer, "Scanning Cavity Microscopy of semiconducting single-walled Carbon Nanotubes", MA thesis (Karlsruher Institut für Technologie, 2019).

[164] F. Frost, B. Ziberi, A. Schindler and B. Rauschenbach, "Surface engineering with ion beams: from self-organized nanostructures to ultra-smooth surfaces", Applied Physics A **91**, 551–559 (2008).

[165] P. R. Dolan, G. M. Hughes, F. Grazioso, B. R. Patton and J. M. Smith, "Femtoliter tunable optical cavity arrays", Optics Letters **35**, 3556 (2010).

[166] F. Beck, "Europium-doped nanocrystals in cryogenic optical microcavities", MA thesis (Ludwig-Maximilians-Universität München, 2016).

[167] T. Gissibl, S. Thiele, A. Herkommer and H. Giessen, "Two-photon direct laser writing of ultracompact multi-lens objectives", Nature Photonics **10**, 554–560 (2016).

[168] S. A. Furman and A. V. Tikhonravov, *Basics of Optics of Multilayer Systems* (World Scientific Publishing Co Pte Ltd, 1996).

[169] C. J. R. Sheppard, "Approximate calculation of the reflection coefficient from a stratified medium", Pure and Applied Optics: Journal of the European Optical Society Part A **4**, 665–669 (1995).

[170] D. I. Babic and S. W. Corzine, "Analytic expressions for the reflection delay, penetration depth, and absorptance of quarter-wave dielectric mirrors", IEEE Journal of Quantum Electronics **28**, 514–524 (1992).

[171] H. A. MacLeod, *Thin-Film Optical Filters, Third Edition (Series in Optics and Optoelectronics)* (CRC Press, 2001).

[172] C. J. Hood, H. J. Kimble and J. Ye, "Characterization of high-finesse mirrors: Loss, phase shifts, and mode structure in an optical cavity", Physical Review A **64** (2001).

[173] E. Janitz, M. Ruf, M. Dimock, A. Bourassa, J. Sankey and L. Childress, "Fabry-Perot microcavity for diamond-based photonics", Physical Review A **92** (2015).

[174] W. Lukosz, "Light emission by magnetic and electric dipoles close to a plane dielectric interface III Radiation patterns of dipoles with arbitrary orientation", Journal of the Optical Society of America **69**, 1495 (1979).

[175] H. C. van de Hulst, *Light Scattering by Small Particles* (Dover Publications, 1st Dec. 1981), 496 pp.

[176] M. Quinten, *Optical Properties of Nanoparticle Systems* (Wiley VCH Verlag GmbH, 14th Jan. 2011).

[177] G. Mie, "Beiträge zur Optik trüber Medien, speziell kolloidaler Metallösungen", Annalen der Physik **330**, 377–445 (1908).

[178] M. M. Wind, J. Vlieger and D. Bedeaux, "The polarizability of a truncated sphere on a substrate I", Physica A: Statistical Mechanics and its Applications **141**, 33–57 (1987).

[179] M. M. Wind, P. A. Bobbert, J. Vlieger and D. Bedeaux, "The polarizability of a truncated sphere on a substrate II", Physica A: Statistical Mechanics and its Applications **143**, 164–182 (1987).

[180] L. Husel, *Rayleigh-Streuung in Fabry-Perot Mikroresonatoren*, Bachelorarbeit, Ludwig-Maximilians-Universität München, 2016.

[181] N. Gisin, G. Ribordy, W. Tittel and H. Zbinden, "Quantum cryptography", Reviews of Modern Physics **74**, 145–195 (2002).

[182] J. F. Clauser, "Experimental distinction between the quantum and classical field-theoretic predictions for the photoelectric effect", Physical Review D **9**, 853–860 (1974).

[183] H. J. Kimble, M. Dagenais and L. Mandel, "Photon Antibunching in Resonance Fluorescence", Physical Review Letters **39**, 691–695 (1977).

[184] D. F. Walls, "Evidence for the quantum nature of light", Nature **280**, 451–454 (1979).

[185] J. F. Clauser and A. Shimony, "Bell's theorem. Experimental tests and implications", Reports on Progress in Physics **41**, 1881–1927 (1978).

[186] A. Aspect, P. Grangier and G. Roger, "Experimental Tests of Realistic Local Theories via Bell's Theorem", Physical Review Letters **47**, 460–463 (1981).

[187] P. Grangier, G. Roger and A. Aspect, "Experimental Evidence for a Photon Anticorrelation Effect on a Beam Splitter: A New Light on Single-Photon Interferences", Europhysics Letters (EPL) **1**, 173–179 (1986).

[188] F. Diedrich and H. Walther, "Nonclassical radiation of a single stored ion", Physical Review Letters **58**, 203–206 (1987).

[189] D. C. Burnham and D. L. Weinberg, "Observation of Simultaneity in Parametric Production of Optical Photon Pairs", Physical Review Letters **25**, 84–87 (1970).

[190] C. K. Hong and L. Mandel, "Experimental realization of a localized one-photon state", Physical Review Letters **56**, 58–60 (1986).

[191] M. Orrit and J. Bernard, "Single pentacene molecules detected by fluorescence excitation in ap-terphenyl crystal", Physical Review Letters **65**, 2716–2719 (1990).

[192] L. Birotheau, A. Izrael, J. Y. Marzin, R. Azoulay, V. Thierry-Mieg and F. R. Ladan, "Optical investigation of the one-dimensional confinement effects in narrow GaAs/GaAlAs quantum wires", Applied Physics Letters **61**, 3023–3025 (1992).

[193] K. Brunner, U. Bockelmann, G. Abstreiter, M. Walther, G. Böhm, G. Tränkle and G. Weimann, "Photoluminescence from a single GaAs/AlGaAs quantum dot", Physical Review Letters **69**, 3216–3219 (1992).

[194] P. Michler, "A Quantum Dot Single-Photon Turnstile Device", Science **290**, 2282–2285 (2000).

[195] C. Santori, M. Pelton, G. Solomon, Y. Dale and Y. Yamamoto, "Triggered Single Photons from a Quantum Dot", Physical Review Letters **86**, 1502–1505 (2001).

[196] M. Keller, B. Lange, K. Hayasaka, W. Lange and H. Walther, "A calcium ion in a cavity as a controlled single-photon source", New Journal of Physics **6**, 95–95 (2004).

[197] M. Keller, B. Lange, K. Hayasaka, W. Lange and H. Walther, "Continuous generation of single photons with controlled waveform in an ion-trap cavity system", Nature **431**, 1075–1078 (2004).

[198] C. Kurtsiefer, S. Mayer, P. Zarda and H. Weinfurter, "Stable Solid-State Source of Single Photons", Physical Review Letters **85**, 290–293 (2000).

[199] R. Brouri, A. Beveratos, J.-P. Poizat and P. Grangier, "Photon antibunching in the fluorescence of individual color centers in diamond", Optics Letters **25**, 1294 (2000).

[200] A. Beveratos, S. Kühn, R. Brouri, T. Gacoin, J.-P. Poizat and P. Grangier, "Room temperature stable single-photon source", The European Physical Journal D - Atomic, Molecular and Optical Physics **18**, 191–196 (2002).

[201] E. Moreau, I. Robert, J. M. Gérard, I. Abram, L. Manin and V. Thierry-Mieg, "Single-mode solid-state single photon source based on isolated quantum dots in pillar microcavities", Applied Physics Letters **79**, 2865–2867 (2001).

[202] M. Pelton, C. Santori, G. S. Solomon, O. Benson and Y. Yamamoto, "Triggered single photons and entangled photons from a quantum dot microcavity", The European Physical Journal D - Atomic, Molecular and Optical Physics **18**, 179–190 (2002).

[203] B. Lounis and M. Orrit, "Single-photon sources", Reports on Progress in Physics **68**, 1129–1179 (2005).

[204] R. Loudon, *The Quantum Theory of Light* (Oxford University Press, 11th Sept. 2000), 448 pp.

[205] X. T. Zou and L. Mandel, "Photon-antibunching and sub-Poissonian photon statistics", Physical Review A **41**, 475–476 (1990).

[206] R. H. Brown and R. Q. Twiss, "Correlation between Photons in two Coherent Beams of Light", Nature **177**, 27–29 (1956).

[207] R. H. Brown and R. Q. Twiss, "A Test of a New Type of Stellar Interferometer on Sirius", Nature **178**, 1046–1048 (1956).

[208] C. Wang, "A Solid-State Single Photon Source Based on Color Centers in Diamond", PhD thesis (Ludwig-Maximilians-Universität München, 2007).

[209] R. Q. Twiss, A. G. Little and R. H. Brown, "Correlation Between Photons, in Coherent Beams of Light, Detected by a Coincidence Counting Technique", Nature **180**, 324–326 (1957).

[210] R. Verberk and M. Orrit, "Photon statistics in the fluorescence of single molecules and nanocrystals: Correlation functions versus distributions of on- and off-times", The Journal of Chemical Physics **119**, 2214–2222 (2003).

[211] M. D. Eisaman, J. Fan, A. Migdall and S. V. Polyakov, "Invited Review Article: Single-photon sources and detectors", Review of Scientific Instruments **82**, 071101 (2011).

[212] C. K. Hong, Z. Y. Ou and L. Mandel, "Measurement of subpicosecond time intervals between two photons by interference", Physical Review Letters **59**, 2044–2046 (1987).

[213] T. Schmitt-Manderbach et al., "Experimental Demonstration of Free-Space Decoy-State Quantum Key Distribution over 144 km", Physical Review Letters **98** (2007).

[214] S. D. Dyer, M. J. Stevens, B. Baek and S. W. Nam, "High-efficiency, ultra low-noise all-fiber photon-pair source", Optics Express **16**, 9966 (2008).

[215] B. J. Smith, P. Mahou, O. Cohen, J. S. Lundeen and I. A. Walmsley, "Photon pair generation in birefringent optical fibers", Optics Express **17**, 23589 (2009).

[216] S. Fasel, O. Alibart, S. Tanzilli, P. Baldi, A. Beveratos, N. Gisin and H. Zbinden, "High-quality asynchronous heralded single-photon source at telecom wavelength", New Journal of Physics **6**, 163–163 (2004).

[217] T. Zhong, X. Hu, F. N. C. Wong, K. K. Berggren, T. D. Roberts and P. Battle, "High-quality fiber-optic polarization entanglement distribution at 1.3 μm telecom wavelength", Optics Letters **35**, 1392 (2010).

[218] A. Kuhn, M. Hennrich, T. Bondo and G. Rempe, "Controlled generation of single photons from a strongly coupled atom-cavity system", Applied Physics B **69**, 373–377 (1999).

[219] T. Legero, T. Wilk, M. Hennrich, G. Rempe and A. Kuhn, "Quantum Beat of Two Single Photons", Physical Review Letters **93** (2004).

[220] J. Beugnon, M. P. A. Jones, J. Dingjan, B. Darquié, G. Messin, A. Browaeys and P. Grangier, "Quantum interference between two single photons emitted by independently trapped atoms", Nature **440**, 779–782 (2006).

[221] P. Maunz, D. L. Moehring, S. Olmschenk, K. C. Younge, D. N. Matsukevich and C. Monroe, "Quantum interference of photon pairs from two remote trapped atomic ions", Nature Physics **3**, 538–541 (2007).

[222] S. Gerber et al., "Quantum interference from remotely trapped ions", New Journal of Physics **11**, 013032 (2009).

[223] M. Hijlkema, B. Weber, H. P. Specht, S. C. Webster, A. Kuhn and G. Rempe, "A single-photon server with just one atom", Nature Physics **3**, 253–255 (2007).

[224] A. Kiraz, M. Ehrl, T. Hellerer, Ö. E. Müstecaplıoğlu, C. Bräuchle and A. Zumbusch, "Indistinguishable Photons from a Single Molecule", Physical Review Letters **94** (2005).

[225] R. Lettow, V. Ahtee, R. Pfab, A. Renn, E. Ikonen, S. Götzinger and V. Sandoghdar, "Realization of two Fourier-limited solid-state single-photon sources", Optics Express **15**, 15842 (2007).

[226] V. Ahtee, R. Lettow, R. Pfab, A. Renn, E. Ikonen, S. Götzinger and V. Sandoghdar, "Molecules as sources for indistinguishable single photons", Journal of Modern Optics **56**, 161–166 (2009).

[227] R. Lettow, Y. L. A. Rezus, A. Renn, G. Zumofen, E. Ikonen, S. Götzinger and V. Sandoghdar, "Quantum Interference of Tunably Indistinguishable Photons from Remote Organic Molecules", Physical Review Letters **104** (2010).

[228] X.-L. Chu, S. Götzinger and V. Sandoghdar, "A single molecule as a high-fidelity photon gun for producing intensity-squeezed light", Nature Photonics **11**, 58–62 (2016).

[229] C. Wang, C. Kurtsiefer, H. Weinfurter and B. Burchard, "Single photon emission from SiV centres in diamond produced by ion implantation", Journal of Physics B: Atomic, Molecular and Optical Physics **39**, 37–41 (2005).

[230] E. Neu, D. Steinmetz, J. Riedrich-Möller, S. Gsell, M. Fischer, M. Schreck and C. Becher, "Single photon emission from silicon-vacancy colour centres in chemical vapour deposition nano-diamonds on iridium", New Journal of Physics **13**, 025012 (2011).

[231] T. Iwasaki et al., “Germanium-Vacancy Single Color Centers in Diamond”, Scientific Reports **5** (2015).

[232] T. Iwasaki, Y. Miyamoto, T. Taniguchi, P. Siyushev, M. H. Metsch, F. Jelezko and M. Hatano, “Tin-Vacancy Quantum Emitters in Diamond”, Physical Review Letters **119** (2017).

[233] E. Neu, M. Agio and C. Becher, “Photophysics of single silicon vacancy centers in diamond: implications for single photon emission”, Optics Express **20**, 19956 (2012).

[234] S. Castelletto, B. C. Johnson, V. Ivády, N. Stavrias, T. Umeda, A. Gali and T. Ohshima, “A silicon carbide room-temperature single-photon source”, Nature Materials **13**, 151–156 (2013).

[235] M. Radulaski et al., “Scalable Quantum Photonics with Single Color Centers in Silicon Carbide”, Nano Letters **17**, 1782–1786 (2017).

[236] T. T. Tran, K. Bray, M. J. Ford, M. Toth and I. Aharonovich, “Quantum emission from hexagonal boron nitride monolayers”, Nature Nanotechnology **11**, 37–41 (2015).

[237] V. Scarani, H. Bechmann-Pasquinucci, N. J. Cerf, M. Dušek, N. Lütkenhaus and M. Peev, “The security of practical quantum key distribution”, Reviews of Modern Physics **81**, 1301–1350 (2009).

[238] K. Takemoto, Y. Nambu, T. Miyazawa, Y. Sakuma, T. Yamamoto, S. Yorozu and Y. Arakawa, “Quantum key distribution over 120 km using ultrahigh purity single-photon source and superconducting single-photon detectors”, Scientific Reports **5** (2015).

[239] D. F. Walls and G. J. Milburn, *Quantum Optics* (Springer Berlin Heidelberg, 1994).

[240] E. S. Polzik, J. Carri and H. J. Kimble, “Spectroscopy with squeezed light”, Physical Review Letters **68**, 3020–3023 (1992).

[241] M. Xiao, L.-A. Wu and H. J. Kimble, “Precision measurement beyond the shot-noise limit”, Physical Review Letters **59**, 278–281 (1987).

[242] V. Giovannetti, S. Lloyd and L. Maccone, “Quantum-Enhanced Measurements: Beating the Standard Quantum Limit”, Science **306**, 1330–1336 (2004).

[243] K. Goda et al., “A quantum-enhanced prototype gravitational-wave detector”, Nature Physics **4**, 472–476 (2008).

[244] Y.-M. He et al., “On-demand semiconductor single-photon source with near-unity indistinguishability”, Nature Nanotechnology **8**, 213–217 (2013).

[245] R. P. Mildren, J. E. Butler and J. R. Rabeau, “CVD-diamond external cavity Raman laser at 573 nm”, Optics Express **16**, 18950 (2008).

[246] A. M. Zaitsev, *Optical Properties of Diamond* (Springer Berlin Heidelberg, 2001).

[247] C. J. Hepp, "Electronic Structure of the Silicon Vacancy Color Center in Diamond", PhD thesis (Universität des Saarlandes, 2014).

[248] I. Aharonovich, S. Castelletto, D. A. Simpson, C.-H. Su, A. D. Greentree and S. Prawer, "Diamond-based single-photon emitters", Reports on Progress in Physics **74**, 076501 (2011).

[249] I. Aharonovich and E. Neu, "Diamond Nanophotonics", Advanced Optical Materials **2**, 911–928 (2014).

[250] M. Leifgen et al., "Evaluation of nitrogen- and silicon-vacancy defect centres as single photon sources in quantum key distribution", New Journal of Physics **16**, 023021 (2014).

[251] A. Gruber, A. Dräbenstedt, C. Tietz, L. Fleury, J. Wrachtrup and C. von Borczyskowski, "Scanning Confocal Optical Microscopy and Magnetic Resonance on Single Defect Centers", Science **276**, 2012–2014 (1997).

[252] C.-H. Su, A. D. Greentree and L. C. L. Hollenberg, "Towards a picosecond transform-limited nitrogen-vacancy based single photon source", Optics Express **16**, 6240 (2008).

[253] G. Davies, "The Jahn-Teller effect and vibronic coupling at deep levels in diamond", Reports on Progress in Physics **44**, 787–830 (1981).

[254] J. Wolters et al., "Enhancement of the zero phonon line emission from a single nitrogen vacancy center in a nanodiamond via coupling to a photonic crystal cavity", Applied Physics Letters **97**, 141108 (2010).

[255] A. Mohtashami and A. F. Koenderink, "Suitability of nanodiamond nitrogen–vacancy centers for spontaneous emission control experiments", New Journal of Physics **15**, 043017 (2013).

[256] A. T. Collins, M. F. Thomaz and M. I. B. Jorge, "Luminescence decay time of the 1.945 eV centre in type Ib diamond", Journal of Physics C: Solid State Physics **16**, 2177–2181 (1983).

[257] J. Wrachtrup and F. Jelezko, "Processing quantum information in diamond", Journal of Physics: Condensed Matter **18**, S807–S824 (2006).

[258] H. Hanzawa, Y. Nisida and T. Kato, "Measurement of decay time for the NV centre in ib diamond with a picosecond laser pulse", Diamond and Related Materials **6**, 1595–1598 (1997).

[259] J. Tisler et al., "Fluorescence and Spin Properties of Defects in Single Digit Nanodiamonds", ACS Nano **3**, 1959–1965 (2009).

[260] A. Dräbenstedt, L. Fleury, C. Tietz, F. Jelezko, S. Kilin, A. Nizovtzev and J. Wrachtrup, "Low-temperature microscopy and spectroscopy on single defect centers in diamond", Physical Review B **60**, 11503–11508 (1999).

[261] E. Togan et al., "Quantum entanglement between an optical photon and a solid-state spin qubit", Nature **466**, 730–734 (2010).

[262] L. Rondin, J.-P. Tetienne, T. Hingant, J.-F. Roch, P. Maletinsky and V. Jacques, "Magnetometry with nitrogen-vacancy defects in diamond", Reports on Progress in Physics **77**, 056503 (2014).

[263] B. Hensen et al., "Loophole-free Bell inequality violation using electron spins separated by 1.3 kilometres", Nature **526**, 682–686 (2015).

[264] T. Müller et al., "Optical signatures of silicon-vacancy spins in diamond", Nature Communications **5** (2014).

[265] L. J. Rogers et al., "All-Optical Initialization, Readout, and Coherent Preparation of Single Silicon-Vacancy Spins in Diamond", Physical Review Letters **113** (2014).

[266] L. J. Rogers et al., "Multiple intrinsically identical single-photon emitters in the solid state", Nature Communications **5** (2014).

[267] A. Sipahigil, K. Jahnke, L. Rogers, T. Teraji, J. Isoya, A. Zibrov, F. Jelezko and M. Lukin, "Indistinguishable Photons from Separated Silicon-Vacancy Centers in Diamond", Physical Review Letters **113** (2014).

[268] B. C. Rose et al., "Observation of an environmentally insensitive solid-state spin defect in diamond", Science **361**, 60–63 (2018).

[269] P. Siyushev et al., "Optical and microwave control of germanium-vacancy center spins in diamond", Physical Review B **96** (2017).

[270] M. Alkahtani, I. Cojocaru, X. Liu, T. Herzig, J. Meijer, J. Küpper, T. Lühmann, A. V. Akimov and P. R. Hemmer, "Tin-vacancy in diamonds for luminescent thermometry", Applied Physics Letters **112**, 241902 (2018).

[271] C. T. Nguyen et al., "All-optical nanoscale thermometry with silicon-vacancy centers in diamond", Applied Physics Letters **112**, 203102 (2018).

[272] T. Gaebel, I. Popa, A. Gruber, M. Domhan, F. Jelezko and J. Wrachtrup, "Stable single-photon source in the near infrared", New Journal of Physics **6**, 98–98 (2004).

[273] I. Aharonovich, S. Castelletto, D. A. Simpson, A. Stacey, J. McCallum, A. D. Greentree and S. Prawer, "Two-Level Ultrabright Single Photon Emission from Diamond Nanocrystals", Nano Letters **9**, 3191–3195 (2009).

[274] A. Gali and J. R. Maze, "Ab initiostudy of the split silicon-vacancy defect in diamond: Electronic structure and related properties", Physical Review B **88** (2013).

[275] E. Neu, C. Hepp, M. Hauschild, S. Gsell, M. Fischer, H. Sternschulte, D. Steinmüller-Nethl, M. Schreck and C. Becher, "Low-temperature investigations of single silicon vacancy colour centres in diamond", New Journal of Physics **15**, 043005 (2013).

[276] U. F. S. D'Haenens-Johansson, A. M. Edmonds, B. L. Green, M. E. Newton, G. Davies, P. M. Martineau, R. U. A. Khan and D. J. Twitchen, "Optical properties of the neutral silicon split-vacancy center in diamond", Physical Review B **84** (2011).

[277] H. A. Jahn, E. Teller and F. G. Donnan, "Stability of polyatomic molecules in degenerate electronic states - I—Orbital degeneracy", Proceedings of the Royal Society of London. Series A - Mathematical and Physical Sciences **161**, 220–235 (1937).

[278] E. Neu, R. Albrecht, M. Fischer, S. Gsell, M. Schreck and C. Becher, "Electronic transitions of single silicon vacancy centers in the near-infrared spectral region", Physical Review B **85** (2012).

[279] E. Neu, "Silicon vacancy color centers in chemical vapor deposition diamond: New insights into promising solid state single photon sources", PhD thesis (Universität des Saarlandes, 2012).

[280] L. Bergman, B. R. Stoner, K. F. Turner, J. T. Glass and R. J. Nemanich, "Microphotoluminescence and Raman scattering study of defect formation in diamond films", Journal of Applied Physics **73**, 3951–3957 (1993).

[281] L. Bergman, M. T. McClure, J. T. Glass and R. J. Nemanich, "The origin of the broadband luminescence and the effect of nitrogen doping on the optical properties of diamond films", Journal of Applied Physics **76**, 3020–3027 (1994).

[282] M. C. Rossi, S. Salvatori, F. Galluzzi, F. Somma and R. M. Montereali, "Diamond photoluminescence spectra: Dependence on excitation energy and microstructure", Diamond and Related Materials **7**, 255–260 (1998).

[283] A. E. Mora, J. W. Steeds and J. E. Butler, "Relationship between grain boundaries and broad luminescence peaks in CVD diamond films", Diamond and Related Materials **12**, 310–317 (2003).

[284] U. Jantzen et al., "Nanodiamonds carrying silicon-vacancy quantum emitters with almost lifetime-limited linewidths", New Journal of Physics **18**, 073036 (2016).

[285] K. Li, Y. Zhou, A. Rasmita, I. Aharonovich and W. Gao, "Nonblinking Emitters with Nearly Lifetime-Limited Linewidths in CVD Nanodiamonds", Physical Review Applied **6** (2016).

[286] A. S. Barnard, I. I. Vlasov and V. G. Ralchenko, "Predicting the distribution and stability of photoactive defect centers in nanodiamond biomarkers", J. Mater. Chem. **19**, 360–365 (2009).

[287] I. I. Vlasov, A. S. Barnard, V. G. Ralchenko, O. I. Lebedev, M. V. Kanzyuba, A. V. Saveliev, V. I. Konov and E. Goovaerts, "Nanodiamond Photoemitters Based on Strong Narrow-Band Luminescence from Silicon-Vacancy Defects", Advanced Materials **21**, 808–812 (2009).

[288] I. I. Vlasov et al., "Molecular-sized fluorescent nanodiamonds", Nature Nanotechnology **9**, 54–58 (2013).

[289] S. Choi, V. Leong, V. A. Davydov, V. N. Agafonov, M. W. O. Cheong, D. A. Kalashnikov and L. A. Krivitsky, "Varying temperature and silicon content in nanodiamond growth: effects on silicon-vacancy centres", Scientific Reports **8** (2018).

[290] A. V. Turukhin, C.-H. Liu, A. A. Gorokhovsky, R. R. Alfano and W. Phillips, "Picosecond photoluminescence decay of Si-doped chemical-vapor-deposited diamond films", Physical Review B **54**, 16448–16451 (1996).

[291] T. Feng and B. D. Schwartz, "Characteristics and origin of the 1.681 eV luminescence center in chemical-vapor-deposited diamond films", Journal of Applied Physics **73**, 1415–1425 (1993).

[292] S. Meesala et al., "Strain engineering of the silicon-vacancy center in diamond", Physical Review B **97** (2018).

[293] S. Maity, L. Shao, Y.-I. Sohn, S. Meesala, B. Machielse, E. Bielejec, M. Markham and M. Lončar, "Spectral Alignment of Single-Photon Emitters in Diamond using Strain Gradient", Physical Review Applied **10** (2018).

[294] Y.-I. Sohn et al., "Controlling the coherence of a diamond spin qubit through its strain environment", Nature Communications **9** (2018).

[295] S. Lindner et al., "Strongly inhomogeneous distribution of spectral properties of silicon-vacancy color centers in nanodiamonds", New Journal of Physics **20**, 115002 (2018).

[296] T. D. Merson, S. Castelletto, I. Aharonovich, A. Turbic, T. J. Kilpatrick and A. M. Turnley, "Nanodiamonds with silicon vacancy defects for nontoxic photostable fluorescent labeling of neural precursor cells", Optics Letters **38**, 4170 (2013).

[297] G. Thiering and A. Gali, "Complexes of silicon, vacancy, and hydrogen in diamond: A density functional study", Physical Review B **92** (2015).

[298] P. Siyushev et al., "Low-temperature optical characterization of a near-infrared single-photon emitter in nanodiamonds", New Journal of Physics **11**, 113029 (2009).

[299] T. T. Tran, M. Kianinia, K. Bray, S. Kim, Z.-Q. Xu, A. Gentle, B. Sontheimer, C. Bradac and I. Aharonovich, "Nanodiamonds with photostable, sub-gigahertz linewidth quantum emitters", APL Photonics **2**, 116103 (2017).

[300] K. Bray, R. Sandstrom, C. Elbadawi, M. Fischer, M. Schreck, O. Shimoni, C. Lobo, M. Toth and I. Aharonovich, "Localization of Narrowband Single Photon Emitters in Nanodiamonds", ACS Applied Materials & Interfaces **8**, 7590–7594 (2016).

[301] *quTAU Time-to-Digital Converter, Manual V4.0*, qutools (Apr. 2016).

[302] C. Bradac et al., "Observation and control of blinking nitrogen-vacancy centres in discrete nanodiamonds", Nature Nanotechnology **5**, 345–349 (2010).

[303] S. P. Russo, A. S. Barnard and I. K. Snook, "Hydrogenation of Nanodiamond Surfaces: Structure and Effects on Crystalline Stability", Surface Review and Letters **10**, 233–239 (2003).

[304] S. Osswald, G. Yushin, V. Mochalin, S. O. Kucheyev and Y. Gogotsi, "Control of sp^2/sp^3 Carbon Ratio and Surface Chemistry of Nanodiamond Powders by Selective Oxidation in Air", Journal of the American Chemical Society **128**, 11635–11642 (2006).

[305] D. Englund, B. Shields, K. Rivoire, F. Hatami, J. Vučković, H. Park and M. D. Lukin, "Deterministic Coupling of a Single Nitrogen Vacancy Center to a Photonic Crystal Cavity", Nano Letters **10**, 3922–3926 (2010).

[306] D. Riedel, I. Söllner, B. J. Shields, S. Starosielec, P. Appel, E. Neu, P. Maletinsky and R. J. Warburton, "Deterministic Enhancement of Coherent Photon Generation from a Nitrogen-Vacancy Center in Ultrapure Diamond", Physical Review X **7** (2017).

[307] S. Bogdanović et al., "Design and low-temperature characterization of a tunable microcavity for diamond-based quantum networks", Applied Physics Letters **110**, 171103 (2017).

[308] S. Häußler, J. Benedikter, K. Bray, B. Regan, A. Dietrich, J. Twamley, I. Aharonovich, D. Hunger and A. Kubanek, "Diamond photonics platform based on silicon vacancy centers in a single-crystal diamond membrane and a fiber cavity", Physical Review B **99** (2019).

[309] E. Knill, R. Laflamme and G. J. Milburn, "A scheme for efficient quantum computation with linear optics", Nature **409**, 46–52 (2001).

[310] P. Kok, W. J. Munro, K. Nemoto, T. C. Ralph, J. P. Dowling and G. J. Milburn, "Linear optical quantum computing with photonic qubits", Reviews of Modern Physics **79**, 135–174 (2007).

[311] S. Wein, N. Lauk, R. Ghobadi and C. Simon, "Feasibility of efficient room-temperature solid-state sources of indistinguishable single photons using ultrasmall mode volume cavities", Physical Review B **97** (2018).

[312] P. Goldner, A. Ferrier and O. Guillot-Noël, "Rare Earth-Doped Crystals for Quantum Information Processing", in *Handbook on the physics and chemistry of rare earths* (Elsevier, 2015), pp. 1–78.

[313] L. Marschall and H. Holdinghausen, *Seltene Erden* (Oekom Verlag GmbH, 2017).

[314] E. Riedel and C. Janiak, *Anorganische Chemie* (De Gruyter, 2011).

[315] C. W. Thiel, T. Böttger and R. L. Cone, "Rare-earth-doped materials for applications in quantum information storage and signal processing", Journal of Luminescence **131**, 353–361 (2011).

[316] T. Böttger, C. W. Thiel, R. L. Cone and Y. Sun, "Effects of magnetic field orientation on optical decoherence in $Er : Y_2SiO_5$", Physical Review B **79** (2009).

[317] J. J. Longdell, E. Fraval, M. J. Sellars and N. B. Manson, "Stopped Light with Storage Times Greater than One Second Using Electromagnetically Induced Transparency in a Solid", Physical Review Letters **95** (2005).

[318] R. Kolesov, K. Xia, R. Reuter, R. Stöhr, A. Zappe, J. Meijer, P. R. Hemmer and J. Wrachtrup, "Optical detection of a single rare-earth ion in a crystal", Nature Communications **3** (2012).

[319] T. Utikal, E. Eichhammer, L. Petersen, A. Renn, S. Götzinger and V. Sandoghdar, "Spectroscopic detection and state preparation of a single praseodymium ion in a crystal", Nature Communications **5** (2014).

[320] I. Nakamura, T. Yoshihiro, H. Inagawa, S. Fujiyoshi and M. Matsushita, "Spectroscopy of single Pr^{3+} ion in LaF_3 crystal at 1.5 K", Scientific Reports **4** (2014).

[321] P. Siyushev et al., "Coherent properties of single rare-earth spin qubits", Nature Communications **5** (2014).

[322] K. Binnemans, "Interpretation of europium(III) spectra", Coordination Chemistry Reviews **295**, 1–45 (2015).

[323] H. Cui, P.-F. Zhu, H.-Y. Zhu, H.-D. Li and Q.-L. Cui, "Photoluminescence properties and energy transfer in $Eu^{3+} : Y_2O_3$ nanophosphors", Chinese Physics B **23**, 057801 (2014).

[324] T. Krom, *Fluoreszenzspektroskopie an Europium mit einem Konfokalmikroskop*, Bachelorarbeit, Karlsruher Institut für Technologie, 2018.

[325] J. Karlsson, N. Kunkel, A. Ikesue, A. Ferrier and P. Goldner, "Nuclear spin coherence properties of $^{151}Eu^{3+}$ and $^{153}Eu^{3+}$ in a Y_2O_3 transparent ceramic", Journal of Physics: Condensed Matter **29**, 125501 (2017).

[326] L. Rippe, B. Julsgaard, A. Walther, Y. Ying and S. Kröll, "Experimental quantum-state tomography of a solid-state qubit", Physical Review A **77** (2008).

[327] K. de Oliveira Lima, R. R. Gonçalves, D. Giaume, A. Ferrier and P. Goldner, "Influence of defects on sub-Å optical linewidths in $Eu^{3+} : Y_2O_3$ particles", Journal of Luminescence **168**, 276–282 (2015).

[328] G. P. Flinn, K. W. Jang, J. Ganem, M. L. Jones, R. S. Meltzer and R. M. Macfarlane, "Anomalous optical dephasing in crystalline $Y_2O_3 : Eu^{3+}$", Journal of Luminescence **58**, 374–379 (1994).

[329] G. P. Flinn, K. W. Jang, J. Ganem, M. L. Jones, R. S. Meltzer and R. M. Macfarlane, "Sample-dependent optical dephasing in bulk crystalline samples of $Y_2O_3 : Eu^{3+}$", Physical Review B **49**, 5821–5827 (1994).

[330] R. M. Macfarlane, A. Arcangeli, A. Ferrier and P. Goldner, "Optical Measurement of the Effect of Electric Fields on the Nuclear Spin Coherence of Rare-Earth Ions in Solids", Physical Review Letters **113** (2014).

[331] T. Lutz, L. Veissier, C. W. Thiel, R. L. Cone, P. E. Barclay and W. Tittel, "Modification of phonon processes in nanostructured rare-earth-ion-doped crystals", Physical Review A **94** (2016).

[332] K. D. Jahnke, A. Sipahigil, J. M. Binder, M. W. Doherty, M. Metsch, L. J. Rogers, N. B. Manson, M. D. Lukin and F. Jelezko, "Electron–phonon processes of the silicon-vacancy centre in diamond", New Journal of Physics **17**, 043011 (2015).

[333] H. Chew, "Radiation and lifetimes of atoms inside dielectric particles", Physical Review A **38**, 3410–3416 (1988).

[334] F. L. Kien, N. H. Quang and K. Hakuta, "Spontaneous emission from an atom inside a dielectric sphere", Optics Communications **178**, 151–164 (2000).

[335] H. Schniepp and V. Sandoghdar, "Spontaneous Emission of Europium Ions Embedded in Dielectric Nanospheres", Physical Review Letters **89** (2002).

[336] C.-K. Duan, M. F. Reid and Z. Wang, "Local field effects on the radiative lifetime of emitters in surrounding media: Virtual- or real-cavity model?", Physics Letters A **343**, 474–480 (2005).

[337] A. Khalid, K. Chung, R. Rajasekharan, D. W. M. Lau, T. J. Karle, B. C. Gibson and S. Tomljenovic-Hanic, "Lifetime Reduction and Enhanced Emission of Single Photon Color Centers in Nanodiamond via Surrounding Refractive Index Modification", Scientific Reports **5** (2015).

[338] T. Zhong, J. M. Kindem, E. Miyazono and A. Faraon, "Nanophotonic coherent light–matter interfaces based on rare-earth-doped crystals", Nature Communications **6** (2015).

[339] M. K. Bhaskar et al., "Quantum Nonlinear Optics with a Germanium-Vacancy Color Center in a Nanoscale Diamond Waveguide", Physical Review Letters **118** (2017).

[340] W. E. Gifford and R. C. Longsworth, "Surface Heat Pumping", in *Advances in cryogenic engineering* (Springer US, 1966), pp. 171–179.

[341] W. E. Gifford, "The Gifford-McMahon Cycle", in *Advances in cryogenic engineering* (Springer US, 1966), pp. 152–159.

[342] N. Kunkel, A. Ferrier, C. W. Thiel, M. O. Ramírez, L. E. Bausá, R. L. Cone, A. Ikesue and P. Goldner, "Rare-earth doped transparent ceramics for spectral filtering and quantum information processing", APL Materials **3**, 096103 (2015).

[343] R. W. P. Drever, J. L. Hall, F. V. Kowalski, J. Hough, G. M. Ford, A. J. Munley and H. Ward, "Laser phase and frequency stabilization using an optical resonator", Applied Physics B Photophysics and Laser Chemistry **31**, 97–105 (1983).

[344] E. D. Black, "An introduction to Pound–Drever–Hall laser frequency stabilization", American Journal of Physics **69**, 79–87 (2001).

[345] H. Brachmann, *Pound-Drever-Hall active length stabilization for fiber cavity*, June 2014.

[346] E. Janitz, M. Ruf, Y. Fontana, J. Sankey and L. Childress, "High mechanical bandwidth fiber-coupled Fabry-Perot cavity", Optics Express **25**, 20932 (2017).

[347] J. H. Kindt, G. E. Fantner, J. A. Cutroni and P. K. Hansma, "Rigid design of fast scanning probe microscopes using finite element analysis", Ultramicroscopy **100**, 259–265 (2004).

[348] B. J. Kenton and K. K. Leang, "Design and Control of a Three-Axis Serial-Kinematic High-Bandwidth Nanopositioner", IEEE/ASME Transactions on Mechatronics **17**, 356–369 (2012).

[349] G. Martinet, B. Blivet, F. Chatelet, M. Fouaidy, N. Hammoudi, A. Olivier and H. Saugnac, "Low temperature properties of piezoelectric actuators used in SRF cavities cold tuning systems", Contribution to the EPAC 06, Edinburgh, UK (2006).

[350] Y. K. Yong, S. O. R. Moheimani, B. J. Kenton and K. K. Leang, "Invited Review Article: High-speed flexure-guided nanopositioning: Mechanical design and control issues", Review of Scientific Instruments **83**, 121101 (2012).

[351] J. Tuttle, E. Canavan and M. DiPirro, "Thermal and electrical conductivity measurements of CDA 510 phosphor bronze", NASA (2009).

[352] C. A. Angell, K. L. Ngai, G. B. McKenna, P. F. McMillan and S. W. Martin, "Relaxation in glassforming liquids and amorphous solids", Journal of Applied Physics **88**, 3113–3157 (2000).

[353] *Teflon PTFE fluoropolymer resin, Properties Handbook*, DuPont (2019).

[354] G. Hartwig, *Polymer Properties at Room and Cryogenic Temperatures* (Springer Science & Business Media, 18th Apr. 2013).

[355] *PTFE-fluoroplastic, Properties and characteristic data*, TEKU GmbH Fluorkunststoffe (2019).

[356] T. Kaiser, *An FFT Primer for physicists*, Institute of Applied Physics, Abbe School of Photonics, Friedrich-Schiller-Universität Jena, June 2014.

[357] M. Kuznetsov, M. Stern and J. Coppeta, "Single transverse mode optical resonators", Optics Express **13**, 171 (2005).

[358] F. Ferdous, A. A. Demchenko, S. P. Vyatchanin, A. B. Matsko and L. Maleki, "Microcavity morphology optimization", Physical Review A **90** (2014).

[359] J. Weitenberg, P. Rußbldt, T. Eidam and I. Pupeza, "Transverse mode tailoring in a quasi-imaging high-finesse femtosecond enhancement cavity", Optics Express **19**, 9551 (2011).

[360] B. T. Walker, L. C. Flatten, H. J. Hesten, F. Mintert, D. Hunger, A. A. P. Trichet, J. M. Smith and R. A. Nyman, "Driven-dissipative non-equilibrium Bose–Einstein condensation of less than ten photons", Nature Physics **14**, 1173–1177 (2018).

[361] D. D. Sukachev, A. Sipahigil, C. T. Nguyen, M. K. Bhaskar, R. E. Evans, F. Jelezko and M. D. Lukin, "Silicon-Vacancy Spin Qubit in Diamond: A Quantum Memory Exceeding 10 ms with Single-Shot State Readout", Physical Review Letters **119** (2017).

[362] R. E. Evans et al., "Photon-mediated interactions between quantum emitters in a diamond nanocavity", Science **362**, 662–665 (2018).

[363] *Materials and Manufacturing: Cryogenic (4 K...293 K) Material Properties*, Janssen Precision Engineering (JPE) (2019).

[364] E. D. Marquardt, J. P. Le and R. Radebaugh, "Cryogenic Material Properties Database", National Institute of Standards and Technology (2000).

[365] H.-J. Bargel and H. Hilbrans, *Werkstoffkunde* (Springer, 2008).

[366] W. M. Haynes, *CRC Handbook of Chemistry and Physics, 92nd Edition* (CRC Press, 2011).

[367] R. K. Kirby, "Thermal Expansion of Polytetrafluoroethylene (Teflon) From −190° to +300° C", Journal of Research of the National Bureau of Standards (1956).

[368] H. Czichos, *Die Grundlagen Der Ingenieurwissenschaften, D Werkstoffe, Wärmeleitfähigkeit von Werkstoffen, 31. Auflage* (Springer, 2000).

[369] *POM-C Datenblatt*, Kunststoff-Fertigteile (2019).

[370] *DuPont Kapton, Summary of properties*, DuPont (2017).

Publications and conference contributions

Publications

- *Transverse-mode coupling and diffraction loss in tunable Fabry–Pérot microcavities*
  J. Benedikter, T. Hümmer, M. Mader, B. Schlederer, J. Reichel, T.W. Hänsch, D. Hunger
  New J. Phys. **17**, 053051 (2015) [94]

- *Purcell-Enhanced Single-Photon Emission from Nitrogen-Vacancy Centers Coupled to a Tunable Microcavity*
  H. Kaupp, T. Hümmer, M. Mader, B. Schlederer, J. Benedikter, P. Haeusser, H.-C. Chang, H. Fedder, T. W. Hänsch, D. Hunger
  Physical Review Applied **6**, 054010 (2016) [46]

- *Cavity-Enhanced Single-Photon Source Based on the Silicon-Vacancy Center in Diamond*
  J. Benedikter, H. Kaupp, T. Hümmer, Y. Liang, A. Bommer, C. Becher, A. Krueger, J. M. Smith, T. W. Hänsch, D. Hunger
  Physical Review Applied **7**, 024031 (2017) [53]

- *Cavity-enhanced spectroscopy of a few-ion ensemble in* $Eu^{3+} : Y_2O_3$
  B. Casabone, J. Benedikter, T. Hümmer, F. Oehl, K. de Oliveira Lima, T. W. Hänsch, A. Ferrier, P. Goldner, H. de Riedmatten, D. Hunger
  New J. Phys. **20**, 095006 (2018) [85]

- *Diamond photonics platform based on silicon vacancy centers in a single-crystal diamond membrane and a fiber cavity*
  S. Häußler, J. Benedikter, K. Bray, B. Regan, A. Dietrich, J. Twamley, I. Aharonovich, D. Hunger, A. Kubanek
  Physical Review B **99**, 165310 (2019) [308]

- *Transverse-mode coupling effects in scanning cavity microscopy*
  J. Benedikter, T. Moosmayer, M. Mader, T. Hümmer, D. Hunger
  submitted (2019) [95]

Conference Contributions

- *Transverse-Mode Coupling and Diffraction Loss in Fiber-Based Microcavities*
  DPG Frühjahrstagung der Sektion AMOP, Poster
  Berlin, Germany, March 2014

- *Transverse-Mode Coupling and Diffraction Loss in Fiber-Based Microcavities*
  DPG Frühjahrstagung der Sektion AMOP, Poster
  Heidelberg, Germany, March 2015

- *Transverse-Mode Coupling and Diffraction Loss in Fibre-Based Microcavities*
  Young Atom Opticians' Conference, Talk
  Zürich, Switzerland, April 2015

- *Transverse-Mode Coupling and Diffraction Loss in Fibre-Based Microcavities*
  Conference on Lasers and Electro-Optics (CLEO) Europe, Poster
  Munich, Germany, June 2015

- *Transverse-Mode Coupling and Diffraction Loss in Fibre-Based Microcavities*
  NIM Conference on Resonator QED, Poster
  Munich, Germany, August 2015

- *Transverse-mode coupling, Efficient single photon source using SiV centres in nanodiamonds, Indistinguishable single photon source*
  Fibre Cavity Workshop organised by Prof. Jakob Reichel, Talk
  Paris, France, September 2015

- *SiV Centres in Microcavities – An Efficient Single Photon Source at Room Temperature*
  DPG Frühjahrstagung der Sektion AMOP, Poster
  Hanover, Germany, March 2016

- *SiV Centres in Microcavities – An Efficient Single Photon Source at Room Temperature*
  Lindau Nobel Laureate Meeting, Poster
  Lindau, Germany, July 2016

- *SiV Centres in Microcavities – An Efficient Single Photon Source at Room Temperature*
  International Conference on Atomic Physics (ICAP), Poster
  Seoul, Korea, August 2016

- *SiV Centres in Microcavities – An Efficient Single Photon Source at Room Temperature*
  Single Photons Single Spins (SPSS) Workshop, Talk
  Oxford, UK, September 2016

- *SiV Centres in Microcavities – An Efficient Single Photon Source at Room Temperature*
  DPG Frühjahrstagung der Sektion AMOP, Poster
  Mainz, Germany, March 2017

- *Introduction to Fibre-Based Microcavities*
  NanOQTech Rare Earth Workshop, Talk
  Paris, France, April 2017

- *SiV Centres in Microcavities – An Efficient Single Photon Source at Room Temperature*
  'Quantum Information meets Nanotechnology' Workshop, poster
  San Sebastian, Spain, August 2017

- *Cavity-enhanced single photon source based on the silicon vacancy centre in diamond*
  Quantum Networks – From Building Blocks to Applications, WE-Heraeus-Seminar, poster, 2nd poster prize
  Bad Honnef, Germany, February 2018

- *Cavity-enhanced spectroscopy of a few-ion ensemble in* $Eu^{3+} : Y_2O_3$
  DPG Frühjahrstagung der Sektion AMOP, Poster
  Erlangen, Germany, March 2018

- *Transverse-mode coupling effects in scanning cavity microscopy*
  DPG Frühjahrstagung der Sektion AMOP, Poster
  Rostock, Germany, March 2019

Danksagung

Nun möchte ich noch all jenen meinen Dank aussprechen, deren Unterstützung und Begleitung während der Jahre der Promotion letztlich zu deren Gelingen geführt haben und die mir über so manch schwere Phase hinweggeholfen haben. Mit so vielen verschiedenen netten und oft beeindruckenden Menschen zusammen zu arbeiten begreife ich als Privileg und der Austausch mit ihnen stellt für mich eine große Bereicherung und eine Erweiterung meines Horizonts dar, die mich geprägt haben und bestimmt noch lange über die Doktorandenzeit hinaus wirken werden.

Mein Dank gilt zunächst Prof. Theodor Hänsch dafür, dass ich an seinem Lehrstuhl arbeiten durfte. Mir ist eigentlich erst mit der Zeit, zum Beispiel in Gesprächen auf Konferenzen, aufgefallen, wie außergewöhnlich die Zusammenstellung dieser Gruppe ist. Ich bin dankbar ihr angehören zu dürfen, insbesondere für die vielen interessanten Gespräche zum Beispiel auf Ringberg und die Unterstützung, die man in diesem Umfeld erfährt. Insbesondere möchte ich mich noch dafür bedanken, dass Prof. Hänsch es mir so unkompliziert und mit viel Verständnis ermöglicht hat nach dem Umzug der Hunger-Gruppe nach Karlsruhe seine Räumlichkeiten und Geräte weiter zu nutzen und weiterhin in die Gruppe integriert zu sein.

Ganz besonders möchte ich meinem Betreuer Prof. David Hunger danken, der mir durch seinen grenzenlosen Optimismus und seine Begeisterungsfähigkeit immer wieder über das ein oder andere Motivationsloch hinweggeholfen hat und dessen ungemeiner Ideenreichtum mich in so manch vermeintlich aussichtsloser Lage weiter brachte. Ich rechne es ihm hoch an, dass er meiner Entscheidung nicht nach Karlsruhe zu gehen mit so viel Verständnis entgegnet ist, auch wenn das für ihn vieles schwieriger gemacht hat. Es hat mich auch weitergebracht auf so viele Konferenzen fahren zu dürfen und so, auch im internationalen Kontext, über den Tellerrand zu schauen. Davids positive und bestärkende Art, mit der er über Rückschläge hinwegsieht und sich, oft mehr als man selbst, über Erfolge freut, macht ihn zu einem Chef, wie ihn sich viele wünschen würden.

Die drei Kollegen Thomas Hümmer, Matthias Mader und Hanno Kaupp haben mich von Beginn meiner Promotion an begleitet, mir alles gezeigt, mir viel geholfen und mir den Arbeitsalltag sehr angenehm gemacht. Thomas möchte ich insbesondere für seine unermüdliche Hilfe mit der Software und seine vielen Ideen zu Verbesserungen der Experimente danken, sowie für die vielen Diskussionen über die Physik hinaus, die mich oft zum Überlegen angeregt und mich auch manchmal zum Umdenken gebracht haben. An ihm bewundere ich nicht nur seine offene und selbstlose Art, sondern auch seine enorme Auffassungsgabe und Kreativität, sowie den Mut unkonventionelle Wege zu gehen und auch das eigene Tun in Frage zu stellen. Matthias hat mir bei vielen technischen Fragestellungen geholfen und mir vor allem auch in schweren Situationen zugehört und ist mir geduldig und ehrlich mit seinem Rat zur Seite gestanden. Seine direkte und ehrliche Art und vor allem sein absolut außergewöhnliches Wissen, das sich auf alle möglichen Bereiche erstreckt und oft ins kleinste Detail geht, machen ihn zu einem besonderen Kollegen und äußerst kurzweiligen Gesprächspartner. Mit Hanno Kaupp habe ich einige Zeit gemeinsam im Labor verbracht; Er hat mir vieles gezeigt und erklärt und durch

seine immer fröhliche und lustige Art sehr zu einer guten Stimmung beigetragen. Ich hoffe, in den dreien nicht nur gute Kollegen, sondern auch Freunde gefunden zu haben.

Als weitere zeitweise Laborgenossen sind Hannes Brachmann, Tolga Bagci, Pradyumna Paranjape, Michael Förg, Larissa Kohler und Bernardo Casabone zu nennen. Hannes hat mir ganz zu Anfang meiner Doktorarbeit in technischen Fragen geholfen. Tolga, Pradyumna, Michi und Larissa danke ich für die angenehme Zeit im Labor und die netten Gespräche. Ein besonderer Dank gilt Bernardo, der mich in das Europium-Experiment eingeführt hat. Es hat mich sehr positiv überrascht und ich habe es sehr zu schätzen gewusst, wie ernst er mich nahm und wie viel er auf meine Meinung gab, obwohl er doch um so viel mehr Erfahrung hatte als ich. Trotz unserer recht verschiedenen Herangehensweise war unsere Zusammenarbeit sehr effizient und wir hatten auch über die Arbeit hinaus, zum Beispiel beim gemeinsamen Bouldern, viel Spaß zusammen. Meinen 'Nachfolgern' Maximilian Pallmann, Kelvin Chung und Timon Eichhorn danke ich für die angenehmen letzten Monate am Experiment und hoffe auf eine erfolgreiche Fortführung.

Ich durfte im Laufe dieser Arbeit zwei Studenten betreuen, Eric Bersin und Lukas Husel, was für mich eine schöne Erfahrung war. Danke dafür!

Im Laufe der Jahre habe ich mir mit Franziska Oehl, Christian Gebhardt und Frederik Bopp ein Büro geteilt, bei denen ich mich für ein angenehmes Miteinander bedanke. Besonders die regelmäßigen Kaffeepausen mit Christian, auf die ich mich immer schon gefreut habe, werden mir in Erinnerung bleiben. Wer hätte gedacht, was daraus noch erwachsen sollte...

Ich danke den Mitarbeitern der Arbeitsgruppe von Prof. Weinfurter für ein nettes Miteinander, schöne Gespräche und eine angenehme Atmosphäre.

Für die präzise Fertigung meiner diversen Bauteile bedanke ich mich bei Herrn Aust und Herrn Großhauser, sowie deren Mitarbeiter. Vielen Dank für die Geduld bezüglich all der Sonderwünsche und nachträglichen Änderungen! Bei Charly Linner und Wolfgang Simon bedanke ich mich für die Anfertigung einiger Spezialteile. Des Weiteren gilt mein Dank Anton Scheich und Helmut Brückner für Elektronikaufgaben. Toni danke ich dabei besonders für seine Geduld und seine freundliche Art gegenüber meiner oftmals vorhandenen Unkenntnis. Insbesondere möchte ich auch Philipp Altpeter danken, der mich sehr geduldig und ausführlich in diverse Geräte im Reinraum eingewiesen hat und mir, als Nicht-Festkörperexpertin, wertvolle Tipps zur Fabrikation gegeben hat. Nicole Schmidt danke ich für die Hilfe mit Chemikalien und Software und Frau Gschwendtner für ihren großen Einsatz in der Administration.

Zu guter Letzt möchte ich den Menschen danken, die mir besonders nahe stehen, die mich in schweren Phasen begleitet und ertragen haben, sich mit mir gefreut haben und immer für mich da waren. Da ist zunächst meine Familie zu nennen, besonders meine Eltern, die mich, was immer auch kommt, bedingungslos unterstützen. Ich möchte hier auch meine guten Freundinnen Isabella Krämer und Frauke Seeßelberg erwähnen, seit Beginn des Studiums meine 'Mitphysikerinnen', mit denen ich mich über die Doktorarbeit und das Leben austauschen konnte und die mir eine große Stütze waren. Mein ganz besonderer Dank gilt meinem Partner Christian, der mein Leben so wunderschön macht, mit dem ich lustig und ernst sein kann, der mich versteht und mich unterstützt, wann immer ich es brauche.

Vielen lieben Dank euch allen!